Plasma Physics Reports, Vol. 30, No. 3, 2004, pp. 187–195. Translated from Fizika Plazmy, Vol. 30, No. 3, 2004, pp. 211–220.
Original Russian Text Copyright © 2004 by Pustovitov.

Error Field Amplification near the Stability Boundary of the Modes Interacting with a Conducting Wall

V. D. Pustovitov

Nuclear Fusion Institute, Russian Research Centre Kurchatov Institute,
pl. Kurchatova 1, Moscow, 123182 Russia

Received June 24, 2003

Abstract—The effect is considered of the amplification of an external resonant error field near the stability boundary of the so-called resistive wall modes observed in the DIII-D tokamak. The analysis is performed in a standard cylindrical approximation. The model is based on Maxwell's equations and Ohm's law; therefore, the results of the analysis are valid for any large-scale modes interacting with a conducting wall. In contrast to earlier approaches, the model considers the resonant field amplification as a dynamic effect. It is shown that, when the effect is the strongest, the stationary solutions proposed earlier are inapplicable. The problem of plasma response to a probing pulse of the resonant field of a given amplitude and duration is analyzed. The relationships obtained explain the basic features of the observed phenomena in the DIII-D tokamak and allow direct experimental verification. *© 2004 MAIK “Nauka/Interperiodica”.*

1. INTRODUCTION

It is well known that, in one of the most attractive tokamak scenarios, the so-called “advanced operation” [1–8], a serious obstacle to large β (the ratio of plasma pressure to magnetic pressure) can be the instability of external kink modes partially stabilized by a conducting wall, which are usually referred to as resistive wall modes (RWMs) [9–12]. In recent years, the RWM physics and methods for suppressing this instability have been actively studied in the DIII-D tokamak [13–26]. An impressive result of these studies is the demonstration of the steady sustainment of the plasma at β values twice exceeding the RWM instability threshold [20–26]. This was achieved when the measures taken earlier to suppress RWMs were combined with the suppression of the so-called error fields—weak stray fields breaking the tokamak symmetry. This happened after it was experimentally demonstrated that these fields play an important role in the RWM dynamics. Before this discovery, the results of experiments on RWM suppression by a feedback system in the DIII-D tokamak were much more modest [13–19].

Convincing experimental evidence that a slowly growing or saturated $n = 1$ perturbation measured outside the plasma is the plasma response to a static resonant error field was presented for the first time in [17, 18]. It was shown that the plasma reacts much more strongly to such a field when $\beta > \beta^{\text{no wall}}$, where $\beta^{\text{no wall}}$ is the stability limit for ideal MHD modes in the absence of a conducting wall. This effect has become an interesting new object of research [17, 18, 21–27] and has received the name “resonant field amplification” (RFA) [21–26].

The RFA effect was discovered experimentally; this happened quite recently, and it remains mysterious in many respects. The very first attempts to describe it are now being made in theory. When discussing the experimental results, paper [28] is always cited; until recently, it is the sole theoretical work completely devoted to the problem of the resonant interaction of plasma with external static perturbations at the stability boundary of RWMs. The interest in this paper stems primarily from the fact that the main statements of [28] qualitatively reflect the observed phenomena. However, the RFA effect is described in [28] rather sparingly, in the context of discussing another phenomenon—the experimentally observed damping of plasma toroidal rotation during RWM onset [13–26]. A recent paper [29] by the same author and on the same subject just briefly repeats the conclusions of [28] regarding RFA; basically, [29] is devoted to the calculation technique. Here, we consider the RFA effect in more detail and analyze the theoretical model and results of [28] to clarify some important points.

The aim of the present paper is to analyze the effect of external resonant magnetic perturbations (error fields) on the RWM dynamics. We are actually going to discuss the strong influence of a weak magnetic perturbation on the behavior of a tokamak discharge.

To describe the RFA effect, the existing theory [28] offers a certain steady-state solution that can become infinite at the RWM stability boundary. This solution is reproduced in different forms in other papers [21, 23, 26, 27, 29]. It will be shown below that, when the RFA effect is the strongest, the steady-state solutions proposed earlier are unacceptable, the process is essentially dynamic, and the “amplification factor” of the error field depends on the time during which the plasma passes through a “dangerous zone” near the RWM stability threshold. We will also consider the problem of plasma response to a pulse of the resonant field. We recall that the RFA effect was discovered with just such plasma probing [17, 18]. The switching on and off of the resonant field of a given amplitude was then exploited to study the quantitative RFA characteristics in DIII-D [21–26]. Naturally, plasma response to pulsed probing should be considered as a dynamic process. The model solution that was discussed in [28] and later in [21, 23, 26, 27, 29] does not describe the RFA dynamics.

Our analysis is performed in a standard cylindrical approximation. The basic equations and the statement of the problem are briefly described in the next section. A nontrivial step there is the closing of the problem by introducing a parameter that, in the strict approach, is determined by the structure of a magnetic perturbation in plasma. The necessary explanations concerning this step are given in Section 3. In Section 4, the amplification of the static error field by the plasma at the RWM stability boundary is considered. In Section 5, the problem of plasma response to a pulse of the resonant field is analyzed. In Section 6, our RFA model and the results obtained are compared to the model and results of [28]. In the conclusion, the basic results are summarized.

2. BASIC EQUATIONS AND THE FORMULATION OF THE PROBLEM

The complete solution of the problem requires the calculation of the perturbed magnetic field in the plasma, vacuum regions, and conducting metal shells outside the plasma. The field in the external (with respect to the plasma) region can be found if the perturbed magnetic field at the plasma boundary is known. In this case, only the plasma boundary appears in the problem as a surface on which boundary conditions should be set. The problem will be considered here in just such a formulation; namely, the plasma will be modeled by a certain perturbation with given properties. Arguments in favor of such a model are given in [30, 31]. The results of numerical calculations [32, 33] confirm that such modeling is quite reliable.

Perturbations in the external region are described by Maxwell’s equations

$$\nabla \times \mathbf{E} = -\frac{\partial \mathbf{B}}{\partial t}, \tag{1}$$

$$\nabla \cdot \mathbf{B} = 0, \tag{2}$$

$$\nabla \times \mathbf{H} = \mathbf{j}, \tag{3}$$

and Ohm’s law,

$$\mathbf{j} = \sigma \mathbf{E}. \tag{4}$$

Here, $\mathbf{E}$ and $\mathbf{H}$ are the electric and magnetic fields, respectively, $\mathbf{B} = \mu_m \mu_0 \mathbf{H}$ is the magnetic induction, μ_m is the magnetic permeability, σ is the conductivity ($\sigma = 0$ in vacuum), and $\mu_0 = 4\pi \times 10^{-7}$ H/m is the permeability of a vacuum.

In tokamaks, the conducting walls are thin compared to the characteristic scales of the problem; therefore, in an RWM analysis, the walls can be regarded as thin shells. For a thin shell with a constant thickness, equations (1)–(4) reduce to

$$\mu_0 \sigma_s \frac{\partial}{\partial t} B_n = \mathbf{n} \cdot \nabla (B_n^{\text{out}} - B_n^{\text{in}}), \tag{5}$$

where σ_s is the surface conductivity (for real conductors, we have $\sigma_s = \sigma d$, d being the wall thickness), $\mathbf{n}$ is the external unit normal to the surface, $B_n = \mathbf{n} \cdot \mathbf{B}$, $\mathbf{B}^{\text{out}}$ is the value of $\mathbf{B}$ on the outer side of the shell (the side to which the normal is directed), and $\mathbf{B}^{\text{in}}$ is $\mathbf{B}$ on the inner side. The model is described in more detail in [30, 31].

Resonant field amplification is observed in experiments as an increase in a magnetic perturbation near the wall, where the measuring magnetic probes are located [21–26]. This increase could be described by Eq. (5) if the jump in the derivative on its right-hand side could be expressed through B_n (the unknown function) and a perturbation from external sources (a parameter). A similar problem was solved in [30, 31] in a cylindrical approximation. Here, we will use the results of [30, 31], ignoring toroidicity. In [21, 23, 26, 28, 29], the RFA effect was also analyzed with the use of equations for a cylindrical configuration. Below, we will consider a cylindrical plasma column surrounded (at a certain distance) with a coaxial conducting shell.

We describe a magnetic field perturbation in vacuum by its radial component

$$b_r = \sum b_m(r, t) \exp(im\theta - in\zeta), \tag{6}$$

where t is time and r, θ, and $\zeta = z/R$ are cylindrical coordinates related to the symmetry axis. Here, instead of the length z, we have introduced the angular coordinate ζ, which is an analogue of the toroidal angle, with $2\pi R$ being the length of the equivalent torus. We are interested in perturbations with low poloidal and toroidal wavenumbers (m and n, respectively). In this case, instead of exact expressions for b_m [34], one can use the approximate expression

$$b_m = B_m^{\text{in}} x^{-\mu-1} + B_m^{\text{out}} x^{\mu-1}, \tag{7}$$

where $x = r/r_w$, r_w is the radius of the conducting wall, $\mu = |m|$ and B_m^{in} and B_m^{out} are time-dependent complex amplitudes. The first term in Eq. (7) describes the contribution to b_m from the inner region with respect to the point x, and the second one, from the outer region. One should remember that, at $x < 1$, the field of the currents flowing in the conducting wall must be included in B_m^{out}, while at $x > 1$, this field must be included in B_m^{in}.

In cylindrical geometry, Eq. (5) for long-wavelength perturbations reduces with the help of Eq. (7) to the following set of equations (see [30, 31] for details):

$$\tau_w \frac{\partial B_m}{\partial t} = \Gamma_m B_m + 2\mu B_m^{\text{ext}}, \tag{8}$$

where $\tau_w = \mu_0 \sigma_s r_w = \mu_0 \sigma d r_w$ is the characteristic time during which the magnetic field penetrates through the wall, $B_m = b_m(r_w) = B_m^{\text{in}} + B_m^{\text{out}}$ is the amplitude of the (m, n)th harmonic of the radial perturbed magnetic field at the wall, B_m^{ext} is that part of B_m that is created by all the sources located outside the shell (in the region $r > r_w$). We note that here τ_w is a constant determined by the wall properties only. The quantity $\tau_w/2\mu$ is sometimes called the resistive wall time.

The parameter Γ_m in Eq. (8) is formally defined by the equality [30, 31]

$$\left.\frac{r b'_m}{b_m}\right|_{\text{in}} \equiv -(\mu + 1) - \Gamma_m, \tag{9}$$

where the index "in" refers to the value at the inner side of the shell, $r = r_w - 0$, and the prime stands for the derivative with respect to the radius r. To make use of Eq. (8) for calculating B_m, we must somehow specify the parameter Γ_m.

3. PARAMETER Γ_m

Substituting expression (7) into equality (9), we obtain

$$\Gamma_m = -2\mu \frac{B_m^{\text{out}}}{B_m^{\text{in}} + B_m^{\text{out}}}, \tag{10}$$

where $B_m^{\text{out}} = B_m^{\text{wall}} + B_m^{\text{ext}}$ is the field created by all the sources external to the plasma. In our case, there are three such sources: the currents induced in the wall; the known currents in the correcting coils; and, generally, unknown sources of the error field. The denominator of expression (10) contains the total field, which can be experimentally determined using magnetic probes. Then, in order to determine B_m^{out} in the numerator, it is necessary to know B_m^{in}—the magnetic field perturbation created by the plasma currents.

In the vacuum gap between the plasma and the wall, we have

$$\frac{r b'_m}{b_m} = -(\mu + 1) - \frac{2\mu \Gamma_m x^{2\mu}}{2\mu + \Gamma_m (1 - x^{2\mu})}. \tag{11}$$

Therefore, the Γ_m value determined by equality (9) can be expressed through $r b'_m / b_m$ at the plasma surface (at $x = r_p/r_w$). Finally, the strict approach requires the calculation of the perturbed magnetic field in the plasma.

Numerical calculations show that variations in the field $\mathbf{B}^{\text{ext}}$ created by the correction coils do not distort the structure of the mode in the plasma at fixed parameters of the equilibrium configuration [12, 19, 35–39]. This effect was investigated in [19] and was called "mode rigidity." It can be explained by the fact that a magnetic field perturbation in the plasma is determined by the current and pressure profiles, which change insignificantly under the action of a weak external field $\mathbf{B}^{\text{ext}}$. This was discussed in more detail in [31]. Certainly, the aforesaid applies to the radial dependence of the perturbation amplitude, but does not allow us to judge its phase. In many cases, the assumption that the phase of the complex quantity b_m is preserved can be quite acceptable; however this point requires a special analysis.

The invariability of $b_m(r)$ in the plasma means that the value of $r b'_m / b_m$ at the plasma surface must remain unchanged when either $\mathbf{B}^{\text{ext}}$ or the mode amplitude vary. Accordingly, Γ_m also will not change.

Following [30, 31] and leaning on the results of [12, 19, 35–39], we will consider the quantity Γ_m in Eq. (8) to be a given (independent of B_m and B_m^{ext}) characteristic of the unperturbed equilibrium configuration. When RWMs are stabilized by a feedback system, the rigidity of the mode structure in a plasma is confirmed not only by MHD calculations, but also by the experimental results from DIII-D [19]. Thus, one can consider the model with a given Γ_m, in particular, with $\Gamma_m = \text{const}$, to be well justified. In some cases below, the latter restriction on Γ_m will not be needed. These cases will be expressly specified.

The parameter Γ_m has a simple physical meaning. According to Eq. (8), in the absence of an external magnetic perturbation ($B_m^{\text{ext}} = 0$), we have

$$\Gamma_m = \tau_w(\gamma_0 + i n \Omega_0), \tag{12}$$

where γ_0 is the growth (decay) rate and Ω_0 is the angular frequency of the mode toroidal rotation. The latter quantities can be found from magnetic measurements outside the plasma, as was done in the DIII-D tokamak [22]. This allows one to close the problem without finding $b_m(r)$ in the plasma.

The plasma is stable at $\gamma_0 < 0$ and unstable at $\gamma_0 > 0$. The stability boundary corresponds to $\gamma_0 = 0$. RWM rotation is never very fast [12–14, 22]. Most dangerous is the full stop of mode rotation—the so-called mode locking [9]. This general information, which is actually a simple phenomenological description of Γ_m, turns out to be sufficient for modeling the RFA effect at $\gamma_0 \leq 0$.

4. AMPLIFICATION OF A STATIC ERROR FIELD NEAR THE RWM STABILITY BOUNDARY

For Γ_m = const and B_m^{ext} = const, which corresponds to a given equilibrium state and fixed external conditions, the solution to Eq. (8) is

$$B_m = -\frac{2\mu}{\Gamma_m}B_m^{\text{ext}} + C\exp(\Gamma_m t/\tau_w), \tag{13}$$

where C is a constant specified by the initial conditions. The additive constant proportional to B_m^{ext} and determining the level of the steady-state solution depends on the plasma properties through the Γ_m value. At $\Gamma_m = 0$, the right-hand side of expression (13) is singular. This singularity can be related either to the accepted assumption Γ_m = const or simply to the fact that the point $\Gamma_m = 0$ must be considered separately. In any case, the presence of Γ_m in the denominator of expression (13) shows that one must pay close attention to the range of small Γ_m values when the plasma response to a static external helical field is being investigated.

In [23, 26–29], it was proposed to consider RFA, at best, as a quasi-steady process. The time dependence in the equations was therefore ignored, so that the solutions presented in [21, 23, 26–29] actually correspond to the steady state described by formula (13) with $C = 0$. As a result, the RFA effect in [23, 26–29] was directly related to the zeroing of the denominator. In particular, it was stated in [29] that this singularity dominates the physics of resistive wall modes and error field amplification.

The description of the RFA effect with the help of formula (13) at $C = 0$ is incomplete or even incorrect. It is obviously incorrect in the most interesting case of $\Gamma_m = 0$. At $\Gamma_m = 0$ and B_m^{ext} = const, Eq. (8) has the following linearly growing solution without singularities:

$$B_m = B_m^0 + 2\mu B_m^{\text{ext}}\frac{t}{\tau_w}. \tag{14}$$

On short time scales, such a growth of B_m is not dangerous, the more so as the growth rate of B_m is proportional to $|B_m^{\text{ext}}|$ and, therefore, can be small. However, at $t \gg \tau_w$, solution (14) gives very large values of B_m. For example, at $t = (50\text{–}100)\tau_w$, which is well below the pulse duration in the DIII-D tokamak, the amplification factor in solution (14) is equal to 200–400. Such an amplification of the resonant field may be considered unlimited since it can result in intolerably large values of B_m. However, this "physical" infinity differs radically from the infinity in expression (13) at $\Gamma_m = 0$.

Generally, solution (14) can be used at any Γ_m satisfying the condition $|\Gamma_m B_m| \ll 2\mu|B_m^{\text{ext}}|$, which, at $B_m^0 = 0$ in formula (14), reduces to

$$|\Gamma_m t| \ll \tau_w. \tag{15}$$

On short time intervals, when inequality (15) is satisfied, no additional restrictions on Γ_m are required. Therefore, it can be stated, e.g., that, if the field B_m is initially zero, it will reach a level of $0.2\mu B_m^{\text{ext}}/|\Gamma_m|$ over the time $t = 0.1\tau_w/|\Gamma_m|$ at any Γ_m. At $|\Gamma_m| = 0.1$, this corresponds to the amplification of the error field by a factor of 2μ.

Condition (15) on t becomes weaker and the applicability range of solution (14) expands when Γ_m evolves toward $\Gamma_m = 0$. This means, in particular, that the effect of the resonant error-field amplification must be observed not only near the stability threshold of conventional RWMs, but also in the vicinity of all other zeros of Γ_m. An important point in our problem is the interaction of the plasma-induced perturbation with the wall; therefore, the term RWM should be considered here as a generic name of all such perturbations, including those destabilized by the current, rather than only by the plasma pressure.

If $\operatorname{Re}\Gamma_m < 0$, then, after a certain period of time, only the first term in solution (13) will survive. This term describes the equilibrium deformation of the plasma column under the action of the static resonant field $\mathbf{B}^{\text{ext}}$. In this case, the RWM is stable by definition; however, this formally stable solution may not be achieved in practice if it gives too large values of B_m at $\Gamma_m \longrightarrow 0$.

Solution (13) with $C = 0$ can also be used at $\Gamma_m = \Gamma_m(t)$ when the left-hand side of Eq. (8) is small. This condition reduces to

$$\tau_w\left|\frac{\partial}{\partial t}\frac{1}{\Gamma_m}\right| \ll 1, \tag{16}$$

since in this case $\Gamma_m B_m = -2\mu B_m^{\text{ext}}$ = const. If, for example, the value of $1/\Gamma_m$ increases by a factor of 10 over the time on the order of $100\tau_w$, then the first term on the right-hand side of expression (13) will increase tenfold. The growth rate of B_m in the course of such Γ_m evolution is much smaller than that given by formula (14). Nevertheless, we again obtain large values of B_m.

Thus, in the dynamic approach, when the B_m evolution is described by formula (14), or in a quasi-steady case, when B_m is described by the first term in expression (13), the static resonant field $\mathbf{B}^{\text{ext}}$ is amplified to very large values (in our model, B_m increases without bounds as $\Gamma_m \longrightarrow 0$). According to formula (10), the equality $\Gamma_m = 0$ corresponds to $B_m^{\text{out}} = 0$. In this case, B_m is the field created by the plasma only and measured at the point $r = r_w$. At the plasma boundary, the amplitude of the perturbed field $b_m(r_p)$ is $(r_w/r_p)^{\mu+1}$ times larger. Large B_m values, irrespective of their origin, may lead to the loss of equilibrium and the collapse of a discharge.

In any case, an important fact is that the amplification factor is time-dependent. This is illustrated most clearly by formula (14) for locked modes at the stability boundary $\Gamma_m = 0$.

At $\gamma_0 \le 0$, the rate of change of B_m is limited from above by the value $2\mu B_m^{\text{ext}}/\tau_w$, which can be very small. Slow plasma deformation related to the slow growth of B_m can cause the slow deterioration of plasma confinement, which can result in a slowing down the growth of β or even lead to a decrease in β. This can stop the growth of γ_0 or even make γ_0 decrease, eventually resulting in the reduction of B_m and the returning of the discharge to its former state. In this case, a “soft” restriction of β will be observed: the discharge will remain stable, resisting an increase in β by an appreciable increase in losses near the RWM stability threshold.

The elimination of $\mathbf{B}^{\text{ext}}$ is the most radical way to resolve the problem. In this case, Eq. (8) will provide a “good” solution even at $\Gamma_m = 0$. However, to completely remove $\mathbf{B}^{\text{ext}}$ is not an easy matter. To avoid too large an amplification of $\mathbf{B}^{\text{ext}}$ near the RWM stability boundary, one must somehow bypass the point $\Gamma_m = 0$. A favorable factor resulting in the shifting of Γ_m away from zero into the complex plane is mode rotation. At $\Omega_0 \neq 0$, the singularity in expression (13) is eliminated. In this case, the RFA effect is still possible, but the field amplification is weaker than at $\Omega_0 = 0$. It worth noting that, in any case, the amplification factor is finite and depends on how long plasma stays in a state with a given Γ_m value.

5. PLASMA RESPONSE TO A PULSE OF THE RESONANT FIELD

Let an additional resonant magnetic field be applied over a finite time interval,

$$B_m^{\text{ext}} = \begin{cases} B_m^{er}, & 0 < t < T \\ 0, & t < 0, t > T, \end{cases} \tag{17}$$

where B_m^{er} is a constant. It is such pulses with well-controlled amplitudes that are used in DIII-D experiments to study the influence of external resonant magnetic perturbations on the RWM dynamics [17, 18, 21–26].

At a constant external perturbation, the general solution to Eq. (8) is

$$B_m = B_m^0 \exp(\Gamma_m t/\tau_w) + \frac{2\mu}{\Gamma_m} B_m^{\text{ext}}[\exp(\Gamma_m t/\tau_w) - 1]. \tag{18}$$

This solution for B_m is applicable at any time. It is only necessary to remember that the constants B_m^0 in solution (18) are different at $t = 0$ and after the end of pulse (17). Clearly, at $\Gamma_m = 0$, solution (18) reduces to formula (14).

We assume that $\gamma_0 = \operatorname{Re}\Gamma_m/\tau_w < 0$, i.e., the plasma is stable with respect to RWMs and, in the initial state (at $t = 0$), $B_m^0 = 0$. In this case, when pulse (17) is switched on, we have

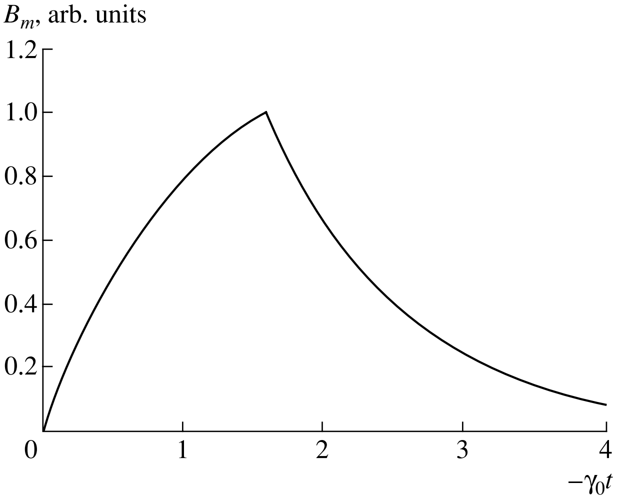

Fig. 1. Plasma response to a short pulse of the resonant field ($-\gamma_0 T = 1.6$).

$$\frac{\partial B_m}{\partial t} = \frac{2\mu}{\tau_w} B_m^{er}. \tag{19}$$

The B_m value grows linearly as long as the inequality $|\Gamma_m B_m| \ll 2\mu B_m^{er}$ is satisfied, which reduces to condition (15).

If probing pulse (17) is very short, $T \ll 1/|\gamma_0|$, B_m grows linearly till the end of the pulse, reaching the value

$$B_m = \frac{2\mu}{\tau_w} B_m^{er} T. \tag{20}$$

Just after the pulse is switched off, we have

$$\frac{\partial B_m}{\partial t} = \frac{\Gamma_m B_m}{\tau_w} = \frac{2\mu}{\tau_w^2} B_m^{er} \Gamma_m T. \tag{21}$$

This decay rate of B_m turns out to be $|\gamma_0|T$ times smaller than the growth rate defined by Eq. (19). We note that formulas (19), (20) and (21) are also applicable at $\gamma_0 = 0$.

In experiments, the right-hand sides of formulas (19) and (20) should be known, while the left-hand sides can be measured. Thus, formulas (19) and (20) allow direct experimental verification. Equation (21) can be used to experimentally estimate the perturbation decay rate entering into the right-hand side of this equation.

The pulse can be considered short if B_m does not reach a saturation level. Solution (18) for this case is shown in Fig. 1. If probing pulse (17) is long enough

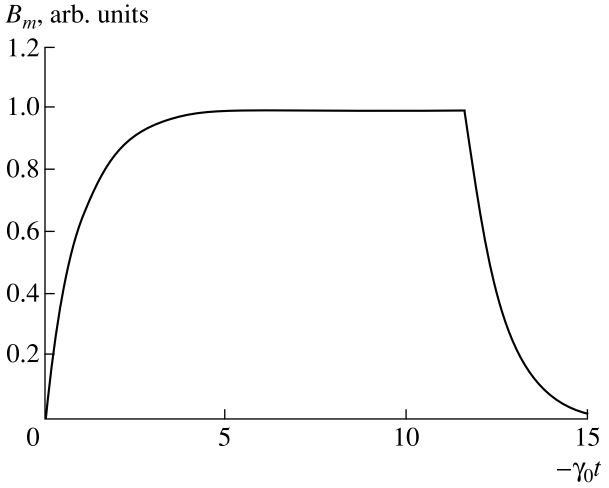

Fig. 2. Plasma response to a long pulse of the resonant field ($-\gamma_0 T = 11.6$).

($T \gg 1/|\gamma_0|$), the exited field (18) grows up to the saturation level

$$B_m^{\max} = -\frac{2\mu}{\Gamma_m} B_m^{er}. \quad (22)$$

The initial growth of a perturbation is described by formula (19) and is determined by the properties of the conducting wall only. Just after the pulse is switched off, we have

$$\frac{\partial B_m}{\partial t} = \frac{\Gamma_m B_m}{\tau_w} = -\frac{2\mu}{\tau_w} B_m^{er}. \quad (23)$$

In this case, the decay rate of B_m is equal to growth rate (19) at the instant at which the probing pulse is switched on. Two latter formulas can also be experimentally verified. The response of B_m to a long pulse of the resonant field is illustrated by Fig. 2. The constants $\gamma_0 T$ in Figs. 1 and 2 are chosen so that these figures could be compared to the measurement results reported in [22]. The agreement turns out to be very good.

It can be seen from expression (10) that, in the absence of a plasma, $\Gamma_m = -2\mu$. In this case, Eq. (22) yields $B_m^{\max} = B_m^{er}$. The amplification of the resonant field ($|B_m^{\max}| > B_m^{er}$) will happen if the ratio $2\mu/|\Gamma_m|$ becomes larger than unity in the course of plasma evolution (an increase in β or a change in the current profile). It follows from (22) that

$$|B_m^{\max}| = \frac{2\mu B_m^{er}}{\tau_w \sqrt{\gamma_0^2 + n^2 \Omega_0^2}}. \quad (24)$$

This formula shows that the effect of amplification is most pronounced when γ_0 passes through zero at the RWM stability boundary and, in addition, the mode does not rotate. At small values of γ_0, the amplification of the resonance field occurs at

$$|n\Omega_0 \tau_w| < 2\mu. \quad (25)$$

In the opposite case, we have $|B_m^{\max}| < B_m^{er}$, which can be called resonant field attenuation.

It should be noted that we are always speaking here about the frequency of toroidal rotation of a magnetic perturbation. This frequency can be measured using a set of magnetic probes. In DIII-D experiments, in the stage of RWM onset and growth, this frequency is substantially smaller than the frequency of plasma rotation, Ω_p [12–14, 22]. According to [14], $\Omega_0 \sim \tau_p^{-1} \ll \Omega_p$ from the onset of RWMs.

Although field (22) can be large, the plasma response to an external resonant field at small negative Γ_m values nevertheless remains finite. Moreover, when a probing pulse is switched off [$t > T$ in formula (17)], the field B_m exponentially decays to zero (see Figs. 1, 2). Such behavior of the measured field B_m has been repeatedly observed in the DIII-D tokamak [17, 18, 21–23, 25, 26].

6. DISCUSSION

Let us compare our analysis to that of [28]. This is not a difficult task since, in [28], the RFA effect was also analyzed in a cylindrical approximation. In that paper, one mode of perturbation was considered and its amplitude was described by an equation similar to Eq. (8). A quantity analogous to Γ_m in Eq. (8) was also assumed to be constant (independent of B_m and B_m^{ext}). However, the choice of this constant was different.

Equation (8) is a consequence of Maxwell's equations and Ohm's law for a conducting wall; therefore, it contains only the wall parameters (τ_w) and the characteristics of the perturbed magnetic field. In [28], the problem was formulated in other terms (certain s and α), which are related to γ_0 and Ω_0 in a rather complicated manner even in a cylindrical model. According to Eq. (8), $\Gamma_m = 0$ with $B_m^{\text{ext}} = 0$ corresponds to a steady state in which B_m does not change with time. At $\gamma_0 = \mathrm{Re}\Gamma_m/\tau_w < 0$, the perturbation B_m decays in the absence of an external resonant field, while at $\gamma_0 > 0$, it increases exponentially. The RWM stability threshold is naturally the point $\gamma_0 = 0$. As was shown above, the RFA effect is strongest in the vicinity of this point.

In [28], the stability boundary was defined in a different way: by the formal equality $s = 0$, without reference to Eq. (8). We will not discuss here the reasons resulting in this difference because, in this case, we would have to go into details of Boozer's model related to the introduction of a certain "control surface" [28, 40–42]. Instead, we will only mention one of the essential statements of [28], supported there by calculations performed in a cylindrical model: the stability boundary in [28] is called a state in which $\gamma_0 \neq 0$ in the presence of mode rotation. For a thus defined stability boundary, the formulas of [28] yield $\gamma_0 > 0$, which is, however, against all logic. Thoroughly examining these formulas, one finds a mistake in the sign of γ_0. However, $\gamma_0 < 0$ as a stability boundary also looks strange. Specifically, at small α, the expression obtained in [28] for the RWM growth rate at Boozer's stability boundary can be written in the form

$$\gamma_0 = -n\Omega_{\max}\left(1-\sqrt{1-\Omega_0^2/\Omega_{\max}^2}\right), \tag{26}$$

where

$$n\Omega_{\max} \equiv \frac{\mu}{\tau_w(1-c)}, \tag{27}$$

$c \equiv (r_p/r_w)^{2\mu}$; and r_p and r_w are the radii of the plasma and the conducting wall, respectively. For $c \neq 1$ (in DIII-D, $c \approx 0.2$) and $\Omega_0 \neq 0$, this equality yields $\gamma_0 < 0$. However, in our case, $\gamma_0 = 0$ at the stability boundary, irrespective of the Ω_0 and c values.

A more thorough examination of the results of [28] reveals another peculiar feature of the model used in that paper: in a general case, it implicitly contains a restriction on the RWM rotation frequency. For example, it follows from the formulas of [28] that

$$\max|\Omega_0| = \Omega_{\max}, \tag{28}$$

where Ω_0 is the quantity entering into expression (26) and $\Omega_{\max}$ is the quantity defined by formula (27). With such a restriction on Ω_0, for the DIII-D tokamak with $c \approx 0.2$, we would obtain from formula (24) that $|B_m^{\max}| > B_m^{er}$ at the stability boundary (either at $\gamma_0 = 0$ or at Boozer's stability boundary). However, Eq. (24) also allows the opposite result if the mode rotation is fast enough.

Restriction (28) arises in [28] only as a consequence of model manipulations in which the quantity Ω_0 appears as a parameter, without any equation for it. Also, the main conclusion of [28] about the damping of plasma rotation at the RWM stability boundary is drawn without reference to the equations of plasma motion.

The strong damping of plasma toroidal rotation at $\beta > \beta^{\text{no wall}}$, accompanied by the fast RWM growth and (if special measures are not taken) by the discharge collapse, is typical of the DIII-D tokamak [13–25]. The statement in [28] agrees with the observations, although, strictly speaking, it remained unproved in [28] even with in the frame of the accepted model assumptions.

If we lean on Eqs. (1)–(4) only, we have no grounds to draw conclusions about plasma rotation, because the latter should be determined from the equations of plasma motion. The quantity Ω_0 entering into formulas (12) and (24) is the frequency of RWM rotation at $\mathbf{B}^{\text{ext}} = 0$, which can differ substantially from the frequency of plasma toroidal rotation [12–14]. Equation (8) allows us to make judgements only about the perturbation amplitude and phase. Therefore, a comparison of our results with the results of [28] cannot go beyond conclusions drawn about RFA, by which the damping of plasma rotation was explained in [28].

According to formulas (13), (18), (22), and (24), the RFA effect is the strongest at $\gamma_0 = 0$, whereas in [28], the point at which RFA is maximum is shifted to negative γ_0 values for $\Omega_0 \neq 0$, as is described by formula (26). The greater the Ω_0 value, the larger this shift. The shift disappears at $s = \alpha = 0$ only; however, in this case, we encounter another, much more serious contradiction: the solution proposed in [28] [similar to that given by Eq. (13) with $C = 0$] turns out unattainable. Instead of such a solution, one must use equality (14).

Formulas (13), (18), (22), and (24) show that mode rotation efficiently counteracts the RFA effect even at the RWM stability boundary. For example, it follows from formula (24) that $|B_m^{\max}| < B_m^{er}$ if Ω_0 does not satisfy inequality (25) and $B_m^{\max} \longrightarrow 0$ when $\Omega_0 \longrightarrow \infty$. However, in [28], large values of Ω_0 are forbidden: $|\Omega_0| \leq \Omega_{\max}$ (note that this restriction was not commented on in [28]; most likely, it was merely not perceived), which, first of all, is inexplicable and, besides, substantially underestimates the role of rotation in suppressing RFA.

In [28], the RFA effect was considered in a steady-state approximation. In this case, B_m is described by formula (13) with $C = 0$. In [28], it was proposed to use such a solution at the RWM stability boundary, where it tends to infinity, which contradicts the initial assumption of [28] about the steady-state nature of RFA. Meanwhile, Eq. (8), which is the starting point of our analysis, shows that, at $\Gamma_m = 0$, a steady-state solution is possible only in the trivial case $B_m^{\text{ext}} = 0$; however, in the case of $B_m^{\text{ext}} \neq 0$, which is of interest to us, it is slowly growing solution (14) that is valid.

The difference between our results and the results of [28] is related to the difference in the formulations of the models. A detailed analysis of Boozer's model is a separate problem. The aforementioned contradictions in applications show that this model is to be revised.

Our model is based on Eqs. (1)–(4). A transition from Eqs. (1)–(4) to Eq. (8) uses only geometrical assumptions (cylindrical geometry, a thin-wall approximation, and long-wavelength perturbations) that underlie whole sections of the MHD plasma theory. The sole nonstandard element is the assumption Γ_m = const (although not always used here), which, in an ideal case, is to be replaced by a proper equation for Γ_m. However, there are solid reasons for such an assumption, as was discussed in Section 3. All our calculations are much simpler than those in [28], which makes them persuasive and allows a reader to independently reproduce all the chain of the proofs offered here.

7. CONCLUSIONS

The proposed RFA model, which is based on Eq. (8), explains the main features of the phenomena observed in experiments carried out in the DIII-D tokamak [17, 18, 21–26]:

(i) The RFA effect is the strongest at the RWM stability boundary [21–26], as follows from Eqs. (13), (18), (22) and (24).

(ii) The growth of B_m can be slow, but can become faster [17, 18] if the plasma, being stable, evolves toward $\Gamma_m \longrightarrow 0$ [see Eqs. (8) and (18)].

(iii) When a pulse of the resonant field is applied, B_m can either grow slowly or, after reaching the saturation level, remain constant [22]. This is shown in Figs. 1 and 2, which illustrate relationships (19), (20), and (22).

(iv) After the pulse is switched off, the B_m perturbation can decay [17, 18] if $\gamma_0 < 0$ [see (21) and Figs. 1, 2].

Our analysis also shows that any mode rotation (even slow) eliminates singularities in expressions (13), (18), (22) and (24), thus significantly reducing the danger of RFA. It should be stressed that we are speaking here about a direct relation between RFA and mode rotation. Plasma rotation, however, never appears in Eqs. (1)–(4), on which our RFA model is based. Rotation certainly must somehow affect the $b_m(r)$ behavior in the plasma and, as a consequence, the Γ_m value. The determination of Γ_m (to be exact, the linking of Γ_m to specific experimental conditions) is a separate task. As was shown above, the RFA effect can be satisfactorily described without detailed information about Γ_m. In our analysis, Γ_m is prescribed as a parameter with properties inferred from numerical calculations [12, 19, 35–39]; this is reliably confirmed by experiments in DIII-D [19].

It can be seen, e.g., from Eqs. (13) and (22) that the RFA effect should manifest itself at $|\Gamma_m| < 2\mu$. The sign of γ_0 is not important here. However, it is much more difficult to observe this effect at $\gamma_0 > 0$, because of the RWM instability. Mode rotation increases $|\Gamma_m|$ and thus always acts against RFA.

The point $\Gamma_m = 0$ (locked modes at the stability boundary) is the most dangerous. At this point, theoretically, an external stationary resonant field (error field) can be amplified without bound if the plasma stays long in this intermediate state. In experiments, this point should be passed as soon as possible for the perturbation to have no time to grow up to a large amplitude. For example, it follows from expression (14) that, if the point $\Gamma_m = 0$ is passed in the quite short time of $10\tau_w$, then the error field with $m = 2$ is amplified by a factor of 40. Let us emphasize that time is a crucial factor here. At $\Gamma_m = 0$, the RFA process is dynamic, the growth of B_m is described by expression (14), and the steady state is not reached. The time dependence of the amplification factor of a stationary error field is an essential point in which our results differ from all previous ones [21, 23, 26–29].

At $\Gamma_m = 0$, even a weak error field can lead to a strong deformation of the plasma column. The concept of a "precision tokamak" [43] appears to be quite reasonable from this standpoint. The aim is complete suppression of the resonant error field. For this purpose, a tokamak should be equipped with a system of correcting coils, as was done, e.g., in the DIII-D tokamak [12, 14, 16–26] and is planned for the Korean KSTAR tokamak [44]. It is now becoming clear that such a system is necessary not only for suppressing RWMs and passing to the range $\beta > \beta^{\text{no wall}}$, but also for weakening the dangerous consequences of RFA at $\beta < \beta^{\text{no wall}}$.

The measurements of the rates of change of B_m and the value of B_m itself by probing the plasma using a pulse of the resonant field [22] can be used to determine the values of τ_w, γ_0, and Γ_m by formulas (19)–(23). The results of our analysis provide a simple theoretical model of RFA, explain the phenomena observed, and allow direct experimental verification in terms of a number of parameters.

ACKNOWLEDGMENTS

I am grateful to Yu.V. Gribov and V.S. Mukhovatov for drawing my attention to this problem and encouraging this study, to N.V. Ivanov for his support, and to V.D. Shafranov for discussing the results obtained. This work was supported in part by the Nuclear Science and Technology Department of the RF Ministry for Atomic Energy and the Russian Federal Program for State Support of Leading Scientific Schools (grant no. 2024.2003.2).

REFERENCES

1. T. S. Taylor, H. St. John, A. D. Turnbull, *et al.*, Plasma Phys. Controlled Fusion **36**, B229 (1994).
2. A. D. Turnbull, T. S. Taylor, M. S. Chu, *et al.*, Nucl. Fusion **38**, 1467 (1998).
3. C. Gormezano, Plasma Phys. Controlled Fusion **41**, B367 (1999).
4. A. Bondeson, D.-H. Liu, F. X. Söldner, *et al.*, Nucl. Fusion **39**, 1523 (1999).
5. T. Fujita, Y. Kamada, S. Ishida, *et al.*, Nucl. Fusion **39**, 1627 (1999).
6. V. S. Chan, C. M. Greenfield, L. L. Lao, *et al.*, Nucl. Fusion **40**, 1137 (2000).
7. O. Gruber, R. Wolf, H.-S. Bosch, *et al.*, Nucl. Fusion **40**, 1145 (2000).
8. Y. Kamada and JT-60 Team, Nucl. Fusion **41**, 1311 (2001).
9. *ITER Physics Basis*, Nucl. Fusion **39**, 2137 (1999).
10. A. B. Mikhailovskii and B. N. Kuvshinov, Fiz. Plazmy **21**, 835 (1995) [Plasma Phys. Rep. **21**, 789 (1995)].
11. D. J. Ward and A. Bondeson, Phys. Plasmas **2**, 1570 (1995).

12. A. D. Turnbull, D. P. Brennan, M. S. Chu, *et al.*, Nucl. Fusion **42**, 917 (2002).
13. A. M. Garofalo, A. D. Turnbull, M. E. Austin, *et al.*, Phys. Rev. Lett. **82**, 3811 (1999).
14. A. M. Garofalo, A. D. Turnbull, E. J. Strait, *et al.*, Phys. Plasmas **6**, 1893 (1999).
15. E. J. Strait, A. M. Garofalo, M. E. Austin, *et al.*, Nucl. Fusion **39** (11Y), 1977 (1999).
16. A. M. Garofalo, E. J. Strait, J. M. Bialek, *et al.*, Nucl. Fusion **40**, 1491 (2000).
17. A. M. Garofalo, J. Bialek, A. H. Boozer, *et al.*, in *Proceedings of the 18th IAEA Fusion Energy Conference, Sorrento, 2000* (IAEA, Vienna, 2001), Report IAEA-CN-77/EXP3/01 (http://www.iaea.org/programmes/ripc/physics/).
18. A. M. Garofalo, M. S. Chu, E. D. Fredrickson, *et al.*, Nucl. Fusion **41**, 1171 (2001).
19. M. Okabayashi, J. Bialek, M. S. Chance, *et al.*, Phys. Plasmas **8**, 2071 (2001).
20. L. C. Johnson, M. Okabayashi, A. M. Garofalo, *et al.*, in *Proceedings of the 28th EPS Conference on Controlled Fusion and Plasma Physics, Funchal, 2001*; ECA **25A**, 1361 (2001); http://www.cfn.ist.utl.pt/EPS2001/fin/pdf/P4.008.pdf.
21. M. Okabayashi, J. Bialek, M. Chance, *et al.*, J. Plasma Fusion Res. SERIES **5**, 42 (2002).
22. A. M. Garofalo, T. H. Jensen, L. C. Johnson, *et al.*, Phys. Plasmas **9**, 1997 (2002).
23. M. Okabayashi, J. Bialek, M. S. Chance, *et al.*, Plasma Phys. Controlled Fusion **44**, B339 (2002).
24. A. M. Garofalo, R. J. La Haye, and J. T. Scoville, Nucl. Fusion **42**, 1335 (2002).
25. E. J. Strait, J. Bialek, N. Bogatu, *et al.*, in *Proceedings of the 19th IAEA Fusion Energy Conference, Lyon, 2002*, Paper IAEA-CN-94/EX/S2-1.
26. E. J. Strait, J. Bialek, N. Bogatu, *et al.*, Nucl. Fusion **43**, 430 (2003).
27. M. S. Chu, M. S. Chance, A. H. Glasser, and M. Okabayashi, Nucl. Fusion **43**, 441 (2003).
28. A. H. Boozer, Phys. Rev. Lett. **86**, 5059 (2001).
29. A. H. Boozer, Phys. Plasmas **10**, 1458 (2003).
30. V. D. Pustovitov, Fiz. Plazmy **27**, 209 (2001) [Plasma Phys. Rep. **27**, 195 (2001)].
31. V. D. Pustovitov, J. Plasma Fusion Res. SERIES **5**, 278 (2002).
32. A. Bondeson, Y. Q. Liu, D. Gregoratto, *et al.*, Nucl. Fusion **42**, 768 (2002).
33. A. Bondeson, Y. Q. Liu, D. Gregoratto, *et al.*, Phys. Plasmas **9**, 2044 (2002).
34. A. I. Morozov and L. S. Solov'ev, in *Reviews of Plasma Physics*, Ed. by M. A. Leontovich (Gosatomizdat, Moscow, 1963; Consultants Bureau, New York, 1966), Vol. 2.
35. Y. Q. Liu and A. Bondeson, Phys. Rev. Lett. **84**, 907 (2000).
36. Y. Q. Liu, A. Bondeson, C. M. Fransson, *et al.*, Phys. Plasmas **7**, 3681 (2000).
37. A. Bondeson, Yueqiang Liu, C. M. Fransson, *et al.*, Nucl. Fusion **41**, 455 (2001).
38. M. S. Chance, M. S. Chu, M. Okabayashi, and A. D. Turnbull, Nucl. Fusion **42**, 295 (2002).
39. S. Yu. Medvedev and V. D. Pustovitov, submitted to Fiz. Plazmy.
40. A. H. Boozer, Phys. Plasmas **5**, 3350 (1998).
41. A. H. Boozer, Phys. Plasmas **6**, 3180 (1999).
42. J. Bialek, A. H. Boozer, M. E. Mauel, and G. A. Navratil, Phys. Plasmas **8**, 2170 (2001).
43. A. P. Popryadukhin, Preprint No. 038-88 (Moscow Institute of Engineering Physics, Moscow, 1988).
44. G. S. Lee, D. P. Ivanov, H. L. Yang, *et al.*, J. Plasma Fusion Res. SERIES **5**, 261 (2002).

Translated by the author

Plasma Physics Reports, Vol. 30, No. 3, 2004, pp. 196–213. Translated from Fizika Plazmy, Vol. 30, No. 3, 2004, pp. 221–240.
Original Russian Text Copyright © 2004 by Bulanov, Esirkepov, Koga, Tajima.

NONLINEAR PHENOMENA

Interaction of Electromagnetic Waves with Plasma in the Radiation-Dominated Regime

S. V. Bulanov[1, 2, 3], T. Zh. Esirkepov[2, 3], J. Koga[2], and T. Tajima[2]

[1] *Prokhorov Institute of General Physics, Russian Academy of Sciences, ul. Vavilova 38, Moscow, 119991 Russia*
[2] *Advanced Photon Research Center, Japan Atomic Energy Research Institute (JAERI-Kansai), 619-0215 Kizu, Kyoto, Japan*
[3] *Moscow Institute of Physics and Technology, Institutskiĭ per. 9, Dolgoprudnyĭ, Moscow oblast, 141700 Russia*

Received July 14, 2003

Abstract—A study is made of the main regimes of interaction of relativistically strong electromagnetic waves with plasma under conditions in which the radiation from particles plays a dominant role. The discussion is focused on such issues as the generation of short electromagnetic pulses in the interaction of laser light with clusters and highly efficient ion acceleration in a thin plasma slab under the action of the ponderomotive pressure of the wave. An approach is developed for generating superintense electromagnetic pulses by means of up-to-date laser devices. *© 2004 MAIK “Nauka/Interperiodica”.*

1. INTRODUCTION

The interaction of a charged particle with an electromagnetic wave is one of the most fundamental physical processes. When the dimensionless wave amplitude $a_0 = eE_0/m_e\omega_0 c$ is much smaller than unity, the electron oscillatory velocity is low in comparison to the speed of light in vacuum, so that, in describing the interaction of an electromagnetic wave with charged particles, relativistic effects can be ignored. Here, E_0 and ω_0 are the electric field and frequency of the electromagnetic wave, m and e are the mass and charge of an electron, and c is the speed of light in vacuum. When the wave is relativistically strong ($a_0 \gg 1$), i.e., when the kinetic energy of a charged particle in the wave field exceeds the particle's rest energy, the dynamics of the particle differs qualitatively from that in the nonrelativistic limit in both classical and quantum mechanics (see [1, 2]).

In the present paper, we mainly focus on the interaction of a charged particle with an electromagnetic wave in regimes in which the particle dynamics is dominated by the radiative friction force. It is well known that the electromagnetic field of a charged particle in a plasma can be conditionally divided into two component. The first, relatively long-wavelength component contributes to collective plasma fields, resulting in changes in the dispersion properties of electromagnetic waves and giving rise to such plasma modes as Langmuir and ion acoustic waves. The second, relatively short-wavelength component is responsible for collisional processes (including bremsstrahlung) in the near zone, while in the wave zone, it corresponds to Thomson or Compton scattering. As the radiation intensity increases, the role of collisional processes decreases, so that they can be ignored in describing a plasma irradiated by a relativistically strong electromagnetic wave. As for Thomson scattering (which, in the relativistic interaction regime, is called nonlinear Thomson scattering [3–6]), it plays a dominant role when an electromagnetic wave propagating in a plasma is sufficiently intense, because the electromagnetic energy scattered by a charged particle per unit time is proportional to the fourth power of the particle's kinetic energy.

In focusing a petawatt laser pulse with a wavelength of 0.8 μm to a spot diameter of about one wavelength, the radiation intensity reaches values on the order of 5×10^{22} W/cm^2, in which case the dimensionless wave amplitude a_0 is equal to 160. (Note that the value $a_0 = 1$ corresponds to an intensity of 1.38×10^{18} W/cm^2.) Thus, the wave field of a petawatt laser is certainly relativistically strong. Higher intensity laser radiation interacts with plasma in a qualitatively new regime in which a significant part of the energy transferred from the wave to the particle is reemitted as high-frequency radiation. Thus, the vector potential of a circularly polarized electromagnetic wave propagating in a collisionless plasma is given by the expression

$$\mathbf{A}_\perp = a_0 \frac{m_e c^2}{e}(\mathbf{e}_y \cos k_0\xi - \mathbf{e}_z \sin k_0\xi), \tag{1}$$

where $k_0\xi = k_0 x - \omega_0 t$ and the energy of an electron is related to the wave amplitude by $\mathcal{E} = m_e c^2(1 + a_0^2)^{1/2}$ [7].

An electron moves along a circular orbit with frequency ω_0 and emits radiation at frequencies that may be as high as $\omega_m = \omega_0\gamma^3$, where the relativistic gamma-factor is equal to $\gamma = \mathcal{E}/m_e c^2$ [7]. The moving electron is subject to a radiative friction force, which is estimated to be on the order of $f_R \approx 8\pi^2 m_e r_e c^2 \gamma^2 a_0^2/3\lambda_0^2$, where $r_e = e^2/m_e c^2 = 2.8 \times 10^{-13}$ cm is the classical electron

1063-780X/04/3003-0196$26.00 © 2004 MAIK “Nauka/Interperiodica”

radius and $\lambda_0 = 2\pi c/\omega_0$ is the laser wavelength. Comparing the radiative friction force with the Lorentz force, equal approximately to $eE_0 = m_e\omega_0 c a_0$, we find that the behavior of a charged particle becomes dominated by radiative friction when the amplitude of an electromagnetic wave satisfies the inequality

$$a_0 > \left(\frac{3\lambda_0}{4\pi r_e}\right)^{1/3}. \tag{2}$$

Hence, the dimensionless parameter that describes the role of the intrinsic radiation of a particle (or, more precisely, the role of Thomson scattering) is defined as

$$\varepsilon_{\rm rad} = \left(\frac{4\pi r_e}{3\lambda_0}\right). \tag{3}$$

For a laser wavelength of $\lambda_0 = 0.8$ μm, this parameter is equal to $(1/408)^3 = 1.48 \times 10^{-8}$.

Nonlinear effects occurring in the interaction of charged particles with electromagnetic waves are, on the one hand, of great interest for numerous astrophysical problems (see [8, 9]) and, on the other hand, have received considerable attention in research on the interaction between petawatt (and higher power) laser pulses with matter. With the advent of petawatt lasers in recent years, it has become possible to investigate such nonlinear interaction regimes experimentally [10].

The paper is organized as follows: In Section 2, we systematize different regimes of the interaction of laser radiation with plasma. We determine the parameter ranges of such regimes as the relativistic interaction regime; the regime dominated by the radiative friction force; and the quantum regime, the upper bound of which corresponds to fields that are so strong that they can produce electron–positron pairs in vacuum. In Section 3, we discuss how the behavior of a charged particle interacting with an electromagnetic wave in a plasma, under conditions such that the ponderomotive pressure force is balanced by the force of the charge-separation electric field, differs from the behavior of a particle interacting with a wave in vacuum, where the ponderomotive force is unneutralized. In Section 4, we present two examples of the results obtained from numerical simulations of the interaction between a strong electromagnetic wave and charged particles in the regime dominated by the radiative friction force. Specifically, we consider the problem of the coherent electromagnetic emission from a cluster in the field of a laser pulse and the problem of the interaction of an electromagnetic wave with a thin foil. In the first problem, the cluster emits a short high-frequency electromagnetic pulse, and, in the second problem, conditions favorable for highly efficient ion acceleration are achieved. In Section 5, we describe the results of computer simulations of the interaction between two laser pulses propagating in a plasma toward one another. We show that, owing to the nonlinear frequency upshifting of the electromagnetic radiation and its focusing, it is possible to amplify the radiation to intensities corresponding to the quantum regime. A fundamentally important point here is that this amplification can be achieved in present-day laser devices. In the conclusion, we summarize the main results of our investigations.

2. EFFECT OF RADIATIVE LOSSES ON THE MOTION OF A CHARGED PARTICLE IN THE FIELD OF AN ELECTROMAGNETIC WAVE PROPAGATING IN A COLLISIONLESS PLASMA

2.1. Motion of an Electron in the Field of a Circularly Polarized Electromagnetic Wave in Plasma

Let us consider in more detail an electron moving without radiative losses in the field of a circularly polarized electromagnetic wave propagating in a plasma (see also [11]). According to [7], the dependence of the wave phase velocity $v_{\rm ph} = \omega_0/k_0$ in expression (1) on the wave frequency ω_0 and wave amplitude a_0 is given by the formula

$$v_{\rm ph} = c\frac{\omega_0(1+a_0^2)^{1/4}}{[\omega_0^2(1+a_0^2)^{1/2} - \omega_{pe}^2]^{1/2}}, \tag{4}$$

where $\omega_{pe} = (4\pi n_0 e^2/m_e)^{1/2}$ is the plasma frequency.

The equations of motion of an electron have the integrals of motion

$$P_y = p_y - m_e c a_y, \tag{5}$$

$$P_z = p_z - m_e c a_z, \tag{6}$$

where $\mathbf{P}_\perp = P_y\mathbf{e}_y + P_z\mathbf{e}_z = P_\perp[\mathbf{e}_y\cos k_0\xi_0 + \mathbf{e}_z\sin k_0\xi_0]$ is the transverse canonical momentum, $\mathbf{p}_\perp = p_y\mathbf{e}_y + p_z\mathbf{e}_z$ is the transverse momentum of the electron, and

$$\mathbf{a}_\perp(\xi) = a_0(\mathbf{e}_y\cos k_0\xi - \mathbf{e}_z\sin k_0\xi). \tag{7}$$

The equations of motion for the longitudinal momentum p_x and longitudinal coordinate x can be written in a Hamiltonian form:

$$\dot{p}_x = -\frac{\partial H}{\partial \xi}, \tag{8}$$

$$\dot{\xi} = \frac{\partial H}{k_0 \partial p_x}, \tag{9}$$

with the Hamiltonian

$$H(p_x, \xi) = [m_e^2c^4 + p_x^2c^2 + (P_y - a_y(\xi))^2c^2 + (P_z - a_z(\xi))^2c^2]^{1/2} - p_x v_{\rm ph}. \tag{10}$$

Since the Hamiltonian does not explicitly depend on time, the condition for the function $H(p_x, \xi) = m_e c^2\gamma - p_x v_{\rm ph} = m_e c^2 h$ to be conserved allows us to determine

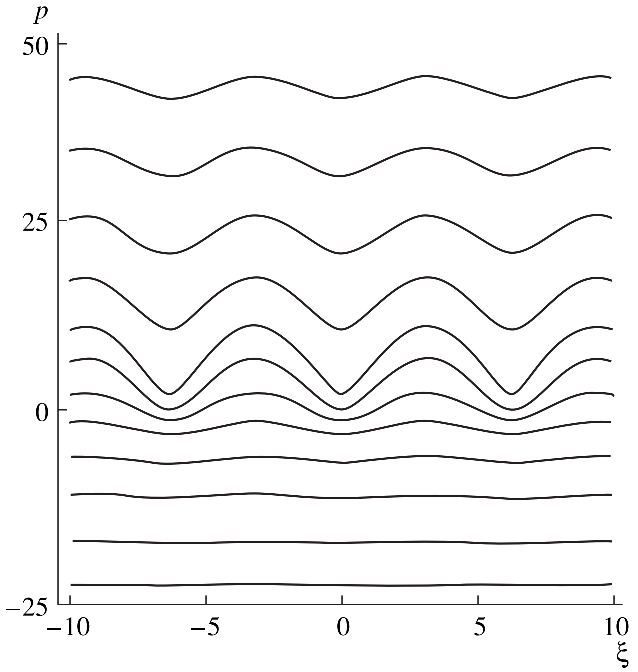

Fig. 1. Phase plane for Eqs. (8) and (9).

the dependence of the longitudinal component p_x of the electron momentum on the variable ξ:

$$\frac{p_x}{m_e c} = \left[\frac{h^2\beta_{\text{ph}}^2}{(\beta_{\text{ph}}^2-1)^2} + \frac{1+\Pi_\perp^2(\xi)-h^2}{\beta_{\text{ph}}^2-1}\right]^{1/2} - \frac{h\beta_{\text{ph}}}{\beta_{\text{ph}}^2-1}. \quad (11)$$

Here, for the electromagnetic wave described by expression (1), the function $\Pi_\perp(\xi)$ has the form

$$\begin{aligned}\Pi_\perp^2(\xi) &= \left[\frac{P_y}{m_e c} + a_y(\xi)\right]^2 + \left[\frac{P_z}{m_e c} + a_z(\xi)\right]^2 \\ &= \left(\frac{P_\perp}{m_e c}\right)^2 + \frac{2eP_\perp A_0}{m_e^2 c^3}\cos(k_0(\xi+\xi_0)) + \left(\frac{eA_0}{m_e c^2}\right)^2\end{aligned} \quad (12)$$

and $\beta_{\text{ph}} = v_{\text{ph}}/c$. It is obvious that, without loss of generality, we can set $\xi_0 = 0$. The phase plane for Hamiltonian equations (8) and (9) is shown in Fig. 1. It can be seen that there are no separatrices or closed orbits.

For each of the main plasma electrons, we have $\mathbf{P}_\perp = 0$ and $h = 0$. Such an electron moves in a circular orbit of constant radius, and the longitudinal component of its momentum remains zero.

For an electron that is initially at rest, the parameters of the solution should be chosen as follows: $P_y = m_e c a_0$, $P_z = 0$, and $h = 1$; i.e., $P_\perp = m_e c a_0$. These initial conditions may refer to the electrons that are produced in a plasma either by ionization [12, 13] or due to the creation of electron–positron pairs [14–18]. The longitudinal component of the momentum of each such electron,

$$\frac{p_x}{m_e c} = \left\{\frac{\beta_{\text{ph}}^2}{(\beta_{\text{ph}}^2-1)^2} + \frac{2a_0^2[1-\cos(k_0\xi)]}{\beta_{\text{ph}}^2-1}\right\}^{1/2} - \frac{\beta_{\text{ph}}}{\beta_{\text{ph}}^2-1} \quad (13)$$

increases from zero to the maximum value $p_{\max} = m_e c[\beta_g/(1-\beta_g^2)][\sqrt{1+4a_0^2(1-\beta_g^2)} - 1]$. Here, we took into account the fact that the phase and group velocities of an electromagnetic wave are related by the relationship $v_{\text{ph}}v_g/c^2 = 1$, which yields $\beta_g = 1/\beta_{\text{ph}}$. Accordingly, the electron energy increases from $m_e c^2$ to $m_e c^2 + p_{\max}c$. The electron orbit is a helix with an axis forming a certain angle with the wave vector of the electromagnetic wave.

2.2. Effect of Radiative Losses on the Interaction of a Charged Particle with an Electromagnetic Wave in Plasma

In the equations of motion, the effects of radiative damping in the interaction of a charged particle with an electromagnetic wave are described by the radiative friction force. We write the equations of motion in standard form [1]:

$$m_e c\frac{du^i}{ds} = \frac{e}{c}F^{ik}u_k + g^i, \quad (14)$$

where $u^i = dx^i/ds = (\gamma, \mathbf{p}/m_e c)$ is the velocity 4-vector, $\gamma = (1 - v^2/c^2)^{-1/2}$, $s = c\int dt/\gamma$, and $F_{ik} = \partial_i A_k - \partial_k A_i$ is the electromagnetic field tensor. The radiative friction force is equal to

$$g^i = \frac{2e^2}{3c}\left(\frac{d^2u^i}{ds^2} - u^i u^k \frac{d^2u_k}{ds^2}\right). \quad (15)$$

The electric and magnetic fields are expressed in terms of vector potential (1) by the familiar relationships $\mathbf{E} = -c^{-1}\partial\mathbf{A}/\partial t$ and $\mathbf{B} = \nabla \times \mathbf{A}$.

The radiative friction force gives rise to a longitudinal force, which is nothing more than a ponderomotive force. Here, we consider the case in which the ponderomotive force acting on an electron is balanced by the force of the charge-separation electric field. As a result, the longitudinal component of the total force vanishes: $eE_x + e(v_yB_z - v_zB_y)/c = 0$. Setting the electron velocity in the wave equal to the speed of light and estimating the charge-separation electric field as $E_x = 4\pi n_0 e l_x$, we find that the mean displacement of the electrons with respect to the ions is $l_x \approx E_0/4\pi n_0 e = d_e a_0(\omega_0/\omega_{pe})$. Under these conditions, an electron does not move along the x axis. In a perpendicular plane, the electron moves along a circle with a frequency equal to the frequency of the electromagnetic wave.

In order to analyze the solutions to Eqs. (14) and (15), we turn to the approach developed in [19–21]. Since the energy of an electron is constant, the temporal component of Eq. (14) has the form

$$0 = \frac{e}{c}F^{0k}u_k + g^0. \tag{16}$$

This equation is equivalent to the condition that there be a balance between the work done by the energy electric field on the electron and the energy emitted by the electron per unit time, $e(\mathbf{E}\cdot\mathbf{v}) = \varepsilon_{\rm rad}\omega_0\gamma^2 p_\perp^2/m_e$, where $\varepsilon_{\rm rad}$ is given by formula (3). The spatial components of Eq. (14) can be written as

$$(p_\perp - a_0 m_e c) = -i\varepsilon_{\rm rad} p_\perp \gamma^3. \tag{17}$$

We represent the electron momentum in a complex form, $p_y + ip_z = p_\perp\exp(-i\omega_0 t)$, where $p_\perp = p\exp(i\varphi)$ is the complex amplitude and φ is the phase equal to the angle between the electron momentum vector and the electric field vector in the wave. We then obtain

$$a_0^2 - \left(\frac{p}{m_e c}\right)^2 = \varepsilon_{\rm rad}^2\left(\frac{p}{m_e c}\right)^2\left[1 + \left(\frac{p}{m_e c}\right)^2\right]^3. \tag{18}$$

It can be seen that, for $a_0 \ll a_{\rm rad} = (\varepsilon_{\rm rad}^{-2/3} - 1)^{1/2} \approx \varepsilon_{\rm rad}^{-1/3}$, the electron momentum is proportional to the electromagnetic wave amplitude, $p \approx a_0 m_e c$, and the electron energy is equal to $\mathcal{E}_\perp \approx m_e c^2(1 + a_0^2)^{1/2}$. In the limit $a_0 \gg a_{\rm rad} = (\varepsilon_{\rm rad}^{-2/3} - 1)^{1/2} \approx \varepsilon_{\rm rad}^{-1/3}$, we have $p \approx m_e c(a_0/\varepsilon_{\rm rad})^{1/4}$ [20]. Figure 2 shows the electron energy $\mathcal{E}_\perp = (m_e^2c^4 + p^2c^2)^{1/2} \equiv m_e c^2\gamma$ as a function of the dimensionless amplitude of the laser pulse a_0 and the parameter $\varepsilon_{\rm rad}$.

The energy flux reemitted by the electron is equal to $e(\mathbf{E}\cdot\mathbf{v}) = \varepsilon_{\rm rad}\omega_0\gamma^2p^2/m_e$. The integral scattering cross section by definition equals the ratio of the reemitted energy to the Poynting vector $P = cE_0^2/4\pi$:

$$\sigma = \sigma_T\frac{\gamma^2}{1 + \varepsilon_{\rm rad}^2\gamma^6}, \tag{19}$$

where the dependence of the electron energy $m_e c^2\gamma$ on the wave amplitude a_0 is given by relationship (18) and the Thomson scattering cross section is $\sigma_T = 8\pi r_e^2/3 = 6.65 \times 10^{-25}$ cm^2. The dependence of the Thomson cross section on the wave amplitude and the parameter $\varepsilon_{\rm rad}$, which characterizes the wave frequency, is shown in Fig. 3.

It follows from expression (19) that, as the wave amplitude increases over the range $1 \ll a_0 \ll a_{\rm rad}$, the scattering cross section increases according to the law $\sigma = \sigma_T(1 + a_0^2)$ and reaches its maximum $\sigma_m \approx \sigma_T a_{\rm rad}^2$ at $a_0 \approx a_{\rm rad}$; for $a_0 \gg a_{\rm rad}$, it decreases according to the law $\sigma \approx \sigma_T a_{\rm rad}^3/a_0$.

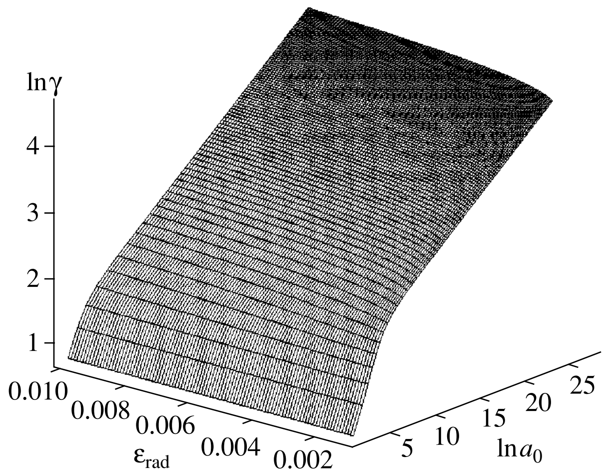

Fig. 2. Dependence of the logarithm of the electron energy on the logarithm of the wave amplitude and on the parameter $\varepsilon_{\rm rad}$.

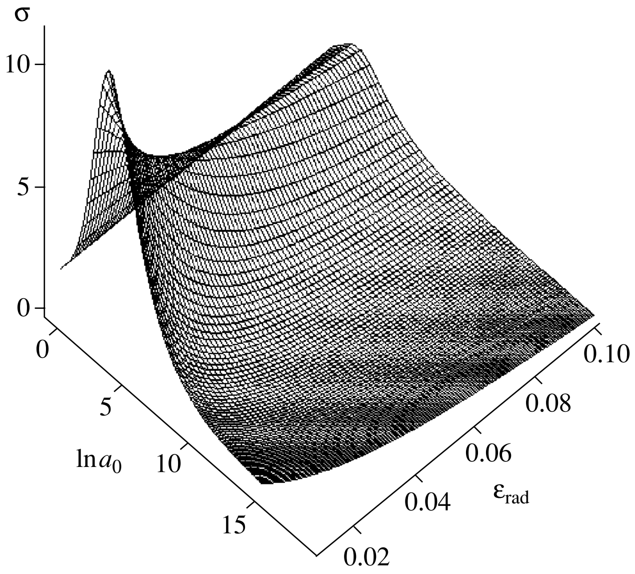

Fig. 3. Dependence of the scattering cross section on the logarithm of the wave amplitude a_0 and on the parameter $\varepsilon_{\rm rad}$.

When radiative losses are taken into account, we arrive at the following dependence of the characteristic frequency of radiation from the electron on the electromagnetic wave amplitude. For $1 \ll a_0 \ll a_{\rm rad}$, the frequency is proportional to the wave amplitude cubed, $\omega_m = \omega_0 a_0^3$. In the limit of high wave intensities such that $a_0 \gg a_{\rm rad}$, we have $\omega_m = \omega_0(a_0/\varepsilon_{\rm rad})^{3/4}$; i.e., the frequency increases far more gradually.

Quantum electrodynamic effects come into play at electron energies at which the energy of a photon emitted by an electron becomes comparable to the electron kinetic energy, i.e., $\hbar\omega_m \approx \mathscr{E}_\perp$. In particular, these effects change the radiative loss function. In the quantum regime, it is necessary to take into account not only radiative damping effects but also recoil momentum effects, which change the direction of motion of the electron because the outgoing photon carries away the momentum $k_m = \omega_m/c$. Since photons are emitted in a statistically random way, the motion of an electron is a superposition of the regular rotation in the wave field and a kind of Brownian random walk. This is a familiar effect in the electron motion in circular accelerators in the limit where quantum electrodynamic effects play a role in synchrotron radiation from the particles [22].

It has been shown above that, when radiative losses are taken into account, an electron in the electromagnetic wave field acquires the energy $\mathscr{E}_\perp = m_ec^2\gamma = m_ec^2(a_0/\varepsilon_{\rm rad})^{1/4}$. Such an electron emits photons with the energy $\hbar\omega_0\gamma^3 = \hbar\omega_0(a_0/\varepsilon_{\rm rad})^{3/4}$. This implies that quantum electrodynamic effects should be taken into consideration for electrons with energies on the order of $\mathscr{E}_\perp = m_ec^2(m_ec^2/\hbar\omega_0)$ and higher or for electromagnetic wave amplitudes equal to $a_0 = \varepsilon_{\rm rad}(m_ec^2/\hbar\omega_0)^2$ and larger. The corresponding threshold Lorentz factor of an electron irradiated by laser radiation with a wavelength of one micron is about $\gamma = (m_ec^2/\hbar\omega_0)^{1/2} \approx 700$. The electromagnetic wave amplitude corresponding to this threshold is equal to

$$a_{\rm qua} = \frac{2e^2m_ec}{3\hbar^2\omega_0} = \frac{r_e\lambda_0}{3\pi\bar{\lambda}_c^2}, \tag{20}$$

the equivalent value of the electric field in the wave being

$$E_{\rm qua} = \frac{2em_e^2c^2}{3\hbar^2} = \frac{r_e}{3\bar{\lambda}_c}E_{\rm Schw}. \tag{21}$$

We can see that the wave electric field is weaker than the limiting electric field $E_{\rm Schw}$ in quantum electrodynamics by a factor of $3\hbar c/e^2 = 3/\alpha$, which is approximately equal to 411. The limiting electric field, which is also called the Schwinger electric field, is given by the expression [23, 24]

$$E_{\rm Schw} = \frac{2m_e^2c^3}{e\hbar}. \tag{22}$$

The Schwinger electric field is so strong that, at a distance equal to the Compton length, it performs the work $2m_ec^2$, sufficient to create an electron–positron pair [23–27].

In the radiation-dominated regime in the quantum limit, we should to use, instead of Eq. (18), the equation

$$a_0^2 - \left(\frac{p}{m_ec}\right)^2 = \varepsilon_{\rm rad}^2\left(\frac{p}{m_ec}\right)^2\gamma^6U^2(\Upsilon). \tag{23}$$

This equation is obtained from Eq. (18) by replacing the energy lost by an electron with the quantum electrodynamic function, which in turn equals the energy emitted by an electron per unit time. In other words, the expression $\approx\varepsilon_{\rm rad}^2(p/m_ec)^8$ should be replaced with the function $\varepsilon_{\rm rad}^2(p/m_ec)^8U^2(\Upsilon)$. The quantum-electrodynamic calculations of this function were performed in the theory of synchrotron radiation [22] and in the theory of the interaction of charged particles with electromagnetic waves [28]. In Eq. (23), we have introduced the dimensionless variable $\Upsilon = (\hbar\omega_0/m_ec^2)(p/m_ec)^2$. The function $U(\Upsilon)$ is expressed in terms of the Airy function and its derivative. In the classical limit ($\Upsilon \ll 1$), this function is close to unity, $U(\Upsilon) \approx 1$, whereas, in the quantum limit ($\Upsilon \gg 1$), it is described by the approximate formula $U(\Upsilon) \approx (128\pi/3^{1/2}81)\Upsilon^{-2/3}$. Substituting this formula into Eq. (23), we determine the change in the electron momentum in the quantum limit ($a_0 > a_{\rm qua}$) as a function of the electromagnetic wave amplitude:

$$p \approx m_ec\left(\frac{\hbar\omega_0}{m_ec^2}\right)^{1/2}\left(0.34\frac{a_0}{\varepsilon_{\rm rad}}\right)^{3/8}. \tag{24}$$

Let us make some estimates. In describing the interaction between plasma and laser radiation with a wavelength of one micron, relativistic effects should be taken into account for $a_0 \geq 1$, which corresponds to laser intensities of $I_{\rm rel} = 1.38 \times 10^{18}$ W/cm^2 and higher. The threshold wave amplitude for the radiation-dominated regime is $a_0 \approx a_{\rm rad}$ with $a_{\rm rad} \approx 400$, which corresponds to a laser intensity of about $I_{\rm rad} = 3 \times 10^{23}$ W/cm^2. The quantum effects come into play for $a_0 \approx a_{\rm qua} \approx 2500$, which gives $I_{\rm qua} = 1.38 \times 10^{25}$ W/cm^2. For the nonlinear quantum electrodynamic regime with electron–positron pair production in a vacuum, the limiting laser pulse field is equal to the Schwinger field $E_{\rm Schw} = 2m_e^2c^3/e\hbar$, which corresponds to the dimensionless wave amplitude $a_{\rm Schw} = 2m_e^2c^2/\hbar\omega_0 \approx 10^6$ and laser intensity $I_{\rm Schw} = 10^{29}$ W/cm^2.

Reemission of the energy of an electromagnetic wave into higher harmonics, which freely escape from the plasma, causes wave damping in a homogeneous plasma or gives rise to a skin layer of finite depth (the depth of penetration of the field into the plasma). Estimating the penetration depth from the balance condition for the scattered energy flux, $\nabla\mathbf{P} = ne(\mathbf{E}\cdot\mathbf{v})$, we obtain $l_\sigma = 1/n\sigma$. At $a_0 \approx a_{\rm rad}$, the skin depth reaches its minimum value of $1/n\sigma_Ta_{\rm rad}^2 \approx 10^{-4}(10^{23}/n)$ cm. This indicates that, in the interaction of a laser pulse with a solid target, the laser energy is fully converted into hard X radiation or gamma radiation in a target layer several microns thick, provided that the laser intensity is equal in order of magnitude to $I_{\rm rad} = 3 \times 10^{23}$ W/cm^2. That this process is important was pointed out in [29].

3. ROLE OF RADIATIVE LOSSES IN THE INTERACTION OF A CHARGED PARTICLE WITH A PLANE ELECTROMAGNETIC WAVE IN VACUUM

For further discussion, we give here some information about the motion of a charged particle in the field of a plane electromagnetic wave in vacuum (see [1, 30]). The equations of motion for charged particles imply that the transverse component of the generalized momentum is constant, $\mathbf{p}_\perp - e\mathbf{A}_\perp/c$ = const. The energy and the longitudinal momentum component are related by the relationship $(m_e^2c^4 + \mathbf{p}_\perp^2 + p_\parallel^2)^{1/2} - p_\parallel c$ = const. The form of this integral of motion stems from the fact that the vector potential $\mathbf{A}_\perp$ describing an electromagnetic wave in vacuum depends on the coordinate and time through the combination $x - ct$. We consider the electron motion in a frame of reference in which the electron is at rest up to the time when it begins to be affected by the electromagnetic wave. This choice of the reference frame determines the constants in the above integrals of motion. As a result, we determine how the kinetic energy $K/m_ec^2 = [1 + (p/m_ec)^2]^{1/2} - 1$ of the electron and its momentum depend on the vector potential $\mathbf{A}_\perp(x - ct)$: $K = m_ec^2|\mathbf{a}_\perp|^2/2$, $\mathbf{p}_\perp = m_ec\mathbf{a}_\perp$, and $p_\parallel = m_ec|\mathbf{a}_\perp|^2/2$. Here, we have introduced the function $\mathbf{a}_\perp = e\mathbf{A}_\perp(x - ct)/m_ec$. These expressions are exact solutions to the equations of motion. Regardless of the strength of the electromagnetic wave field, the kinetic energy of an electron is expressed through the transverse or the longitudinal momentum component as $K = p_\perp^2/2m_e$ or $K = p_\parallel c$. The Lorentz gamma-factor (the electron energy normalized to m_ec^2) is equal to $\gamma = \mathcal{E}/m_ec^2 = [1 + (p/m_ec)^2]^{1/2} = 1 + |\mathbf{a}_\perp|^2/2$. From this, we can determine the electron velocity: the longitudinal and transverse velocity components are equal to $v_\parallel = c|\mathbf{a}_\perp|^2/(2 + |\mathbf{a}_\perp|^2)$ and $\mathbf{v}_\perp = 2c\mathbf{a}_\perp/(2 + |\mathbf{a}_\perp|^2)$. It is seen that, in the nonrelativistic limit ($a_0 \ll 1$), the transverse component of the electron momentum is much larger than its longitudinal component. In the opposite (ultrarelativistic) limit ($a_0 \gg 1$), the longitudinal momentum component is much larger than the transverse component. These relationships can be derived from formulas (4)–(13) in the limit $\beta_{\rm ph} \longrightarrow 1$.

In the accompanying frame in which the electron is, on average, at rest, the dimensionless wave amplitude is nearly the same as that in the laboratory frame of reference, $\bar{a}_0 = a_0$; this is a consequence of the relativistic invariance of the transverse component of the vector potential. Here, the superior bar denotes the values of the quantities in the accompanying frame. In contrast, the parameter $\varepsilon_{\rm rad}$, which is given by expression (3), is not relativistically invariant. It is easy to show that $\bar{\varepsilon}_{\rm rad} = 4\pi r_e/3\bar{\lambda}_0 = \varepsilon_{\rm rad}/(1 + a_0^2)^{1/2}$. To do this, it is necessary to take into account the fact that, in the rest frame of the electron, the wavelength of the radiation is equal to $\bar{\lambda}_0 = \lambda_0[(c + v_\parallel)/(c - v_\parallel)]^{1/2} = \lambda_0(1 + a_0^2)^{1/2}$. The bound of the radiation-dominated regime can be found from the condition $a_0 \approx \bar{\varepsilon}_{\rm rad}^{-1/3}$. In the laboratory frame, we obtain $a_0 \approx \varepsilon_{\rm rad}^{-1/2}$. It can be shown that quantum effects come into play for electromagnetic waves whose amplitudes correspond to the limiting electric field in quantum electrodynamics.

An analytic description of the interaction of a charged particle with an electromagnetic wave in vacuum runs into serious difficulties even for waves with circular polarization. This is why we will consider the particle motion in crossed constant electric and magnetic fields. Ritus [28] noted that the dynamics of a charged particle in crossed fields exhibits the main features characteristic of both classical and quantum physics. The reason for this is the following: In the accompanying frame of reference, in which a relativistic (in the laboratory frame) particle is at rest, an arbitrary electromagnetic field is nearly transverse, with mutually orthogonal electric and magnetic fields having almost equal magnitudes.

We consider a charged particle that is initially at rest. We choose the reference frame in which the magnetic field $\mathbf{B}$ points along the z axis and the electric field $\mathbf{E}$ is parallel to the y axis and assume that the electric and magnetic fields are equal to one another, $E = B$. In this case, it is convenient to express the radiative friction force in terms of the external electric and magnetic fields [1]. For particles with ultrarelativistic energies, we have

$$\mathbf{g} = -\frac{2r_e^2}{3}\frac{\mathbf{p}}{m^3c^3\gamma}[(mc\gamma\mathbf{E} + \mathbf{p}\times\mathbf{B})^2 - (\mathbf{p}\cdot\mathbf{E})^2], \qquad (25)$$

where we have retained only the lowest order terms in the expansion in powers of the parameter γ in the limit $\gamma \longrightarrow \infty$. Accordingly, in crossed electric and magnetic fields, the radiative friction force is

$$\mathbf{g} = -\frac{2r_e^2}{3c}E^2\mathbf{v}\left(\gamma - \frac{p_x}{mc}\right)^2. \qquad (26)$$

As a result, the equations of particle motion can be written as

$$\dot{p}_x = \frac{e}{c}E\dot{y} - \frac{2r_e^2}{3c}E^2\dot{x}\gamma^2\left(1 - \frac{\dot{x}}{c}\right)^2, \qquad (27)$$

$$\dot{p}_y = eE\left(1-\frac{\dot{x}}{c}\right)-\frac{2r_e^2}{3c}E^2\dot{y}\gamma^2\left(1-\frac{\dot{x}}{c}\right)^2. \quad (28)$$

We switch to dimensionless variables in which the coordinates, momentum, and velocity are expressed in units of r_e, mc, and c, respectively; the time is normalized to r_e/c; and the electric field is given in units of $E_e = m_e^2c^4/e^3 = e/r_e^2$ (i.e., in units of $E_{\mathrm{Schw}}/2\alpha$). We switch from the independent variable t to the variable $a = E(x - ct)$, which is merely the value of the vector potential of the wave at the particle's position. In these new variables, Eqs. (27) and (28) reduce to

$$p_x' = -\frac{p_y}{\gamma - p_x} + \kappa p_x\gamma\left(1-\frac{p_x}{\gamma}\right), \quad (29)$$

$$p_y' = -1 + \kappa p_y\gamma\left(1-\frac{p_x}{\gamma}\right), \quad (30)$$

where $\kappa = 2E/3$ and the prime denotes the derivative with respect to a.

In the limit of relatively weak fields ($E \ll 1$), Eqs. (27) and (28) have a solution that coincides with the solution presented in [1]:

$$p_x = a^2/2, \quad p_y = -a, \quad p_z = \text{const}. \quad (31)$$

This solution demonstrates the particular case of the dependence of the particle momentum that has been discussed above, namely, $\mathbf{p}_\perp = m_ec\mathbf{a}_\perp$ and $\mathbf{p}_\parallel = m_ec|\mathbf{a}_\perp|^2/2$. We see that, in the ultrarelativistic limit, the longitudinal momentum component increases most rapidly. The particle trajectory in the coordinate plane is implicitly determined by the equations

$$x = a^3/6E, \quad y = a^2/E, \quad Et + a + a^3/6E = 0. \quad (32)$$

In the (x, y) plane, the trajectory has the form $9x^2 - 4Ey^3 = 0$. On infinitely long time scales ($t \longrightarrow \infty$), the particle energy changes in time according to the law $m_ec^2\gamma \approx (m_ec^2/2)(6eEt/m_ec)^{2/3}$. This asymptotic formula is written in the above dimensional variables.

Using relationships (31) and (32), we find that radiative losses begin to play an important role in the dynamics of a charged particle when $a \approx a_{\mathrm{rad}} = E^{-1}$. In this limit, using the condition $p_x \gg p_y$, we can represent the gamma-factor of the particle as $\gamma = p_x + p_y^2/2p_x + \ldots$. Substituting this representation into Eqs. (29) and (30), we obtain

$$p_x' = -\frac{2p_x}{p_y} + \kappa p_y^2, \quad (33)$$

$$p_y' = -1 + \kappa\frac{p_y^3}{p_x}. \quad (34)$$

which yield

$$\frac{dp_x}{dp_y} = \frac{p_x}{p_y}\left(\frac{2p_x - \kappa p_y^3}{p_x - \kappa p_y^3}\right). \quad (35)$$

This equation has the solution

$$p_x = \kappa p_y^3 \pm p_y^2[(\kappa p_y)^2 + C]^{1/2}, \quad (36)$$

where C is an arbitrary constant. In the limit $\kappa \ll 1$, solution (36) should yield the same relationship between p_x and p_y as that following from solution (31); in other words, we must have $p_x = p_y^2/2$. This gives $C = 1/4$, in which case the second term on the right-hand side of Eq. (36) should be written with the plus sign. In the opposite limit $p_y \gg 1/2\kappa$ (i.e., for $|a| \gg 3/2E$), Eq. (36) yields $p_x \approx 2\kappa p_y^3$. Using this relationship and Eq. (34), we obtain

$$p_x = -\frac{1}{4}\kappa a^3, \quad p_y = -\frac{1}{2}a, \quad 20Et = \kappa^2a^5. \quad (37)$$

On infinitely long time scales ($t \longrightarrow \infty$), the particle energy changes in time according to the law $\gamma \sim t^{3/5}$.

4. RADIATION-DOMINATED REGIMES OF THE INTERACTION OF AN ELECTROMAGNETIC WAVE WITH A CLUSTER AND A THIN FOIL

Above, we considered the interaction of laser light with a charged particle in the point-particle approximation. Another approximation in which the effects similar to those caused by radiative damping play a key role is associated with targets whose sizes are less than the laser wavelength. It is well known that, in this approximation, a target behaves as a particle whose charge is equal to the total charge of the target's electrons. Examples of such targets are cluster targets and thin foils.

4.1. Interaction of an Electromagnetic Wave with a Cluster

As was pointed out in [31], the interaction of a laser pulse with a cluster is accompanied by the conversion of laser energy into the energy of the scattered radiation. Under typical conditions, the cluster sizes are much smaller than the laser wavelength, so that the laser radiation is scattered in the collective regime, in which the scattering cross section is larger than that in the single-particle regime by a factor of N^2, where N is the number of electrons involved in the scattering process. This can be explained in terms of the familiar expression for the total cross section for electromagnetic wave scattering by a small spherical particle, $\sigma = 8\pi|\alpha|^2V^2\omega^4/3c^4$ [32], which is valid for small-amplitude waves. Here, V is the particle volume and $\alpha = (3/4\pi)[(\varepsilon(\omega) - 1)/(\varepsilon(\omega) + 2)]$ is the polarizability, in

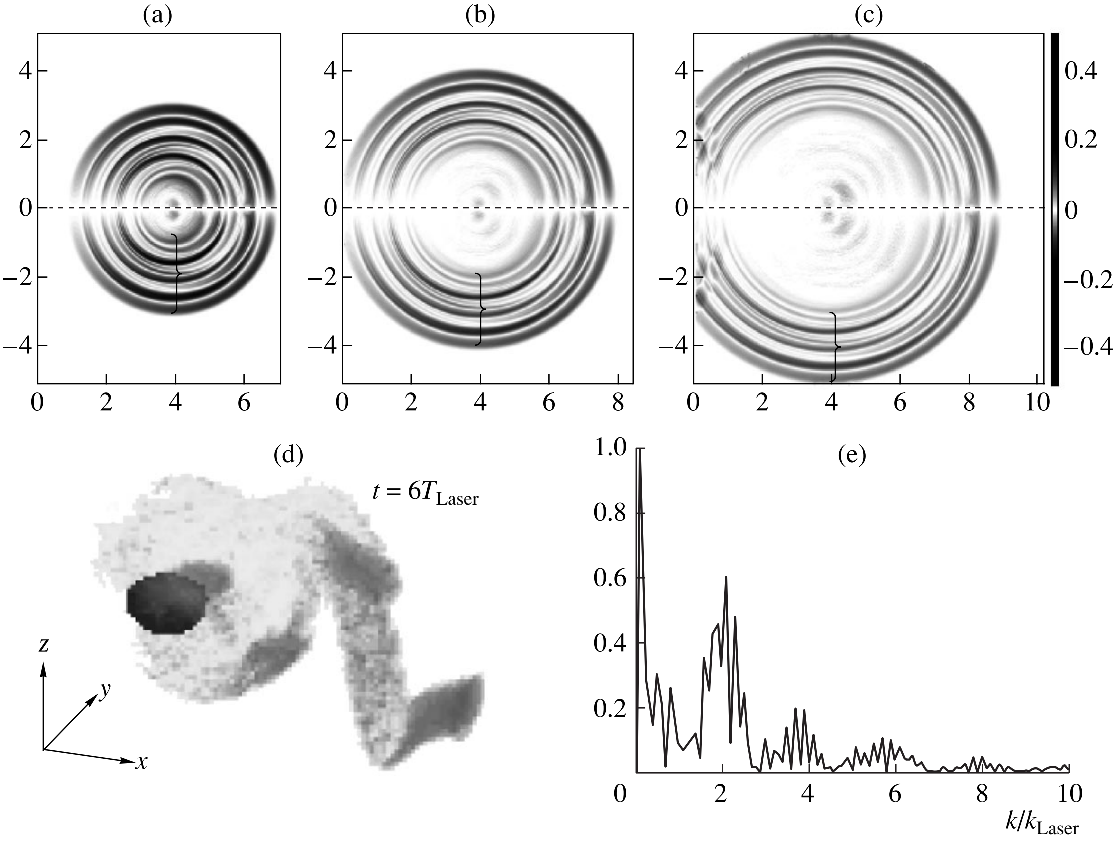

Fig. 4. Emission of a high-frequency radiation pulse in the interaction of an electromagnetic wave with a cluster: the distributions of the z component of the magnetic field in the (x, y) plane at the times t = (a) $7 \times 2\pi/\omega_0$, (b) $8 \times 2\pi/\omega_0$, and (c) $9 \times 2\pi/\omega_0$; (d) an electron cloud that forms under the action of laser radiation and the distribution of protons; and (e) the spectrum of high-frequency radiation from the cluster.

which the dielectric function $\varepsilon(\omega)$ for a plasma is equal to $1 - \omega_{pe}^2/\omega^2$. For $\omega > \omega_{pe}$, we obtain $\sigma = \sigma_T(nV)^2 = \sigma_T N^2$. The total number of electrons in a cluster can be estimated at $N \approx 10^8$ for a cluster having a typical radius of $r_{\text{cl}} \approx 10^{-5}$ cm and at $N \approx 10^{11}$ for a micron-size cluster. Regarding the cluster as a macroparticle with an electric charge of eN and using the above results, we can determine the dimensionless amplitude of laser radiation at which it is necessary to take into account the effects of the radiative friction force: $a_{\text{rad}} = (4\pi N r_e/3\lambda_0)^{-1/3}$. This amplitude, which is about 500 times smaller than that in the case of scattering by one electron, corresponds to the laser intensity $I_{\text{cl}} = 10^{18}$ W/cm^2 at an operating wavelength of one micron. It has been shown above that, at this laser intensity, the scattering cross section is maximum. Hence, the case under consideration, on the one hand, can serve to model the radiation-dominated interaction regime and, on the other hand, is of interest for creating high-power sources of hard electromagnetic radiation.

Under the action of a sufficiently strong electromagnetic wave, the electrons escape from the cluster. This process is sometimes called cluster ionization. Obviously, under conditions such that the kinetic energy acquired by the electrons in the wave field is higher than the Coulomb potential of the ion cluster component, all electrons leave the cluster. At lower intensities of the laser electromagnetic radiation, only some of the electrons are pushed away from the cluster by the laser wave (the corresponding limits are discussed in [33–36]). Note that, in the context of our analysis, the wave is regarded as being weak if its electric field is much less than the electric field at the boundary of a fully ionized cluster, $E_0 < 4\pi n e r_{\text{cl}}/3$. At both strong and weak fields, an electron bunch forms whose dimensions are smaller than the laser wavelength. During several periods of the electromagnetic wave, the bunch is accelerated as a single entity and, consequently, emits radiation coherently. A relatively weak electromagnetic wave gives rise to a bunch in which the number of electrons is equal in order of magnitude to $\delta N \approx E_0 r_{\text{cl}}^2/e$. The electromagnetic radiation emitted by the bunch is illustrated in Fig. 4, which shows the results of a three-dimensional particle-in-cell (PIC) simulation of the interaction of a laser pulse with a cluster.

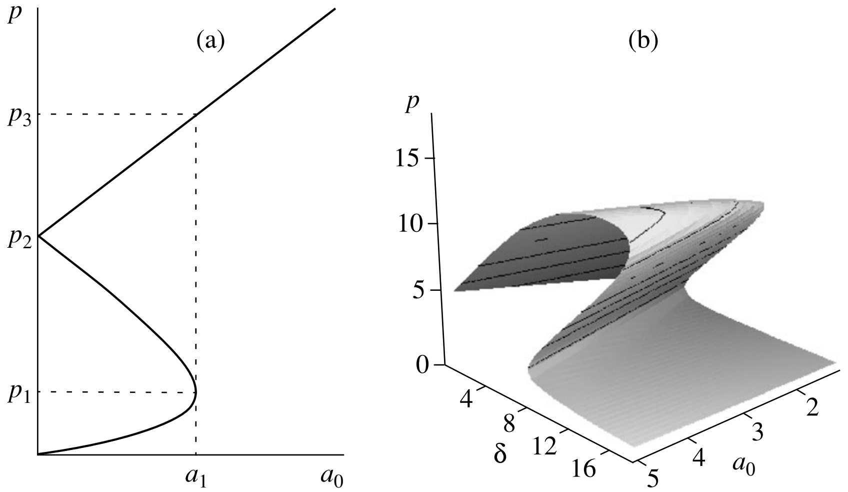

Fig. 5. (a) Dependence of the momentum of an electron on the wave amplitude within the cluster and (b) surface in the (p, δ, a_0) space that corresponds to this dependence.

In this version of numerical simulations, a semi-infinite laser pulse propagates along the x axis. The dimensionless pulse amplitude $a_0 = 10$ corresponds to an intensity of 1.37×10^{20} W/cm^2 at the wavelength $\lambda_0 = 1$ μm. At the pulse front, the electromagnetic field varies on a scale of $3\lambda_0$. A spherical cluster 0.2 μm in diameter is at the center of the computation region, which has the form of a cube of side $10.2\lambda_0$. The cluster is assumed to be composed of an electron–proton ($m_p/m_e = 1836$) plasma of density $n_0 = 100n_{\rm cr}$. The number of cells in the numerical grid is 1024^3, the total number of macroparticles being 3×10^6. The simulations were carried out using the REMP code [37].

In Fig. 4d, we can see that, in the course of several periods of laser radiation, all electrons escape from the cluster, leaving the net electric charge of the cluster's ions unneutralized. Under the action of repulsive forces between like charges, the ion cloud begins to expand; this phenomenon is known as Coulomb explosion. Figure 4e shows the spectrum of radiation from the cluster. It can be seen that the spectrum contains high harmonics of the laser carrier frequency.

In the opposite limit, in which the wave amplitude is about $4\pi ner_{\rm cl}/3$ or greater, the number of electrons that have not been ejected from the cluster is relatively small in comparison with the total number of cluster's ions. Under the action of the electromagnetic field of the laser pulse, the electrons that remain in the cluster circulate within it. Taking into account the smallness of the cluster in comparison with the laser wavelength, we describe the motion of an electron bunch as the motion of a charged particle (macroelectron) with an electric charge of eN_e. The momentum of the electrons can be determined from Eq. (18), which must be modified to include the electric field of the ions, $\mathbf{E} = 4\pi ne\mathbf{r}/3$. This in turn requires that the condition $N_e \ll 4\pi n r_{\rm cl}^3/3$ be satisfied. As a result, we obtain the equation

$$a_0^2 - \left(\frac{p}{m_e c}\right)^2 \left[1 - \frac{\delta m_e c}{(m_e^2 c^2 + p^2)^{1/2}}\right]^2 = \tilde{\varepsilon}_{\rm rad}^2 \left(\frac{p}{m_e c}\right)^2 \left[1 + \left(\frac{p}{m_e c}\right)^2\right]^3, \qquad (38)$$

where $\delta = (\omega_{pe}/3\omega_0)^2 \gg 1$ and $\tilde{\varepsilon}_{\rm rad} = 4\pi r_e N_e/3\lambda_0$. The dependence of the momentum p on the electromagnetic wave amplitude a_0 is depicted in Fig. 5. For $0 < a_0 < a_1$ (where $a_1 \approx \delta$), the momentum can take on three different values. This is characteristic of the nonlinear resonance described by Eq. (38). At $a_0 = a_1$, the momentum increases in a jumplike manner from $p_1 \approx m_e c\delta^{1/3}$ to $p_3 \approx m_e c(a_0/\tilde{\varepsilon}_{\rm rad})^{1/4}$, passing through the value $p_2 \approx m_e c\delta$. The upper branch of the solution shown in Fig. 5 corresponds to the radiation-dominated regime.

That processes similar to plasma resonance play an important part in the interaction of strong electromagnetic radiation with cluster targets was pointed out in [38–41], though, in the first two of these papers, such targets were not referred to as cluster ones.

4.2. Regime of Highly Efficient Ion Acceleration in the Interaction of a Laser Pulse with a Thin Foil

It is well known that, in the interaction of laser radiation with thin solid targets (foils), fast ion beams are generated such that the number of ions in the beam is fairly large and the transverse beam emittance is small. The acceleration of ions is a direct consequence of the acceleration of electrons. Since the mass of the electron component is small, the laser energy is converted primarily into the kinetic energy of electrons. The electron component is displaced and its density changes; as a result, spatial regions appear in which the charge separation is great and the electric fields are strong. In the simplest one-dimensional case, when a wide laser pulse is incident on a thin foil, an electron layer is displaced with respect to the ion layer; as a result, the electric field produced in the region between the layers accelerates the ions. In the non-one-dimensional situation, the high symmetry of one-dimensional processes is violated by such factors as the finite transverse size of the laser pulse, the instability of the wide wave packet of electromagnetic radiation in the plasma, and the Coulomb explosions of electron and ion layers. However, as will be shown below, the process of ion acceleration in the radiation-dominated regime of the interaction of an electromagnetic wave with a target exhibits qualitatively new features. In particular, the electromagnetic pulse and the accelerated charged-particle beam do not break into smaller bunches. The electrons are accelerated under the action of the ponderomotive force of the wave. It should be noted that the ion acceleration mechanism under discussion is closely associated with the ion acceleration mechanism proposed by V.I. Veksler [42]. Veksler's concept of the collective acceleration of ions in an electron–ion bunch moving under the action of the ponderomotive force of an electromagnetic wave has had a profound effect on the development of accelerator physics and plasma physics. Below, we will present the results of numerical simulations that give (to the best of our knowledge) the first demonstration of this acceleration mechanism. Our numerical results show that, in the radiation-dominated regime of the interaction of an electromagnetic wave with a thin plasma slab, the ion layer moves with approximately the same velocity as the electron layer. This indicates that the ion kinetic energy is substantially higher than the electron kinetic energy. The ions are accelerated as a result of the action of the ponderomotive force on the electron component and the energy transfer to them through the charge-separation electric field. The main results of two-dimensional PIC simulations are shown in Figs. 6–8.

In this version of numerical simulations, a linearly polarized (*s*-polarized) laser pulse interacts with a thin film. The pulse is assumed to be Gaussian, with effective sizes of $10\lambda_0 \times 10\lambda_0$ and the amplitude $a_0 = 316$. This amplitude value corresponds to a pulse intensity of 1.37×10^{23} W/cm^2 at the wavelength $\lambda_0 = 1$ μm, in which case the electrons in the wave are ultrarelativistic. However, in accordance with the above parameter values, radiation effects for individual electrons can still be ignored. The thickness of the foil is equal to $l_0 = \lambda_0/4$, and its density is sixteen times higher than the critical density, $n_0 = 16n_{cr}$.

A foil interacting with a laser pulse becomes deformed and changes into a "cocoon," which, in turn, traps the electromagnetic wave (see Figs. 6, 7). The leading edge of the cocoon moves at a relativistic speed. As a result of this process, a plasma layer with an overcritical density, moving at nearly the speed of light, interacts with the electromagnetic wave and reflects it. In other words, electromagnetic radiation is reflected from a relativistic mirror. In the laboratory frame $\mathscr{L}$, the electromagnetic pulse and the mirror move in the same direction. We denote the propagation velocity of the relativistic mirror by V and make the

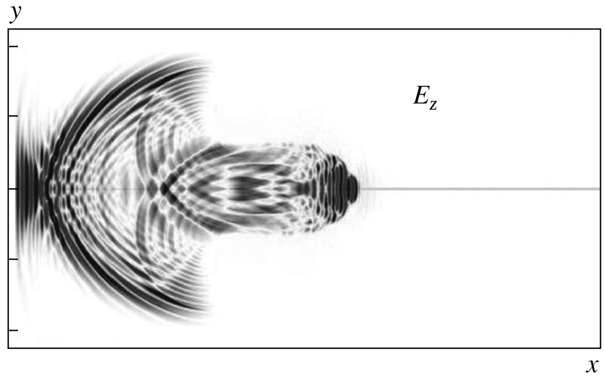

Fig. 6. Distribution of the z component of the electric field in the (x, y) plane at the time $t = 87.5 \times 2\pi/\omega_0$. The wavelength of the reflected electromagnetic wave is seen to be much shorter than the wavelength of the driving electromagnetic pulse. (In this and other figures, the driving pulse propagates from right to left.)

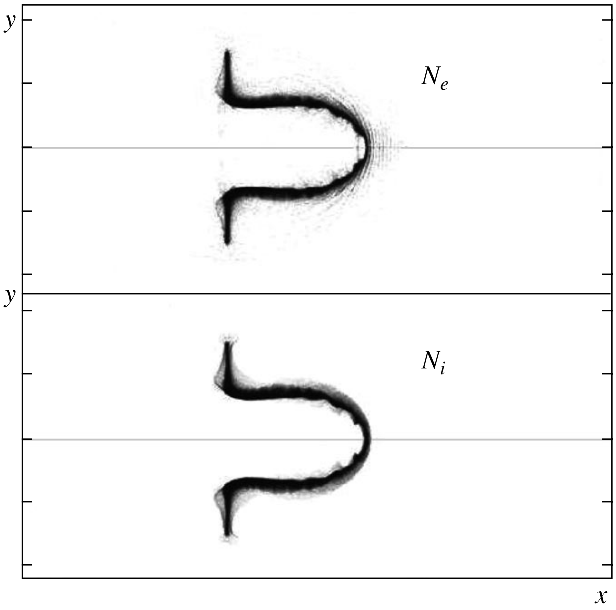

Fig. 7. Distributions of the electron density (on top) and ion density (on bottom) in the (x, y) plane at the time $t = 87.5 \times 2\pi/\omega_0$. The electrons and ions are seen to move in essentially the same manner, forming a cocoon in which the electromagnetic radiation is localized.

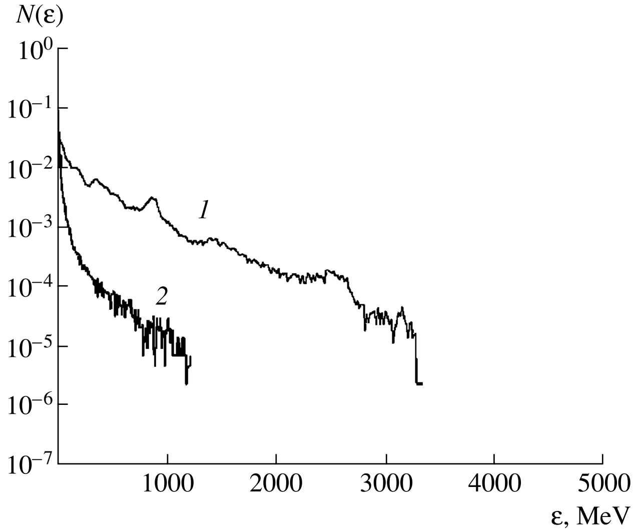

Fig. 8. Energy spectra of (*1*) protons and (*2*) electrons at the time $t = 87.5 \times 2\pi/\omega_0$.

Lorentz transformation to the frame of reference $\mathcal{M}$ in which the mirror is at rest in the $x' = 0$ plane. The time and coordinate (t', x') in frame $\mathcal{M}$ are related to the time and coordinate (t, x) in laboratory frame $\mathcal{L}$ by the relationships

$$x' = \gamma_M(x - Vt), \quad t' = \gamma_M(t - Vx/c^2), \qquad (39)$$

where $\gamma_M = (1 - \beta_M)^{-1/2}$ and $\beta_M = V/c$. In the accompanying frame $\mathcal{M}$, the wave frequency is equal to $\omega' = \omega_0[(1 - \beta_M)/(1 + \beta_M)]^{1/2} \approx \omega_0/2\gamma_M$, the wave vector being $k'_x = \omega'/c$.

In the mirror-at-rest frame $\mathcal{M}$, the plasma density is higher than the critical density calculated with allowance for the relativistic dependence of the plasma frequency on the wave amplitude, $n > \omega'^2 m_e(1 + a_0^2)^{1/2}/4\pi e^2 \approx \omega_0^2 m_e a_0/\gamma_M^2 \pi e^2$ [7], and the thickness of the plasma layer is larger than the collisional skin depth. In this frame, the wave is totally reflected from the mirror. In the Lorentz transformation to a moving frame of reference $\mathcal{M}$, the electric field strength in the wave is transformed according to the law $E' = E_0(\omega'/\omega_0)$; consequently, the pressure (the force per unit area of the mirror) is equal to $E_0^2(\omega'/\omega_0)^2/2\pi = (E_0^2/2\pi)(1 - \beta_M)/(1 + \beta_M)$. It is well known that this pressure is relativistically invariant [43]. As a result, the equation of motion for the leading edge of the cocoon in the laboratory frame $\mathcal{L}$ can be represented in the form

$$\frac{dp}{dt} = \frac{E_0^2}{2\pi n_0 l_0}\left(\frac{(m_p^2c^2 + p^2)^{1/2} - p}{(m_p^2c^2 + p^2)^{1/2} + p}\right). \qquad (40)$$

This equation has the solution

$$\frac{2p^3 + 2(m_p^2c^2 + p^2)^{3/2}}{3m_p^2c^2} + p = \frac{E_0^2}{2\pi n_0 l_0}t + m_p c, \qquad (41)$$

where the integration constant is chosen to satisfy the condition $p = 0$ at $t = 0$. In parametric form, the time dependence of the momentum can be written as

$$p = m_p c\left[\sinh(u) - \frac{1}{4\sinh(u)}\right], \qquad (42)$$

where

$$u = \frac{1}{3}\operatorname{arcsinh}\left(\frac{3E_0^2 t}{2\pi n_0 l_0 m_p c} + 2\right). \qquad (43)$$

In the limit $t \longrightarrow \infty$, we have $p \approx m_p c(3E_0^2 t/8\pi n_0 l_0 m_p c)^{1/3}$ or

$$p \approx m_p c\left(\frac{3}{2}a_0^2\frac{m_e}{m_p}\left(\frac{\omega_0}{\omega_{pe}}\right)^2\frac{ct}{l_0}\right)^{1/3}. \qquad (44)$$

Note that formulas (40)–(44) are clearly analogous to the solution to the problem about the motion of a charged particle under the action of the ponderomotive pressure force of an electromagnetic wave (in the limit $v \longrightarrow c$, the corresponding expression given in [1] can be rewritten as $\overline{W}\sigma_T t/mc \approx (2^{1/2}/3)/(1 - v^2/c^2)^{3/2}$, with $\overline{W} = E_0^2/4\pi$). In the case at hand, the role of the effective scattering cross section is played by the quantity $2/n_0 l_0$.

From relationships (41)–(44), it follows that, with the parameter values chosen for numerical simulations, protons are accelerated to relativistic energies on a characteristic time scale approximately equal to ten periods of the electromagnetic wave. From Fig. 8, we see that, by the time $t = 87.5 \times 2\pi/\omega_0$, the maximum proton energy attains a value of about 34 GeV, the energy of the electrons being about three times lower, ≈1.2 GeV.

The intensity of the wave reflected from the relativistic mirror is equal to $I_r = I_0[(1 - \beta_M)/(1 + \beta_M)]^2 \approx I_0/(16\gamma_{\mathrm{ph}}^4)$. In the limit $\gamma_{\mathrm{ph}} \gg 1$, this intensity is negligibly low in comparison to the intensity of the original laser pulse. Taking into account the change in the pulse length in the reflection process, we find the energy of the reflected wave in frame $\mathcal{L}$: $\mathcal{E}_r = \mathcal{E}_0(1 - \beta_M)/(1 + \beta_M)$. Since the energy of the electromagnetic pulse reflected from the relativistic mirror in the laboratory frame $\mathcal{L}$ is much lower than the original laser pulse energy, the wave energy is absorbed by the plasma almost completely. It can be seen in Fig. 8 that the ions are accelerated to energies that are considerably higher than the energy acquired by the electrons. This is explained by the fact that the velocities of the electron and ion layers are of the same order of magnitude, as is seen in Fig. 7.

Since the mass of the ions is much larger than the mass of the electrons, the ion energy is appreciably higher than the electron energy. Hence, the laser energy is almost completely converted into the energy of the ion component.

Numerical simulations show that the acceleration process is highly stable. Its stability results from the relativistic slowing down of the rate at which the transverse modes develop. In other words, since the longitudinal momentum of the particles is much larger than their transverse momentum, the transverse velocity is much lower than the longitudinal velocity. Consequently, the plasma in the interaction region expands on a time scale longer than the characteristic time for the acceleration of charged particles.

5. AMPLIFICATION OF ELECTROMAGNETIC RADIATION IN ITS INTERACTION WITH A PARABOLIC RELATIVISTIC MIRROR FORMING IN THE WAKE WAVE OF A SHORT LASER PULSE

The above regimes of the interaction of electromagnetic radiation with plasma can occur only when the electric field in the electron's frame of reference is sufficiently strong. However, such electric fields are substantially stronger than those achievable at the present time (the only exception being the problem of a cluster in the field of laser radiation).

The maximum electric field amplitudes that are of interest in the context of our discussion correspond to the critical field at which nonlinear quantum electrodynamic effects in vacuum come into play. One possible way of achieving this maximum was demonstrated in experiments at Stanford University [44–46] on the interaction between a beam of ultrarelativistic electrons and a laser pulse propagating toward it. In those experiments, the electromagnetic wave amplitude in the electron's frame of reference was as large as 25% of the critical field in quantum electrodynamics.

A feasible but technically complex method of increasing laser power through the compression of megajoule laser radiation by seven orders of magnitude was discussed by Tajima and Mourou [47]. They suggested that this may be done at two laser sources that are now under construction—the National Ignition Facility (NIF) in the United States and the megajoule laser system in France. It is expected that a power close to 0.1×10^{21} W, or 0.1 ZW (zetawatt), can be achieved by compressing original laser pulses to a duration of 10 fs with an efficiency of 70%.

Another possible approach is to use high-frequency electromagnetic pulses and to focus them to a spot diameter of about one wavelength. In this way, the expected gain in laser intensity is to be achieved geometrically with X-ray lasers [48–50].

Shen and Yu [51] proposed to generate electromagnetic fields of moderate strength, $\approx 10^{24}$ W/cm^2, by exciting a quasi-soliton standing wave between two foils by an external pump laser pulse of sufficiently large amplitude.

One of the most attractive methods for solving the problem of electromagnetic wave amplification is to use a combination of the two effects—field frequency upshifting and laser pulse compression. That these effects can indeed be involved has been demonstrated in many experiments; but they were generally achieved by different mechanisms. Thus, the amplification of an electromagnetic wave during its reflection from an oppositely propagating layer of relativistic electrons was discussed in [52–55]. The frequency upshifting during reflection from a propagating ionization front was investigated in [56–59]. A technique for frequency upshifting that utilizes the reflection of an electromagnetic wave from a nonlinear Langmuir wave propagating toward it was proposed in [60]. All these proposals are based on the phenomenon of the frequency upshifting of an electromagnetic wave during its reflection from a relativistic mirror. The problem of a uniformly moving relativistic mirror was discussed as early as 1905 by Einstein [61]. Note that an elegant solution to the problem of reflection from a uniformly accelerated relativistic mirror was given in [30].

There exists substantial literature on the amplification of electromagnetic pulses propagating toward one another in a plasma [62–65]. Under the conditions in question, the waves are amplified by parametric processes.

It is well known that the frequency of an ultrashort electromagnetic pulse can be upshifted in its interaction with a Langmuir wave propagating in the same direction. In [66], this phenomenon was called photon acceleration. It received considerable attention in [67–69]. However, in this interaction regime, the maximum frequency upshift and the maximum degree of wave amplification are appreciably smaller than those in the case in which a pulse and a wave propagate toward one another.

In the present paper, we propose to use highly nonlinear wake waves to form parabolic relativistic mirrors with the objective of achieving the following three effects simultaneously: during the reflection from the mirror, the frequency of an electromagnetic radiation pulse is upshifted and the pulse is accordingly compressed in the longitudinal direction, which is accompanied by a great pulse compression in the transverse direction at the expense of focusing. These three effects act to form a narrow, ultrashort, highly directed pulse of high-intensity high-frequency coherent radiation. In comparison with the approaches discussed above, this scheme is very stable (stiff). A brief description of the scheme was given in [70].

The model proposed here makes use of the characteristic features of wake plasma waves generated by ultrashort laser pulses (drivers) in a subcritical plasma. Since the group velocity of an electromagnetic pulse in a subcritical plasma is close to the speed of light, the phase velocity $v_{\rm ph}$ of a Langmuir wave generated by a short electromagnetic pulse is equal to the group velocity of the driver and thus is close to the speed of light [71]. In a nonlinear wake wave, the electron density is modulated in such a way that the electrons form relatively thin layers moving with the velocity $v_{\rm ph}$. It is assumed that the second laser pulse (signal) propagates toward the first laser pulse (driver) and, accordingly, toward the wake wave. Under certain necessary conditions, the signal is partially reflected from the wake wave, which thereby plays the role of a relativistic mirror. The Lorentz factor of the moving mirror is equal to $\gamma_{\rm ph} = (1 - \beta_{\rm ph}^2)^{-1/2} \approx \omega_d/\omega_{pe}$, where ω_d is the driver frequency and ω_{pe} is the Langmuir frequency. As the wake wave amplitude approaches the threshold for wave breaking (i.e., when the electron velocity in the wave approaches the wave phase velocity), the electric field profile in the wave steepens nonlinearly and localized peaks form in the electron density profile [7]. At the breaking point, the electron density formally tends to infinity, which, however, is an integrable singularity, $\int_{-\varepsilon}^{\varepsilon} n_e(x)dx \neq \infty$ (see [33] for details). In the context of the question discussed in this section, an important point is that the singularity does indeed exist; this corresponds to partial reflection of the electromagnetic pulse energy. The reflection coefficient depends on $\gamma_{\rm ph}$. Below, we will show that the amount of the reflected energy is proportional to $\gamma_{\rm ph}^{-1}$. According to the familiar theory in [61], the frequency is upshifted by a factor of

$$\frac{\omega_r}{\omega_s} = \frac{1 + \beta_{\rm ph}}{1 - \beta_{\rm ph}} \approx 4\gamma_{\rm ph}^2, \tag{45}$$

where ω_s is the frequency of the incident electromagnetic signal and ω_r is the frequency of the reflected wave. Another important point is that, since the frequency of a relativistically strong Langmuir wave depends on its amplitude, a laser pulse (driver) of finite width excites plasma waves in the form of paraboloids of revolution [72–76]. Consequently, we are dealing with reflection from a parabolic mirror. This leads not only to the frequency upshifting of the reflected wave and its compression in the longitudinal direction but also to its focusing, which results in an additional compression. During reflection from a moving parabolic mirror, the frequency of the reflected wave depends on the angle of reflection according to the law

$$\omega_r(\theta) = \omega_s \frac{1 + \beta_{\rm ph}}{1 - \beta_{\rm ph}\cos\theta}, \tag{46}$$

where θ is the angle between the line of sight and the propagation direction of the driver. As is seen, formula (46) implies that the frequency of the reflected wave is maximum at $\theta = 0$ and that radiation at the maximum frequency is highly directed (i.e., is confined within an angular range of $\Delta\theta \approx 1/\gamma_{\rm ph}$). The above dependence of the frequency of the reflected radiation on the viewing angle is an important feature of the mechanism under discussion that is to be verified experimentally.

A parallel beam of light reflected from a parabolic mirror is focused to a region with a characteristic diameter on the order of one wavelength. This conclusion concerns an immobile mirror. The frame of reference $\mathcal{K}$ in which a parabolic mirror is at rest moves with the speed $v_{\rm ph}$ with respect to the laboratory frame $\mathcal{L}$. In the mirror-at-rest frame, the wavelength of both the incident and reflected wave is equal to $\lambda_s' = \lambda_s[(1 - \beta_{\rm ph})/(1 + \beta_{\rm ph})]^{1/2} \approx \lambda_s/2\gamma_{\rm ph}$, where λ_s is the wavelength of the laser pulse (signal). We carry out the Lorentz transformation back to the laboratory frame $\mathcal{L}$ and take into account the shortening of longitudinal scale length and the fact that the transformation leaves the transverse sizes of the focal region unchanged. As a result, we find that an electromagnetic wave reflected from an oppositely propagating parabolic mirror is focused into a focal region of radius $\approx\lambda_s(2\gamma_{\rm ph})$ and length $\approx\lambda_s/(4\gamma_{\rm ph}^2)$.

We now determine the energy of the reflected wave and its intensity. We again denote by $\mathcal{E}_0$ the energy of the electromagnetic pulse before its interaction with the mirror in the laboratory frame $\mathcal{L}$. In the accompanying frame $\mathcal{K}$, the pulse energy is equal to $\mathcal{E}_0' = \mathcal{E}_0[(1 + \beta_{\rm ph})/(1 - \beta_{\rm ph})]^{1/2} \approx \mathcal{E}_0 2\gamma_{\rm ph}$. After reflection, the pulse energy becomes $\kappa\mathcal{E}_0[(1 + \beta_{\rm ph})/(1 - \beta_{\rm ph})]^{1/2} \approx \kappa\mathcal{E}_0 2\gamma_{\rm ph}$, where κ is the reflection coefficient to be calculated below. Performing the Lorentz transformation back to the laboratory frame, we see that the energy is equal to $\kappa\mathcal{E}_0[(1 + \beta_{\rm ph})/(1 - \beta_{\rm ph})]^{1/2} \approx \kappa\mathcal{E}_0 4\gamma_{\rm ph}^2$. If the volume of the original pulse is $\pi D^2 L_0$ (where D and L_0 are, respectively, the transverse and longitudinal sizes of the pulse before its interaction with the mirror), then the volume of the pulse near the focal region is $\pi\lambda_s'^2 L_0(1 - \beta_{\rm ph})/(1 + \beta_{\rm ph})$. This, in turn, indicates that, as a result of longitudinal compression and focusing into a region with the transverse size λ_s', the intensity of the radiation pulse reflected from a parabolic mirror increases by a factor of about $\kappa[(1 + \beta_{\rm ph})/(1 - \beta_{\rm ph})]^3(D/\lambda_s)^2 \approx \kappa 64\gamma_{\rm ph}^6 (D/\lambda_s)^2$.

Then, we calculate the reflection coefficient κ, which is defined as the ratio of the energy of the reflected wave flowing through a unit area of the medium to the energy of the incident wave flowing through a unit area in the laboratory frame $\mathcal{L}$. We consider the interaction of a plane electromagnetic wave with a localized maximum in the electron density that forms during the breaking of the wake wave. Under the assumption that the wave amplitude is small, the wave-breaking process in the laboratory frame is described by the equation

$$\partial_{tt}A_z - c^2\Delta A_z + \frac{4\pi e^2 n_e(x-\beta_{\rm ph}t)}{m_e\gamma_e}A_z = 0. \tag{47}$$

Here, $A_z(\mathbf{r}, t)$ is the vector potential of the field of the signal; $n_e(x - \beta_{\rm ph}t)$ is the electron density profile; and $\gamma_e = \mathscr{E}_e/m_ec^2$ is the gamma-factor of the electrons, which is equal to $\gamma_{\rm ph}$ near the breaking point (i.e., near the maximum in the electron density profile).

According to the results obtained by Akhiezer and Polovin [7], the density of the electron component and its velocity in a relativistic Langmuir wave are related by $n = n_0v_{\rm ph}/(v_{\rm ph} - v_e)$. It can be seen that, at the breaking point, at which $v_e = v_{\rm ph}$ (i.e., $\gamma_e = \gamma_{\rm ph}$), the electron density becomes infinite. Since, in a steady-state Langmuir wave near the breaking threshold, the electron velocity changes within the limits $-v_{\rm ph} < v_e < +v_{\rm ph}$, the minimum electron density is equal to $n_0/2$. In a nonlinear wave, roughly half of the electrons are in the narrow peaks; the other half are equally distributed in the regions between the peaks and have the density $n_e = n_0/2$ (see, e.g., Fig. 1 in [76]). Hence, the function $n_e(x - \beta_{\rm ph}t)$ can be approximated by the expression

$$n_e(x-\beta_{\rm ph}t) = (n_0/2)[1+\lambda_p\delta(x-\beta_{\rm ph}t)], \tag{48}$$

where $\delta(x)$ is the Dirac delta function and λ_p is the wavelength of the wake wave. This approximation is valid under the conditions for the breaking of a Langmuir wave, i.e., when the wavelength of the electromagnetic pulse is short and the skin depth c/ω_{pe} is small as compared to the thickness of the electron layer.

Transforming to the reference frame $\mathscr{K}$, which accompanies the wake wave, does not change the form of Eq. (47). The Lorentz transformation to this frame is given by Eqs. (39) with $V = -v_{\rm ph}$. Let us determine the coefficient of reflection of an electromagnetic wave from a partially transparent relativistic mirror—a thin plasma layer moving with a relativistic velocity. We seek a solution to Eq. (47) in the form $A_z(x', t') = \mathscr{A}(x')\exp[-i(\omega_s't' + k_x'x' + k_y'y' + k_z'z')]$, where $\omega_s' = (\omega_s + k_xv_{\rm ph})\gamma_{\rm ph}$, is the frequency in frame $\mathscr{K}$, $k_x' = (k_x + \omega_sv_{\rm ph}/c^2)\gamma_{\rm ph}$ and $k_\perp' = k_\perp$ are the components of the wave vector $\mathbf{k}' = (k_x', k_\perp')$ in this frame, and $k_x' > 0$. Using these formulas, we reduce Eq. (47) in the moving frame to the form

$$\frac{d^2\mathscr{A}}{dx'^2} + q^2\mathscr{A} = \chi\delta(x')\mathscr{A}, \tag{49}$$

where $q^2 = \omega_s'^2/c^2 - k_\perp^2 - \omega_{pe}^2/(2\gamma_{\rm ph}c^2)$ and $\chi = \omega_{pe}^2\lambda_p/c^2$. The boundary conditions for the equation can be specified as follows:

$$\mathscr{A}(x') = \exp(iqx') + \rho(q)\exp(-iqx') \tag{50}$$

for $x' < 0$ (which corresponds to an incident and a reflected wave) and

$$\mathscr{A}(x') = \tau(q)\exp(iqx') \tag{51}$$

for $x' > 0$ (which indicates that, in the half-space $x' > 0$, there is only a reflected wave). The problem as formulated is equivalent to the problem of scattering by a potential in the form of a delta function. The coefficients $\rho(q)$ and $\tau(q)$ are determined from the condition that the function $A(x', t')$ is continuous at the mirror,

$$\{\mathscr{A}(x')\}_0 = \mathscr{A}(+0) - \mathscr{A}(-0) = 0, \tag{52}$$

and the condition that the jump in its derivative is equal to

$$\left\{\frac{d\mathscr{A}}{dx'}\right\}_0 = \chi\mathscr{A}(0). \tag{53}$$

As a result, we obtain

$$\rho(q) = -\frac{\chi}{\chi + 2iq}, \quad \tau(q) = \frac{2iq}{\chi + 2iq}. \tag{54}$$

From this, it follows easily that $|\rho(q)|^2 + |\tau(q)|^2 = 1$.

The wavelength of a nonlinear Langmuir wave depends on its amplitude [7]. For a wake wave excited in a plasma by a short laser pulse, this dependence can be represented as $\lambda_p \approx 4(2\gamma_{\rm ph})^{1/2}c/\omega_{pe}$ [33, 76], which is valid in the limit of relativistically strong waves near the breaking threshold ($\gamma_e \approx \gamma_{\rm ph}$). In this case, we have $\chi = 4(2\gamma_{\rm ph})^{1/2}\omega_{pe}/c$. Taking into account the relationships $\omega_s'^2 = 4\gamma_{\rm ph}^2\omega_s^2$ and $\gamma_{\rm ph} = \omega_d/\omega_{pe}$, we find the reflection coefficient in the accompanying frame of reference:

$$\kappa^{(\mathscr{K})} \approx (\omega_d/\omega_s)^2/(2\gamma_{\rm ph}^3). \tag{55}$$

In the laboratory frame, the reflection coefficient for a plane wave incident normally on the thin plasma layer that forms during the breaking of the wake wave takes the form

$$\kappa^{(\mathscr{L})} \approx 8(\omega_d/\omega_s)^2\gamma_{\rm ph}. \tag{56}$$

With allowance for the change in the volume of the electromagnetic pulse as a result of its focusing into a region with a transverse size of $\approx\lambda_s' = \lambda_s/2\gamma_{\rm ph}$, we find that the intensity of the reflected wave increases by a factor of

$$\frac{I_{sf}}{I_s} \approx 32\left(\frac{\omega_d}{\omega_s}\right)^2\left(\frac{D}{\lambda_s}\right)^2\gamma_{\rm ph}^3. \tag{57}$$

Using this relationship and taking into account the fact that the reflected pulse is compressed by a factor of

$\approx 4\gamma_{\mathrm{ph}}^2$, we obtain the ratio of the energy of the reflected pulse to the energy of the incident wave:

$$\frac{\mathcal{E}_{sf}}{\mathcal{E}_s} \approx 2\left(\frac{\omega_d}{\omega_s}\right)^2 \frac{1}{\gamma_{\mathrm{ph}}}. \tag{58}$$

In future studies, the above estimates of the intensity of the reflected wave will have to be refined, in particular, by accounting for both the nonlinear processes and the effect of the non-one-dimensional geometry of reflection on the value of the reflection coefficient.

One of the nonlinear effects in question is associated with the ponderomotive force exerted by a signal electromagnetic wave on the relativistic mirror produced by the wake wave. As a result, the parameters of the mirror should change. Using the reflection coefficient given by expression (55) or (56), we determine the strength of the ponderomotive force:

$$P = \kappa^{(\mathcal{L})}\frac{c}{4\pi}E_s^2 \approx \frac{2c}{\pi}E_s^2\left(\frac{\omega_d}{\omega_s}\right)^2\gamma_{\mathrm{ph}}. \tag{59}$$

The time required for the ponderomotive force to perform work comparable to the kinetic energy of the reflecting electron layer ($\approx n_0 m_e c^2 \lambda_p \gamma_{\mathrm{ph}}/2$) is equal in order of magnitude to $\Delta t \approx 2^{-1}\omega_{pe}^{-1} a_{0,s}^{-2}(2\gamma_{\mathrm{ph}})^{1/2}$. This relationship restricts the duration and/or amplitude of an incident laser pulse, for each of which the nonlinear processes occurring during reflection can legitimately be ignored. Another nonlinear effect stems from the transparency of a relativistic dense plasma layer [7, 77] and takes place for relativistically strong electromagnetic waves with a dimensionless amplitude larger than unity, $a_{0,s} > 1$. Using the results obtained in [78] (see also [79–81]), in which the coefficient of reflection of a relativistically strong electromagnetic pulse from a thin dense plasma layer was calculated, we can show that accounting for the effect at hand should reduce the reflection coefficient. As a consequence, expression (56) becomes $\kappa^{(\mathcal{L})} \approx 8(\omega_d/\omega_s)^2\gamma_{\mathrm{ph}}/a_{0,s}$.

As an example, we consider the generation of a wake wave in a plasma with the density $n_e = 10^{17}$ cm^{-3} by a short electromagnetic pulse (driver) with a wavelength of one micron. The wavelength of the wake field that corresponds to these parameters is equal to $\lambda_p \approx 100$ μm, so that the Lorentz factor γ_{ph} is $\gamma_{\mathrm{ph}} = \omega_d/\omega_{pe} = 100$. Let a laser pulse (signal) propagating toward the driver have a wavelength of one micron and the intensity $I_s = 10^{17}$ W/cm^2 (which corresponds to a dimensionless amplitude of $a_{0,s} \approx 0.27$). In this situation, the signal is partially reflected from the peak in the electron density in the wake wave and is focused by this wave. If the effective transverse size of the signal equals $D = 200$ μm, then, from expression (57), it follows that the intensity of the reflected radiation in the focal region is approximately equal to $I_{sf} \approx 1.5 \times 10^{29}$ W/cm^2. For a driver generating a wake wave to be capable of producing a wide parabolic mirror in the plasma, its intensity must be sufficiently high and its transverse size must be sufficiently large. Let the intensity of the driver be equal to $I_d = 10^{18}$ W/cm^2 and let its diameter be $D_d = 800$ μm. In this case, we find that the more intense and less intense laser pulses under consideration, each of which is as long as several wavelengths, have energies of several tens of joules and of several joules, respectively. These energies are achievable with laser devices that are now in use in many laboratories around the world. We can thus conclude that, by implementing the above scenario of the amplification of electromagnetic radiation, it will be possible to achieve electric fields in the focal region that are as strong as the critical field in quantum electrodynamics.

We now present the results of two-dimensional simulations of the process under discussion here—the interaction between two laser pulses propagating toward one another in a low-density plasma. PIC simulations were carried out using the REMP numerical code [37].

In the model, a driver propagates along the x axis from left to right. The dimensionless driver amplitude is $a_d = 1.7$, which corresponds to the intensity 4×10^{18} W/cm^2 $(1\ \mu\mathrm{m}/\lambda_d)^2$. The driver is polarized by an electric field pointing along the y axis and is Gaussian in shape in both longitudinal and transverse directions, with sizes $3\lambda_d \times 6\lambda_d$. The wavelength of the signal propagating toward the driver is two times longer, $\lambda_s = 2\lambda_d$. In order to ignore the nonlinear effects occurring during the reflection of the signal, its amplitude was set sufficiently small, $a_s = 0.05$. The signal is rectangular in shape in the longitudinal direction and is Gaussian in shape in the transverse direction, the corresponding sizes being $3\lambda_s \times 3\lambda_s$. In order to distinguish between the electromagnetic fields of the driver and of the signal, the polarization of the signal is assumed to be linear, namely, the signal electric field is chosen parallel to the z axis and, accordingly, perpendicular to the polarization direction of the driver. The two laser pulses propagate in a low-density plasma layer with the electron density $n_0 = 0.09 n_{\mathrm{cr}}$, which corresponds to the Langmuir frequency $\omega_{pe} = 0.3\omega_d$. In the longitudinal direction, the plasma layer occupies the interval $2\lambda_d < x < 13\lambda_d$. The size of the computation region is $19.5\lambda_d \times 22\lambda_d$. The number of cells in the numerical grid was chosen to be large enough to ensure the desired resolution of the structure of the short-wavelength reflected radiation pulse at the frequency predicted by formula (43). Specifically, the grid consisted of 1950×2200 cells, the spatial step being $dx = \lambda_d/100$. At the left and right boundaries of the computation region, the boundary conditions corresponded to complete absorption of both the electromagnetic field and the particles. At the upper and lower boundaries, the boundary conditions were assumed to be periodic.

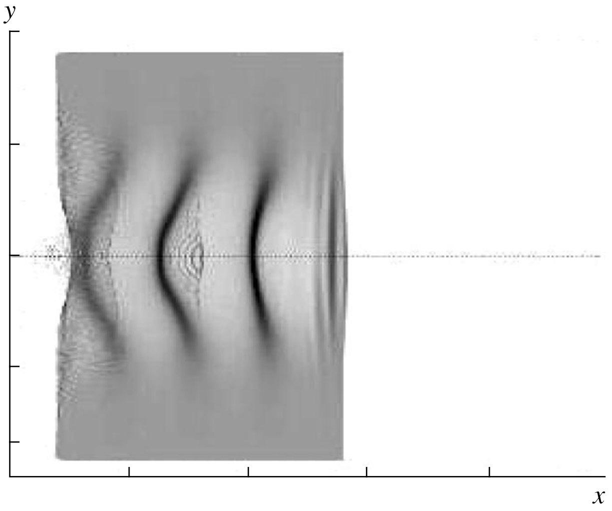

Fig. 9. Electron density distribution within the plasma layer in a wake plasma wave. The density is maximum near parabolic surfaces.

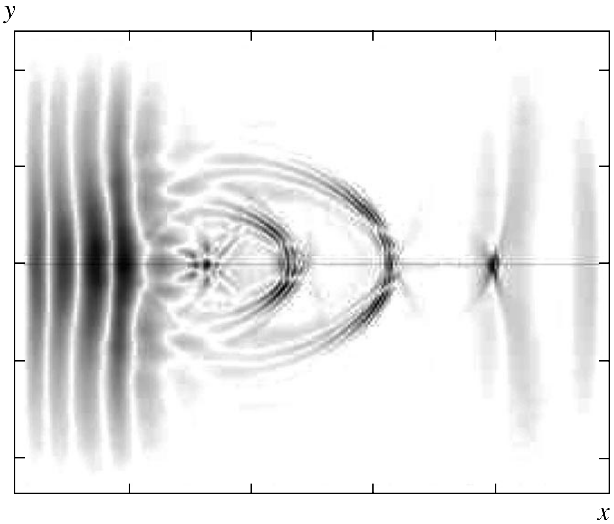

Fig. 10. Projection of the *z* component of the electric field of the passing incident laser radiation (on the left of the figure) and the radiation reflected and focused by the wake wave of the laser pulse.

The results of numerical simulations are illustrated in Figs. 9 and 10.

In Fig. 9, we see a parabolic modulation of the electron density in a wake plasma wave excited by the driver. The transverse scale length of the modulation exceeds the transverse size of the signal, which is reflected from the peaks in the electron density propagating toward it. Figure 10 shows the distribution of the *z* component of the electric field of the laser radiation in the (x, y) plane. The radiation passes through the wake wave (see the left part of Fig. 10) and is partially reflected by it. We can see that a substantial portion of the signal is reflected and is focused into regions whose sizes are considerably smaller than the original laser wavelength. This indicates, in particular, that the frequency of the reflected electromagnetic wave is upshifted.

For the parameter values chosen in numerical simulations, the phase velocity of the wake wave corresponds to the value $\beta_{ph} = 0.87$, i.e., to $\gamma_{ph} = 2$. The number of waves in the reflected electromagnetic pulse is the same as that in the incident pulse by virtue of the fact that the number of waves in the wave packet is relativistically invariant. The frequency of the reflected electromagnetic wave is 14 times higher than the wave frequency in the incident pulse. This degree of upshift is in complete agreement with that predicted by formula (43), because, in this case, we have $(1 + \beta_{ph})/(1 - \beta_{ph}) \approx 14.4$. The electric field of the reflected and focused radiation is stronger than that in the incident pulse by a factor of approximately 16, which corresponds to an increase in the radiation intensity by a factor of 256. On the outside of the focal region, the radiation propagates in the form of an expanding wave whose frequency depends on the propagation angle in accordance with formula (44). Most of the radiation energy is confined within the angular range $\Delta\theta \approx 1/\gamma_{ph}$, indicating the formation of a narrow beam of high-intensity high-frequency radiation.

At this point, we should emphasize that, in accordance with the conclusions of [60] (see also [33]), efficient reflection of the electromagnetic radiation from the wake wave can only be achieved during the breaking process, i.e., during the formation of sharp peaks in the electron density in the wake wave.

We have considered a situation in which both of the interacting pulses are produced in a controlled manner. However, the processes (similar to those discussed above) that are responsible for the frequency upshifting of electromagnetic radiation can occur in the plasma spontaneously. This can happen, for example, when the laser pulse generating a wake wave undergoes stimulated Raman backscattering and emits part of its energy in the form of a wave packet propagating in the opposite direction. This can also happen as a result of the scattering (reflection) of electromagnetic radiation from plasma inhomogeneities. The model described above implies that, if a propagating electromagnetic wave meets a nonlinear wake wave moving toward to it with a relativistic speed (i.e., with $\gamma_{ph} \gg 1$), then such processes as reflection, frequency upshifting, focusing, the amplification of radiation, and the formation of a collimated (within an angle of about $\approx 1/\gamma_{ph}$) beam of electromagnetic radiation will also occur in the plasma.

6. CONCLUSIONS

We have classified different regimes of the interaction of electromagnetic waves with plasmas in terms of the wave amplitude. We have shown that, over the entire range of the wave amplitudes under consideration, there is a wide intermediate range (between the range dominated by relativistic effects and that dominated by nonlinear quantum electrodynamic effects) in which radiative friction forces and then (for larger amplitudes) quantum processes become of fundamental importance.

The main characteristic features of the radiation-dominated regime have been demonstrated using the interaction of high-power laser radiation with a cluster and a thin foil as examples.

In the example of the interaction with a cluster, we have demonstrated the generation of a short pulse of high-frequency coherent radiation.

The interaction of an electromagnetic wave with a thin foil in the radiation-dominated regime is of particular interest because we have demonstrated that, in this case, the efficiency of the conversion of laser energy into the energy of fast ions is high. We have also shown that this ion acceleration scheme is stable. In the situation considered above, the mechanism for collective ion acceleration is associated with the reflection of a strong electromagnetic wave from a relativistic mirror—a dense plasma layer moving with relativistic velocity. The wave is reflected from a mirror moving in the propagation direction of the laser electromagnetic pulse. This is why the acceleration process is stable and highly efficient. The stability is ensured by the relativistic slowing down of the rate at which the transverse modes develop (or the plasma expands into a vacuum). The efficiency with which the electromagnetic wave energy is converted into the kinetic energy of the directed motion of charged particles is high because, in the laboratory frame, the intensity of the reflected wave is negligibly low, so that the energy of the wave and its momentum are almost entirely transferred to the particles.

In order for the above regimes of the interaction of radiation with matter to be implemented, it is necessary to have laser sources with parameters unachievable at the present time. However, with the approach proposed here, which makes use of two simultaneous effects—frequency upshifting and the focusing of laser pulses—it is possible to generate the required very high-intensity electromagnetic pulses by means of state-of-the-art laser devices.

ACKNOWLEDGMENTS

This work was supported in part by INTAS (grant no. 001-0233) and the Russian Foundation for Basic Research (project no. 02-02-16756a).

REFERENCES

1. L. D. Landau and E. M. Lifshitz, *The Classical Theory of Fields* (Nauka, Moscow, 1973; Pergamon Press, Oxford, 1975).
2. V. B. Berestetskii, E. M. Lifshitz, and L. P. Pitaevskii, *Quantum Electrodynamics* (Nauka, Moscow, 1980; Pergamon, New York, 1982).
3. E. Sarachik and G. Schappert, Phys. Rev. D **1**, 2738 (1970).
4. S.-Y. Chen, A. Maksimchuk, and D. Umstadter, Nature **396**, 653 (1998).
5. Y. Ueshima, Y. Kishimoto, A. Sasaki, and T. Tajima, Laser Part. Beams **17**, 45 (1999).
6. Y. Y. Lau, F. He, D. P. Umstadter, and R. Kowalczyk, Phys. Plasmas **10**, 2155 (2003).
7. A. I. Akhiezer and R. V. Polovin, Zh. Éksp. Teor. Fiz. **30**, 915 (1956) [Sov. Phys. JETP **3**, 696 (1956)].
8. J. E. Gunn and J. P. Ostriker, Phys. Rev. Lett. **22**, 728 (1969).
9. V. S. Berezinskii, S. V. Bulanov, V. L. Ginzburg, *et al.*, *Astrophysics of Cosmic Rays* (Elsevier, Amsterdam, 1990).
10. G. A. Mourou, C. P. J. Barty, and M. D. Perry, Phys. Today **51**, 22 (1998).
11. V. A. Buts and A. V. Buts, Zh. Éksp. Teor. Fiz. **110**, 818 (1996) [JETP **83**, 449 (1996)].
12. L. G. Glazov and A. A. Rukhadze, Fiz. Plazmy **19**, 1289 (1993) [Plasma Phys. Rep. **19**, 679 (1993)].
13. C. I. Moore, A. Ting, S. J. McNaught, *et al.*, Phys. Rev. Lett. **82**, 1688 (1999).
14. J. W. Shearer, J. Garrison, J. Wong, and J. E. Swain, Phys. Rev. A **8**, 1582 (1973).
15. G. S. Bisnovatyĭ-Kogan, Ya. B. Zel'dovich, and R. Syunyaev, Astron. Zh. **48**, 24 (1971) [Sov. Astron. **48**, 17 (1971)].
16. E. P. Liang, S. C. Wilks, and M. Tabak, Phys. Rev. Lett. **81**, 4887 (1998).
17. C. Gahn, G. D. Tsakiris, G. Pretzler, *et al.*, Phys. Plasmas **9**, 987 (2002).
18. K. Nakashima and H. Takabe, Phys. Plasmas **9**, 1505 (2002).
19. Ya. B. Zel'dovich and A. F. Illarionov, Zh. Éksp. Teor. Fiz. **61**, 880 (1971) [Sov. Phys. JETP **34**, 467 (1971)].
20. Ya. B. Zel'dovich, Usp. Fiz. Nauk **115**, 161 (1975) [Sov. Phys. Usp. **18**, 79 (1975)].
21. A. D. Steiger and C. H. Woods, Phys. Rev. E **5**, 1467 (1972).
22. A. A. Sokolov and I. M. Ternov, *Synchrotron Radiation* (Pergamon, New York, 1968).
23. W. Heisenberg and H. Z. Euler, Z. Phys. **98**, 714 (1936).
24. J. Schwinger, Phys. Rev. **82**, 664 (1951).
25. E. Brezin and C. Itzykson, Phys. Rev. D **2**, 1191 (1970).
26. N. B. Narozhnyĭ and A. I. Nikishov, Zh. Éksp. Teor. Fiz. **65**, 862 (1973) [Sov. Phys. JETP **38**, 427 (1973)].
27. V. S. Popov, Zh. Éksp. Teor. Fiz. **121**, 1235 (2002) [JETP **94**, 1057 (2002)].
28. V. I. Ritus, Tr. Fiz. Inst. Akad. Nauk SSSR **111**, 6 (1979).
29. A. Zhidkov, J. Koga, A. Sasaki, and M. Uesaka, Phys. Rev. Lett. **88**, 185002 (2002).
30. F. V. Hartemann, *High-Field Electrodynamics* (CRC, New York, 2002).

31. Y. Kishimoto and T. Tajima, *High Field Science*, Ed. by T. Tajima, K. Mima, and H. Baldis (Plenum, New York, 1999), p. 85.
32. L. D. Landau and E. M. Lifshitz, *Electrodynamics of Continuous Media* (Nauka, Moscow, 1982; Pergamon, New York, 1984).
33. S. V. Bulanov *et al.*, Rev. Plasma Phys. **22**, 227 (2001).
34. K. Nishihara, H. Amitani, M. Murakami, *et al.*, Nucl. Instrum. Methods Phys. Res. A **464**, 98 (2001).
35. V. P. Krainov and M. B. Smirnov, Phys. Rep. **370**, 237 (2002).
36. B. Breĭzman and A. V. Aref'ev, Fiz. Plazmy **29**, 642 (2003) [Plasma Phys. Rep. **29**, 593 (2003)].
37. T. Zh. Esirkepov, Comput. Phys. Commun. **135**, 144 (2001).
38. V. B. Gil'denburg, Yu. M. Zhidkov, I. G. Kondrat'ev, and M. A. Miller, Izv. Vyssh. Uchebn. Zaved., Radiofiz. **10**, 1358 (1967).
39. G. A. Askar'yan and S. V. Bulanov, Pis'ma Zh. Tekh. Fiz. **9**, 1243 (1983) [Sov. Tech. Phys. Lett. **9**, 533 (1983)].
40. V. Kumarapan, V. Krishnamurphy, and D. Mathur, Phys. Rev. A **66**, 033203 (2002).
41. V. Kumarapan, V. Krishnamurphy, and D. Mathur, Phys. Rev. A **67**, 043204 (2003).
42. V. I. Veksler, in *Proceedings of the CERN Symposium on High Energy Accelerators and Pion Physics, Geneva, 1956*, Vol. 1, p. 80.
43. W. Pauli, *The Theory of Relativity* (Pergamon Press, Oxford, 1958; Gostekhizdat, Moscow, 1947).
44. C. Bula, K. T. McDonald, E. J. Prebys, *et al.*, Phys. Rev. Lett. **76**, 3116 (1996).
45. D. L. Burke, R. C. Feld, G. Horton-Smith, *et al.*, Phys. Rev. Lett. **79**, 1626 (1997).
46. C. Bamber, S. J. Boege, T. Koffas, *et al.*, Phys. Rev. D **60**, 092004 (1999).
47. T. Tajima and G. Mourou, Phys. Rev. ST Accel. Beams **5**, 031301 (2002).
48. A. Ringwald, Phys. Lett. B **510**, 107 (2001).
49. R. Alkofer, M. B. Hecht, C. D. Roberts, *et al.*, Phys. Rev. Lett. **87**, 193902 (2001).
50. T. Tajima, Fiz. Plazmy **29**, 231 (2003) [Plasma Phys. Rep. **29**, 207 (2003)].
51. B. Shen and M. Y. Yu, Phys. Rev. Lett. **89**, 275004 (2002).
52. K. Landecker, Phys. Rev. **86**, 852 (1952).
53. L. A. Ostrovskiĭ, Usp. Fiz. Nauk **116**, 315 (1975) [Sov. Phys. Usp. **18**, 452 (1975)].
54. F. R. Arutyunian and V. A. Tumanian, Phys. Lett. **4**, 176 (1963).
55. Y. Li, Z. Huang, M. D. Borland, and S. Milton, Phys. Rev. ST Accel. Beams **5**, 044701 (2002).
56. V. I. Semenova, Izv. Vyssh. Uchebn. Zaved., Radiofiz. **10**, 599 (1967).
57. W. B. Mori, Phys. Rev. A **44**, 5118 (1991).
58. R. L. Savage, Jr., W. B. Mori, and C. Joshi, Phys. Rev. Lett. **68**, 946 (1992).
59. J. M. Dias, N. C. Lopes, L. O. Silva, *et al.*, Phys. Rev. E **66**, 056406 (2002).
60. S. V. Bulanov, I. N. Inovenkov, V. I. Kirsanov, *et al.*, Kratk. Soobshch. Fiz. **6**, 9 (1991).
61. A. Einstein, Ann. Phys. (Leipzig) **17**, 891 (1905).
62. G. Shvets, N. J. Fisch, A. Pukhov, and J. Meyer-ter-Vehn, Phys. Rev. Lett. **81**, 4879 (1998).
63. Y. Ping, I. Geltner, N. J. Fisch, *et al.*, Phys. Rev. E **62**, R4532 (2000).
64. P. Zhang, N. Saleh, S. Chen, *et al.*, Phys. Plasmas **10**, 2093 (2003).
65. N. J. Fisch and V. M. Malkin, Phys. Plasmas **10**, 2056 (2003).
66. S. C. Wilks, J. M. Dawson, W. B. Mori, *et al.*, Phys. Rev. Lett. **74**, 4428 (1989).
67. S. V. Bulanov, V. I. Kirsanov, F. Pegoraro, and A. S. Sakharov, Laser Phys. **3**, 1078 (1993).
68. A. A. Solodov, P. Mora, and P. Chessa, Phys. Plasmas **6**, 503 (1999).
69. J. T. Mendonca, *Photon Acceleration in Plasmas* (Inst. Phys. Publ., Bristol, 2001).
70. S. V. Bulanov, T. Zh. Esirkepov, and T. Tajima, Phys. Rev. Lett. **91**, 085001 (2003).
71. T. Tajima and J. M. Dawson, Phys. Rev. Lett. **43**, 267 (1979).
72. S. V. Bulanov and A. S. Sakharov, Pis'ma Zh. Éksp. Teor. Fiz. **54**, 208 (1991) [JETP Lett. **54**, 203 (1991)].
73. S. V. Bulanov, F. Pegoraro, and A. M. Pukhov, Phys. Rev. Lett. **74**, 710 (1995).
74. S. V. Bulanov, F. Pegoraro, A. M. Pukhov, and A. S. Sakharov, Phys. Rev. Lett. **78**, 4205 (1997).
75. Z.-M. Sheng, Y. Sentoku, K. Mima, and K. Nishihara, Phys. Rev. E **62**, 7258 (2000).
76. S. V. Bulanov, V. A. Vshivkov, G. I. Dudnikova, *et al.*, Fiz. Plazmy **25**, 764 (1999) [Plasma Phys. Rep. **25**, 701 (1999)].
77. P. Kaw and J. Dawson, Phys. Fluids **13**, 472 (1970).
78. A. V. Vshivkov, N. M. Naumova, F. Pegoraro, and S. V. Bulanov, Phys. Plasmas **5**, 2727 (1998); S. V. Bulanov, Izv. Vyssh. Uchebn. Zaved., Radiofiz. **18**, 1511 (1975).
79. V. L. Bratman and S. V. Samsonov, Phys. Lett. A **206**, 377 (1995).
80. A. S. Il'in, V. A. Cherepenin, and V. V. Kulagin, Fiz. Plazmy **27**, 1111 (2001) [Plasma Phys. Rep. **27**, 1048 (2001)].
81. B. Shen and J. Meyer-ter-Vehn, Phys. Rev. E **65**, 16405 (2002).

Translated by O.E. Khadin

Plasma Physics Reports, Vol. 30, No. 3, 2004, pp. 214–217. Translated from Fizika Plazmy, Vol. 30, No. 3, 2004, pp. 241–244.
Original Russian Text Copyright © 2004 by Zaburdaev, Smirnov, Chukbar.

NONLINEAR PHENOMENA

Nonlinear Dynamics of Electron Vortex Lattices

V. Yu. Zaburdaev, V. V. Smirnov, and K. V. Chukbar

Russian Research Centre Kurchatov Institute, pl. Kurchatova 1, Moscow, 123182 Russia

Received April 14, 2003; in final form, July 24, 2003

Abstract—Weak and strong nonlinearities that determine the evolution of regular ensembles of electron vortices in a magnetized plasma are analyzed. Qualitative differences in behavior between such a medium and standard nonlinear media are revealed. © *2004 MAIK "Nauka/Interperiodica".*

In recent years, it has become rather popular to represent magnetized plasma as a medium filled with two-dimensional vortices, vortex filaments, or other vortex structures (see, e.g., [1]). Therefore, investigation into the dynamics of large chaotic or regular vortex ensembles seems to be a very interesting and challenging problem. In [2], the following equation describing the evolution of long-wavelength nonlinear perturbations in a triangular lattice (the only one that is stable) of identical electron-type two-dimensional point vortices was derived:

$$\frac{\partial \boldsymbol{\xi}}{\partial t} = -R\mathbf{e}_z \times \boldsymbol{\nabla}(\nabla \cdot \boldsymbol{\xi}) + D\boldsymbol{\nabla}(\mathbf{e}_z \cdot (\nabla \times \boldsymbol{\xi})) + \frac{R}{2}\mathbf{e}_z \times \boldsymbol{\nabla}\left[(\nabla \cdot \boldsymbol{\xi})^2 + \frac{\partial \xi_\alpha}{\partial x_\beta}\frac{\partial \xi_\beta}{\partial x_\alpha}\right], \qquad (1)$$

where $\boldsymbol{\xi} = \{\xi_x, \xi_y\}$ is the two-dimensional deformation (displacement) vector of the vortex crystalline medium treated as a continuous medium and summation is performed over repeated Greek indices. Equation (1) can be regarded as an analog of the acoustic equation for ordinary crystals. In [2], its linear properties were mainly analyzed. Below, we will study specific nonlinear properties of Eq. (1).

First, we will comment on this basic equation (see [2] for details). It is derived through a series expansion in the vortex displacement from the lattice points. Therefore, Eq. (1) is valid when the deformation is small ($|\boldsymbol{\xi}| \ll a$, where a is the distance between the neighboring lattice points; more precisely, it is the difference between the displacements of the neighbors that must be small) and, accordingly, the nonlinearity is small. By the point vortex, we mean a vortex whose core (a domain with a nonzero curl of the generalized electron momentum) is small compared to a. Microscopic vortices are characterized by their (identical) intensities q_0 and the screening-type flux function $\psi(|\mathbf{r}|/b)$ with the screening scale $b \gg a$. Both these parameters describe the flow produced by each vortex (for a vortex located at $\mathbf{r} = 0$, we have $\mathbf{v} = q_0\mathbf{e}_z \times \boldsymbol{\nabla}\psi$) and the vortex interaction energy $\mathscr{E} = q_0^2\sum_{i<j}\psi(\mathbf{r}_i - \mathbf{r}_j)$, where summation is performed over the entire lattice. In the continuous medium approximation adopted here, the sum is replaced with an integral over a plane (see [2]). The local nature of Eq. (1) (although, as follows from the form of the function ψ, the motion of each vortex is determined by its neighbors, which are $\sim(b/a)^2$ in number) is associated with the fact that the characteristic perturbation wavelength meets the inequality $\lambda \gg b$. The lattice elasticity moduli, which characterize the response of the lattice to uniform compression and torsion (shear), are time-independent (depend on its unperturbed structure alone),

$$R = \frac{2q_0}{\sqrt{3}a^2}\int\psi dxdy, \quad D \sim q_0|\psi(a)|$$

and differ significantly from each other: $D \sim R(a/b)^2$. The reason is that the discrete lattice demonstrates poor compressibility in vortex flows. For electron vortices in the electron magnetohydrodynamics [3], using the results of [2] and the pioneering work on vortex lattices [5], we obtain

$$R = \frac{4\pi q_0}{\sqrt{3}}\left(\frac{b}{a}\right)^2, \quad D = \frac{q_0}{8}$$

(the same behavior is typical of vortexes in superconductors [4], in which ψ is the Macdonald function $K_0(r\omega_{pe}/c)$).

It can be seen that, within Eq. (1), nonlinear waves can be analyzed in terms of the normal coordinates of shear and compression deformations, $\mathbf{e}_z \cdot (\nabla \times \boldsymbol{\xi})$ and $\nabla \cdot \boldsymbol{\xi}$.[1] For nonlinear effects, it turns out to be more convenient to consider potentials of these deformations by representing the displacement vector as $\boldsymbol{\xi} = \mathbf{e}_z \times \boldsymbol{\nabla}\phi + \boldsymbol{\nabla}\varphi$.

---

[1] The fact that only one type of waves that interrelate these deformations exists in two-dimensional media (unlike ordinary crystals, in which they evolve independently) is caused by Cartesian rather than Newtonian vortex mechanics (the position of a particle determines its velocity rather than acceleration). As a result, the two-dimensional vortex problem is, in a sense, equivalent to an ordinary one-dimensional problem (see [2]).

Interestingly, the Schrödinger character of the phonon spectrum of a triangular electron vortex lattice ($\omega \propto k^2$) can be emphasized by combining these potentials into the wave function $\Phi = \phi + i\sqrt{R/D}\varphi$, which reduces the linear portion of Eq. (1) to:

$$i\frac{\partial \Phi}{\partial t} + \sqrt{RD}\Delta\Phi = 0$$

(removing the ∇ operator from both sides of the equation produces constant terms, which are hereafter set equal to zero; this, however, has no effect on the physically observed quantity $\boldsymbol{\xi}$). This expression also clearly demonstrates that, since in linear waves the ratio D/R is small, shear deformations dominate over uniform compression: $\phi \sim b/a\varphi$ (cf. [2]).

Let us start our nonlinear analysis with the study of stationary weakly nonlinear traveling acoustic waves. For these waves, an important effect is that the nonlinearity depends on the shape of the leading edge. In fact, it can easily be seen that the terms of Eq. (1) that are quadratic in $\boldsymbol{\xi}$ contain both ϕ and φ. However, for plane waves, $\boldsymbol{\xi}(x - ut)$, because of the geometrical degeneration, the much stronger (due to the deformation hierarchy $\phi \gg \varphi$ indicated above) nonlinearity ϕ^2 (as well as the weaker nonlinearity $\phi\varphi$) does not contribute to the equation

$$\varphi'' - (\varphi'')^2 + \frac{u^2}{RD}\varphi = 0 \qquad (2)$$

(here, the prime stands for the derivative with respect to the independent argument described above), which follows from Eq. (1). As a result, this equation contains only the weakest nonlinearity related to φ^2. Single integration of Eq. (2) (taking into account the smallness of the nonlinear term) yields the following equation for cnoidal waves (i.e., waves that can be represented in terms of elliptical functions; there are no solitons here):

$$\varphi'^2 + \frac{u^2}{RD}\varphi^2 - \frac{2}{3}\left(\frac{u^2}{RD}\right)^2\varphi^3 = \text{const}. \qquad (3)$$

The form of this equation is quite typical. However, for nonplanar wave fronts, nonlinear torsion effects are "switched on." These effects, as can easily be seen, become dominant at $\lambda/r \gg (a/b)^2$, where r is the radius of curvature of the wave front [cf. Eq. (2) and (4)]. Strictly speaking, a curved traveling wave is unsteady; however, at $\lambda \ll r$, the unsteady behavior of the wave is not pronounced and the evolution of perturbations of the form $\boldsymbol{\xi}(r - ut)$ (where r is the radius in polar coordinates) can be studied using the equation

$$\phi'' + \frac{u^2}{RD}\left(\phi + \frac{R}{2ur}\phi'^2\right) = 0, \qquad (4)$$

which follows from Eq. (1) when the above inequalities are satisfied. Here, the radius r in the coefficient by the nonlinear term can be considered constant. Unlike usual equation (2), new equation (4) is sensitive to the sign of u (i.e., whether the traveling wave is converging or diverging) and the sign of q_0 (i.e., the twist direction of microscopic flows in the crystal). Single integration now yields a more exotic relationship for weakly nonlinear cnoidal waves

$$\phi'^2 + \frac{u^2}{RD}\phi^2 - \frac{u^3}{3RD^2r}\phi^3 = \text{const}\left(\frac{u}{Dr}\phi - 1\right), \qquad (5)$$

which cannot be reduced to an ordinary Sagdeev potential.

The strongly nonlinear evolution described by Eq. (1) is of particular interest. The possibility of this kind of evolution, in spite of the above assumptions used in deriving this equation, is also associated with the small value of a/b. In fact, the nonlinearity appears when quadratic (with respect to the deformation) corrections are taken into account in the first term on the right-hand side, which is proportional to R. This term can significantly exceed the second (caused by dispersion) linear term, which is proportional to D. For purely shear deformations ($\varphi \equiv 0$), the largest term vanishes, which yields the following equation ($D \longrightarrow 0$):

$$\frac{\partial \phi}{\partial t} = R\left[\frac{\partial^2\phi}{\partial x^2}\frac{\partial^2\phi}{\partial y^2} - \left(\frac{\partial^2\phi}{\partial x\partial y}\right)^2\right], \qquad (6)$$

which contains the Hessian on its right-hand side and has a very symmetric form: Eq. (6) remains unchanged under the scaling transformations $x \longrightarrow \alpha x$, $y \longrightarrow \beta y$, $\phi \longrightarrow \gamma\phi$, and $t \longrightarrow \alpha^2\beta^2/\gamma t$ and under any rotation of the xy coordinate system. Although the approximation $D = 0$ is physically justified, it significantly changes the form of the equation, so that the evolution no longer has a wave character. For ordinary continuous media, this is equivalent of completely ignoring the crystal elasticity (although we partially take it into account here) or the temperature (i.e., pressure) of an ideal gas (see below).

Equation (6) can be written in terms of the variational derivative as

$$\frac{\partial \phi}{\partial t} = R\frac{\delta\mathcal{U}}{\delta\phi},$$

where

$$\mathcal{U} = \int \phi_x\phi_y\phi_{xy}dxdy,$$

or, in a more invariant form,

$$\mathcal{U} = -\frac{1}{4}\int(\nabla\phi)^2\Delta\phi dxdy.$$

It can easily be seen from these expressions that, since the density $\mathcal{U}$ is a homogeneous function with respect to derivatives in ϕ, solutions to Eq. (6) satisfy the following evolutionary relationships:

$$\frac{d}{dt}\int\phi^2 dxdy = 6R\mathcal{U},$$

$$\text{or} \quad \frac{d^2}{dt^2}\int\phi^2 dxdy = 6\int\left(\frac{\partial\phi}{\partial t}\right)^2 dxdy.$$

Further, the right-hand side of Eq. (6) is a meaningful block of the Monge–Ampére equation [6], associated with the differential geometry of surfaces. This block vanishes as the Gaussian curvature of the surface $z = \phi(x, y)$ vanishes. In other words, a nonuniform deformation of the vortex crystal is static if ϕ describes a developable surface (a cylindrical or conical surface or a surface produced by tangents to an arbitrary three-dimensional curve). The general parametric expression for such ϕ has the form [6]

$$\phi = \zeta x + f(\zeta)y + g(\zeta), \quad x + f'(\zeta)y + g'(\zeta) = 0,$$

where $f(\zeta)$ and $g(\zeta)$ are arbitrary functions. In fact, since the physically observed quantity is the deformation $\boldsymbol{\xi}$ itself (rather than its potentials), the configurations for which the Hessian of ϕ is constant are also static. They can also be described by a general parametric expression, but this is only possible when this constant is negative [6].

If we expand the right-hand side of Eq. (6) in a power series in x and y, then the nontrivial evolution starts with the emergence of linear terms. Moreover, if $\phi_{xx}\phi_{yy} - (\phi_{xy})^2 = c_1x + c_2y$, then the deformations can easily be seen to increase by a linear ballistic law:

$$\boldsymbol{\xi}(x, y, t) = \boldsymbol{\xi}(x, y, 0) + (c_1\mathbf{e}_y - c_2\mathbf{e}_x)t. \tag{7}$$

There is a very wide range of initial deformation configurations (not only power functions) that produce such an evolution [6]. For example, at $c_1 = -1$ and $c_2 = 0$ (in view of the symmetries of Eq. (6), this does not limit the generality of our consideration), a suitable initial condition in the region $x > 0$ is

$$\phi_0 = \pm\frac{2}{3}x^{3/2}y + f(x) + C_y, \tag{8}$$

where the function f and constant C are arbitrary. Of course, such deformations grow without limit as $x \longrightarrow \infty$ (seemingly, such behavior is unavoidable in this case, because it is only singularities at infinity that can allow a nonuniformly deformed crystal to be displaced as a whole). However, because of the local character of the equations, if condition (8) holds only over a bounded region, then the evolution described by Eq. (7) can last here over a fairly long time.

As a rule, the greatest amount of information about the evolution described by nonlinear equations can be obtained from studying the possible singularities that exhibit themselves in a finite time. Three types of such singularities can be distinguished (since Eq. (6) is local, we expand ϕ about the singularity point (0, 0)):

$$\phi = -\frac{x^2y^2}{12R(t_0 - t)}, \quad \phi = \frac{(x^2 + y^2)^2}{48R(t_0 - t)}, \quad \phi = -\frac{(x - Ay^2)^3}{36RA(t_0 - t)}. \tag{9}$$

However, as $t \longrightarrow t_0$, higher order nonlinearities and/or dispersion effects prevent the deformations from growing without limit. The last singularity in (9) differs from the others in that it appears on a line rather than at a point. It is also of interest because, in the variables $\zeta = x - Ay^2$ and t, the one-dimensional Hessian is autonomous with respect to the independent argument and Eq. (6) transforms to the solvable equation

$$\frac{\partial\phi}{\partial t} = -2AR\frac{\partial\phi}{\partial\zeta}\frac{\partial^2\phi}{\partial\zeta^2},$$

which reduces to the classical nonlinear diffusion equation through the simple change of variables $\phi_\zeta = T$ (it is relevant to refer here to the excellent handbook [6]):

$$\frac{\partial T}{\partial t} = -2AR\frac{\partial}{\partial\zeta}\left(T\frac{\partial T}{\partial\zeta}\right). \tag{10}$$

Negative values of ART lead to the well-known monotonic spread of the T profile according to the attractive self-similarity law, i.e., to the disappearance of the perturbation, whereas in the case of $ART > 0$, the profile collapses in an explosive manner, which generalizes the last local singularity in (9):

$$T = \frac{1}{6[2AR(t_0 - t)]^{1/3}}\left(\zeta_0^2 - \frac{\zeta^2}{[2AR(t_0 - t)]^{2/3}}\right) \tag{11}$$

at $\zeta^2 < \zeta_0^2\,[2AR(t_0 - t)]^{2/3}$ and $T = 0$ outside the indicated interval. In fact, solution (11) describes both these cases (at $t > t_0$ and $t < t_0$, respectively). The amplitude of T at $\zeta = 0$ (i.e., the parameter ζ_0) is uniquely determined by the integral

$$\int\limits_{-\infty}^{+\infty} Td\zeta = \frac{4}{3}\zeta_0^3,$$

which remains constant in the course of evolution. Peaking solution (11) describes the explosive growth of shear deformation along the lines ζ = const with the same torsion (clockwise or counterclockwise) as that of the flow produced by an individual vortex of the lattice.

Let us stress once again that the applicability of Eq. (6) to real lattices is limited in space (because of problems arising at $|x|, |y| \longrightarrow \infty$) and time (because we ignored lattice rigidity with respect to shear). The increase in the magnitude of the deformation vector $\boldsymbol{\xi}$ and the decrease in its scale length near the singularity points also violate the approximations of small nonlinearity and locality ($\lambda \gg b$). At the same time, the evolution described by Eq. (6) is non-Hamiltonian (which clearly exhibits itself in the case of diffusion described by Eq. (10)) with a tendency toward single-sided growth (which is seen from the fact that $d(RU)/dt > 0$), which raises the question of the problem of energy conservation in the system. However, it can be seen that, by the definition of this energy for Eq. (6) (taking the unperturbed state of the lattice as the reference state), it is equal to

$$\mathcal{E} = q_0 R \int \left[\frac{\partial^2 \phi}{\partial x^2} \frac{\partial^2 \phi}{\partial y^2} - \left(\frac{\partial^2 \phi}{\partial x \partial y} \right)^2 \right] dx dy,$$

because, since ψ simultaneously contributes to the dynamics and energy of the vortex ensembles, their energy density is proportional to the term under the operator $\mathbf{e}_z \times \boldsymbol{\nabla}$ in the dynamic equation for $\boldsymbol{\xi} = \mathbf{e}_z \times \boldsymbol{\nabla}\phi$. Since this energy density is proportional to the total derivative, the total energy of any localized perturbation is identically equal to zero (of course, only within this approximation). As for the “time arrow” in the direction of evolution, it is more correct to talk about a tendency toward the increase in $\boldsymbol{\nabla} \times \boldsymbol{\xi}$ (i.e., $\Delta\phi$, which determines the sign of $\mathcal{U}$) in accordance with the microscopic characteristic q_0 (which determines the sign of R), because the preferred rotation direction of the continuous flow about certain vortexes destroys the chiral symmetry.[2]

Thus, the above analysis has demonstrated that there is a qualitative difference between the nonlinear dispersion hierarchy of a vortex plasma (more precisely, the vortex ensemble in plasma) and that of a usual wave media described by equations like that of Korteweg–de Vries. Such peculiar behavior and its sensitivity to the internal chirality would seem to be of particular interest.

ACKNOWLEDGMENTS

This work was supported by the Russian Foundation for Basic Research (project no. 03-02-16765) and the Russian Federal Program for State Support of Leading Scientific Schools (project no. 2292.2003.2).

REFERENCES

1. B. N. Kuvshinov, J. Rem, I. J. Shep, and E. Westerhof, Phys. Plasmas **8**, 3232 (2001).
2. V. V. Smirnov and K. V. Chukbar, Zh. Éksp. Teor. Fiz. **120**, 145 (2001) [JETP **93**, 126 (2001)].
3. A. S. Kingsep, K. V. Chukbar, and V. V. Yan’kov, in *Reviews of Plasma Physics*, Ed. by B. B. Kadomtsev (Énergoizdat, Moscow, 1987; Consultants Bureau, New York, 1990), Vol. 16.
4. G. Blatter, M. V. Feigel’man, V. B. Geshkenbein, *et al.*, Rev. Mod. Phys. **66**, 1125 (1994).
5. V. K. Tkachenko, Zh. Éksp. Teor. Fiz. **50**, 1573 (1966) [Sov. Phys. JETP **23**, 1049 (1966)].
6. A. D. Polyanin and V. F. Zaĭtsev, *Handbook of Nonlinear Equations of Mathematical Physics* (Fizmatlit, Moscow, 2002), p. 247.

Translated by A.D. Khzmalyan

---

[2] The change in the type of the equation when two Hamiltonian variables (ϕ and φ) are reduced to one is not unique. As a crude analogue of this effect in an ordinary medium, one can consider a one-dimensional (see above) flow of a compressible gas (for which these two variables are the potential of the velocity field and the density) at a zero temperature. The classic dynamic equation for the velocity $\partial v/\partial t + \partial(v^2/2)\partial x = 0$, which remains meaningful, can be rewritten for the potential $v = \varphi_x$ as $\partial\varphi/\partial t = -\varphi_x^2/2$, which quite clearly defines the time arrow for the functional $\tilde{\mathcal{U}} = -\int \varphi\varphi_x^2 dx$: $d\tilde{\mathcal{U}}/dt > 0$. Of course, the evolution described by Eq. (6) is much more complicated and diversified.

Plasma Physics Reports, Vol. 30, No. 3, 2004, pp. 218–227. Translated from Fizika Plazmy, Vol. 30, No. 3, 2004, pp. 245–255.
Original Russian Text Copyright © 2004 by Aleksandrov, Volkov, Grabovskiĭ, Zukakishvili, Zurin, Mitrofanov, Nedoseev, Oleĭnik, Porofeev, Samokhin, Sasorov, Smirnov, Frolov.

PLASMA DYNAMICS

Interferometric Measurements of the Plasma Density at the Z-Pinch Periphery in the Angara-5-1 Facility

V. V. Aleksandrov*, G. S. Volkov*, E. V. Grabovskiĭ*, G. G. Zukakishvili*, M. V. Zurin*, K. N. Mitrofanov*, S. L. Nedoseev*, G. M. Oleĭnik*, I. Yu. Porofeev*, A. A. Samokhin*, P. V. Sasorov, V. P. Smirnov*, and I. N. Frolov***

** Troitsk Institute for Innovation and Fusion Research, Troitsk, Moscow oblast, 142190 Russia*

*** Institute of Theoretical and Experimental Physics, Bol'shaya Cheremushkinskaya ul. 25, Moscow, 117218 Russia*

Received May 19, 2003; in final form, July 25, 2003

Abstract—Knowledge of spatial mass distribution is important for understanding the physics of implosion of megaampere-current wire arrays. The paper presents results from studying the electron density distribution at the periphery of a tungsten wire array near the instant of maximum compression by using laser interferometry at $\lambda = 0.69$ μm. It is found that, at the instant of maximum compression (~100 ns after the beginning of the discharge), the estimated maximum local electron density inside the wire array reaches $\sim 10^{18}$ cm^{-3} at a distance of 0.3–3 mm from the initial wire positions. Assuming the average tungsten ion charge to be 10, the local linear mass density in this region turns out to be 30 μg/cm, which amounts to about 10% of the total linear mass density of the liner. A fraction of the generator current flows through this plasma. The duration of the soft X-ray pulse is 5–8 ns, which indicates the achievement of a fairly high compression ratio. © *2004 MAIK "Nauka/Interperiodica".*

1. INTRODUCTION

In recent years, there has been increased interest in Z-pinches formed in the implosion of high-current wire arrays. This interest stems primarily from fact that such pinches can be used in inertial confinement fusion research as sources of high-power soft X-ray (SXR) emission for igniting indirect thermonuclear targets [1–3].

In order to understand the physics of implosion of high-current wire arrays, it is important to know the spatial distributions of the mass and current inside a wire array. The current distribution was studied in [4, 5]. The spatial distribution of the plasma density is expected to significantly affect the current distribution, magnetic energy dissipation, and SXR yield.

To determine the amount of substance remaining at the periphery of the wire array at the instant of maximum compression is an important problem of the physics of wire array implosion. Immediately before the maximum compression, when the liner radius is already small, while the implosion velocity is still high, the electric field at the periphery of the wire array can exceed 1 MV/cm. If, at this moment, there is a sufficient amount of well-conducting plasma at the initial liner radius, then the plasma is able to partially shunt the liner current and decrease the efficiency of implosion. Estimates show that even a relatively small amount of plasma (a few percent of the initial liner mass) is sufficient to intercept a significant fraction of the current and, hence, reduce the X-ray yield in the course of implosion.

In this study, we investigate the distribution of the plasma density at the periphery of a wire array near the instant of maximum compression. By the periphery, we mean the zone between two coaxial cylindrical surfaces, the outer of which coincides with the initial position of the wires, while the inner one is shifted inward by a distance from a fraction of millimeter to 2–3 mm. The measurements were performed using laser interferometry, with a laser beam propagating perpendicular to the discharge axis.

2. EXPERIMENTAL SETUP

We employed the following diagnostic techniques:

(i) a frame microchannel plate (MCP) pinhole camera for recording X-ray images of an imploding liner,

(ii) a streak camera for recording the evolution of the radial profile of visible liner emission,

(iii) SXR diagnostics consisting of four vacuum X-ray diodes (XRDs) equipped with absorbing filters for recording the evolution of the SXR emission power, and

(iv) active frame laser shadowgraphy and interferometry for determining the spatial distribution of the plasma density in a wire array in the course of its implosion.

1063-780X/04/3003-0218$26.00 © 2004 MAIK "Nauka/Interperiodica"

The total current flowing through the liner was recorded with eight magnetic probes placed at a distance of 55 mm from the liner axis.

X-ray images of the imploding liner were taken with the help of a four-frame X-ray camera equipped with a sectioned MCP image intensifier. The X-ray images at the entrances of the MCP sections were produced by four pinhole cameras. The frame exposure, which was specified by a gating pulse applied to the MCP section, was 1.5 ns. The frame X-ray camera was sensitive to X-ray photons with energies from twenty to a few thousand electronvolts with maximum sensitivity at ~200 eV. A 2.5-μm-thick Mylar filter was installed at the entrance of the MCP camera. The spatial resolution of this diagnostics in the object plane was 85–120 μm for X-ray photons with energies of 250–600 eV.

The time resolution of an SFER-2 visible-light streak camera was 0.3 ns. The spatial resolution and the focal depth in the object plane were <80 μm and ±23 mm, respectively.

A set of four XRDs was placed at a distance of 3.5 m from the wire array axis. The time resolution of the recording system was 0.7 ns. The X-ray emission power was measured in the 0.1- to 2-keV photon energy range [6].

The main technique for determining the spatial distribution of the electron density at the periphery of a wire array was laser interferometry. We used a Rb laser shift interferometer operating at $\lambda = 0.69$ μm.

The laser system consisted of a driving Rb laser (8 mm in diameter and 120 mm in length), a Pockels-cell switch, an external electrooptical shutter forming a short pulse with a duration 3–5 ns, and two optically isolated two-passage laser amplifiers. The beam generated by the driving laser was amplified and then passed through a telescopic system, where it was expanded to a diameter of 40 mm. To prevent stray exposure caused by daylight and liner radiation, we used a special cartridge protected with a KS-19 light filter and a photographic camera equipped with a 40 × 180-mm electromechanical shutter remotely controlled by the operator. In each experiment, we controlled and recorded the instant of laser probing with respect to the liner current pulse.

The energy of the probing laser pulse was 100 mJ and the full width at half-maximum was 3–5 ns. The spatial resolution in the object plane was 50 μm.

The optical scheme of the laser shift interferometer is shown in Fig. 1. This interferometer was previously used in studying the initial stage of plasma formation in experiments on the implosion of wire arrays [7].

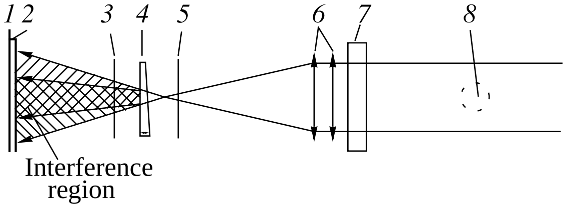

Fig. 1. Schematic of the shift interferometer: (*1*) photofilm, (*2*) optical filter, (*3*, *5*) polarizers, (*4*) birefringent wedge (Iceland spar crystal), (*6*) focusing lenses, (*7*) vacuum chamber window, and (*8*) wire array.

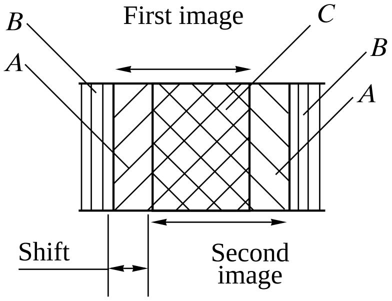

Fig. 2. Schematic of a shift interference pattern.

The laser radiation passed through liner *8* enters the interferometer. The key element of the shift interferometer is wedge *4* made of Iceland spar crystal with a wedge angle of 3°. After passing through polarizer *5*, laser radiation is split by the wedge into ordinary and extraordinary polarized beams shifted with respect to each other. These beams form two images of the plasma object on photographic film *1*. Polarizer *3* is set after the Iceland spar crystal to superimpose the ordinary and extraordinary beams and to enable interference between them. The superimposed beams produce an interference pattern (laser interferogram) on the photographic film. Varying the angle between the polarization planes of polarizers *3* and *5*, it is possible to change the contrast of the interference pattern. At low contrast, the interferogram contains both the result of interference and the shadow image produced by one of the beams. This may be used, e.g., for positioning the interference pattern or analyzing the character of implosion in a particular experiment.

Laser shadowgraphs show that there is no plasma beyond the region initially enclosed by the wire array. Therefore, this region can be considered unperturbed; i.e., laser radiation passing outside the wire array does not undergo phase shift, whereas inside the array, the phase of the laser radiation is affected by the plasma produced in the course of wire evaporation. Hence, the interference pattern can be divided into several zones as is shown in Fig. 2.

In zones *B* residing on the left and right margins of the interferogram, the interference pattern is produced by the unperturbed parts of the laser beams and has the form of parallel interference fringes. In zones *A*, the perturbed part of one laser beam interferes with the unperturbed part of the other laser beam. In zone *C*, the perturbed parts of the laser beams interfere with each other.

3. PRECONDITIONS FOR EFFICIENT LASER INTERFEROMETRY

In the absence of a magnetic field, there are three factors determining the interferogram contrast:

(i) absorption of laser radiation,

(ii) variations in the electron density during the laser pulse (unsteadiness of the interference pattern), and

(iii) loss of spatial coherence because of electron density fluctuations.

3.1. Absorption of Radiation

The attenuation coefficient of laser radiation in a tungsten plasma can be estimated from above by taking into account the multiplier 0.55 in the expression for Gaunt factor and replacing the Coulomb logarithm with unity. The attenuation coefficient for Rb laser radiation is then

$$\exp\left(2.4\int_0^S (Z/T^{1.5})n_e^2 ds\right),$$

where S (in cm) is the path length of the probing beam, Z is the average ion charge, T (in eV) is the plasma temperature, and n_e (in units of 10^{19} cm^{-3}) is the electron density.

For an average ion charge of $Z = 10$, a plasma temperature of 100 eV, an electron density of 10^{19} cm^{-3}, and a liner radius of 0.6 cm, the laser beam intensity decreases by a few percent. When probing the liner periphery along an arc chord, the maximum admissible density is inversely proportional to the chord length. Hence, we can conclude that, under our conditions, absorption insignificantly affects the interference pattern.

3.2. Effect of the Exposure Time

Plasma unsteadiness imposes a strict restriction on the exposure time t_L. The phase velocity V_f of the interference pattern on the film is limited by the condition

$$V_f < b/t_L,$$

where b is the width of the interference fringe on the film. We note that, in the presence of a plasma, the fringe width b is smaller than the fringe width b_0 related to the phase shift caused by a birefringent wedge alone.

The doubling of the fringe number in a layer of thickness $h = 0.05$ cm at the liner periphery is sufficient to reliably diagnose plasma. It was shown in [8] that, in this case, the phase velocity V_f is typically less than 7 cm/μs and the density is $n_e \sim 3 \times 10^{17}$ cm^{-3}. Identifying the velocity V_f with the plasma mass velocity, we obtain the following restriction on the temporal variations in the linear mass density:

$$\frac{dm}{dt}\ [\mathrm{g/(cm\ s)}] < \frac{817}{\lambda_L\ [\mu\mathrm{m}]\ t_L\ [\mathrm{ns}]}\frac{A}{Z}\sqrt{h(R_L-h)},$$

where Z is the average ion charge, λ_L is the laser wavelength, and A is the atomic mass. For tungsten, at Z = 5–10, $t_L = 3$ ns, $\lambda_L = 0.69$ μm, $h = 0.1$ cm, and a liner radius of $R_L = 0.6$ cm, we have $dm/dt <$ 1.6–3.2 μg/(cm ns).

This restriction seems to be significant because the average rate of the mass inflow into the liner interior is ~3 μg/ns, whereas the maximum value of dm/dt can exceed the average value by nearly two times.

3.3. Spatial Coherence

Phase fluctuations destroy the interference pattern when the two following conditions are met [8, 9]:

$$\frac{\delta n_e}{\lambda_L n_{\mathrm{cr}}}\sqrt{\delta l_{\parallel} l} > 1, \quad \delta l_{\perp} < b.$$

Here, δn_e is the deviation of the electron density from its average value, l is the beam path length in the plasma, n_{cr} is the critical electron density for a given laser wavelength, $\delta l_{\parallel}$ is the inhomogeneity scale length, and $\delta l_{\perp}$ is the transverse (with respect to the laser beam) correlation length of plasma density fluctuations. Assuming for estimates that $\delta l_{\perp} = \delta l_{\parallel}$, $b \sim 100$ μm, R_L = 0.6 cm, and the probing beam passes along a chord 0.1 cm distant from the initial liner radius, we find that $l = 0.66$ cm and the amplitude of plasma density fluctuations is limited by $\delta n_e < 2 \times 10^{18}$ cm^{-3}. Hence, we can conclude that, for a dense plasma with $n_e \sim 10^{19}$ cm^{-3}, no interference pattern occurs. In contrast, for a rarefied plasma with $n_e < 10^{18}$ cm^{-3}, density fluctuations are of minor importance. Spatial coherence is violated in the denser part of a discharge. On the whole, the problem of plasma fluctuations needs further investigation.

Thus, plasma unsteadiness and spatial fluctuations in the electron density are the main factors limiting the contrast of the interference pattern. These factors are responsible for the absence of an interference pattern at $n_e > 10^{19}$ cm^{-3}. In contrast, for a rarefied plasma with $n_e < 10^{18}$ cm^{-3}, density fluctuations affect the interference pattern only slightly. For $R_L = 0.6$ cm and a plasma thickness of 1 mm, a one-fringe shift corresponds to $m_{\min} = 26/Z$ μg/cm; consequently, at $Z = 7$, we have $m_{\min} \simeq 3$ μg/cm.

4. INVESTIGATIONS OF THE PLASMA DENSITY PROFILE AT THE WIRE ARRAY PERIPHERY IN THE FINAL STAGE OF IMPLOSION

In these experiments, the liners consisted of two or three coaxial cylindrical wire arrays. A 1.5- to 2-mm-diameter agar–agar foam column doped with micron-size tungsten powder with a total linear mass of 170–300 μg/cm was installed on the liner axis. In some experiments, we used a 6-mm-diameter wire array consisting of sixteen to forty 6-μm tungsten wires with a total linear mass of 110–380 μg/cm. When studying the mass distribution at the liner periphery, the region around the outer wire array is of the most interest. This array was composed of 24–40 tungsten wires 5–8 μm in diameter placed along a 12-mm-diameter circle; the total linear mass density was 120–380 μg/cm.

The laser shift interferometer was adjusted so that the probing was performed almost at the instant of maximum compression. The instant of probing ΔT, counted from the SXR burst, was varied from –12 to +35 ns. The implosion lasted for 120–150 ns. The current through the liner in the final stage of implosion was 3–3.5 MA.

As an example, we consider the experimental data obtained using a composite liner with the following parameters: The outer 12-mm-diameter wire array consisted of 40 6-μm tungsten wires with a total linear mass density of 220 μg/cm. The inner 6-mm-diameter wire array consisted of twenty 6-μm tungsten wires with a total linear mass density of 110 μg/cm. A 1.5-mm-diameter agar–agar foam column doped with micron-size tungsten powder with a total linear mass of 250 μg/cm was installed on the liner axis. Figure 3 shows the waveforms of the current, the current time derivative, and the SXR intensity, while Fig. 4 shows the waveforms of the laser and SXR intensities. As is seen from Fig. 3, the implosion lasted for 140 ns. Laser probing was performed at the leading edge of the SXR pulse, 5 ns before the instant of the maximum SXR intensity (see Fig. 4).

Figure 5 presents two interferograms obtained (a) before the discharge (a “cold” interferogram) and (b) at the instant of maximum compression (a “hot” interferogram). The intensities of the two interfering beams were different; it was therefore also possible to observe the liner shadow. In Figs. 5a and 5b, the x axis is directed along a horizontal and the y axis is directed along a vertical and coincides with the liner axis.

The four vertical lines in each interferogram correspond to x = 2.34, 1.75, 1.25, and 0.65 cm. Let us recall that the interferogram is a result of the interference of two laser beams shifted in the horizontal direction with respect to each other. The right vertical line (x = 2.34 cm) corresponds to the right boundary of the liner for the right beam. The left line (x = 0.65 cm) corresponds to the left boundary of liner for the left beam. In the regions $x > 2.34$ cm and $x < 0.65$ cm (regions B in Fig. 2), both of the laser beams did not traverse the liner; hence, the interferograms obtained before the discharge and during implosion were expected to be the same in these regions. In fact, they differ because a certain amount of plasma expands beyond the region initially enclosed by the liner.

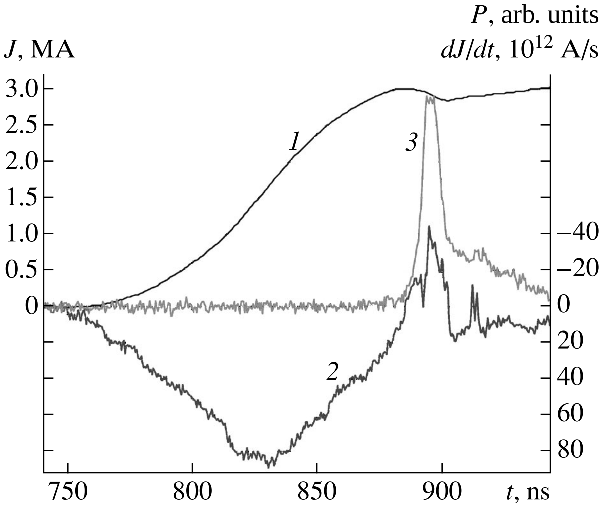

Fig. 3. Waveforms of the (*1*) current J, (*2*) current time derivative dJ/dt, and (*3*) SXR intensity P.

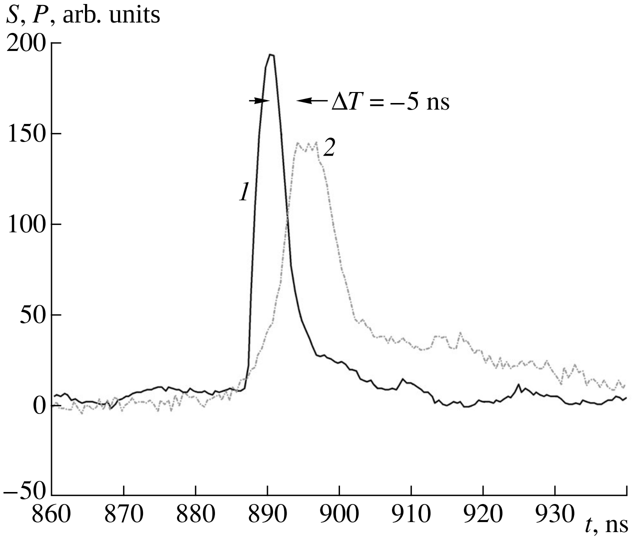

Fig. 4. Waveforms of the (*1*) laser intensity S and (*2*) SXR emission intensity P (ΔT is the time shift of the laser pulse with respect to the SXR burst).

In the regions $1.75 < x < 2.34$ cm and $0.65 < x < 1.25$ cm (regions A in Fig. 2), the laser beam perturbed by the plasma interferes with the unperturbed laser beam.

At $1.25 < x < 1.75$ cm (region C), both beams are perturbed by the plasma. In this region, no interference fringes were recorded; hence, this part of the interferogram was not processed.

In regions A and B, the interferograms were processed as follows: First, we calculated the phase shift for both the hot and cold interferograms as a function of x and y. The phase shift was measured by the number of

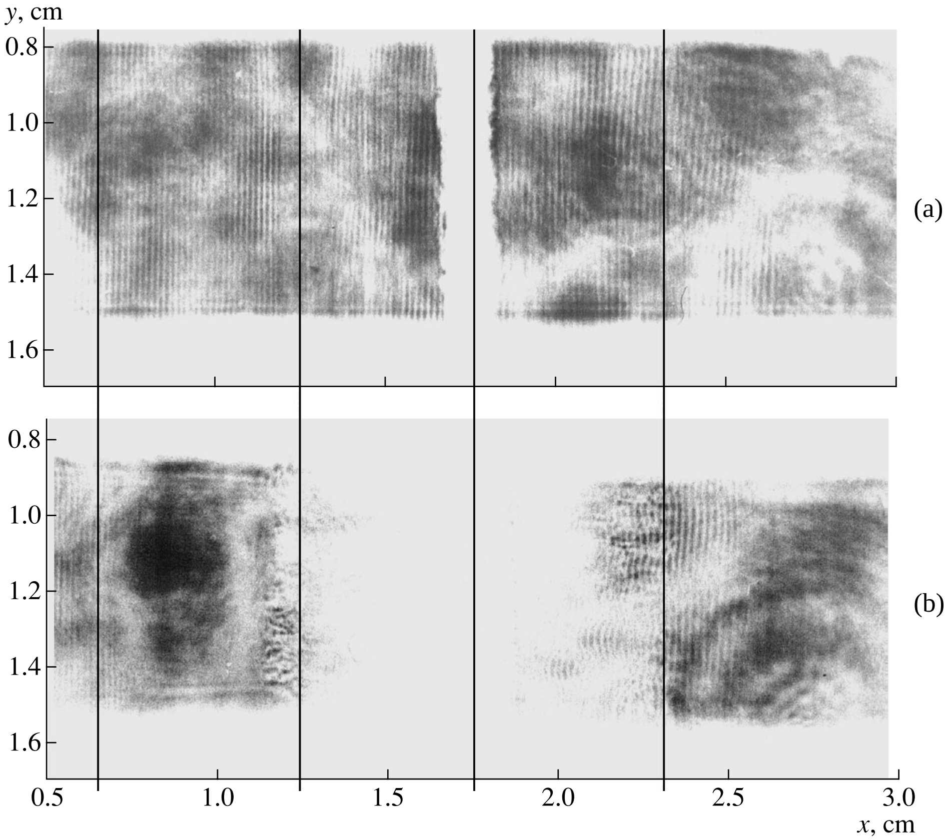

Fig. 5. Two interferograms of the same wire array (a) before the discharge (a "cold" interferogram) and (b) 5 ns before the SXR burst (a "hot" interferogram).

interference fringes. One fringe corresponded to a phase shift of 2π. In fact, we determined the coordinates corresponding to the maxima and minima of the blackening density. Between the maxima and minima of the blackening density, the phase shift was calculated by linear interpolation.

At $x > 1.75$ cm, the phase shift was determined by summing the number of fringes moving from right to left, starting from the maximum value of x at which the interference pattern could be detected. At $x < 1.25$ cm, the phase shift was determined by summing the number of fringes moving from left to right, starting from the minimum value of x at which the interference pattern could be detected. Obviously, the phase shift at a certain point can be determined only if there are interference fringes along the entire path from region *B* to region *A*.

The effects related to plasma dynamics in the liner reflect themselves in the phase difference between the hot and cold interferograms. A phase difference of 2π corresponds to the surface density $\int ndl = 3.17 \times 10^{17}$ cm^{-2}, where the integral is taken along the laser beam.

Figure 6 shows an idealized radial profile of the phase difference $\Delta\varphi$ in the right part of the liner: to the right of the liner boundary (at $x > 2.34$ cm), Δx is a constant (because it is supposed that there is no plasma beyond the liner boundary), while when moving to the left from the liner boundary, the phase difference related to the presence of plasma appears.

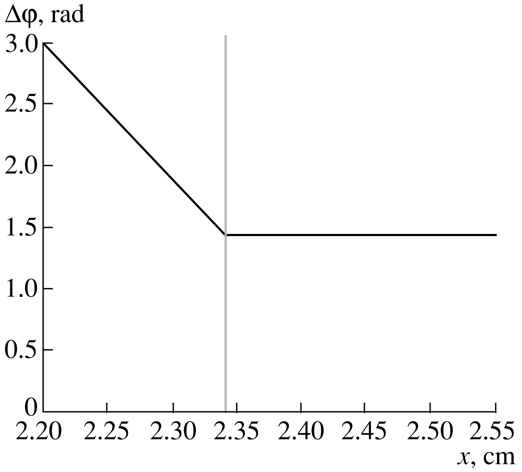

Fig. 6. Idealized radial profile of the phase difference $\Delta\varphi$ in the right part of the liner. The vertical line at $x = 2.34$ cm shows the right boundary of the liner.

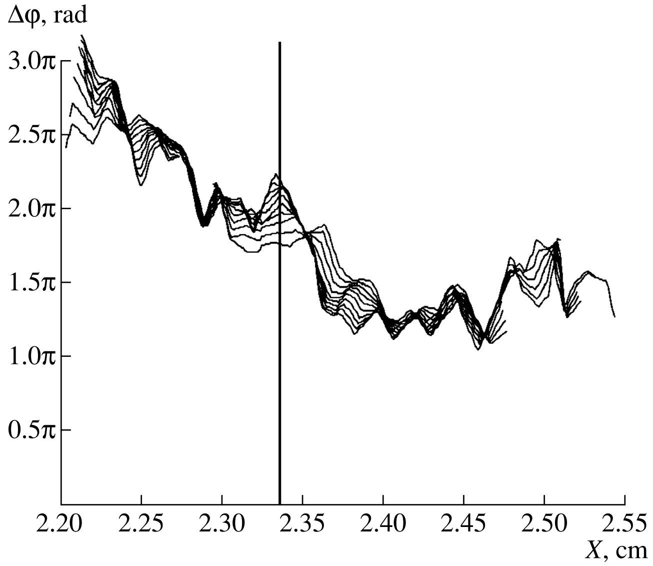

Fig. 7. Measured phase difference Δφ in the right part of the liner as a function of x for different horizontal cross sections in the range $1.3 < y < 1.4$ cm. The right boundary of the liner is shown by the vertical line at $x = 2.34$ cm.

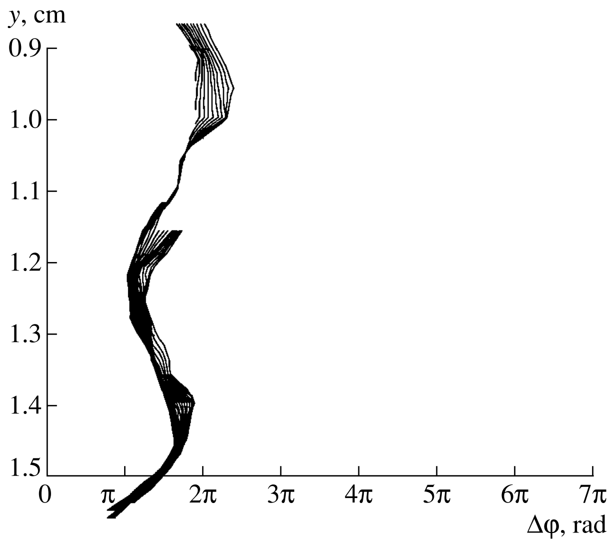

Fig. 8. Measured phase difference Δφ in the right part of the liner as a function of y for different vertical cross sections in the range $2.36 < x < 2.38$ cm. The right boundary of the liner is at $x = 2.34$ cm.

It should be noted that the interference pattern was not observed over the entire region where the two interfering beams overlap. Generally, there were certain intervals along the axis within which the interference pattern was observed. Moreover, it is observed not over the entire range of the radial coordinate but only over a distance Δx from the initial radius of the wire array toward the liner axis. Below, the distance Δx will be referred to as the probing layer depth.

We recall once again that the phase difference Δφ is a function of x and y. Figure 7 shows the radial profile of the phase difference in different horizontal cross sections, and Fig. 8 shows the axial profile of the phase difference in different vertical cross sections. It can be seen from Fig. 7 that, for horizontal cross sections lying at 1.3 cm < y < 1.4 cm, interference fringes are seen only at a distance of $\Delta x = 0.14$ cm from the liner boundary. For other cross sections, the probing layer depth Δx is usually smaller or even equals zero.

To move from the surface plasma density to the volumetric density, it is necessary to solve an ill-posed problem by applying the Abel inversion procedure. Keeping in mind that the Abel problem for the electron density can be correctly solved only in the case of cylindrical symmetry (which is generally not the case), we nevertheless attempted to estimate the electron density. The electron density profile $n(r)$ beyond the liner boundary was assumed to be zero, whereas inside the liner, it was sought in the form

$$n(r) = n_{\Delta x}[(R_L - r)/\Delta x]^{0.5},$$

where R_L is the initial liner radius and $n_{\Delta x}$ is the electron density at the radius $R_L - \Delta x$. The phase difference profile calculated for such an electron density profile turned out to be very close to the profile shown in Fig. 6. The value of $n_{\Delta x}$ was determined from the condition that the phase difference at the distance Δx from the liner boundary for the given profile $n(r)$ be equal to the measured phase difference.

The interferometry technique enables the determination of the electron density. To move from the electron density to the mass density, it is necessary to know the average ion charge. Since direct measurements of the average ion charge were not performed and estimates based on the numerical simulations of radiative processes and indirect measurements provide rather low accuracy, the only result of our interferometric measurements is the electron density. The natural question arises as to what the mass density for any arbitrary ion charge Z is, provided the electron density is measured. Here and below, we assume that $Z = 10$. For other values of the average charge Z, the mass density can be calculated by multiplying the density so obtained by a factor of 10/Z. An argument in favor of choosing Z =10 is that the Z-pinch emission spectrum corresponds to an electron temperature ranging from 30 to 100 eV. It is unlikely that, for such an emission spectrum, the average ion charge is higher than 10. If the average ion charge is lower than 10, then the mass density at the liner periphery will be somewhat higher. Therefore, it should be remembered that, wherever it is encountered below, we mean by the measured plasma mass, a mass obtained under the assumption that the average ion charge is equal to 10.

As was mentioned above, the interference pattern was not observed over the entire region where the two

The measured local surface electron density and the estimated plasma linear mass density at the liner periphery

Instant of probing ΔT, ns	Recorded local phase shift $\Delta\varphi$, rad	Probing layer depth Δx, cm	Estimated maximum local electron density in the Δx layer, cm^{-3}	Estimated local ion linear mass density within the Δx layer, μg/cm	Initial linear mass density of the outer wire array, μg/cm
–12	7.8	0.03	14×10^{17}	125	380
–10	3.1	0.03	6×10^{17}	47	220
–5	4.1	0.14	3.5×10^{17}	13–30	220
+1	6.3	0.15	5×10^{17}	5–16	380
+15	3.1	0.3	2×10^{17}	3–13	120
+25	18.8	0.2	14×10^{17}	31	120
+33	9.4	0.25	7×10^{17}	9–16	160
+35	3.1	0.16	3×10^{17}	9	160

interfering beams overlap. For this reason, we will consider the local linear mass density in regions where the interference patterns occur, rather than the mass of the liner as a whole. Nothing can be said about the plasma density in regions where no interference patterns were observed. The measured local surface electron density in regions where it could be measured and the estimated plasma linear mass density in these regions for several discharges are presented in the table.

It can be seen from the table that, in some discharges, the estimated local electron density at the liner periphery reaches ~10^{18} cm^{-3}. The corresponding probing layer depth ranges from 0.3 to 3 mm. At the instant of maximum compression, the local linear mass density inside the probing layer is ~10–30 μg/cm, which amounts to about 10% of the initial linear mass density of the wire array. If we assume that the plasma density in regions where no interference pattern was observed is the same, then this estimate can be applied to the entire liner. Hence, by the instant of the SXR burst, almost all the liner mass is located inside a region 6 mm in diameter. At the periphery of the initial wire array, inside a layer with a depth of up to 3 mm, the measured linear mass of the plasma is ~10–30 μg/cm. This is about 10% of the initial mass of the outer wire array. Nevertheless, 10% of the initial mass is quite a significant amount because this plasma may be sufficient to shunt an appreciable fraction of the liner current.

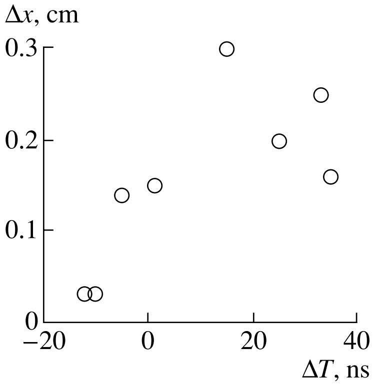

Fig. 9. Probing layer depth Δx (reckoned from the liner edge) vs. time shift ΔT of the laser pulse with respect to the SXR burst.

It is of interest to analyze how the parameters of the interference pattern depend on the time shift ΔT of the laser pulse with respect to the SXR burst.

Figure 9 presents the dependence of the probing layer depth Δx (reckoned from the liner edge) on the time shift ΔT of the laser pulse with respect to the SXR burst. One can see that the probing layer depth increases with increasing time shift. Such behavior indicates that the liner material still continues moving toward the axis. The interelectrode gap at the liner periphery becomes more transparent for laser radiation because of the decrease in the plasma mass in this region.

Although the plasma mass detected in different discharges resides inside layers of different thickness and the amount of the undetected plasma mass is unknown, it is nevertheless possible to trace how the detected mass within the probing layer depends on the time shift ΔT of the laser pulse with respect to the SXR burst (see Fig. 10). As was expected, the plasma linear mass density at the periphery decreases as the instant of probing approaches the maximum of the SXR intensity. At the instant of maximum compression, it reaches 10–30 μg/cm. A certain increase in the linear mass density at the liner periphery 20–30 ns after the instant of maximum compression is probably related to pinch expansion.

5. DISCUSSION

A preliminary analysis of the interferograms shows a significant inhomogeneity of both the interference pattern and the liner shadow. This points to the axial nonuniformity of the implosion process. The presence of such a nonuniformity is also confirmed by Fig. 8, which shows the profiles of the phase difference in different vertical cross sections located in the vicinity of the right boundary of the liner, at $2.36 < x < 2.38$ cm (the right boundary of the liner is at $x = 2.34$ cm). It can be seen from Fig. 8 that the electron density at the liner periphery is nonuniform along the axis and variations in the phase difference reach a value corresponding to a half-fringe.

In some regions, there is no interference pattern at all. The absence of interference fringes could be caused by the high density gradients, which would lead to large-angle deflections of the laser beam and its escape from the optical system. However, this is not the case, because in regions where no interference fringes are observed, the average blackening density of the film is nearly the same as in the neighboring regions with interference fringes. The absence of an interference pattern can be related to the fairly large duration of the probing laser pulse (3–5 ns). Over this time, the interference fringes can shift by a distance comparable to the fringe width, as was described in Section 3; as a result, the interference pattern becomes smeared out.

In some discharges, the estimated local electron density at the periphery of the initial wire array reached $\sim 10^{18}$ cm^{-3}. The thickness of the layer with such an electron density ranges from 0.3 to 3 mm. Under the assumption that the average plasma ion charge is close to 10, we find that, at the instant of pinching, there are regions at the liner periphery in which the estimated local linear mass density is ~10–30 μg/cm (i.e., about 10% of the linear mass of the initial wire array). Thus, after the SXR burst, almost all the liner mass resides near the axis, inside a cylinder 1–6 mm in diameter. Nevertheless, as was said above, a plasma with a mass equal to 10% of the initial liner mass may be sufficient to shunt an appreciable fraction of the liner current.

It is of interest to evaluate the accuracy of the above estimates. The minimum estimated error in calculating the phase difference using linear interpolation between the maxima and minima of the blackening density is $\pi/3$ rad. The oscillations with a characteristic amplitude of 0.3π in Fig. 7 agree with this value. The recorded phase differences lie in the range 3–20 rad. Thus, the relative error in determining the phase difference and the surface electron density along the laser beam is 5–30%. The abelianization procedure significantly increases the error in determining the density at a radius of $R_L - \Delta x$ (the quantity $n_{\Delta x}$). If one could guarantee the cylindrical symmetry of the liner under study, the relative error would be slightly larger than 5–30%. However, the recorded interference pattern is clearly asymmetric. In this case, it is reasonable to talk about the averaged value of $n_{\Delta x}$, which can differ from that obtained by abelianization procedure by a factor of 1.5–2. The next reason is the uncertainty in the average ion charge, which can result in an additional error factor of 1.5. Since these factors are independent, the resulting error in determining the local linear mass at the liner periphery can reach a factor of 2–2.5. Remember that these estimates refer only to regions in which the phase shift was measured.

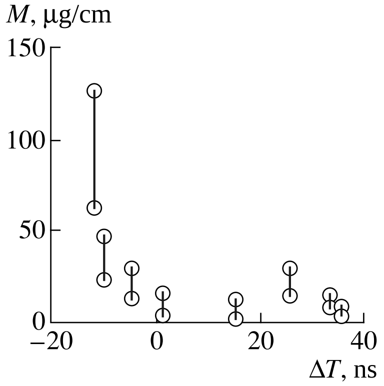

Fig. 10. Measured linear mass density M of the peripheral plasma within the probing layer vs. time shift ΔT of the laser pulse with respect to the SXR burst.

Nevertheless, in spite of the low accuracy in determining the absolute value of the local linear mass density, we succeeded in detecting the presence of a plasma at the periphery of the initial wire array at the instant of maximum compression. The linear density of this plasma was estimated roughly.

The presence of a significant amount of plasma at the liner periphery is also confirmed by the fact that the plasma is seen on the shadow images of the Z-pinch at the instant of liner stagnation.

Indirect confirmation of the presence of plasma at the liner periphery is provided by the measurements of the voltage across the gap at $r = 6$ cm. As was noted above, at the instant of pinching, the voltage across a 1-cm-long gap should be higher than 1 MV. However, the measured maximum voltage does not exceed 0.5 MV. This indicates that a fraction of the current flows aside the pinch. Note that the plasma residing at the liner periphery at the instant of maximum compression is also observed with the help of alternative diagnostics (see Figs. 11 and 12).

Figure 11 shows the evolution of the radial distribution of the optical emission intensity from an imploding liner. It can be seen that, the glow from a plasma that is accelerated toward the liner axis arises at the periphery of the initial wire array (in the lower part of the figure) near the instant of maximum compression.

Figure 12 presents photographs of a Z-pinch taken in its own SXR emission with an exposure time of 1.5 ns for two discharges near the instant of maximum compression. It can be seen that there is a plasma at the periphery of the initial wire array. The irregular structure of the plasma glow at the liner periphery complies with the irregular interference pattern discussed above.

The question is how any plasma can remain at the periphery of the initial wire array at the instant of maximum compression. Indeed, all the plasma should be

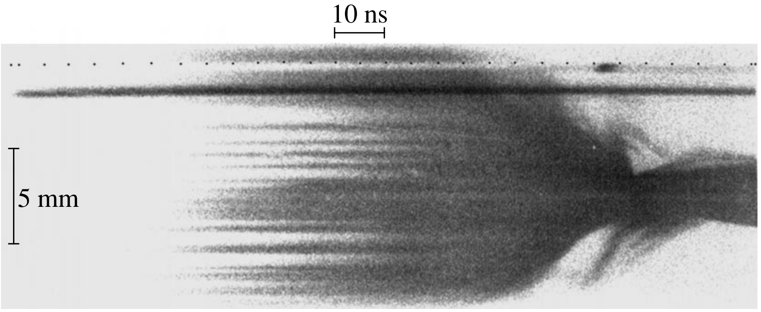

Fig. 11. Streak image showing the radial distribution of the optical emission intensity from an imploding liner.

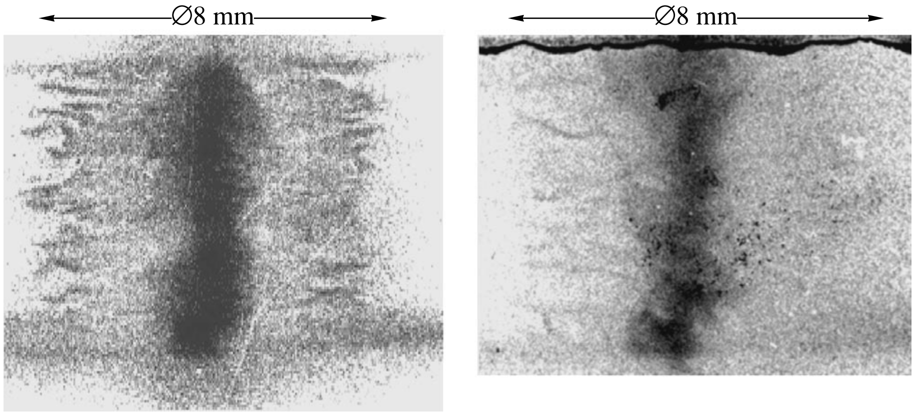

Fig. 12. Photographs of a Z-pinch taken in its own SXR emission with an exposure time of 1.5 ns for two discharges near the instant of maximum compression.

driven by the Ampére force toward the liner axis. One possible explanation is that the plasma continues to be produced in the course of implosion. By the instant of maximum compression, most of the plasma-forming substance has already been converted into plasma, which drifts toward the liner axis together with the magnetic field frozen in it. However, a certain fraction of the plasma-forming substance in the form of droplets and small wire residues remains near their initial positions. The substance in these residues is a dense, poorly conducting plasma that does not impede the penetration of the magnetic field into the axial region of the liner. The hot plasma continues to be produced from the surfaces of these residues. This plasma is seen in a streak image that shows the evolution of the radial distribution of the optical emission intensity from an imploding liner (Fig. 11), as well as in shift interferograms of the liner periphery. Places in which the residues of the plasma-forming substance were located can also be seen in frames taken with an X-ray MCP camera near the instant of maximum compression (see Fig. 12).

6. CONCLUSIONS

The plasma density at the periphery of a wire array at the instant of maximum compression was measured using a technique based on laser shift interferometry.

It was found that, at the instant of maximum compression (~100 ns after the beginning of the discharge), the estimated maximum local electron density at a distance of 0.3–3 mm from the initial wire positions reaches ~10^{18} cm^{-3}. Assuming that the average tungsten ion charge is $Z = 10$, we find that the local linear mass density in this region is 30 μg/cm, which amounts to about 10% of the total linear mass density of the liner. This plasma is likely to be formed from localized wire residues. A fraction of the liner current flows through this plasma. The duration of the SXR pulse is 5–8 ns, which indicates the achievement of a fairly high compression ratio.

ACKNOWLEDGMENTS

This study was supported in part by the Russian Foundation for Basic Research, project nos. 01-02-17319 and 02-02-17200.

REFERENCES

1. R. B. Spielman, C. Deeney, G. A. Chandler, *et al.*, Phys. Plasmas **5**, 2105 (1998).
2. S. V. Lebedev, F. N. Beg, S. N. Bland, *et al.*, Phys. Plasmas **8**, 3734 (2001).
3. V. V. Alexandrov, I. N. Frolov, M. V. Fedulov, *et al.*, in *Proceedings of the 5th International Conference on Dense Z-Pinches, Albuquerque, 2002*, Ed. by J. Davis, C. Deeney, and N. Pereira; AIP Conf. Proc. **651**, 91 (2002).
4. V. V. Alexandrov, I. N. Frolov, E. V. Grabovsky, *et al.*, IEEE Trans. Plasma Sci. **30**, 559 (2002).
5. V. V. Alexandrov, I. N. Frolov, M. V. Fedulov, *et al.*, in *Proceedings of the 5th International Conference on Dense Z-Pinches, Albuquerque, 2002*, Ed. by J. Davis, C. Deeney, and N. Pereira; AIP Conf. Proc. **651**, 87 (2002).
6. A. V. Branitskiĭ and G. M. Oleĭnik, Prib. Tekh. Éksp., No. 4, 58 (2000).
7. V. Alexandrov, A. Branitskii, E. Grabovsky, *et al.*, in *Proceedings of the 1st International Conference on Inertial Fusion Sciences and Application, Bordeaux, 1999*, Ed. by Ch. Labaune, W. J. Hogan, and K. A. Tanaka (Elsevier, St. Louis, 1999), p. 591.
8. J. W. Goodman, *Statistical Optics* (Wiley, New York, 1985; Mir, Moscow, 1988).
9. A. A. Samokhin, Preprint No. 0100-A (Troitsk Institute for Innovation and Fusion Research, 2002).

Translated by N.N. Ustinovskiĭ

Plasma Physics Reports, Vol. 30, No. 3, 2004, pp. 228–234. Translated from Fizika Plazmy, Vol. 30, No. 3, 2004, pp. 256–262.

DUSTY PLASMA

Surface Activity of Dust with Variable Charge

A. M. Ignatov

Prokhorov Institute of General Physics, Russian Academy of Sciences, ul. Vavilova 38, Moscow, 119991 Russia

Received May 28, 2003; in final form, July 10, 2003

Abstract—A simple model is developed for the self-consistent charging of a dust layer in an electrode plasma sheath, as well as for the force balance in this layer. The anisotropy of the plasma pressure near the plasma boundary makes it possible to introduce the notion of surface tension. The equilibrium charge, the height at which the dust layer levitates above the electrode, and the plasma surface tension are calculated numerically as functions of the dust density. In all of the cases under analysis, the presence of dust is shown to increase the plasma surface tension, which indicates that the plasma sheath may become structurally unstable. *© 2004 MAIK "Nauka/Interperiodica".*

1. INTRODUCTION

The parameters of a thin low-temperature plasma sheath near a discharge chamber wall (or near an electrode) differ considerably from those of the plasma volume [1]. If, for example, the electrode is at a floating potential, then, at distances of about several Debye radii from the electrode surface, the plasma quasineutrality is violated, a strong electric field appears, the electron density decreases markedly, and an electrode-directed ion flow forms.

It is under these conditions that experiments with dust grains are often carried out. A certain number of specially prepared dust grains (or, sometimes, only one grain), usually several microns in diameter, are placed above a horizontally positioned electrode. The plasma may be created either by applying a high-frequency voltage to the electrode or by external sources. In some experiments, the electrode is also negatively biased. Under these conditions, the grains acquire fairly large negative electric charges, so that their weights are balanced by the electric field in the electrode sheath (see Fig. 1). A detailed discussion of numerous experiments can be found in review [2].

Since the plasma parameters and the electric field are essentially nonuniform across the electrode sheath, the charge of a grain changes with the distance from the electrode surface. Consequently, at a certain height above the electrode (which depends on the grain size and mass), the total vertical force acting on the grain vanishes; sometimes, there are several heights at which such equilibrium conditions are satisfied. The questions about the equilibrium charge of the grain and the height at which the grain is in equilibrium, as well as of how the dependence of the grain charge on height affects the vertical oscillations of the grains, have been discussed in a number of papers [3–6]. On the other hand, the presence of many charged grains in the sheath can substantially change the electric field distribution and the distributions of the electron and ion densities. This point too has been investigated both theoretically [7, 8] and experimentally [9].

It was shown in recent papers [10, 11] that even a few charged dust grains can significantly change the surface tension of an electrode plasma sheath. Since, in this context, the notion of surface tension was apparently introduced only quite recently [11], it is necessary to discuss it in more detail. Let an electrode be placed at the $z = 0$ plane, the ion velocity in the electrode sheath being directed downward (Fig. 1). At sufficiently great heights above the electrode, the plasma is quasineutral. Let us consider the momentum balance in the electrode sheath. Since, under conditions typical of most experiments, the collisions of plasma particles with neutrals can be ignored, the plasma momentum is conserved. Assuming that all the quantities are independent of the transverse coordinates and that there are no external charges (dust grains) in the plasma, we can write the momentum conservation equation in the form $\partial P_{iz}/\partial z = 0$. The momentum flux tensor P_{ij} is represented as a sum of the plasma pressure (which is generally anisotropic) and the Maxwell stress tensor. If all

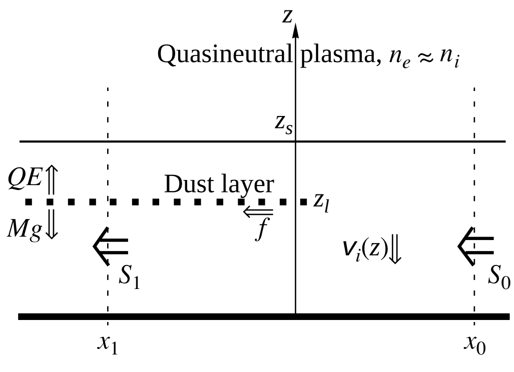

Fig. 1. Schematic representation of a dust layer near the electrode.

1063-780X/04/3003-0228$26.00 © 2004 MAIK "Nauka/Interperiodica"

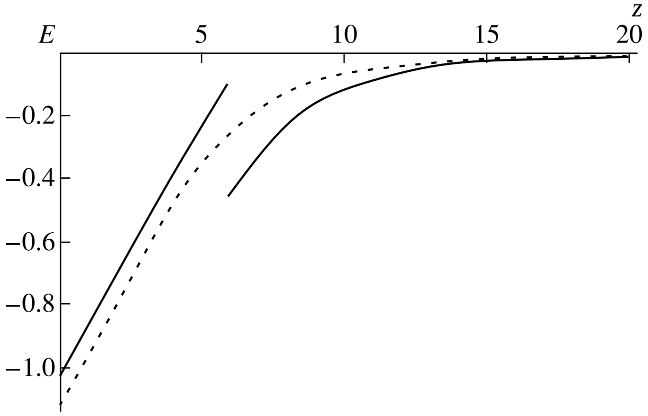

Fig. 2. Electric field profiles. The solid curve is for a dust layer with $\alpha = 0.05$ and $\beta = 1$. The dashed curve is for an electrode sheath without dust ($\alpha = 0$).

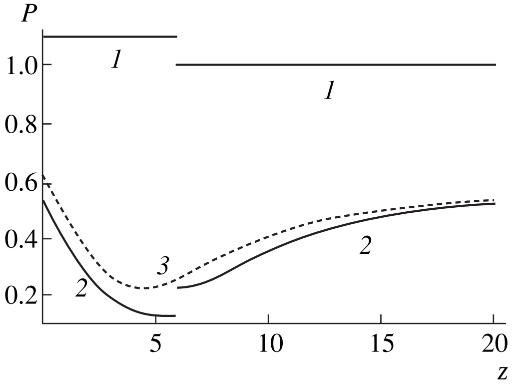

Fig. 3. Pressure profiles. Curves *1* and *2* are, respectively, for the longitudinal and transverse pressures described by formulas (12) and (13) with $\alpha = 0.05$ and $\beta = 1$. Curve *3* is for the transverse pressure in the absence of dust.

the quantities depend solely on the z coordinate, then symmetry considerations obviously imply that the momentum flux tensor has only three nonzero components, $P_{zz} = P_l(z)$ and $P_{yy} = P_{xx} = P_{\text{tr}}(z)$. By virtue of the conservation of momentum, the component $P_l(z)$ should be constant, whereas the transverse momentum flux $P_{\text{tr}}(z)$ may be a function of the z coordinate. If we disregard possible pressure anisotropy (e.g., due to ionization in an rf field) in a quasineutral plasma, then, at great heights above the electrode, we have $P_{\text{tr}}(z) \approx P_l = P_0$. The characteristic profile of the transverse pressure $P_{\text{tr}}(z)$ in the model to be discussed below is shown by curve *3* in Fig. 3.

Of course, in the plasma volume, the collisions of plasma particles with neutrals play a significant role and, on a spatial scale of about the mean free path λ_n or the discharge chamber length L, the longitudinal pressure P_l can depend on the coordinates. In what follows, it is assumed that the electrode sheath thickness, which is determined by the electron Debye radius λ_{De}, is much smaller than any other characteristic scale length of the system, so that it is possible to choose a certain distance L_0 such that it satisfies the conditions $\lambda_{\text{De}} \ll L_0 \ll L, \lambda_n$. We can also assume that, at the surface $z = L_0$, the plasma is quasineutral and its pressure is equal to $P_{\text{tr}}(L_0) = P_0$.

The deviation of the transverse plasma pressure from being constant is characterized by the quantity

$$s = \int_0^{L_0} dz(P_0 - P_{\text{tr}}(z)), \quad (1)$$

which has a quite simple physical meaning. Imagine that the entire plasma volume is cut into two parts by, e.g., the $x = x_0$ plane (Fig. 1). As may be seen, the force pushing these parts away from one another is roughly equal to P_0S_0, where S_0 is the cross-sectional area. Since quantity (1) characterizes the decrease in this repulsive force per unit length of surface, it can be identified with the plasma surface tension.

In gas discharge physics, the surface tension is usually of minor importance. However, it may have a decisive impact on the horizontal force acting on an inhomogeneous charged dust layer. For instance, let there be a semi-infinite ($x < 0$) dust layer with a certain surface charge density at a height z_l above the electrode (Fig. 1). The horizontal force acting on the charged layer is equal to the difference between the fluxes of the x component of the momentum through the planes $x = x_{0,1}$. If the distances $x_{0,1}$ from the planes to the layer edge are chosen to be sufficiently large, then, in calculating the momentum flux tensor at $x = x_{0,1}$, we can ignore the dependence of all the quantities on x. In this case, the total horizontal force per unit length is equal to $f = s_0 - s_1$, where the quantities $s_{0,1}$ are determined by integral (1) at $x = x_{0,1}$. Based on similar considerations, we can also relate the density of the horizontal force acting on a weakly inhomogeneous charged layer to the derivative of surface tension (1) with respect to the charge density.

Hence, the main interest lies not so much in the surface tension itself as in its dependence on the density of additional charges, e.g., charged dust grains. This dependence was calculated in [10, 11] on the basis of two simple models. It was found that additional negative charges introduced in an electrode sheath often enhance the surface tension, in which case the force acting on the external charges tends to push them away from the sheath (as is shown in Fig. 1). Sometimes, however, additional changes reduce the surface tension, which indicates that the force acts in the opposite direction. In this respect, the charged dust behaves as a surface-active substance. There is no need to remind the reader of the enormous variety of phenomena occurring in interactions between surface-active substances and water. It may be hoped that, with cleverly prepared experiments, the relevant dusty plasma physics will be equally rich.

In [11], it was assumed that each grain carries a constant charge but the height at which it is in equilibrium above the electrode can change. In the hydrodynamic model developed here, the somewhat unrealistic assumption of a constant grain charge is removed. A description of the model is given in Section 2. Section 3 presents the method for solving the model equations numerically and shows how the equilibrium charge of a dust layer, the height at which it is in equilibrium, and the plasma surface tension depend on the dust density. In the conclusion, it is inferred that a charged dust layer may be structurally unstable.

2. MODEL

This section presents the hydrodynamic model proposed to describe an electrode plasma sheath. All the quantities are assumed to depend only on the z coordinate. The ions are described by the continuity equation

$$\frac{dn_i(z)v_i(z)}{dz} = \nu_{\rm ion} n_e(z) \qquad (2)$$

(where $\nu_{\rm ion}$ is the electron-impact ionization rate) and the momentum balance equation

$$\frac{dm_i n_i(z)v_i^2(z)}{dz} + en_i(z)\frac{d\phi(z)}{dz} = 0. \qquad (3)$$

The electrons are assumed to obey a Boltzmann distribution, $n_e(z) = n_0 \exp(e\phi(z)/T_e)$, where n_0 is the equilibrium electron density in the plasma volume, and the electron temperature is assumed to be constant. The set of model equations is closed by Poisson's equation

$$\frac{d^2\phi(z)}{dz^2} = 4\pi e(n_e(z) - n_i(z)) - 4\pi\rho_d(z), \qquad (4)$$

where $\rho_d(z)$ is the charge density of dust.

At sufficiently great heights above the electrode ($z \approx L_0$), the plasma is quasineutral. Under the assumption that there is no dust at such heights, namely, $\rho_d(z) = 0$ and $n_e(z) = n_i(z)$, Eqs. (2) and (3) are easy to solve (see, e.g., [12]). For the ion density distribution, we have

$$n_i^{(b)}(z) = \frac{n_0 c_s^2}{c_s^2 + v_i^{(b)}(z)^2}. \qquad (5)$$

Here, $c_s = \sqrt{T_e/m_i}$ is the ion-acoustic velocity, the superscript $^{(b)}$ denotes the values of the quantities in the plasma volume, and the dependence of the ion velocity on z is defined implicitly by

$$z - z_0 = \frac{v_i(z)}{\nu_{\rm ion}} - 2\frac{c_s}{\nu_{\rm ion}}\arctan\frac{v_i(z)}{c_s}, \qquad (6)$$

where z_0 is an integration constant. The electric field in the quasineutral plasma region is expressed from formulas (5) and (6) with the help of Eq. (3). These expressions are assumed to be valid for $z > L_0$. The integration constant in expression (6) is chosen so that the ion velocity at $z = L_0$ takes on a certain value, $v_i^{(b)}(L_0) = v_{i0}$. The boundary conditions for Eqs. (2)–(4) are specified by the formulas

$$\begin{gathered} n_i(L_0) = n_i^{(b)}(L_0), \quad v_i(L_0) = v_{i0}, \\ \phi(L_0) = \frac{T_e}{e}\ln\frac{n_i^{(b)}(L_0)}{n_0}, \\ \left.\frac{d\phi}{dz}\right|_{z=L_0} = -\frac{1}{en_i^{(b)}(z)}\left.\frac{dm_i n_i^{(b)}(z)v_i^{(b)2}(z)}{dz}\right|_{z=L_0}. \end{gathered} \qquad (7)$$

In the problem as formulated, the distance L_0 remains unknown. It can be determined by imposing an additional condition at the electrode. This may be done, e.g., by specifying the potential at $z = 0$. In what follows, we assume that the electrode is at the floating potential, i.e., that the total current at $z = 0$ is zero,

$$n_i(0)v_i(0) + n_e(0)\sqrt{\frac{T_e}{2\pi m_e}} = 0. \qquad (8)$$

The model proposed here is, in essence, a slightly modified version of the Langmuir–Tonks model [13]. The ionization rate in Eq. (2) is assumed to be sufficiently low, $\nu_{\rm ion} \ll c_s/L_0$. In other words, the model under discussion is in fact a collisionless one: the ionization rate merely determines the spatial scale in the quasineutral plasma region [see expression (6)] and enters only into boundary conditions (7). Of course, under actual conditions, the frequency of collisions with neutrals can appreciably exceed the ionization rate. If we assume that the mean free path is much greater than the electrode sheath thickness, then we can see that Eqs. (2)–(4) remain valid and that taking into account collisions with neutrals leads to a modification of solution (6) (see, e.g., [12, 14]) and, accordingly, boundary conditions (7). As a result, the plasma density in the volume changes considerably, while the pressure distribution over the electrode sheath changes insignificantly. This is why the model developed here on the basis of Eqs. (2)–(4) is the simplest possible one: the presence of collisions with neutrals is not necessary for the existence of a discharge, but ionization is. In this model, there is no need to solve the well-known problem of matching the equations for the plasma wall sheath with those for the plasma volume. Recall that, in accordance with the Bohm criterion, they are usually matched at the surface where $|v_i| = c_s$, and the boundary velocity $|v_{i0}|$ is chosen far below the ion-acoustic velocity. Numerical solutions of Eqs. (2)–(4) showed that the final results are weakly sensitive to the value of the boundary velocity $|v_{i0}|$, provided that it is chosen to be $|v_{i0}| < 0.1c_s$.

It is also important to point out the following circumstance. In what follows, the normalizing density n_0 is assumed to be constant. Although this assumption appears at first glance to be quite realistic, it nevertheless requires justification. The equilibrium density is determined by the balance between ionization and losses and is thus an eigenvalue of the equations describing the plasma as a whole. In principle, even a small amount of dust in the electrode sheath changes the electric field distribution and thereby may affect the equilibrium density n_0. This can happen, in particular, if charged particles are lost by diffusion toward the walls. Under actual conditions, plasma density variations δn_0 in an electrode sheath with dust seem to be negligible. However, variations in the plasma surface tension, which are estimated to be $\delta n_0 T_e \lambda_n$, may be substantial. On the whole, this problem requires further investigation and will not be considered in this paper. For simplicity, we assume that the equilibrium density n_0 is governed by internal plasma processes (such as recombination or detachment) and is thus independent of the dust density.

In the model to be constructed, dust is regarded as a thin monolayer at a certain height z_l above the electrode surface. The dust charge density is written as $\rho_d(z) = -Q\sigma\delta(z - z_l)$, where $Q > 0$ is the absolute value of the charge of an individual grain and σ is the surface density of the dust grains. Simple estimates show that, even when the surface charge density σ is fairly high (e.g., is at a level corresponding to dust plasma crystals), the dust grains absorb only a small amount of plasma. Consequently, for $z \neq z_l$, the plasma is described by Eqs. (2)–(4) with $\rho_d = 0$, and the effect of dust is described by the additional boundary condition

$$\phi'(z_l + 0) - \phi'(z_l - 0) = 4\pi Q\sigma, \tag{9}$$

the remaining parameters, namely, $n_i(z)$, $v_i(z)$, and $\phi(z)$, being continuous at $z = z_l$.

The force balance equation for a charged dust layer in the Earth's gravity field (in Fig. 1, the gravity force points downward) has the form

$$\frac{1}{2}Q\sigma(\phi'(z_l + 0) + \phi'(z_l - 0)) - \sigma Mg = 0, \tag{10}$$

where M is the mass of an individual grain. In Eq. (10), the first term is the electric force per unit area of the layer and the second term is the weight of dust per unit area of the layer. It should be noted that total force balance equation (10) does not contain the ion drag force because simple estimates show that it is much less than the weight of a grain.

Up to this point, the charge of a grain has not been determined. In order to see how the grain charge is related to the plasma parameters, we turn to the simplest possible approximation—the so-called orbit motion limited (OML) approach, in which the grain is treated as an absorbing center with a certain effective absorption cross section. The condition for the total electric current onto the surface of an individual grain to be zero is written as [3]

$$\begin{aligned} J_d = {} & \sqrt{\frac{8T_e}{\pi m_e}}n_0\exp\left(\frac{e\phi(z_l)}{T_e} - \frac{eQ}{aT_e}\right) \\ & - n_i(z_l)|v_i(z_l)|\left(1 + \frac{2eQ}{am_i v_i^2(z_l)}\right) = 0, \end{aligned} \tag{11}$$

where a is the grain radius, which is much smaller than the electron Debye radius.

Numerical solution of Eqs. (2)–(4) with boundary conditions (7) and (8) and with additional relationships (9)–(11) makes it possible to self-consistently determine the dependence of the plasma parameters on z, as well as the equilibrium grain charge Q and the height z_l at which the dust layer is in equilibrium above the electrode, provided that the surface charge density σ is specified in advance.

Having found the solution, we can calculate the pressure tensor elements. In the model in question, they are equal to

$$P_l(z) = m_i n_i(z) v_i(z)^2 + n_e(z)T_e - \frac{1}{8\pi}E(z)^2, \tag{12}$$

$$P_{\text{tr}}(z) = n_e(z)T_e + \frac{1}{8\pi}E(z)^2, \tag{13}$$

where $E(z) = -\phi'(z)$ is the electric field. In the absence of dust, longitudinal pressure (12) is an integral of Eqs. (2)–(4). Since the ions move only along the z axis and their temperature is assumed to be negligibly low, they do not contribute to transverse pressure (13). The most important point is, however, that the electric field pressure, which is described by the Maxwell stress tensor, is always anisotropic. As a consequence, the squares of the electric field enter into the expressions for the longitudinal and transverse pressure components with opposite signs.

3. CALCULATED RESULTS

Problem (2)–(4) and (7)–(11) is a set of differential equations with nonlinear boundary conditions. There are no standard numerical methods for solving this and similar problems. The numerical results presented below were obtained by means of the following algorithm: A certain charge Q is specified in advance, and the electric field below and above the charged dust layer is calculated as a function of the charge and mass of a grain by using relationships (9) and (10): $\phi'(z_l \pm 0) = Mg/Q \pm 2\pi Q\sigma$. Equations (2)–(4) are solved by the standard Runge–Kutta method with initial conditions (7), in which case the initial value of z is chosen arbitrarily (e.g., it can be set equal to zero). The initial values of the ion velocity are chosen sufficiently low. The results

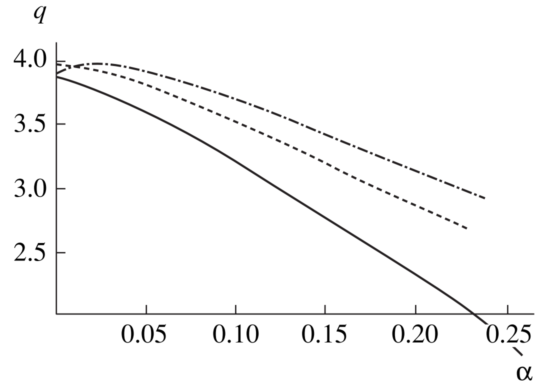

Fig. 4. Dependence of the charge on the dust density. The solid curve is for $\beta = 1$, the dashed curve is for $\beta = 0.5$, and the dashed-and-dotted curve is for $\beta = 0.1$.

presented below were computed for $v_{i0} = -0.01c_s$. The solution to Eqs. (2)–(4) is constructed by integrating them in the direction of decreasing z until the derivative of the potential becomes equal to the value $\phi'(z) = Mg/Q + 2\pi Q\sigma$ calculated earlier. The z coordinate at which this value is reached is equal to $z_l - L_0$.

Next, Eqs. (2)–(4) are again integrated in the direction of decreasing z, in which case the values of the potential, density, and velocity do not change but the derivative of the potential at $z = z_l - L_0$ is equal to $\phi'(z_l - L_0) = Mg/Q - 2\pi Q\sigma$. The process of constructing the solution is continued until the total current (8) at the electrode vanishes (in this way, it is also possible to impose some other condition, e.g., to fix the potential). The calculated value of the z coordinate is equal to $-L_0$. The constant displacement L_0 is then added to each of the z coordinates of the entire set of solutions.

Hence, for a given charge Q, the algorithm calculates the distributions of all the quantities and the height z_l at which the dust layer is in equilibrium above the electrode. In particular, the total electric current J_d onto the surface of an individual grain [see expression (11)] is calculated as a function of Q. The zeros of the function $J_d(Q)$ are sought by standard methods, whereby it becomes possible to determine the equilibrium charge and equilibrium height, as well as the corresponding spatial distributions of all the quantities.

The surface tension is calculated from formula (1). In the algorithm described here, the length L_0 of the computation region depends on the dust density. Although the difference in the length L_0 between the examples given below is small (only fractions of one percent), it may nonetheless play a role in taking the integral in formula (1). This is why, in calculating the surface tension as a function of the dust density, the upper integration limit in Eq. (1) was chosen to be the same for all density values. The relative difference between the longitudinal and transverse pressures at $z \approx L_0$ is on the order of 10^{-4}.

All simulations were carried out in terms of dimensionless quantities. In the figures, the length is expressed in units of the electron Debye radius $\lambda_{\mathrm{De}} = \sqrt{T_e/4\pi e^2 n_0}$, the electric field is in units of $T_e/e\lambda_{\mathrm{De}}$, the pressure is normalized to n_0T_e, and the surface tension is in units of $n_0T_e\lambda_{\mathrm{De}}$. The dimensionless charge is $q = eQ/aT_e$, the dust density is characterized by the dimensionless quantity $\alpha = 2\pi a\lambda_{\mathrm{De}}\sigma$, and the dimensionless weight of a grain is characterized by $\beta = Mge^2\lambda_{\mathrm{De}}/aT_e^2$. Under actual conditions, we have $\alpha \ll 1$ and the quantity β may amount to unity. In simulations, the ionization rate was chosen sufficiently low ($\nu_{\mathrm{ion}}\lambda_{\mathrm{De}}/c_s = 10^{-3}$) and the electron-to-ion mass ratio in formulas (8) and (11) corresponded to argon. For these parameter values, the length of the computation region is about $L_0 \approx 570$.

A representative profile of the electric field is displayed in Fig. 2, in which the dashed curve shows the dependence of the electric field on z in the absence of dust and the solid curve shows the same dependence in the presence of a dust layer with the dimensionless density $\alpha = 0.05$ and dimensionless weight $\beta = 1$. The solid curve is discontinuous at the equilibrium height, which, in the case at hand, is equal to $z_l = 5.9$, the dimensionless charge of the grains being $q = 3.58$. The position of the electrode sheath boundary z_s determined from the Bohm criterion (i.e., the position of the surface at which $|v_i(z_s)| = c_s$) depends on the dust density: in the absence of dust, we have $z_s \approx 15.38$, while the Bohm boundary of a sheath with a dust layer is displaced to the surface $z_s \approx 17.13$. Hence, the dust layer plays the role of a virtual wall that serves to reduce the entire plasma volume.

Figure 3 shows the pressure profiles calculated for the same parameters as in Fig. 2. In the absence of dust, longitudinal pressure (12) is equal to unity. In Fig. 3, straight line *1* shows the longitudinal pressure in the presence of a dust layer of nonzero density. The jump in pressure at a height at which the layer is located balances the layer's weight. Dashed curve *3* in Fig. 3 shows the transverse pressure in a dust-free electrode sheath. We can see that the transverse pressure is appreciably lower than the longitudinal pressure. For the given ionization rate, the pressures become equal at approximately $z \approx 200$—this is apparently a specific feature of the collisionless model under discussion. Finally, the point of greatest interest is the change in the transverse pressure due to the presence of dust. It is important that, in an electrode sheath with the above parameters, the dust significantly (by a factor of almost 2) reduces the transverse pressure in the space between the layer and the electrode. This effect is associated largely with a decrease in the absolute value of the electric field (Fig. 2).

Figure 4 shows how the equilibrium charge depends on the density of a dust layer for grains of different masses. For sufficiently heavy grains, the charge decreases as the density increases. For lighter grains, an

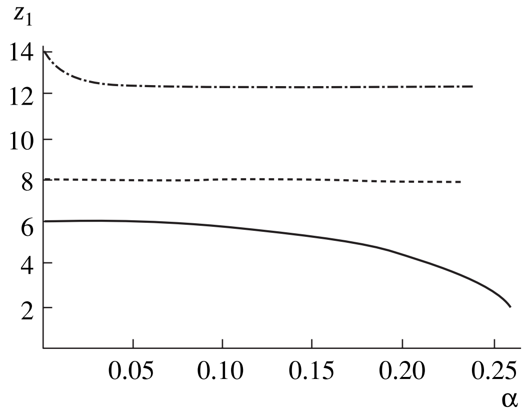

Fig. 5. Dependence of the equilibrium height on the dust density. The solid curve is for $\beta = 1$, the dashed curve is for $\beta = 0.5$, and the dashed-and-dotted curve is for $\beta = 0.1$.

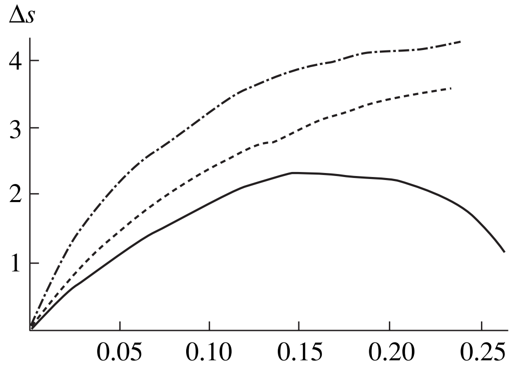

Fig. 6. Dependence of the plasma surface tension on the dust density. The solid curve is for $\beta = 1$, the dashed curve is for $\beta = 0.5$, and the dashed-and-dotted curve is for $\beta = 0.1$.

increase in the density can lead to an insignificant increase in the charge. The equilibrium height also decreases as the density increases (Fig. 5).

For a dust layer of heavy grains with $\beta = 1$, a solution exists only when the dust density is not too high. For $\alpha \geq 0.26$, the equation $J_d(q) = 0$ has no solutions, which indicates that such a dense and heavy layer cannot be in equilibrium at any height above the electrode. Along with the solutions illustrated by the profiles in Figs. 4 and 5 at $\beta \geq 0.7$, there exists another steady state corresponding to far smaller charges ($q \approx 1$) and far lesser heights ($z_l \leq 1$). Presumably, this second steady state, which has already been discussed in the literature (see, e.g., [3]), is unstable again vertical oscillations, as in the case of a single grain.

Figure 6 illustrates the dependence of variations in surface tension, $\Delta s(\alpha) = s(\alpha) - s(0)$, on the density α for grains of different masses. The curves shown in the figure are smoothed because, although the accuracy of the solution to Eqs. (2)–(4) is high, the errors in taking the integral in formula (1) numerically are fairly large (of about several percent). For all the parameter values used in computations, the surface tension of an electrode sheath with a dust layer was found to be higher than that in the absence of dust. This is the main difference from the case of a fixed charge that was investigated in [11] and in which the surface tension in the presence of dust was found to be lower.

It has already been mentioned that, in the model under discussion, the plasma density far above the electrode remains unknown—it must be determined by solving the problem for the entire discharge volume rather than for the electrode sheath alone. For the parameter values that are characteristic of many experiments (namely, an equilibrium electron density of $n_0 = 10^8$ cm^{-3} and an electron temperature of $T_e = 2$ eV, the specific weight of the grain material being 1.5 g/cm^3), the above values of the dimensionless parameters $\alpha = 0.05$ and $\beta = 1$ correspond to dust grains of radius $a = 2.6$ μm and a dust layer with a surface charge density of about $\sigma \approx 280$ cm^{-2}, in which case the layer is in equilibrium at a height of about 5 mm above the electrode. The dimensionless charge of the grains $q = 3.5$ corresponds to the dimensional electric charge $Q = 1.2 \times 10^4 e$. The value of the ionization rate used in computations, $\nu_{\text{ion}} \approx 2 \times 10^3$ s^{-1}, corresponds to a neutral argon density on the order of 10^{14} cm^{-3}.

4. CONCLUSIONS

In the present paper, the charged dust layer is treated as being infinitely thin and perfectly rigid. In reality, however, the grains are interacting and, at sufficiently small distances, repulse one an other. The elastic properties of the layer are characterized by the dependence of the surface pressure $p_s(\sigma)$ on density [15]. When the interaction force between the grain is repulsive, the surface pressure is always positive.

The surface tension that has been discussed above originates from the self-consistent response of the electrode sheath to external charges. The fact that the surface tension turns out to be positive indicates an efficient long-range attraction between grains. In a certain approximation, the total equation of state for the dust layer that describes the balance of horizontal forces can be written as $p_s(\sigma) - s(\sigma) = f$, where f is the density of the external forces acting on the layer. It thus appears that the equilibrium density of a dust layer and the possibility of forming different dust structures are governed by the competition between two different processes. Postponing the discussion of these problems to the future, note only that, if the grains interact through the Yukawa potential, then, as $\sigma \longrightarrow 0$, the surface pressure $p_s(\sigma)$ behaves as $\exp(-1/\lambda_{\text{De}}\sigma^{1/2})$, while the dependence of the surface tension on density is linear. This indicates that the compressibility of a dust layer of sufficiently low density is negative and that the layer itself is unstable against density variations.

ACKNOWLEDGMENTS

This work was supported in part by the Russian Foundation for Basic Research, project no. 02-02-16439.

REFERENCES

1. Yu. P. Raizer, *Gas Discharge Physics* (Nauka, Moscow, 1987; Springer-Verlag, Berlin, 1991).
2. H. Thomas, G. E. Morfill, and V. N. Tsytovich, Fiz. Plazmy **29**, 963 (2003) [Plasma Phys. Rep. **29**, 895 (2003)].
3. S. V. Vladimirov and N. F. Cramer, Phys. Rev. E **62**, 2754 (2000).
4. S. V. Vladimirov, N. F. Cramer, and P. V. Shevchenko, Phys. Rev. E **60**, 7369 (1999).
5. A. V. Ivlev, U. Konopka, and G. Morfill, Phys. Rev. E **62**, 2739 (2000).
6. You-Nian Wang, Lu-Jing Hou, and Xiaogang Wang, Phys. Rev. Lett. **89**, 155001 (2002).
7. V. N. Tsytovich, S. V. Vladimirov, and S. Benkadda, Phys. Plasmas **6**, 2972 (1999).
8. V. N. Tsytovich, G. E. Morfill, and H. Thomas, Fiz. Plazmy **29** (2004) (in press).
9. C. Arnas, M. Mikikian, G. Bachet, and F. Doveil, Phys. Plasmas **7**, 4418 (2000).
10. A. M. Ignatov, P. P. J. M. Schram, and S. A. Trigger, New J. Phys. **5**, 43.1 (2003).
11. A. M. Ignatov, P. P. J. M. Schram, and S. A. Trigger, J. Phys. D **36**, L83 (2003).
12. K.-U. Riemann, J. Phys. D **24**, 493 (1991).
13. L. Tonks and I. Langmuir, Phys. Rev. **34**, 876 (1929).
14. R. N. Franklin and J. Snell, Phys. Plasmas **8**, 643 (2001).
15. G. A. Hebner, M. E. Riley, and K. E. Greenberg, Phys. Rev. E **66**, 046407 (2002).

Translated by I.A. Kalabalyk

Plasma Physics Reports, Vol. 30, No. 3, 2004, pp. 235–240. Translated from Fizika Plazmy, Vol. 30, No. 3, 2004, pp. 263–268.

PLASMA DIAGNOSTICS

Feasibility of Stabilizing a Vacuum-Diode X-ray Source with a Laser-Plasma Cathode

A. S. Kishinets*, Yu. V. Korobkin*, I. V. Romanov*, A. A. Rupasov*, A. S. Shikanov*, A. Moorti, P. A. Naik**, and P. D. Gupta****

** Lebedev Physical Institute, Russian Academy of Sciences, Leninskiĭ pr. 53, Moscow, 119991 Russia*

*** Center of Advanced Technology, Indore 452013, India*

Received July 24, 2003

Abstract—Results are presented from experimental studies of discharge instabilities and the energy and temporal characteristics of a vacuum-diode X-ray source with a laser plasma cathode over a wide range of energies, intensities, and durations of the plasma-forming laser pulse. It is experimentally shown that the vacuum-discharge dynamics and radiation processes in different discharge stages substantially depend on the parameters of the laser radiation. The shortest recorded pulse duration (10 ns) of Ti K-line radiation (4.5 keV) with a total photon number of 10^{11} is achieved when the laser plasma cathode is produced by a laser pulse with a duration of 27 ps and an intensity of 10^{13} W/cm^2. It is found that the contrast of characteristic emission against the bremsstrahlung background is maximum when discharge instabilities are suppressed and the accelerating voltage is three to four times higher than the threshold voltage for line excitation. *© 2004 MAIK "Nauka/Interperiodica".*

1. INTRODUCTION

It is well known that pulsed X-ray tubes with explosive cathodes mainly emit X-ray bremsstrahlung and do not provide high contrast of the characteristic line emission. This is related to the high threshold voltage (no lower than 50 kV) and the design features of these tubes. Generally, commercial X-ray tubes operate in a regime in which the discharge time of the storage capacitor is shorter than the time during which the cathode plasma bridges the interelectrode gap. Otherwise, the energy remaining in the storage capacitor after bridging the gap turns out to be sufficient for igniting a vacuum arc, which leads to a strong erosion of the electrodes. Thus, X-ray generation occurs at the trailing edge of an anode voltage pulse; as a result, bremsstrahlung is smeared out over spectrum, thereby substantially reducing the contrast of the characteristic lines. Therefore, in experiments in which high contrast of the pulsed characteristic X-ray emission is required, it is reasonable to use vacuum-diode X-ray sources with laser plasma cathodes. A compact quasi-point (with an emission zone of ~250 μm in size) source of characteristic Ti K-line (~4.5 keV) radiation with a spectral radiance of ~10^{21} photon/(cm^2 s sr keV), pulse duration of 20 ns, and a total number of photons of 10^{11} was described in [1, 2]. The source was controlled by laser pulses with a duration of ~10–30 ns and an energy of ≤1 J. The feasibility of the source operation at any required voltage U made it possible to satisfy the condition $U = (3–4)U_0$ (where U_0 is the threshold voltage for the excitation of the characteristic emission series), which enabled the maximum contrast of the characteristic emission against the bremsstrahlung background. An acceptable constancy of the anode voltage in the initial stage of the discharge was produced by the fact that the amount of the total charge carried by an electron beam emitted from a laser plasma created at the cathode was low compared to the charge accumulated in the storage capacitor. A further discharge of the capacitor through the interelectrode gap filled with the laser plasma and the anode plasma plume led to the erosion of the conical Ti anode: after 500 discharge cycles, the diameter of the anode tip increased from 200 to 300 μm. We note, however, that such an increase is quite admissible for laboratory experiments.

In the wavelength range 0.24–0.30 nm, the measured contrast of Ti K-lines was higher than 100. However, the contrast decreased substantially when the laser plasma cathode was produced by a laser pulse with an energy of ≤5 mJ. Spectroscopic studies performed by the filter method revealed the presence of a hard X-ray component with photon energies higher than the energy of bremsstrahlung photons corresponding to the applied voltage. At a discharge voltage of 20 kV, we observed X-ray photons that were emitted from the anode with energies exceeding 25 keV. The probable reasons for the emergence of such high-energy photons are (i) instabilities of a low-pressure (p ~ 10^{-4}–10^{-6} torr) discharge, accompanied by partial current breaks and jumps in the discharge voltage [3–5], and (ii) the micropinching of the plasma channels [6–8]. In this context, we investigated the conditions for current flow through the discharge gap and the conditions for the onset of discharge instabilities in a vacuum-diode X-ray source with a laser plasma cathode.

1063-780X/04/3003-0235$26.00 © 2004 MAIK "Nauka/Interperiodica"

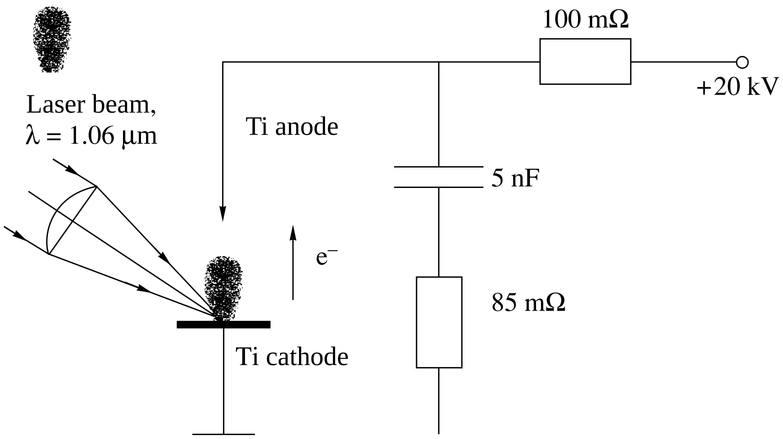

Fig. 1. Schematic of the vacuum diode with the laser plasma cathode.

2. EXPERIMENTAL SETUP

A schematic of the experiment is shown in Fig. 1. The discharge circuit of the vacuum diode consisted of a 5-nF capacitor, a massive grounded Ti target (cathode), and a conical Ti anode with a tip diameter of ~250 μm. The capacitor was charged by a dc power supply to a voltage of 3–20 kV. The interelectrode distance could be varied from 1 to 20 mm. The pressure in the vacuum-diode chamber was $\sim 4 \times 10^{-5}$ torr. The inductance of the discharge circuit was generally determined by the stray inductance of the storage capacitor and varied from 0.2 to 0.8 μH, depending on the electrode configuration. The cathode plasma was produced by a Nd laser ($\lambda = 1.06$ μm) beam focused on the target surface into a 200-μm-diameter spot. The electrons emitted from the cathode plasma were accelerated by the electric field toward the Ti anode and gave rise to X-ray emission in the characteristic Ti K- and L-lines, as well as to X-ray bremsstrahlung with maximum intensity at λ [nm] = $1.86/U$ [kV]. To widen the range of the available laser beam intensities on the cathode and to study the effect of the laser pulse duration on the process of X-ray generation, we used a Q-switched laser with a pulse duration of $\tau = 20$ ns and an energy of $E \leq 120$ mJ and a passive-mode-locking laser with $\tau = 27$ ps and $E \leq 2$ J (both located at the Centre for Advanced Technology, Indore, India). The discharge current and voltage were measured with a frequency-balanced coaxial shunt (with a resistance of 85 mΩ) and a resistive divider, respectively. The X-ray intensity was measured with Quantrad 100-PIN-250 silicon pin diodes with a response of 0.2 C/J. The signals were recorded with a Lecroy 9350A oscilloscope with a 500-MHz bandwidth. In these experiments, the Faraday cup technique, which is commonly used to measure the anode current in vacuum discharges [3], was not employed because of the complicated diode configuration. Instead, we monitored the time evolution of the X-ray intensity, which closely reproduced the current behavior in the early stage of the discharge and during the onset of instabilities.

3. EXPERIMENTAL RESULTS AND DISCUSSION

Figure 2 shows typical waveforms of the discharge voltage and X-ray intensity for different energies of a 27-ps laser pulse. The maximum contrast of Ti K-lines was achieved at an initial discharge voltage of 20 kV. The interelectrode distance was 4 mm, the electric circuit inductance was 0.2 μH, and the discharge current was no higher than 3 kA. In the early stage of the discharge, the anode voltage decreases slowly and the current obeys the 3/2 law. The increase in the current is related to a decrease in the gap length and an increase in the emissive area of the laser plasma. The generation of an electron beam carrying the discharge current is accompanied by an X-ray burst. In this stage, the discharge voltage decreases by no more than 15% of its initial value. Such a decrease only slightly affects the contrast of the X-ray characteristic lines. In the next discharge phase, the voltage decreases at a gradually increasing rate; this is related to the effect of ion accumulation in the discharge gap and the emergence of a region with a potential exceeding the applied voltage (a "potential hump" [5]). This region acts as an electrostatic trap of electrons. Inside this region, the residual gas and the vapor of the electrode material are efficiently ionized, which leads to the rapid expansion of the plasma and an increase in the discharge current. It can be seen in Fig. 2 that the higher the laser pulse energy, the faster the decrease in the discharge voltage. In our case, an important role is also played by the anode plasma plume because, in view of the small electrode area, the electron beam power per unit area of the anode surface can exceed 10^9 W/cm^2, thus providing conditions for intense plasma generation. A specific feature of the waveforms obtained at an energy of the

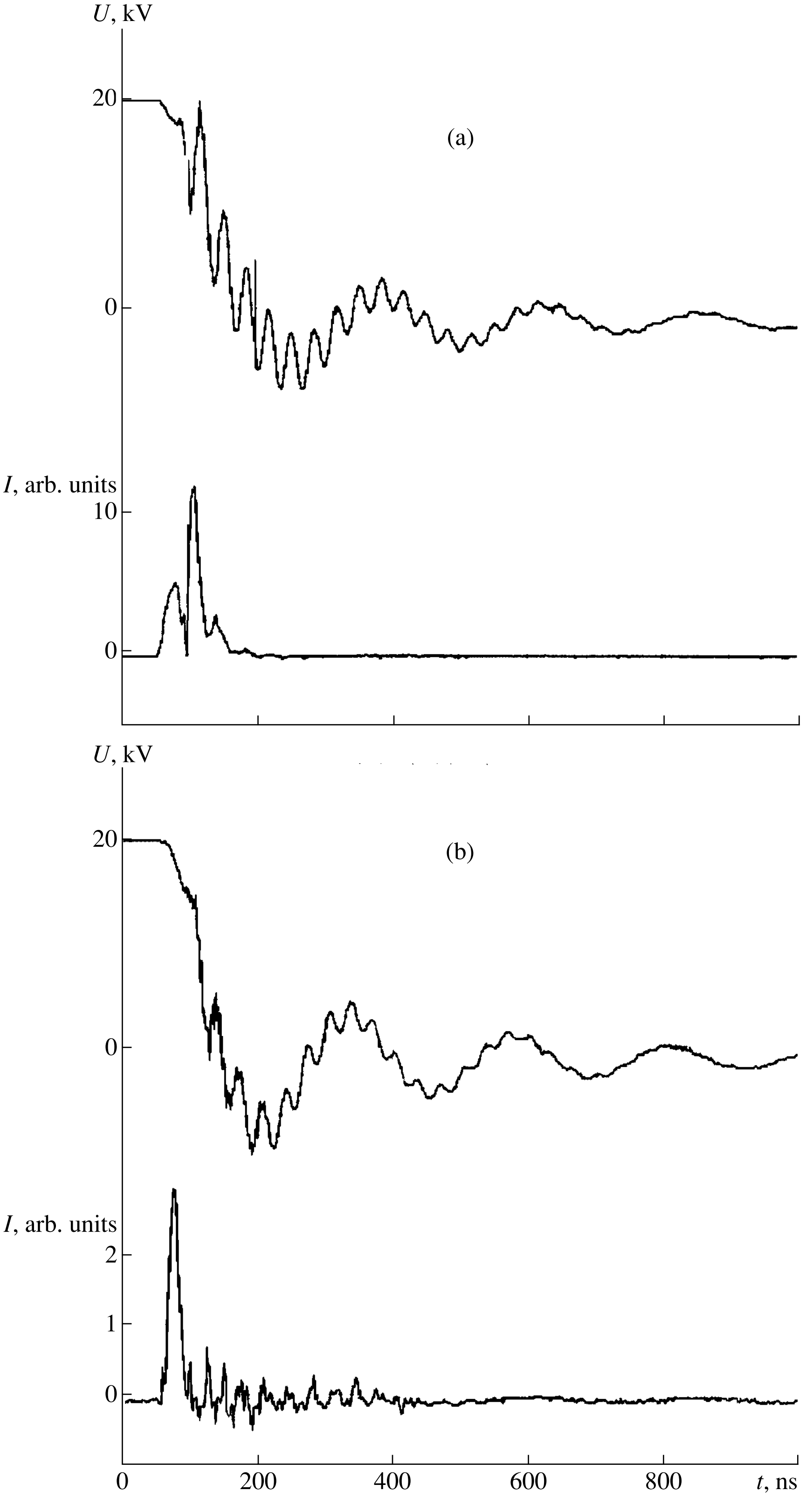

Fig. 2. Waveforms of the discharge voltage *U* and X-ray intensity *I* for an interelectrode gap length of $d = 4$ mm, a laser pulse duration of $\tau = 27$ ps, and laser energy of $E = 2$ (a) and 100 (b) mJ.

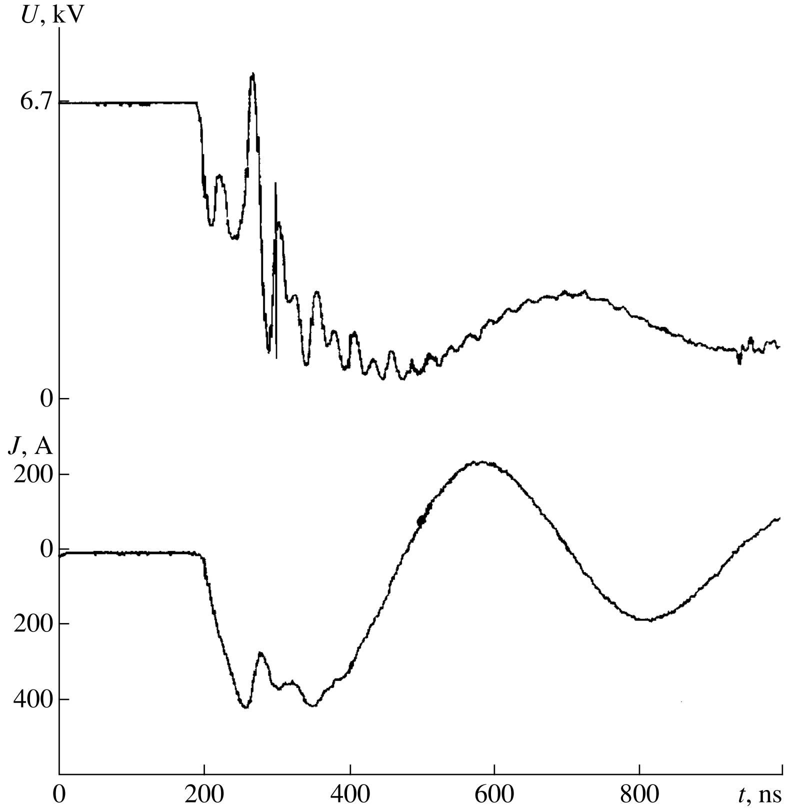

Fig. 3. Waveforms of the discharge current J and voltage U. The laser pulse duration and energy are $\tau = 27$ ps and $E = 2$ mJ, respectively; the laser intensity on the cathode is $\sim 2 \times 10^{11}$ W/cm^2; and the interelectrode gap length is $d = 2$ mm.

plasma-forming laser pulse of $E = 2$ mJ is the generation of X-ray bursts and jumps in the anode potential in the second stage of the discharge. This indicates the onset of instability. A decrease in the contrast of the X-ray characteristic lines emitted by the source in this stage of the discharge is explained by the unsteady behavior of the anode potential and the generation of electron beams in a wide energy range. The presence of X-ray photons with energies exceeding that corresponding to the initial discharge voltage is related to the onset of instabilities (see [3, 6–11] for details). At present, the most developed hypotheses of the anomalous particle acceleration in a vacuum discharge are (i) the formation of a deep nonsteady potential near the front of the cathode plume, due to delivering the cathode material into the discharge gap via the ecton mechanism [3, 9], and (ii) the pinching of the plasma jet at high growth rates of the discharge current [8]. In [12], we studied the spatial distribution of the X-ray intensity. It was shown that there are no extra sources of X-rays with photon energies higher than 1 keV in the interelectrode gap. This fact indicates that, under our experimental conditions, the discharge plasma is not pinched as a whole, but it splits into filaments whose temperature can be as high as several hundred electronvolts. These filaments can act as sources of electrons with energies higher than those corresponding to the initial discharge voltage. The experimental studies of the dynamics of X-ray emission from the discharge plasma in the photon energy range ≤1 keV, as well as the spectral measurements of the anode emission in the photon energy range >20 keV, will be described in a separate paper.

The studies of various operating regimes showed that two types of time-separated instabilities may occur in the source. The first of them occurs in the initial stage of the discharge (Fig. 2a). The second one develops in the stage of intense electron emission. This type of instability is accompanied by sharp breaks of the discharge current and jumps in the discharge voltage. In our experiments, the second type of instability was clearly observed at an initial discharge voltage of 6.7 kV. The waveforms of the discharge current and voltage for this case are shown in Fig. 3. The interelectrode distance was 2 mm, the electric circuit inductance was 0.8 μH, and the current at the instant of the break was 410 A. We did not measure the X-ray yield because, according to [1], it is low at voltages of <10 kV. It can be seen from the waveforms that the first type of instability hardly occurs at low initial voltages. In our opinion, the onset of the second kind of instability is related to plasma breaking, which leads to the

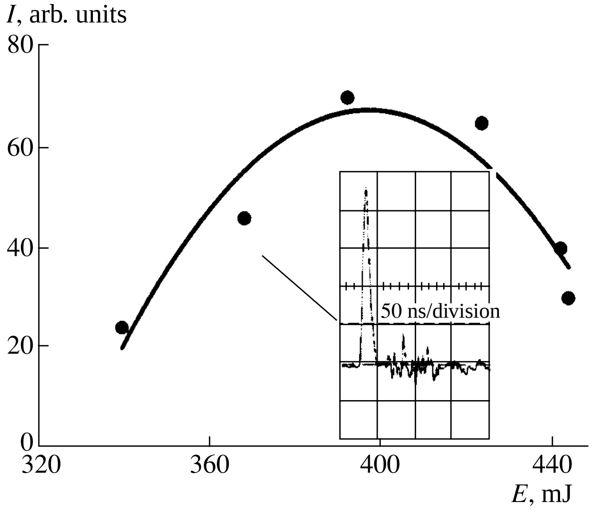

Fig. 4. X-ray intensity as a function of the energy of a 27-ps laser pulse for $U = 20$ kV and $d = 10$ mm. The inset shows the waveform of the X-ray pulse at a laser pulse energy of 370 mJ.

emergence of a double electric layer [13–15] near the anode and the generation of an additional e.m.f. accelerating the electron flow.

As was mentioned above, discharge instabilities arise when the cathode plasma is produced by nanosecond laser pulses. In connection with this, we studied the source operation at different intensities of the laser beam at the cathode. At a fixed interelectrode distance of $d = 4$ mm and an initial discharge voltage of $U = 20$ kV, the vacuum discharge was triggered by a 100-mJ laser pulse of either picosecond or nanosecond duration with a focal spot intensity of $P = 10^{13}$ or 1.6×10^{10} W/cm^2, respectively. In both cases, the increase in the laser pulse energy was not accompanied by the onset of discharge instabilities. This indicates that it is the energy deposited by laser radiation that determines the stability of the diode discharge. As for the X-ray pulse duration, it depended on the laser intensity on the cathode. In the first case, the X-ray pulse duration was 18 ns; in the second case, it was 27 ns. Thus, an increase in the rate of laser plasma expansion decreases the duration of the generated X-ray pulse. At reduced energies of the nanosecond laser pulse, the first type of discharge instability was observed. However, it was not so pronounced as in Fig. 2a. An interesting feature in the time evolution of the X-ray intensity in the laser energy range 10–50 mJ is its fine structure, which could be due to the instability of the sharp boundary of the cathode plasma. Theoretical studies [16, 17] showed that, in this case, the plasma emitter can split into jets; this is related to the onset of perturbations propagating along the emitter surface and decaying on both sides from it. On the whole, the results obtained in the case of a nanosecond plasma-forming laser pulse allow us to suggest that an increase in the pulse duration stabilizes the discharge.

In [1], the intensity, duration, and contrast of X-ray characteristic emission were optimized by varying the interelectrode distance *d*, the laser intensity *P* on the cathode, and the initial discharge voltage *U*. The results of the above measurements show that the set of the parameters *P*, *d*, and *U* should be supplemented with the laser pulse energy. At a given initial discharge voltage, the intensity of the X-ray pulse is determined by the nonlinear dependences $I_{d\,=\,\mathrm{const}} = f(P)$ and $I_{P\,=\,\mathrm{const}} = f(d)$, which have pronounced maxima. Hence, in choosing the source operation regime, one should keep in mind that an increase in the laser pulse energy (with the aim of suppressing discharge instabilities) should be accompanied by an increase in the interelectrode distance. Figure 4 shows the X-ray intensity as a function of the energy of a picosecond laser pulse at $d = 10$ mm. In this energy range, the duration of the X-ray pulse is 10 ns (see inset in Fig. 4) and the spectral radiance at $E = 390$ mJ is $\leq 10^{21}$ photon/(cm^2 s sr keV).

4. CONCLUSIONS

Based on the experimental data obtained, we can make the following recommendations for the operating regime of a vacuum-diode X-ray source with a laser plasma cathode: In order to achieve the characteristic X-ray emission consisting of contrast K-lines of the anode material in pulses with a duration of $\tau \sim 10$ ns and a total photon number of $N \sim 10^{11}$, it is necessary

(i) to ensure a constant anode voltage in the initial phase of the discharge by keeping the total charge of the electron beam emitted from the laser plasma much lower than the charge accumulated in the storage capacitor,

(ii) to suppress discharge instabilities by creating a plasma emitter of electrons with the help of a picosecond laser pulse with an intensity on the cathode of $P \geq 10^{13}$ W/cm^2 and energy of $E \geq 100$ mJ, and

(iii) to choose an optimum interelectrode distance (in the regime with suppressed instabilities) corresponding to the maximum intensity of the X-ray source.

ACKNOWLEDGMENTS

This study was supported in part by the Russian Foundation for Basic Research (project nos. 03-02-16366, 01-02-17589, and 02-02-16966), the Russian Federal Program Integratsiya (contract no. I-0651), and the Indian–Russian ILTP Collaboration Program.

REFERENCES

1. Yu. V. Korobkin, I. V. Romanov, A. A. Rupasov, *et al.*, Phys. Scr. **60**, 76 (1999).

2. A. A. Erokhin, Yu. V. Korobkin, I. V. Romanov, *et al.*, Kratk. Soobshch. Fiz., No. 1, 30 (2000).
3. G. A. Mesyats, *Ectons in Vacuum Discharge* (Nauka, Moscow, 2000), p. 206.
4. N. N. Koval’, Yu. D. Korolev, V. B. Ponomarev, *et al.*, Fiz. Plazmy **15**, 747 (1989) [Sov. J. Plasma Phys. **15**, 432 (1989)].
5. A. V. Bolotov, A. V. Kozyrev, A. V. Kolesnikov, *et al.*, Zh. Tekh. Fiz. **61** (1), 40 (1991) [Sov. Phys. Tech. Phys. **36**, 23 (1991)].
6. N. Vogel, Pis’ma Zh. Éksp. Teor. Fiz. **67**, 622 (1998) [JETP Lett. **67**, 647 (1998)].
7. N. Vogel and V. A. Skvortsov, IEEE Trans. Plasma Sci. **25**, 557 (1997).
8. S. P. Gorbunov, V. I. Krasov, and V. L. Paperny, J. Phys. D **30**, 122 (1997).
9. S. A. Barengol’ts, G. A. Mesyats, and É. A. Perel’shteĭn, Zh. Éksp. Teor. Fiz. **118**, 1358 (2000) [JETP **91**, 1176 (2000)].
10. K. V. Suladze and A. A. Plyutto, Zh. Tekh. Fiz. **37**, 72 (1967) [Sov. Phys. Tech. Phys. **12**, 48 (1967)].
11. E. D. Korop and A. A. Plyutto, Zh. Tekh. Fiz. **40**, 2534 (1970) [Sov. Phys. Tech. Phys. **15**, 1986 (1970)].
12. A. A. Erokhin, A. A. Kishinets, Yu. V. Korobkin, *et al.*, Zh. Éksp. Teor. Fiz. **119**, 1151 (2001) [JETP **92**, 998 (2001)].
13. E. I. Lutsenko, N. D. Sereda, and V. D. Dimitrova, Fiz. Plazmy **10**, 151 (1984) [Sov. J. Plasma Phys. **10**, 87 (1984)].
14. K. V. Suladze, B. A. Tskhadaya, and A. A. Plyutto, Pis’ma Zh. Éksp. Teor. Fiz. **10**, 282 (1969) [JETP Lett. **10**, 180 (1969)].
15. N. V. Filippov, Fiz. Plazmy **9**, 25 (1983) [Sov. J. Plasma Phys. **9**, 14 (1983)].
16. O. V. Batishchev and Yu. S. Sigov, Preprint No. 87 (Institute of Applied Mathematics, USSR Acad. Sci., Moscow, 1987).
17. V. P. Sidorov, S. Yu. Udovichenko, and P. E. Belensov, Zh. Tekh. Fiz. **61** (7), 37 (1991) [Sov. Phys. Tech. Phys. **36**, 741 (1991)].

Translated by N.N. Ustinovskiĭ

Plasma Physics Reports, Vol. 30, No. 3, 2004, pp. 241–248. Translated from Fizika Plazmy, Vol. 30, No. 3, 2004, pp. 269–276.
Original Russian Text Copyright © 2004 by Zvonkov, Skovoroda.

PLASMA INSTABILITY

Stability of a Quasi-Flute Mode under the Bernstein–Kadomtsev Condition in a Toroidal Confinement System

A. V. Zvonkov and A. A. Skovoroda

Institute of Nuclear Fusion, Russian Research Centre Kurchatov Institute, pl. Kurchatova 1, Moscow, 123182 Russia

Received February 5, 2003; in final form, September 17, 2003

Abstract—It is shown that the growth rate of the MHD instability in toroidal configurations is slower in a situation in which the Bernstein–Kadomtsev condition is satisfied while the Mercier stability criterion is not. Under the Bernstein–Kadomtsev condition, Alfvénic Mercier modes are not excited, but quasi-flute acoustic Mercier modes develop instead. In confinement systems with closed magnetic field lines, the Bernstein–Kadomtsev condition ensures MHD stability; however, a small rotational transform produced by magnetic perturbations can give rise to a quasi-flute acoustic instability whose growth rate is proportional to the perturbation amplitude, in which case the fastest growing oscillations are those with the shortest wavelengths. *© 2004 MAIK “Nauka/Interperiodica”.*

1. INTRODUCTION

For flute oscillations (those with a zero longitudinal wavenumber, $k_{\|} = 0$) to be stable in toroidal confinement systems with closed magnetic field lines and with a zero rotational transform, it is necessary and sufficient to satisfy the following condition [1, 2], which will be referred below to as the Bernstein–Kadomtsev (BK) condition:

$$-\left(\oint B dl\right)\frac{(\nabla U)^2}{U^2} < \nabla p \cdot \nabla U < \frac{\gamma_0 p(\nabla U)^2}{|U|}. \qquad (1)$$

Here, p is the equilibrium plasma pressure, γ_0 is the adiabatic index, and $U = -\oint\frac{dl}{B}$ = const is the label of the equilibrium magnetic surface. For configurations with a magnetic well ($\nabla U > 0$), the right-hand inequality in BK condition (1) holds for a decreasing plasma pressure profile ($\nabla p < 0$), so that the problem is to satisfy the left-hand inequality. Otherwise, for systems with a magnetic hill ($\nabla U < 0$), the left-hand inequality holds, so that the problem is to satisfy the right-hand inequality. There exists a neutrally stable decreasing pressure profile, $p \sim U^{-\gamma_0}$, which reduces the right-hand inequality in condition (1) to an identity. It is this possibility of achieving MHD stabilization by means of plasma compressibility that is utilized in some advanced systems [3–6] and is the main subject of our study.

The assumption that the magnetic field lines are closed over the entire volume of a confinement system is a theoretical idealization. In a real situation, the field lines are unclosed because of the possible magnetic field perturbations. Thus, in a confinement system in which the magnetic field lines are closed poloidally [3–5], they are made unclosed by the toroidal magnetic field, and, in a confinement system in which the magnetic field lines are closed toroidally [6], they are made unclosed by the vertical magnetic field. On the other hand, the poloidal drift motion of charged particles ensures that the surfaces of constant plasma pressure are topologically stable. That is why, at a finite plasma pressure, the topological stability of a magnetic configuration with a vertical perturbation of the magnetic field can be provided by the plasma currents that produce a small rotational transform. That this is so is confirmed by experiments [7].

In analyzing the stability of confinement systems with closed magnetic field lines, it is logical to consider how it is affected by a small perturbation that makes the lines slightly unclosed. For toroidal systems with a nonzero rotational transform, the Mercier criterion is known to serve as a necessary condition for the stability of local ideal modes (those having $k_{\|} = 0$ at rational magnetic surfaces). Since the Mercier criterion does not contain any compressibility term, it predicts that a system with a small shear of the magnetic field lines and without a magnetic well is unstable. Mikhaĭlovskiĭ and Skovoroda [8] showed that taking plasma compressibility into account can substantially change the growth rate of the MHD instability that develops when the Mercier criterion is violated. Under an inequality similar to the right-hand inequality in condition (1) (see the Appendix), the instability grows not at the rate of development of Alfvén modes ($\gamma \sim c_A/L_s$) but at the rate of development of acoustic modes ($\gamma \sim c_s/L_s$), which is substantially slower at low plasma pressures (at low β). Here, $c_A = B/\sqrt{\rho}$ is the Alfvén speed, $c_s = \sqrt{\gamma_0 p/\rho}$ is the acoustic speed, L_s is the shear length, and ρ is the mass density. It is in this sense that Mikhaĭlovskiĭ and Skovoroda [9] spoke of “the suppression of flute Alfvén perturbations and the growth of quasi-flute acoustic perturbations.” Note that similar conditions were considered by Kadomtsev [10] and Solov’ev [11].

Since it is possible that, in the confinement systems under discussion (namely, those in which MHD stability is provided by plasma compressibility), a small rotational transform can be produced, there are two question that have to be answered: whether “acoustic” oscillations are stable under small perturbations that make the magnetic field lines slightly unclosed and what is their expected growth rate. Note that, when the degree to which the Mercier criterion is violated is small, the growth rate is exponentially slow [8, 12, 13].

To illustrate the effect of small perturbations that make toroidally closed magnetic field lines unclosed, we will consider a straight cylinder with identified ends, $B_\varphi \ll B_z$. The effect of the perturbations that make poloidally closed field lines unclosed will be considered using a cylinder with $B_z \ll B_\varphi$ as an example. In the Appendix, it is shown that the results obtained are also valid in toroidal geometry.

2. QUASI-FLUTE ACOUSTIC INSTABILITY

The familiar exact equation for small radial displacements in cylinder geometry [12, 14, 15] can be written in the form

$$\frac{C_{12}}{r}\frac{d}{dr}\left(\frac{r^3\rho(\gamma^2+k_\parallel^2c_A^2)}{C_{12}}\frac{d\xi}{dr}\right)-W\xi = 0,$$

$$W = \rho(\gamma^2+k_\parallel^2c_A^2)(m^2-1+k_z^2r^2-\chi r^2)$$

$$+2rk_z^2\frac{dp}{dr}+\frac{4rk_z^2\rho c_s^2}{R}\frac{\gamma^2}{\gamma^2(1+\beta)+k_\parallel^2c_s^2}-\gamma^2 r\frac{d\rho}{dr}$$

$$-2B_\varphi\frac{d(rB_\varphi\chi)}{dr}+\frac{r}{C_{12}}\frac{dC_{12}}{dr}(\rho(\gamma^2+k_\parallel^2c_A^2)-C_{11}), \qquad (2)$$

$$C_{12} = -m^2-k_z^2r^2+r^2\chi,$$

$$C_{11} = 2\left(\frac{mB_\varphi}{r}k_\parallel B-B_\varphi^2\chi\right),$$

$$\chi = -\frac{\gamma^4}{c_A^2(\gamma^2(1+\beta)+k_\parallel^2c_s^2)},\quad \beta = \frac{c_s^2}{c_A^2},\quad \frac{1}{R} = \frac{B_\varphi^2}{rB^2},$$

where R^{-1} is the magnetic field line curvature, k_z is the wavenumber along the cylinder axis, m is the azimuthal mode number, and $B_{z,\varphi}$ are the magnetic field components. In this representation, the plasma compressibility is explicitly accounted for by the third term in the expression for W.

As an example of a simple model of a confinement system with toroidally closed magnetic field lines, we consider a straight cylinder with identified ends, $B_\varphi \ll B_z$. We are interested in the case $\beta \ll 1$, $k_z^2r^2 \ll m^2$, $\gamma^2 \ll c_A^2/r^2$, and $m \gg 1$, in which we have $C_{12} \sim -m^2$ and $\chi r^2 \ll 1$ and Eq. (2) reduces to

$$\frac{1}{r}(r^3\rho(\gamma^2+k_\parallel^2c_A^2)\xi')'$$
$$-\xi\left(\rho(\gamma^2+k_\parallel^2c_A^2)m^2+2rk_z^2p'+\frac{4rk_z^2\gamma_0p\gamma^2}{R(\gamma^2+k_\parallel^2c_s^2)}\right) = 0, \qquad (3)$$

where the prime denotes the derivative with respect to r and the term with the derivative of the density is omitted for simplicity.

We multiply Eq. (3) by $r\xi(\gamma^2+k_\parallel^2c_s^2)$ and integrate the resulting equation over the radius with allowance for the boundary condition $\xi(a) = 0$ to obtain the following quadratic equation for γ^2:

$$S\gamma^4+T\gamma^2+P = 0, \qquad (4)$$

where

$$S = \int_0^a\rho(r^2\xi'^2+m^2\xi^2)rdr,$$

$$T = \int_0^a(k_\parallel^2B^2(r^2\xi'^2+m^2\xi^2)$$
$$+2rk_z^2(p'+2\gamma_0p/R)\xi^2)rdr,$$

$$P = \int_0^a(rk_\parallel^2c_s^2(k_\parallel^2B^2(r^2\xi'^2+m^2\xi^2)+2\xi^2rk_z^2p')$$
$$-\frac{1}{2}\xi^2(r^3k_\parallel^2B^2(k_\parallel^2c_s^2)')')dr.$$

To determine the growth rate, we must know the eigenfunction ξ. At this point, however, some qualitative knowledge on the subject can be acquired from Eq. (4). Since the ratio $\beta = c_s^2/c_A^2$ is small, the two roots of this equation differ greatly in magnitude, in which case the larger (“Alfvénic”) root is determined by the equality $\gamma^2 = -T/S$, while the smaller (“acoustic”) root is given by $\gamma^2 = -P/T$. For large values of $k_\parallel^2$, all coefficients in Eq. (4) are positive and both roots are negative, which indicates that the plasma is stable. For small values of $k_\parallel^2$, the coefficient P can become negative, which indicates that one of the roots is unstable. Which of the two roots (Alfvénic or acoustic) will be unstable is determined by BK condition (1). If this condition is satisfied, then it is the smaller root that corresponds to the instability growing at the rate of acoustic perturbations.

In a shearless configuration with closed magnetic field lines, perturbations with $k_\parallel(r) \equiv 0$ (a flute mode) can exist, in which case one of the roots of Eq. (4)

equals zero and the other is stable under BK condition (1). Since solution (3) should be periodic along closed field lines, the longitudinal wavenumber $k_\parallel$ can take on only discrete values. Then, for a sufficiently low pressure, $\beta < k^2_{\parallel\min} m^2 a/k_z^2 r = k^2_{\parallel\min} aR$ (where $k_{\parallel\min}$ is the minimum nonzero value of $k_\parallel$), the coefficient P is positive and the plasma is stable. At pressures above a certain limiting pressure, modes can develop that grow at the rate $\gamma \sim \sqrt{\beta} c_s/\sqrt{aR}$, which is slower than the growth rate of the conventional flute instability because it contains the factor $\sqrt{\beta}$. For actual confinement systems, in which the magnetic field is nonuniform and the magnetic field lines are curved, the limiting stable pressure is defined as the minimum pressure for which the equation for ballooning modes with $k_\parallel \neq 0$ can have a solution [1]; i.e., we can say that it is again determined by the value $k_{\parallel\min}$.

Hence, if the stability of the flute modes ($k_\parallel = 0$) is ensured by the plasma compressibility, then, at sufficiently low pressures, the plasma will be stable against the modes with $k_\parallel \neq 0$ because of the discreteness of the allowed $k_\parallel$ values; this is a consequence of the field-line closure. In a configuration with a sheared magnetic field with unclosed lines, the situation is radically different: in a plasma, there are rational magnetic surfaces at which $k_\parallel(r_0) = \dfrac{k_z B_z + m B_\varphi/r_0}{B} = 0$ and near which, generally speaking, local modes with small longitudinal wavenumbers $k_\parallel$ can be excited. To analyze the possible instability of the local modes, it is necessary to solve a problem that takes into account the radial structure of the mode.

In order to consider the local modes in a sheared magnetic field, we use the following local approximation of the longitudinal wavenumber near the rational surface: $k_\parallel = -x/L_s$, where $x = m(r - r_0)/r$ and the shear length L_s is given by the relationship $L_s^{-1} = [(B_\varphi^2/rBB_z)(rB_z/B_\varphi)']_{r = r_0}$. With this approximation, we arrive at the equation

$$\frac{d}{dx}\left(x^2\frac{d\xi}{dx}\right) - x^2\xi + x_A^2\frac{d^2\xi}{dx^2} - \left(U_0 + \frac{U_c}{1 + x^2/x_s^2} + x_A^2\right)\xi = 0, \tag{5}$$

where $U_0 = 2L_s^2 p'/R\rho c_A^2$, $U_c = 4L_s^2 c_s^2/R^2 c_A^2$, $x_A = \gamma L_s/c_A$, and $x_s = \gamma L_s/c_s$. This equation was analyzed in detail in [8]. Note that, with the corresponding redefinitions, Eq. (5) is also valid in toroidal geometry (see [8–10] and the Appendix). The results of the analysis of Eq. (5) that was carried out in [8] may be briefly summarized as follows: If the Mercier criterion $U_0 + 1/4 > 0$ is satisfied, then the configuration is stable. If $U_0 + 1/4 < 0$ and if the BK condition is satisfied, then a quasi-flute acoustic instability is excited and grows at a rate that is proportional to the acoustic speed rather than to the Alfvén speed.

Here, we give merely a qualitative explanation of why local unstable quasi-flute modes are excited near the rational magnetic surfaces. At this point, we consider localized perturbations with $m \gg 1$ without making any assumptions about the dependence $k_\parallel = k_\parallel(x)$. We introduce the effective wavenumbers through the relationships $k_A^2 = \gamma^2/c_A^2$, $k_s^2 = \gamma^2/c_s^2$, $k_W^2 = -2p'/R\rho c_A^2$, and $k_C^2 = 4c_s^2/R^2 c_A^2$ and also the parameter $Q = k_C^2/k_W^2 - 1$, which characterizes the range where the BK condition is satisfied ($Q \geq 0$). We nondimensionalize the wavenumbers by dividing by k_W to reduce Eq. (3) to

$$\frac{d}{dx}(k_\parallel^2 + \beta k_s^2)\frac{d\xi}{dx} - \left(k_\parallel^2 + \beta k_s^2 + \frac{Qk_s^2 - k_\parallel^2}{k_s^2 + k_\parallel^2}\right)\xi = 0, \tag{6}$$

where $x = m(r - r_0)/r_0$. By making the replacement $\zeta = (k_\parallel^2 + \beta k_s^2)^{1/2}\xi$, we further simplify this equation to

$$\frac{d^2\zeta}{dx^2} - f(x)\zeta = 0, \tag{7}$$

$$f(k_\parallel(x)) = 1 + \frac{Qk_s^2 - k_\parallel^2}{(k_s^2 + k_\parallel^2)(\beta k_s^2 + k_\parallel^2)} + \frac{1}{\sqrt{\beta k_s^2 + k_\parallel^2}}\frac{d^2 k_\parallel}{dx^2}. \tag{8}$$

For $k_\parallel \longrightarrow 0$, the absolute value of function (8) is large and the sign of the function is the same as the sign of the parameter Q: $f(0) \sim \dfrac{Q}{\beta k_s^2}$. As $k_\parallel \longrightarrow \infty$, the function approaches unity. In addition, if we ignore the last term in expression (8), we then find that, for $Q > 0$, the function is equal to unity, $f = 1$, at $k_{\parallel 1}^2 = Qk_s^2$ and has a minimum at $k_{\parallel 2}^2 = k_s^2(Q + \sqrt{(\beta + Q)(Q + 1)})$.

Figure 1 shows the dependence of the function $(f - 1)k_s^2$ on $k_\parallel^2/k_s^2$ for $\beta = 0.05$ and for three different values of the parameter Q: 0.1, 0, and –0.1. We can see that, for $Q < 0$ and for a sufficiently low plasma pressure, there is a deep potential well at $k_\parallel = 0$, which indicates that there may be quasi-flute Alfvénic Mercier modes. As k_s^2 approaches zero, the condition that there be no solutions localized near a zero value of the longitudinal wavenumber coincides with the Suydam stabil-

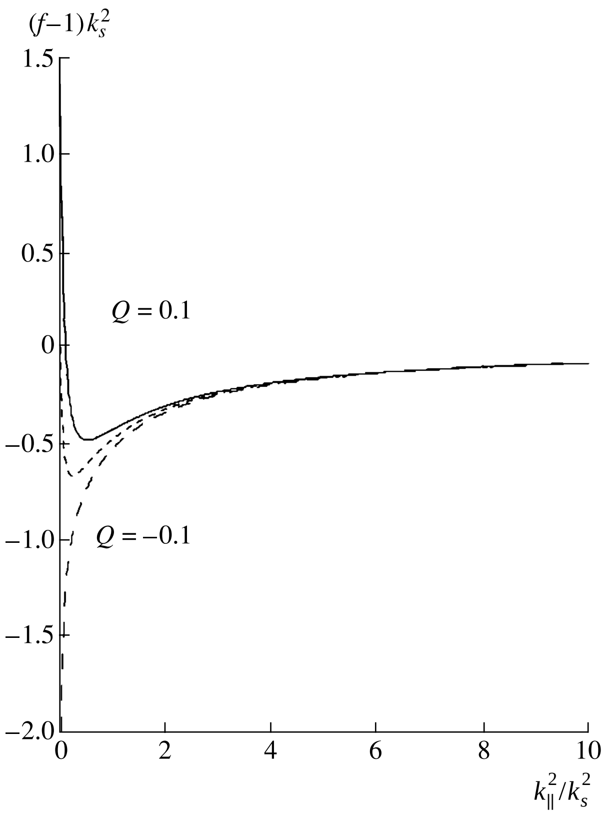

Fig. 1. Dependence of $(f-1)k_s^2$ on $k_\parallel^2/k_s^2$ for $Q = -0.1$ (the Bernstein–Kadomtsev condition is violated), $Q = 0$, and $Q = 0.1$ (the Bernstein–Kadomtsev condition is satisfied).

ity criterion. In the notation adopted here, this criterion has the form

$$k_\parallel'^2/4 > 1. \tag{9}$$

For $Q > 0$, the potential has a minimum at $k_\parallel \neq 0$, which indicates that there may be quasi-flute acoustic Mercier modes [8]. In order to show that these modes can actually be excited, we convert Eq. (7) to the form of the Schrödinger equation:

$$\frac{d^2\zeta}{dx^2} + (E - U(x))\zeta = 0,$$

where the "energy" $E = -f(k_{\parallel 2})$ and the "potential" $U = f(k_\parallel) - f(k_{\parallel 2})$ are given by the formulas

$$E = \frac{1}{k_s^2(\sqrt{1+Q}+\sqrt{\beta+Q})^2} - 1,$$

$$U = \frac{1}{k_s^2(\sqrt{1+Q}+\sqrt{\beta+Q})^2} + \frac{Qk_s^2 - k_\parallel^2}{(k_s^2+k_\parallel^2)(\beta k_s^2 + k_\parallel^2)}.$$

The potential energy so defined is everywhere positive except at the bottom of the well, where it is equal to zero. The walls of the well are of different heights. From the side of a zero value of the longitudinal wavenumber ($k_\parallel = 0$), the height of the barrier is $U_0 = \frac{1}{k_s^2}\left(\frac{1}{(\sqrt{1+Q}+\sqrt{\beta+Q})^2} + \frac{Q}{\beta}\right)$, and, at $k_\parallel \longrightarrow \infty$, the height of the barrier is $U_1 = \frac{1}{k_s^2(\sqrt{1+Q}+\sqrt{\beta+Q})^2}$. The width of the well can be estimated to be $2\sqrt{k_{\parallel 2}^2 - k_{\parallel 1}^2}$. Assuming now a linear dependence $k_\parallel = k_\parallel' x$, we obtain the following formula for the spatial width of the potential well:

$$\Delta x = 2\frac{k_s}{k_\parallel'}((\beta+Q)(Q+1))^{1/4}.$$

It is well known [16] that, in order for an asymmetric potential well (at small β values, the left potential barrier is much higher than the right barrier, $U_0 \gg U_1$) to have no discrete energy levels, it is necessary to satisfy the condition $\Delta x\sqrt{U_1} < 1$, or, equivalently,

$$k_\parallel'^2/4 > \frac{\sqrt{\beta+Q}\sqrt{1+Q}}{(\sqrt{1+Q}+\sqrt{\beta+Q})^2}.$$

For $Q \sim 1$, the right-hand side of this condition coincides in order of magnitude with the right-hand side of Suydam criterion (9). Under the opposite condition, the well may have positive-energy levels, $E > 0$, which imposes an upper limit on the growth rate of the quasi-flute acoustic instability:

$$\gamma < \frac{c_s k_W}{\sqrt{1+Q}+\sqrt{\beta+Q}}. \tag{10}$$

This growth rate is $1/\sqrt{\beta}$ times slower than the characteristic growth rate of the quasi-flute Alfvén instability. Note that relationship (10) does not contain shear, so that the question arises of how the instability growth rate behaves when the shear approaches zero.

To answer this question, we first consider numerical solutions to the equations presented in our study. Figure 2 shows the characteristic eigenfunctions of the equation obtained in the Appendix under conditions corresponding to Mercier instability. As may be seen, the calculations confirm the qualitative pattern of the instability described above. When the BK condition is not satisfied, the eigenfunction has a maximum at the point $x = 0$ ($k_\parallel = 0$) and the solution is seen to be highly localized in space ($x \sim 1$). Under the BK condition, the eigenfunction has a maximum at a point other than the point $x = 0$ (i.e., at $k_\parallel \neq 0$). Figure 3 shows the eigenfunction for a very small shear. We can see that, as the shear decreases, the eigenfunction describing acoustic modes becomes wider ($x \geq 1$) and the region where the perturbations are localized becomes increasingly broader.

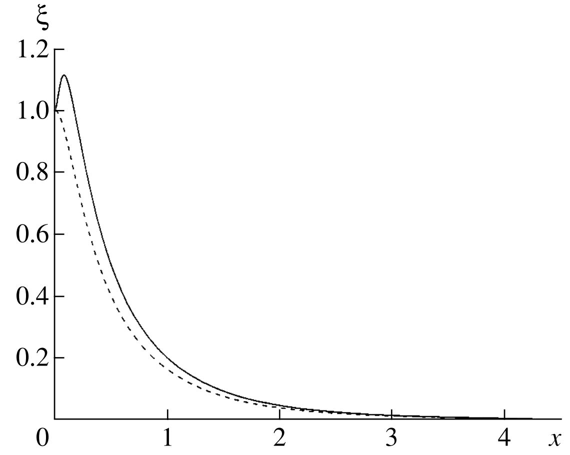

Fig. 2. Eigenfunctions of Eq. (A.1) for $H = 0.1$, $K = 1$, and $U_0 = -1$. The dashed curve is for $U_c = 0.5$ (the Bernstein–Kadomtsev condition is violated), while the solid curve is for $U_c = 1.5$ (the Bernstein–Kadomtsev condition is satisfied).

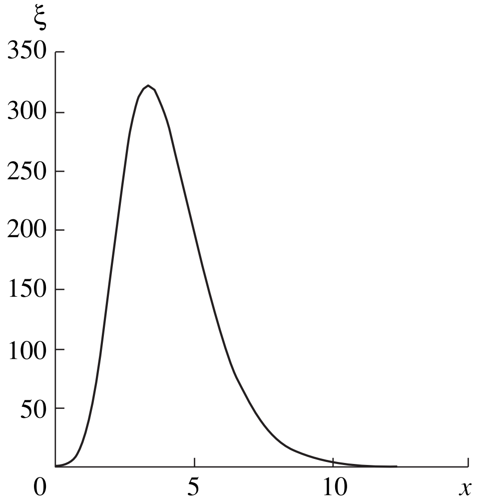

Fig. 3. Eigenfunction of Eq. (A.1) for $H = 0$, $K = 0.1$, $U_0 = -40$, and $U_c = 80$ (the Bernstein–Kadomtsev condition is satisfied). The eigenvalue is $x_s = 2.06$, which corresponds to $\xi(x = 0) = 1$.

3. GROWTH RATE OF THE QUASI-FLUTE ACOUSTIC INSTABILITY IN THE LIMIT OF VANISHING SHEAR

As a model of a confinement system with poloidally closed magnetic field lines, we use a straight cylinder in which the magnetic field has the only nonzero component B_φ. In this case, the effect of perturbations that make the field lines unclosed is modeled by a weak uniform magnetic field $B_z \ll B_\varphi$. We consider a low-pressure plasma, $\beta \ll 1$, and a mode with a zero azimuthal number, $m = 0$ (at $B_z = 0$, the longitudinal wavenumber may equal zero, $k_\parallel = 0$, only for $m = 0$), and assume that the BK condition $p' + 2\gamma_0 p/r > 0$ is satisfied. Since the growth rate of the acoustic instability is estimated to be $\gamma^2 \sim k_\parallel^2 c_s^2 \ll k_\parallel^2 c_A^2$, we can assume that $k_z^2 \gg \chi$ to obtain $C_{12} \sim -k_z^2 r^2$ and $C_{11} \sim 0$. This allows us to rewrite Eq. (2) as

$$r(rk_\parallel^2 B^2\xi')' - \xi\left(k_\parallel^2 B^2(1 + k_z^2 r^2) + 2rk_z^2 p' + \frac{4k_z^2\gamma_0 p\gamma^2}{\gamma^2 + k_\parallel^2 c_s^2}\right) = 0. \tag{11}$$

Since $k_\parallel^2 = k_z^2 B_z^2/B^2$ and $k_z \neq 0$, we divide Eq. (11) by k_z^2 and arrive at the equation

$$B_z^2 r(r\xi')' - \xi\left(B_z^2(1 + k_z^2 r^2) + 2rp' + \frac{4\gamma_0 p\gamma^2}{\gamma^2 + k_\parallel^2 c_s^2}\right) = 0. \tag{12}$$

For $\gamma = 0$, this equation concides with Eq. (8.6) in [17]. Equation (12) yields the well-known result: at a sufficiently strong field B_z, the mode in question is stabilized. However, we are interested here in a configuration with a very weak field B_z (that for which instability is possible). Introducing the new variable $\zeta = \sqrt{r}\xi$, we reduce Eq. (12) to the standard form

$$B_z^2\zeta'' - F\zeta = 0,$$

where $F = \frac{2}{r}\left(p' + \frac{2\gamma_0 p\gamma^2}{r(\gamma^2 + k_\parallel^2 c_s^2)}\right) + B_z^2\frac{k_z^2 r^2 + 3/4}{r^2}$. If the quantity F vanishes at a surface of radius r_0 inside the plasma, then, for a weak field B_z, this equation has a solution with zero boundary conditions (specifically, the solution that oscillates rapidly on one side away from the surface of radius r_0 and decreases exponentially on the other side away from the surface). From the condition $F(r_0) = 0$ we obtain the relationship

$$\gamma^2 = -k_z^2 c_s^2 \frac{B_z^2}{B^2}\frac{2r_0 p' + B_z^2\left(k_z^2 r_0^2 + \frac{3}{4}\right)}{2r_0 p' + 4\gamma_0 p + B_z^2\left(k_z^2 r_0^2 + \frac{3}{4}\right)}.$$

Under the BK condition, the denominator is positive, so that the condition $F(r_0) = 0$ can be satisfied for unstable oscillations ($\gamma^2 > 0$), provided that the numerator is negative,

$$2r_0 p' + B_z^2\left(k_z^2 r_0^2 + \frac{3}{4}\right) < 0. \tag{13}$$

Such a surface always exists for a sufficiently weak field B_z, although, at $B_z = 0$, the growth rate equals zero.

The upper limit on the growth rate can be estimated by multiplying Eq. (12) by $\xi(\gamma^2 + k_\parallel^2 c_s^2)/r$ and integrating over the entire plasma radius. Using the expression for the growth rate

$$\gamma^2 = -\frac{P}{T}, \qquad (14)$$

where

$$T = \int_0^a \left(rB_z^2\left(\xi'^2 + \frac{1+k_z^2r^2}{r^2}\xi^2\right) + 2\xi^2\left(p' + 2\frac{\gamma_0 p}{r}\right)\right)dr,$$

$$P = \int_0^a \left(\xi^2 k_\parallel^2 c_s^2\left(2p' + \frac{1+k_z^2r^2}{r}B_z^2\right) + rB_z^2k_\parallel^2c_s^2\xi'^2 - \frac{1}{2}\xi^2B_z^2(r(k_\parallel^2c_s^2)')'\right)dr,$$

we arrive at the following estimate for the upper limit at a fixed wavenumber k_z:

$$\gamma^2 \sim -k_z^2B_z^2\int_0^a \xi^2\frac{c_s^2}{B^2}p'dr\Big/\int_0^a\xi^2\left(p'+2\frac{\gamma_0 p}{r}\right)dr.$$

We can see that the growth rate approaches zero as B_z approaches zero and that the growth rate increases with k_z. However, an increase in k_zB_z is restricted by the stabilization condition $k_z^2B_z^2 \sim -p'/r$ [see condition (13)], which leads to the maximum possible growth rate (10).

For $m \neq 0$ and $B_z = 0$, oscillations with large longitudinal wavenumbers $k_\parallel = m/r$ are stabilized at low β values. This conclusion, which also remains valid for a weak field B_z satisfying the condition $k_zB_z/B_\varphi \ll m/r$, fails to hold only for large k_z values such that $k_zB_z/B_\varphi \sim m/r$, i.e., $k_\parallel \sim 0$. In this case, using the inequality $k_z^2r^2 \gg m^2$, we convert Eq. (2) to the form

$$(rk_\parallel^2B^2\xi')' - k_z^2 r\left(k_\parallel^2B^2 + \frac{2}{r}p' + \frac{4\gamma_0 p}{r^2}\frac{\gamma^2}{\gamma^2+k_\parallel^2c_s^2}\right)\xi = 0. \qquad (15)$$

In order to estimate the maximum growth rate, we multiply Eq. (15) by $\xi(\gamma^2 + k_\parallel^2 c_s^2)$ and integrate over the entire plasma radius. As a result, we arrive at growth rate (14) in which the coefficients are given by the formulas

$$T = \int_0^a \left(rk_\parallel^2B^2(\xi'^2 + k_z^2\xi^2) + 2k_z^2\xi^2\left(p' + 2\frac{\gamma_0 p}{r}\right)\right)dr,$$

$$P = \int_0^a \left(k_z^2 r\xi^2k_\parallel^2c_s^2\left(\frac{2}{r}p' + k_\parallel^2B^2\right) + rk_\parallel^4B^2c_s^2\xi'^2 - \frac{1}{2}\xi^2(rk_\parallel^2B^2(k_\parallel^2c_s^2)')'\right)dr.$$

For modes with $k_\parallel = 0$ near the surface of radius $r = r_0$, we can use the representation $k_\parallel \sim \frac{k_z}{L_s}(r - r_0)$, where the shear length is equal to $L_s^{-1} = \frac{1}{B_z}[r(B_\varphi/r)']_{r=r_0}$. As a result, we arrive at the following estimate of the upper limit on the characteristic growth rate of these modes with a fixed wavenumber k_z:

$$\gamma \sim \frac{c_{s0}}{L_s}k_z\Delta r,$$

where c_{s0} is the maximum acoustic speed and Δr is the size of the region in which the solution is localized. As in the case $m = 0$, we see that the growth rate approaches zero as B_z approaches zero and that the growth rate increases with k_z. However, an increase in $k_z\Delta r/L_s$ is restricted by the stabilization condition $k_z^2\Delta r^2/L_s^2 \sim -p'/aB^2$, which again leads to the maximum possible growth rate (10).

The case $m \gg 1$, in which $B_z \gg B_\varphi$, is analyzed in an analogous manner. For $m^2 \gg k_z^2r^2$, Eq. (2) reduces to

$$\frac{1}{r}(r^3k_\parallel^2B^2\xi')' - m^2\left(k_\parallel^2B^2 + \frac{2}{R}p' + \frac{4\gamma_0 p}{R^2}\frac{\gamma^2}{\gamma^2+k_\parallel^2c_s^2}\right)\xi = 0. \qquad (16)$$

Multiplying Eq. (16) by $r\xi(\gamma^2 + k_\parallel^2c_s^2)$ and integrating over the entire plasma radius, we obtain growth rate (14) with the coefficients

$$T = \int_0^a \left(k_\parallel^2B^2(r^2\xi'^2 + m^2\xi^2) + \frac{2m^2\xi^2}{R}\left(p' + 2\frac{\gamma_0 p}{R}\right)\right)rdr,$$

$$P = \int_0^a \left(m^2 r\xi^2k_\parallel^2c_s^2\left(\frac{2}{R}p' + k_\parallel^2B^2\right) + r^3k_\parallel^4B^2c_s^2\xi'^2 - \frac{1}{2}\xi^2(r^3k_\parallel^2B^2(k_\parallel^2c_s^2)')'\right)dr.$$

For modes with $k_\parallel = 0$ near the surface of radius $r = r_0$, we can use the representation $k_\parallel \sim k_\parallel'(r - r_0)$, where $k_\parallel' = m/r_0L_s$ and the shear length approaches infinity,

$L_s \longrightarrow \infty$, as $B_\varphi \longrightarrow 0$. As a result, we arrive at the following estimate of the upper limit on the characteristic growth rate of these modes with a fixed number m:

$$\gamma \sim m\frac{c_{s0}}{L_s}\frac{\Delta r}{r_0}.$$

As in the cases considered above, we again see that the growth rate approaches zero as the perturbation amplitude approaches zero and that the growth rate increases with m. Since an increase in $m\Delta r/L_s r_0$ is restricted by the stabilization condition $(m\Delta r/L_s r_0)^2 \sim -p'/RB^2$, we again arrive at the maximum possible growth rate (10).

Hence, in a magnetic configuration with a small rotational transform (small shear), the quasi-flute acoustic instability is excited and grows at a rate proportional to the amplitude of the magnetic perturbation, in which case the fastest growing modes are those with the shortest wavelengths.

4. CONCLUSIONS

We have shown that the growth rate of the MHD instability in toroidal configurations is reduced in a situation in which the Bernstein–Kadomtsev condition is satisfied while the Mercier stability criterion is not. This reduction is due to the excitation of slow quasi-flute acoustic Mercier modes instead of fast flute Alfvénic Mercier modes. In configurations with closed magnetic field lines, the Bernstein–Kadomtsev condition ensures MHD stability. If a small rotational transform is produced by a magnetic perturbation, there may be a quasi-flute acoustic instability that grows at a rate proportional to the perturbation amplitude. The slow growth rate of the quasi-flute acoustic instability can be influenced by kinetic effects, resistivity, and other factors not accounted for in our study.

ACKNOWLEDGMENTS

We are grateful to A.B. Mikhaĭlovskiĭ and V.P. Pastukhov for their valuable remarks and fruitful discussions. This work was supported in part by the Department of Atomic Science and Technology of the Ministry of Atomic Industry of the Russian Federation, the Russian Federal Program for State Support of Leading Scientific Schools (project no. NSh-2024.2003.2), and the Russian Foundation for Basic Research (project no. 03-02-16768).

APPENDIX 1

In arbitrary geometry, the local modes are described by the Glasser parameters [18]:

$$E = \frac{\langle B^2/|\nabla V|^2\rangle}{\Lambda^2}\left(-I'\Phi'' + J'\psi'' + \Lambda\frac{\langle\sigma B^2\rangle}{\langle B^2\rangle}\right),$$

$$F = \frac{\langle B^2/|\nabla V|^2\rangle}{\Lambda^2} \times\left(\langle\sigma^2 B^2/|\nabla V|^2\rangle - \frac{\langle\sigma B^2/|\nabla V|^2\rangle^2}{\langle B^2/|\nabla V|^2\rangle} + p'^2\left\langle\frac{1}{B^2}\right\rangle\right),$$

$$G = \frac{\langle B^2\rangle}{M\gamma_0 p},$$

$$H = \frac{\langle B^2/|\nabla V|^2\rangle}{\Lambda}\left(\frac{\langle\sigma B^2/|\nabla V|^2\rangle}{\langle B^2/|\nabla V|^2\rangle} - \frac{\langle\sigma B^2\rangle}{\langle B^2\rangle}\right),$$

$$K = \frac{\Lambda^2}{Mp'^2}\frac{\langle B^2\rangle}{\langle B^2/|\nabla V|^2\rangle},$$

$$M = \langle B^2/|\nabla V|^2\rangle \times\left[\langle|\nabla V|^2/B^2\rangle + \frac{1}{p'^2}\left(\langle\sigma^2 B^2\rangle - \frac{\langle\sigma B^2\rangle^2}{\langle B^2\rangle}\right)\right],$$

$$\sigma = \mathbf{j}\cdot\mathbf{B}/B^2, \quad \Lambda = \Phi'\psi'' - \psi'\Phi''.$$

Here, the prime denotes the derivative with respect to the volume V enclosed by a magnetic surface; ψ and I are the external poloidal magnetic flux and the external poloidal current; Φ and J are the toroidal magnetic flux and the toroidal current; Λ is the shear; and $\alpha = 2\pi n/\Phi' = 2\pi m/\psi'$, with n and m being the toroidal and poloidal mode numbers. The averaging over magnetic surfaces is performed in a standard fashion, $\langle A\rangle \equiv \oint\frac{dl}{B}A/\oint\frac{dl}{B} = \oint d\theta A/\oint d\theta$.

In sheared magnetic configurations, local ideal perturbations are described by the equation for the radial displacements ξ that was obtained in [8]:

$$\frac{d}{dx}\left[\left(1 + \frac{KH^2}{G+KF}\frac{1}{1+x^2/x_s^2}\right)x^2\frac{d\xi}{dx}\right] + x_A^2\frac{d^2\xi}{dx^2} - x^2\xi + (E+F+H)\left[1 - \frac{K(E+F+H)}{G+KF}\frac{1}{1+x^2/x_s^2} + \frac{KH}{G+KF}\frac{d}{dx}\left(\frac{x}{1+x^2/x_s^2}\right)\right]\xi = 0, \quad \text{(A.1)}$$

where $x = (r - r_0)k_y$, r_0 is the radial coordinate of the rational surface, $x_s^2 = \gamma^2(G + KF)\rho M/(\alpha^2\Lambda^2)$, $x_A^2 = \gamma^2\rho M/(\alpha^2\Lambda^2)$, γ is the growth rate, and ρ is the mass density. In this case, the Mercier stability criterion for local modes has the form

$$E + F + H - 1/4 < 0.$$

When the Mercier criterion is violated but the condition

$$\frac{1}{4}-\frac{(G-KE)(E+F+H)}{G+K(F+H^2)}>0$$

is satisfied, the instability grows at the rate of acoustic perturbations rather than at the rate of Alfvén perturbations [8].

In the limit of a small shear, the factors in the numerator in the last condition become

$$G-KE\sim\frac{I'\Phi''}{p'^2}+\frac{1}{\gamma_0 p},$$

$$E+F+H\sim\frac{\langle B^2/|\nabla V|^2\rangle}{\Lambda^2}$$

$$\times\left(-I'\Phi''+p'^2\left\langle\frac{1}{B^2}\right\rangle+\langle\sigma^2B^2/|\nabla V|^2\rangle-\frac{\langle\sigma B^2/|\nabla V|^2\rangle^2}{\langle B^2/|\nabla V|^2\rangle}\right).$$

Taking into account the fact that the denominator in the last condition is positive, we can see that, for small shear, this condition is satisfied when the first of these two expressions is negative and the second is positive. In this case, we arrive at inequalities analogous to BK condition (1).[1] Note that, for confinement systems with a magnetic well and with closed magnetic field lines, these inequalities were first derived by Spies [19].

The field-line closure is, as a rule, provided by the mirror-image symmetry of the magnetic configuration. This indicates that there exists a plane that is perpendicular to the magnetic axis of the configuration and with respect to which the magnetic field lines are in a mirror-image arrangement. For such configurations, the Glasser parameter H is zero, and the equation for radial displacements can be reduced to a form typical of cylindrical geometry:

$$\frac{d}{dx}\left(x^2\frac{d\xi}{dx}\right)-x^2\xi+x_A^2\frac{d^2\xi}{dx^2}$$

$$-\left(U_0+\frac{U_c}{1+x^2/x_s^2}+x_A^2\right)\xi\ =\ 0,$$

where

$$U_c\ =\ \frac{K(E+F)(E+F)}{G+KF},$$

$$U_0\ =\ -(E+F).$$

REFERENCES

1. A. B. Bernstein, E. A. Friemen, M. D. Kruskal, and R. M. Kulsrud, Proc. R. Soc. London, Ser. A **244**, 17 (1958); *Controlled Thermonuclear Reactions* (Atomizdat, Moscow, 1960), p. 226.
2. B. B. Kadomtsev, in *Plasma Physics and the Problem of Controlled Thermonuclear Reactions*, Ed. by M. A. Leontovich (Izd. Akad. Nauk SSSR, Moscow, 1958; Pergamon, London, 1959), Vol. 4.
3. P. N. Vabishevich, L. M. Degtyarev, V. V. Drozdov, *et al.*, Fiz. Plazmy **7**, 981 (1981) [Sov. J. Plasma Phys. **7**, 536 (1981)].
4. A. I. Morozov, V. P. Pastukhov, and A. Yu. Sokolov, in *Proceedings of the Workshop on D-^{3}He Based Reactor Studies, Moscow, 1991*, p. 1C1.
5. A. Hasegava, L. Chen, and M. E. Mauel, Nucl. Fusion **30**, 2405 (1990).
6. V. V. Arsenin, E. D. Dlougach, V. M. Kulygin, *et al.*, Nucl. Fusion **41**, 945 (2001).
7. S. Ma and J. M. Dawson, Phys. Plasmas **1**, 1251 (1994).
8. A. B. Mikhailovskii and A. A. Skovoroda, Plasma Phys. Controlled Fusion **44**, 2033 (2002).
9. A. B. Mikhaĭlovskiĭ and A. A. Skovoroda, Dokl. Akad. Nauk **383**, 758 (2002) [Dokl. Phys. **47**, 294 (2002)].
10. B. B. Kadomtsev, Zh. Éksp. Teor. Fiz. **37**, 1646 (1959) [Sov. Phys. JETP **10**, 1167 (1960)].
11. L. S. Solov’ev, Zh. Tekh. Fiz. **48**, 21 (1978) [Sov. Phys. Tech. Phys. **23**, 12 (1978)].
12. A. B. Mikhaĭlovskiĭ, *Plasma Instabilities in Magnetic Confinement Systems* (Atomizdat, Moscow, 1978).
13. S. Gupta, J. D. Callen, and C. C. Hegna, Phys. Plasmas **9**, 3395 (2002).
14. L. S. Solov’ev, in *Reviews of Plasma Physics*, Ed. by M. A. Leontovich (Gosatomizdat, Moscow, 1972; Consultants Bureau, New York, 1975), Vol. 6.
15. G. Bateman, *MHD Instabilities* (MIT Press, Cambridge, 1978; Énergoizdat, Moscow, 1982).
16. L. D. Landau and E. M. Lifshitz, *Quantum Mechanics: Non-Relativistic Theory* (Nauka, Moscow, 1989; Pergamon, New York, 1977).
17. B. B. Kadomtsev, in *Reviews of Plasma Physics*, Ed. by M. A. Leontovich (Gosatomizdat, Moscow, 1963; Consultants Bureau, New York, 1966), Vol. 2.
18. A. H. Glasser, J. M. Greene, and J. L. Johnson, Phys. Fluids **18**, 875 (1975).
19. G. O. Spies, Phys. Fluids **17**, 400 (1974).

Translated by I.A. Kalabalyk

---

[1] An unimportant deviation concerns only the left-hand inequality in condition (1). A possible reason for this is that the perturbations under analysis are of different types.

Plasma Physics Reports, Vol. 30, No. 3, 2004, pp. 249–254. Translated from Fizika Plazmy, Vol. 30, No. 3, 2004, pp. 277–282.
Original Russian Text Copyright © 2004 by Nazarenko, Antsiferov, Dorokhin, Koshelev.

LOW-TEMPERATURE PLASMA

Evolution of a Capillary Discharge Induced by a Semiconductor Current Generator

A. V. Nazarenko, P. S. Antsiferov, L. A. Dorokhin, and K. N. Koshelev
Institute of Spectroscopy, Russian Academy of Sciences, Troitsk, Moscow oblast, 142190 Russia

Received June 30, 2003; in final form, September 2, 2003

Abstract—Results are presented from the intermediate stage of work on creating a current generator in a circuit with an inductive energy storage and a semiconductor opening switch made of 40 SDL-800 diodes. A six-diode generator prototype has been created with a current pulse amplitude of ~4.5 kA and a leading edge duration of ~10–20 ns at an inductive load of 30–35 nH. The generator was used to study discharges in capillaries filled with argon or hydrogen. It is shown that, in a 2-mm-diameter capillary, the initial azimuthal asymmetry of a structure arising during the breakdown ceases as the discharge evolves, whereas in a 0.8-mm-diameter capillary, it is retained. Time-resolved spectroscopic studies of the plasma reveal the presence of line emission of highly ionized argon (ArVII and ArVIII) in the hottest phase of the discharge, which indicates that a temperature of 20–40 eV has been achieved. *© 2004 MAIK “Nauka/Interperiodica”.*

1. INTRODUCTION

At present, capillary discharges are taken to mean high-current electric discharges initiated in a dielectric tube with a large length-to-diameter ratio. Great interest in such discharges stems from their application in the production of inverse media emitting in the XUV range [1, 2], as well as in the creation of optical plasma waveguides based on such discharges [3, 4]. In the former case, the capillary diameter is typically 2–5 mm and the discharge current is 20–50 kA. In the latter case, the diameter is 0.1–0.5 mm and the current is 200–500 A. Although the processes occurring in such discharges have been thoroughly investigated [5], it seems worthwhile to carry out experiments in the intermediate range of discharge parameters (a diameter of 1–2 mm and a current of 1–10 kA) in order to gain better insight into the physics of these processes. In the last few years, experiments on capillary discharges with the use of an inductive-storage current source have been carried out at the Laboratory of Plasma Spectroscopy of the Institute of Spectroscopy of the Russian Academy of Sciences [6, 7]. In these experiments, we used a semiconductor opening switch based on SDL diodes. At present, we are designing a device with 40 such diodes connected in parallel. The driver will be able to provide current pulses through a 30-nH inductive load (a typical capillary inductance) with an amplitude up to 30 kA and a current rise time as short as 10–20 ns. These parameters will be sufficient to obtain stimulated emission of radiation at the $3s$–$3p$ transition of neon-like argon [2]. To date, a six-diode prototype generator has been created. The device provides a reproducible fast increase in the current through a 30-nH inductive load (up to 4–4.5 kA in a time of 10–20 ns), so it can be used to study capillary discharges in the above intermediate parameter range. The use of an XUV diagnostic system with a recorder based on a microchannel plate (MCP) makes it possible to gain information about the spatial and spectral structure of a capillary discharge with a time resolution of 10 ns.

2. EXPERIMENTAL TECHNIQUES

The main problem in operating with inductive storage is the necessity of breaking the current circuit in a time of several units to tens of nanoseconds when a current of several tens of kiloamperes is switched to the load [8]. This problem imposes rigid requirements on the choice of the opening switch. In our study, a semiconductor opening switch was chosen as a current driver in a circuit with inductive energy storage because of the stable and reproducible operation of this switch as compared to the plasma opening switch used previously in [9]. The semiconductor opening switch is based on the experimentally observed effect that, after a high-current pulse has passed through a diode in the forward direction, the diode recovers its blocking properties with some delay, so that, for a certain time, it can conduct current in the reverse direction. In more detail, the mechanism for current breaking in a diode is described in [10]. A circuit diagram of the current-pulse former used in our experiments is described in [11]. A schematic of the current driver is shown in Fig. 1. The main capacitor bank $C1$ consists of K-15-10 ceramic capacitors with a capacitance of 4700 pF and an operating voltage of up to 50 kV. Six SDL-0.4-800 diodes connected in parallel are used as an opening switch. After bridging controlled spark gap $G1$, the current I_0 begins to flow in the forward direction through the diodes and a return conductor B (in Fig. 1, this current direction is shown on bottom). The total inductance of the capacitors, feed circuit, spark gaps, and return cir-

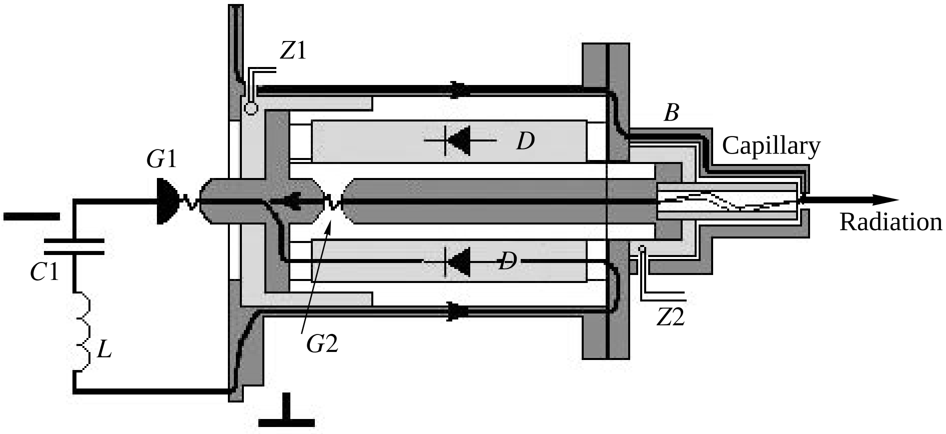

Fig. 1. A schematic of the current driver for a capillary discharge: (*C*1) main capacitor bank, (*G*1,*G*2) spark gaps, (*B*) return conductor, (*D*) diodes, and (*Z*1, *Z*2) magnetic probes.

cuit is labeled in Fig. 1 by the letter *L*; in fact, it is this inductance in which energy is stored. After the polarity has changed, the current begins to flow in the reverse direction and, near the maximum of the second half-period, the diodes become blocked. The overvoltage arising across the diodes breaks the sharpening spark gap *G*2, and the current I_1 is switched to a capillary (in Fig. 1, this current direction is shown on top). The currents in the main and capillary circuits are measured by magnetic probes *Z*1 and *Z*2, respectively. The main improvement compared to [11] is that the number of parallel-connected diodes is increased from two to six, which has made it possible to increase the switched current from 1.5 to 4.5 kA. At the same time, the duration of the leading edge of the current pulse has remained within the range 10–20 ns. This means that the time constant of the load–diode circuit *L*/*R* (where *L* is the load inductance and *R* is the effective diode resistance at the instant of current break) is much shorter than the characteristic time of diode blocking. This circumstance is of crucial importance for the formation of the leading edge of the current pulse. Hopefully, the duration of the leading edge will remain the same and, consequently, the current growth rate *dI*/*dt* will increase with increasing number of parallel-connected diodes. Characteristic waveforms of the current in the main and load (capillary) circuits are shown in Fig. 2.

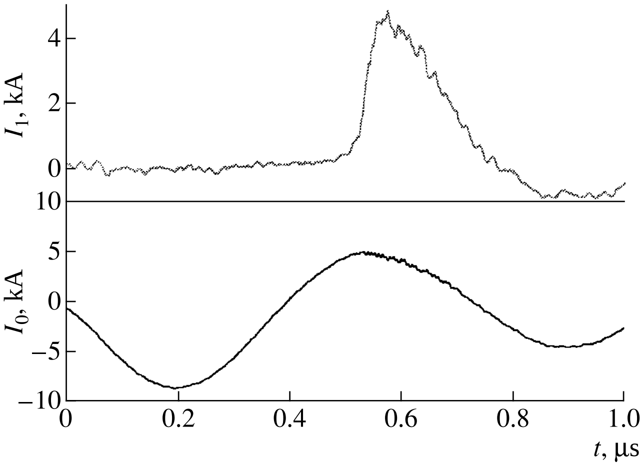

Fig. 2. Waveforms of the current I_0 in the main circuit and the current I_1 through a 2-mm-diameter capillary (the inductive load is ~30 nH).

We carried out a series of experiments with 2-mm-diameter and 15-mm-long capillaries filled with argon or hydrogen at a pressure of 500 mtorr and 0.8-mm-diameter and 15-mm-long capillaries filled with argon at the same pressure. In the experiments, we recorded plasma emission spectra and photographed discharges with the help of a pinhole camera. A 100-µm-diameter pinhole was located at the capillary axis at a distance of 20 mm from the capillary end. In the case of a 2-mm-diameter capillary, the distance from the pinhole to the image plane was about 150 mm, which corresponded to a 7.5-fold magnification. Pinhole images of a 0.8-mm-diameter capillary were produced at a longer distance between the pinhole and the image plane; in this case, the magnification was about 15. The plasma emission spectra were recorded with the help of a 600-grove/mm grazing-incidence grating with an incidence angle of 5° and a Rowland circle diameter of 1 m. The spectrograph measured spectra in the wavelength range of $\lambda = 3$–40 nm with a relative resolution of $\delta\lambda/\lambda \sim 1/500$, which was determined primarily by the width of the entrance slit. The pinhole images, as well as the emission spectra, were recorded on a film with the help of an MCP image intensifier with a high sensitivity in the wavelength range of $\lambda < 1000$ Å. The time resolution was determined by the duration of the MCP gate signal and was equal to 10 ns. Since emission lines of oxygen adsorbed on the capillary wall are usually dominant in the spectra of capillary discharges, the capillary wall was cleaned by a 200-μA dc glow discharge. This allowed us to eliminate oxygen lines in the emission spectra from 2-mm-diameter capillaries; however, we failed to completely eliminate these lines in 0.8-mm-diameter capillaries. This may be explained by the fact that, as the capillary diameter decreases, the ratio of the wall area to the volume increases, so that the discharge is more strongly affected by the wall processes (pinhole images show, in 0.8-mm-diameter capillaries, the plasma was not detached from the wall; see below). Nevertheless, in this case, argon lines could be reliably distinguished in the discharge spectra.

3. RESULTS AND DISCUSSION

Figure 3 presents a series of pinhole images of discharges in a 2-mm-diameter capillary filled with argon at a pressure of 0.5 torr. The images were obtained in a series of discharges with different time delays from the beginning of the discharge, so they illustrate the discharge evolution. In the first image, corresponding to the instant of breakdown (a delay time of 0–10 ns), the discharge glow is highly asymmetric, which may be attributed to the breakdown inhomogeneity. Bright spots in the image may be interpreted as projections of streamers developing along the capillary wall. Then, the plasma detaches from the wall and shrinks to a diameter of 0.7–0.8 mm (the second and third images, corresponding to delay times of 20–30 ns and 56–66 ns, respectively). In contrast to a 0.8-mm-diameter capillary, the initial azimuthal asymmetry disappears and the glowing region looks like an axially symmetric column. Later (the fourth image, 92–102 ns), a characteristic annular structure similar to that observed in [6] forms. We note that the lifetime of this structure amounts to several tens of nanoseconds, which is on the order of the characteristic hydrodynamic time equal to the plasma diameter divided by the ion-acoustic velocity:

$$\tau_{\mathrm{MHD}} = d/[(kT_e + \gamma kT_i)/M_i]^{1/2}$$
$$\sim (0.06\ \mathrm{cm})/(1.2 \times 10^6\ \mathrm{cm/s}) = 50\ \mathrm{ns},$$

where d is the diameter of the plasma column; k is the Boltzmann constant; T_e, T_i, and M_i are the electron and ion temperatures and the ion mass, respectively; and γ is the specific heat ratio C_p/C_V.

Then, 250–270 ns after the beginning of the discharge, the glow intensity gradually decreases with decreasing the discharge current.

In the case of a 0.8-mm-diameter capillary, the discharge evolution is quite different (Fig. 4). Azimuthal asymmetry arising in the initial stage of the discharge is observed in this case too (the first image, 0–10 ns); however, this asymmetry is retained over the entire discharge phase. The glow region 0.4–0.5 mm in diameter does not detach from the capillary wall, and the glow ceases after 50–60 ns, i.e., much sooner than in the case

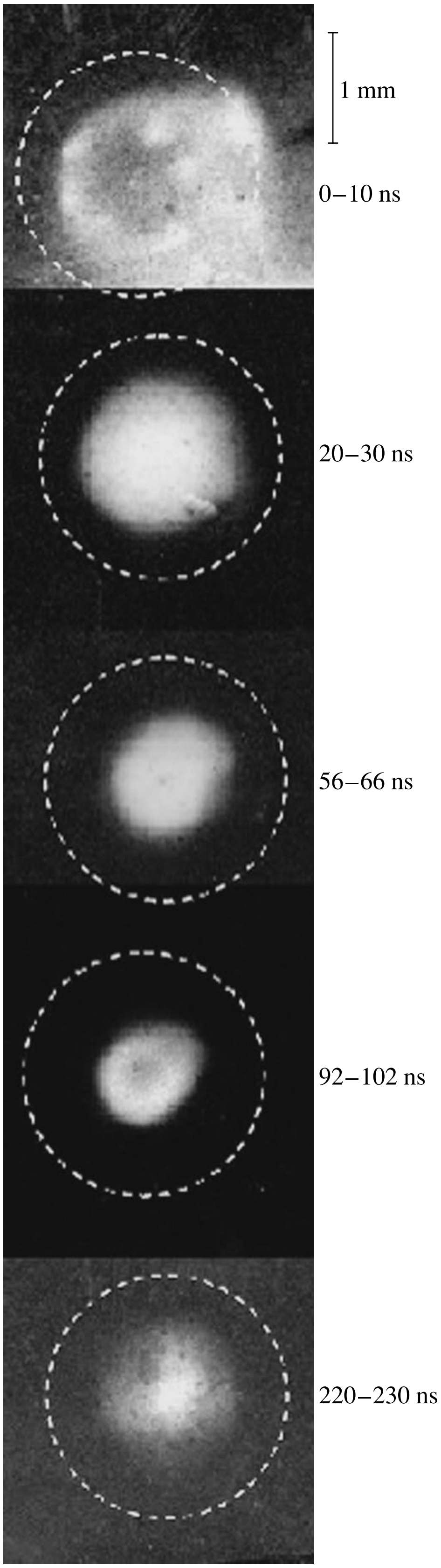

Fig. 3. Pinhole images illustrating the evolution of a discharge in a 2-mm-diameter capillary filled with argon at a pressure of 500 mtorr.

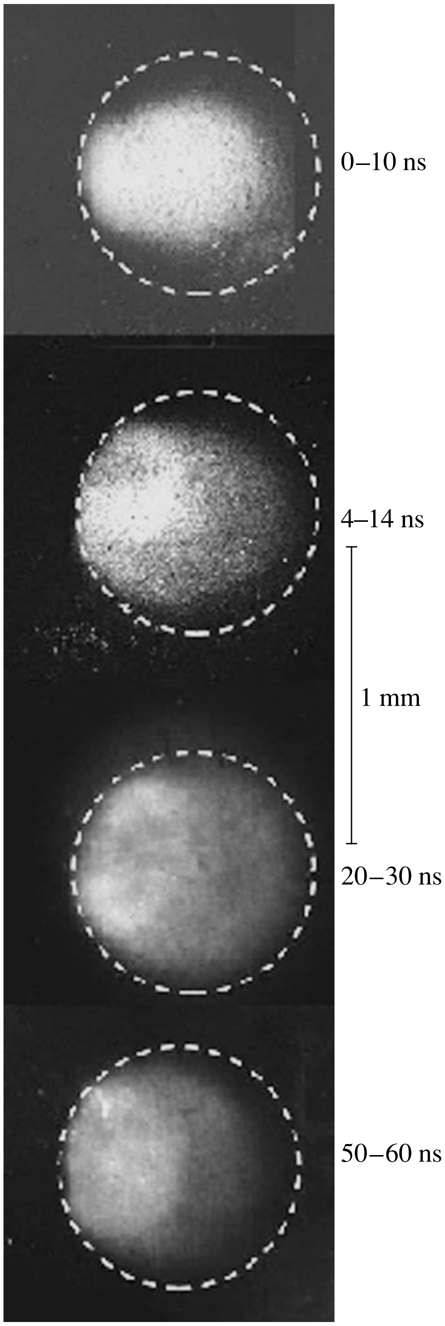

Fig. 4. Pinhole images illustrating the evolution of a discharge in a 0.8-mm-diameter capillary filled with argon at a pressure of 500 mtorr.

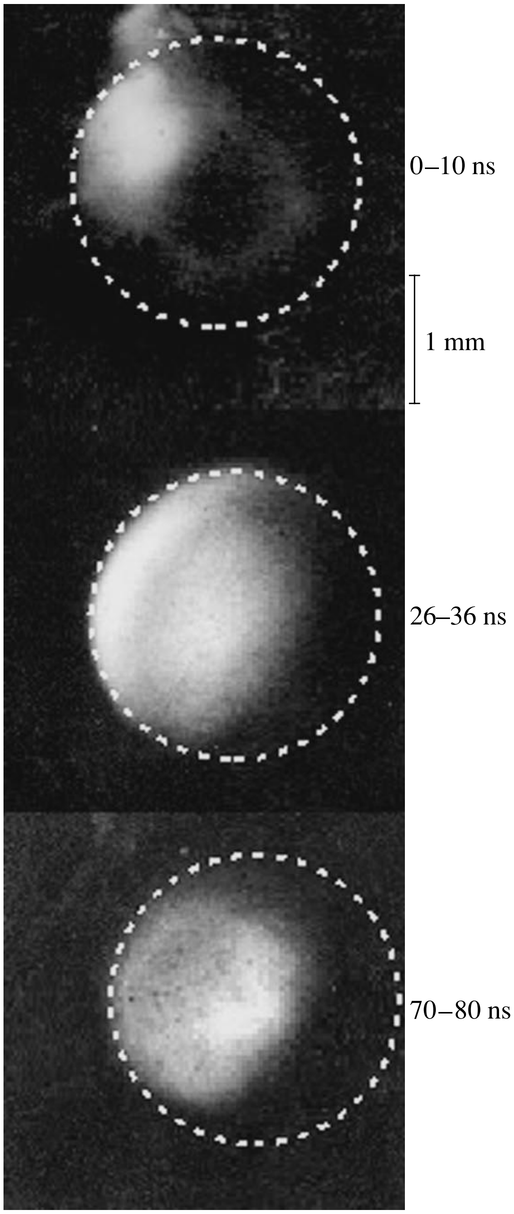

Fig. 5. Pinhole images illustrating the evolution of a discharge in a 2-mm-diameter capillary filled with hydrogen at a pressure of 500 mtorr.

of a 2-mm-diameter capillary, which may be attributed to a more efficient cooling of the plasma due to its contact with the wall.

A similar picture is observed in a 2-mm-diameter capillary filled with hydrogen (Fig. 5). In this case too, a single streamer forms (seen in the first image, 0–10 ns), which then evolves into an azimuthally asymmetric glow region adjacent to the capillary wall. The glow is quenched 70–80 ns after the beginning of the discharge, i.e., long before a substantial decrease in the discharge current. In the first image, along with a streamer breakdown along the wall, one can see a low-intensity annular region corresponding to the far end of the capillary.

Along with studying pinhole images, we also examined plasma emission spectra. Figure 6 shows a series of spectra corresponding to different phases of a discharge in a 2-mm-diameter capillary filled with argon (under conditions similar to those in Fig. 3). It can be seen that the spectra correspond to a relatively cold plasma with a maximum degree of ionization of 5 to 6

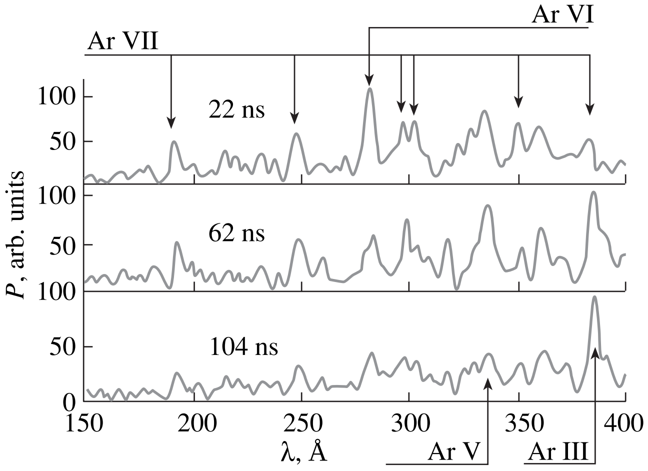

Fig. 6. Emission spectra from a discharge in a 2-mm-diameter capillary filled with argon at a pressure of 500 mtorr for different instances from the beginning of the discharge.

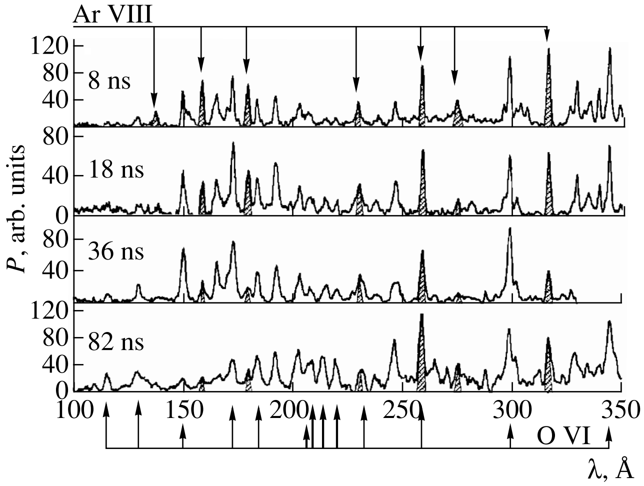

Fig. 7. Emission spectra from a discharge in a 0.8-mm-diameter capillary filled with argon at a pressure of 500 mtorr at different instances from the beginning of the discharge.

(ArVI–ArVII). The absence of ArVIII lines indicates that the plasma temperature is below 20 eV. In the course of discharge evolution, the amount of ArVI and ArVII ions rapidly decreases, so that, at 104 ns, a single intense ArII line (the $3p^4$–$3p4d$ transition, 383 Å) is present in the spectrum. Emission spectra from a thinner capillary (Fig. 7) indicate a substantially stronger plasma heating. In this case, ArVIII and OVI lines are clearly observed and the intensity ratio between them varies with time in favor of the latter, which may be attributed to a continuous influx of atoms of the wall material. The presence of the lines of these ions in the spectra indicates that the temperature is no lower than 20–30 eV. We note that, the last spectrum, recorded at 82 ns, contains a high-intensity Rydberg series of OVI lines with wavelengths in the range 100–110 Å (the spectra are recorded in the second order, and the lines are marked by heavy arrows). This fact can be interpreted as a result of intense recombination population of the upper levels of OVI ions during the fast cooling of the plasma due to its contact with the cold capillary wall.

Hence, we can conclude that, in a 2-mm-diameter capillary, a current pulse with an amplitude of 4.5 kA is sufficient to separate the plasma from the capillary wall and somewhat compress it, although plasma heating is insignificant and the temperature does not exceed 20 eV. Equilibrium that is then established is probably related to the Bennet equilibrium in a magnetic field produced by the discharge current. In contrast, in a thinner capillary, the plasma is heated to a significantly higher temperature (due to a higher energy deposition per one particle). In this case, the plasma continues to interact with the wall over the entire discharge phase, which results in its faster cooling. It should be noted that, in our experiments, the degree of asymmetry of a capillary discharge (in particular, in the initial stage of the discharge) is substantially higher than in other experiments with capillary discharges (see [1, 3, 4]). This is probably related to the fact that those experiments were carried out at different current amplitudes and different current growth rates.

Let us estimate the plasma electron density for a 2-mm-diameter capillary filled with argon. Assuming that all the plasma is accumulated in the central column, the degree of ionization is equal to 5, and the volumetric compression ratio N is equal to 8, the electron density can be estimated at $n_e \sim ZNn_0 \sim 5 \times 10^{17}$ cm^{-3}. Estimates also show that, with allowance for possible errors, the thermal and magnetic pressures in this plasma are of the same order of magnitude; i.e., the plasma column can be under the Bennet equilibrium conditions, which is confirmed by its fairly long stable existence.

4. CONCLUSIONS

The experiments have shown that the smaller the capillary diameter, the stronger the influence of the capillary wall on the discharge evolution. The most efficient way of decreasing this influence is to increase the current growth rate dI/dt at the leading edge of the current pulse [1, 2]. This can lead to the formation of a shock wave and, thus, to a more rapid separation of the current-carrying layer from the capillary wall and a stronger compression of the central region of the plasma column. This is partially confirmed by the results of [12], in which the plasma pinching and heating were observed in a 1-mm-diameter capillary at close current values but at a significantly higher current growth rate: $dI/dt \sim 10^{12}$ A/s. In contrast, when studying the interaction of a hot plasma with a cold wall (e.g., when investigating inversion schemes for the generation of enhanced spontaneous radiation via recombination or resonant charge exchange), it is expedient to operate at lower values of dI/dt. The above annular structure, also observed in [6], can be of interest from the standpoint of developing plasma waveguides [3, 4]; however, this requires additional interferometric studies of the radial profile of the electron density.

All the results presented in this paper were obtained with the use the multipurpose XUV diagnostic system that was developed over the last few years at the Laboratory of Plasma Spectroscopy of the Institute of Spectroscopy of the Russian Academy of Sciences. This system combines the following advantages: high spectral and spatial resolution, high sensitivity (up to single photon counting), high reliability, and ease of use. Owing to these properties, the device could find wide application in experiments on studying the spectral and spatial characteristics of various plasma objects [9, 12].

It should be noted that a theoretical description of the evolution of an electric discharge along a solid surface, as well as investigation of the mechanisms underlying this evolution, still remains a very challenging problem. Therefore, study of the influence of the capillary diameter and the type of filling gas on the breakdown dynamics could become a starting point for further theoretical research.

REFERENCES

1. J. J. Rocca, D. C. Beethe, and D. Voorhees, Opt. Lett. **13**, 565 (1988).
2. B. R. Benware, C. H. Moreno, D. J. Burd, *et al.*, Opt. Lett. **22**, 796 (1997).
3. Y. Ehrlich, A. Zigler, C. Cohen, *et al.*, Phys. Rev. Lett. **77**, 4186 (1996).
4. D. J. Spence and S. M. Hooker, Phys. Rev. E **63**, 015401 (2001).
5. A. Esaulov, P. Sasorov, L. Soto, *et al.*, Plasma Phys. Controlled Fusion **43**, 571 (2001).
6. P. S. Antsiferov, L. A. Dorokhin, E. Yu. Khautiev, *et al.*, J. Phys. D **31**, 2013 (1998).
7. P. S. Antsiferov, S. S. Churilov, L. A. Dorokhin, *et al.*, Phys. Scr. **62**, 127 (2000).
8. K. H. Schoenbach, M. Kristiansen, and G. Shaffe, Proc. IEEE **72**, 28 (1984).
9. P. S. Antsiferov, L. A. Dorokhin, A. V. Nazarenko, *et al.*, in *Proceedings of the 7th International Conference on X-ray Lasers, Saint-Malo, 2000,* p. 120.
10. S. A. Darznek, G. A. Mesyats, and S. N. Rukin, Zh. Tekh. Fiz. **67** (10), 64 (1997) [Tech. Phys. **42**, 1170 (1997)].
11. A. V. Nazarenko, P. S. Antsiferov, L. A. Dorokhin, *et al.*, Prib. Tekh. Éksp., No. 1, 60 (2003).
12. L. Soto, A. Esaulov, J. Moreno, *et al.*, Phys. Plasmas **8**, 2572 (2001).

Translated by N.F. Larionova

Plasma Physics Reports, Vol. 30, No. 3, 2004, pp. 255–262. Translated from Fizika Plazmy, Vol. 30, No. 3, 2004, pp. 283–291.
Original Russian Text Copyright © 2004 by Gritsinin, Knyazev, Kossyĭ, Malykh, Misakyan.

LOW-TEMPERATURE PLASMA

A Pulse-Periodic Torch in a Coaxial Waveguide: Formation Dynamics and Spatial Structure

S. I. Gritsinin, V. Yu. Knyazev, I. A. Kossyĭ, N. I. Malykh, and M. A. Misakyan
Prokhorov Institute of General Physics, Russian Academy of Sciences, ul. Vavilova 38, Moscow, 119991 Russia

Received May 28, 2003

Abstract—Results are presented from experimental studies of the formation dynamics, spatial structure, and parameters of a pulse-periodic microwave discharge excited in a coaxial waveguide. The experimental setup allows the stable generation of a plasma jet in molecular and atomic gas flows at pressures close to atmospheric pressure without applying additional initiators. The complicated sequence of processes leading to torch formation cannot be adequately described with conventional models of a discharge sustained by a surface electromagnetic wave. *© 2004 MAIK “Nauka/Interperiodica”.*

1. INTRODUCTION

Microwave torches are widely used as plasma sources in various technologies and as an efficient experimental tool in physical studies (see, e.g., [1–4]). Active research on the parameters and features of microwave torches began about 20 years ago, and the literature on this subject remains impressive.

In this paper, we describe the main characteristics of microwave torches (microwave plasmatrons), whose design and operating regimes, first described in [5–7], differ from those used in [1–4]. The main difference is that the torch is generated and sustained in a coaxial waveguide; this allows one to utilize the microwave generator energy in the most efficient way. Moreover, the torch operates in a pulse-periodic mode, rather than in a continuous one, which may be of particular interest for plasmochemical applications.

2. MICROWAVE-TORCH DESIGN AND EXPERIMENTAL SETUP

A schematic of the microwave plasmatron is shown in Fig. 1. The plasmatron is powered with a rod antenna connected to a commercial magnetron operating at a frequency of $f \cong 2.45$ GHz. Microwave energy is first introduced into a rectangular resonator in the form of microwave pulses with a duration of $\tau_i \cong 8$ ms, the time interval between the pulses being $\tau_d \cong 12$ ms. The average microwave power is $P \cong 1$ kW. From the rectangular resonator, microwave energy is transferred to a coaxial line with the help of a current loop, whose extension is the inner electrode of the coaxial line. The loop and its extension are made of a hollow tube, which is used to supply the torch with the working gas. The inner electrode of the coaxial line ends with a nozzle made of a refractory metal and has a sharp edge to facilitate gas breakdown. A distinctive feature of this line from conventional coaxial lines is that the outer coaxial electrode is longer than the inner electrode. Such a design radically changes the mechanisms for discharge initiation and maintenance. Due to such a shortened inner electrode, an electromagnetic wave with $\lambda = c/f \cong 12.24$ cm that propagates along a coaxial line with an outer electrode diameter of $d_{\text{ext}} \cong (2–5)$ cm undergoes a jumplike transition when passing from the coaxial line to a circular below-cutoff waveguide (i.e., the region where the outer electrode diameter is $d_{\text{ext}} < d_{\text{cr}} \equiv 1.84c/\pi f \cong 7.17$ cm). We note that, according to [8], electromagnetic waves with a wavelength of $\lambda = 12.24$ cm cannot propagate in this circular waveguide at all.

In order to provide access to the torch, which is situated inside the outer electrode of the coaxial line, this electrode is made of a set of thin metal rods 2–3 mm in diameter that are placed at a distance of 0.5–1 cm from one another (Fig. 1b). Since a running coaxial mode induces longitudinal currents in the outer electrode wall, these rods serve as a solid electrode for this mode. At the same time, this design provides free access to the torch for diagnostic and technological purposes.

The microwave energy reflected from the circular waveguide propagates backward along the coaxial line and is accumulated in a set of resonators formed by the rectangular waveguide, the coaxial line, and the magnetron cavity. The length of the inner electrode of the coaxial line is chosen such that the nozzle end is situated in an antinode of the standing wave formed due to the reflection of the running wave from the circular below-cutoff waveguide. As the energy is accumulated in the standing wave, the electric field at the sharp edge of the nozzle progressively increases and, eventually, reaches the value required for gas breakdown. Thus, in spite of a rather low microwave power, it is possible to achieve breakdown (with the subsequent formation of a torch) in various gases (argon, nitrogen, air, carbonic acid, hydrogen, methane, propane, CFC-12, and others)

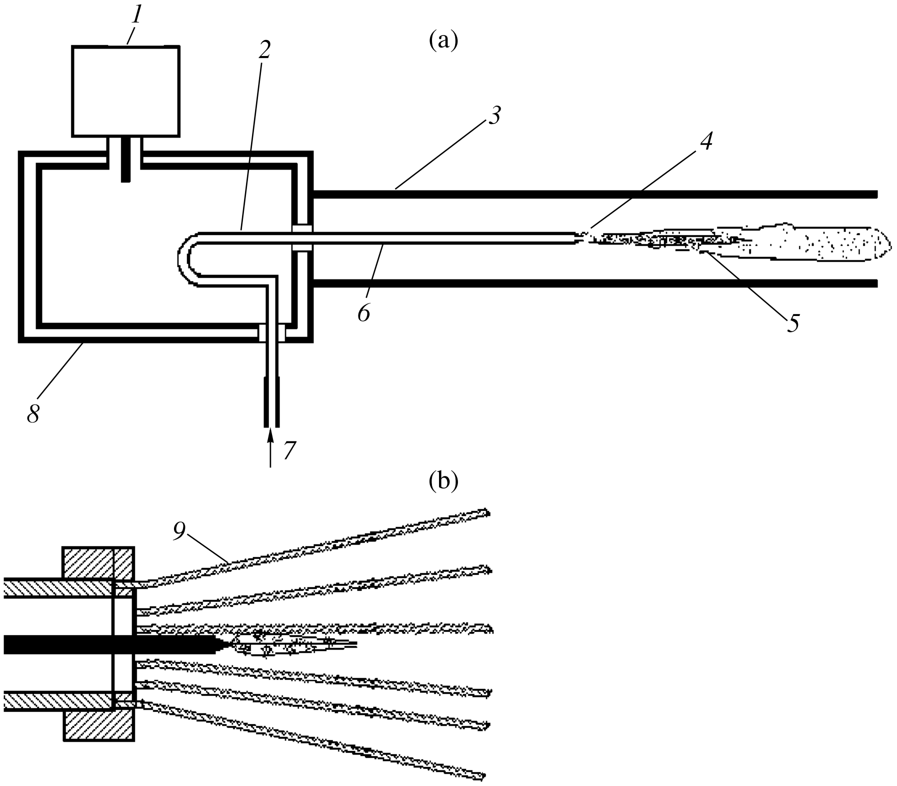

Fig. 1. (a) Schematic of a coaxial microwave plasmatron with the usual design of a coaxial line, and (b) an outer coaxial electrode that ends with a set of rods: (*1*) magnetron, (*2*) loop, (*3*) outer coaxial electrode, (*4*) nozzle, (*5*) plasma jet, (*6*) inner electrode, (*7*) working gas, (*8*) rectangular resonator, and (*9*) copper rods.

over a wide pressure range, including atmospheric pressure. In our experiments, the plasma jet (the torch) was ejected into atmospheric air. The working-gas flow rate through the central electrode was 4–100 l/min.

The plasma produced by gas breakdown near the nozzle is entrained by the working-gas flow, and the plasma jet produced in this way serves as an extension the inner electrode of the coaxial line, through which microwaves can propagate to the torch end. After falling into the circular below-cutoff waveguide, the microwave is reflected backward; as a result, the microwave energy is primarily absorbed in the torch plasma.

Below, we present the results of studies of the formation and propagation of the torch and the data from measurements of the parameters of the plasma jet.

Figure 2 shows a schematic of the experimental setup and diagnostics employed. The torch plasma emission was measured by photomultipliers and photodiodes. An FER-7 streak camera allowed us to photograph the torch in a scanning regime with a high temporal resolution. The electron density in the torch was measured with the help of laser and microwave interferometers. The spectrum of the visible torch emission was recorded with an S 2000 (Ocean Optics) spectrometer.

3. MEASUREMENT RESULTS

The microwave generator operated in the pulse-periodic regime. In every pulse, the torch passed through the stages of initiation, inflammation, and growth along the waveguide axis to a certain finite length. The experiments demonstrate a rather complicated behavior of the torch glow and the medium parameters.

When the working gas is argon (or some other noble gas), time-integrated photographs show a bright cylindrical region (“core”) near the nozzle (see Fig. 3). The core is 1–2 mm in diameter and 1–2 cm long. Downstream from the core, there is an extended, less bright region with curved boundaries. The volume of this region is 2–3 orders of magnitude greater than the core volume.

When operating with molecular gases (nitrogen or air), a well-defined bright core is absent.

Figure 4 shows the time dependence of the torch length measured with the help of a collimated photodiode. One can see that, over the time interval $0.5 \le t \le 4$ ms, the front of the glow propagates from the nozzle with an almost constant velocity of $v_z \cong 23$–24 m/s and travels a distance that is close to the maximum torch length ($L_z^{\max} \cong 11$ cm for the particular experimental

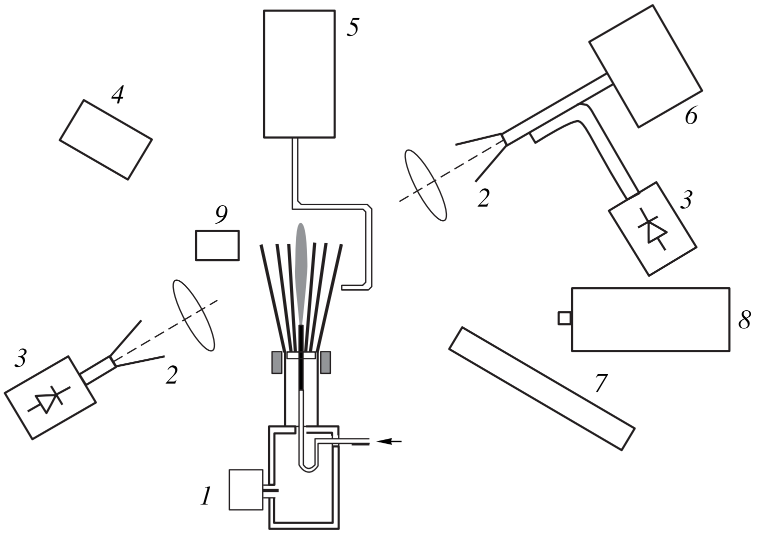

Fig. 2. Experimental setup: (*1*) microwave plasmatron, (*2*) diagnostic microwave horn antennas and lenses, (*3*) microwave detector, (*4*) HCN laser, (*5*) additional gas injector, (*6*) diagnostic microwave oscillator, (*7*) photomultiplier, (*8*) FER-7 streak camera, and (*9*) collimated photodiode.

conditions). Near the nozzle, the glow propagates with a velocity close to the gas flow velocity.

The axial propagation of the glow was also studied with the help of an FER-7 streak camera whose slit was oriented along the axis of the coaxial line. Figure 5 shows streak images of the torch propagation in argon and nitrogen. A streak image taken with a relatively low sweep speed (Fig. 5b) shows that, in the initial stage of the discharge, which lasts about 0.5 ms from the beginning of the microwave pulse, the argon torch exists only in the core region, which spreads out over a distance of 1–2 cm from the nozzle. Then, a less bright glow wave detaches from the core and propagates along the system axis. The propagation velocity of the glow front measured with the help of the streak camera is close to the velocity measured with the help of the collimated photodiode (Fig. 4). It is worth noting that, after the primary glow front has detached from the core, secondary waves accompanied by periodic bursts of the core glow are generated. The secondary glow waves catch up with the primary front, thus forming the resulting glow wave.

At a higher sweep speed (Figs. 5c and 5d), high-frequency modulation of the core glow is observed in the initial stage of the discharge, before the appearance of the glow wave. It can be seen that the core glow intensity rapidly increases and then decays almost to zero with a characteristic time of 5–10 μs. The modulation

Fig. 3. Time-integrated photograph of a microwave torch. The working gas is argon.

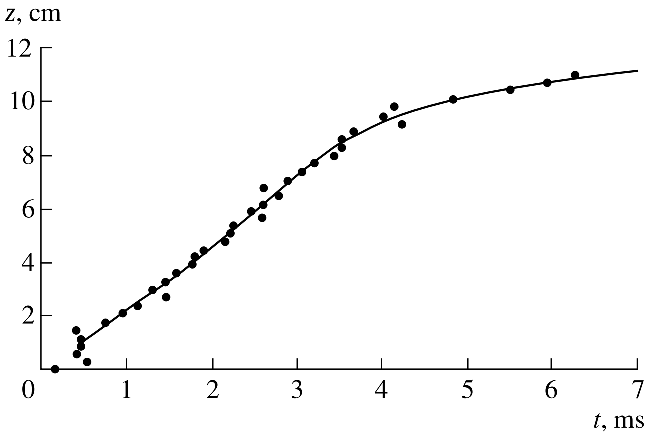

Fig. 4. Evolution of the torch length during a microwave pulse.

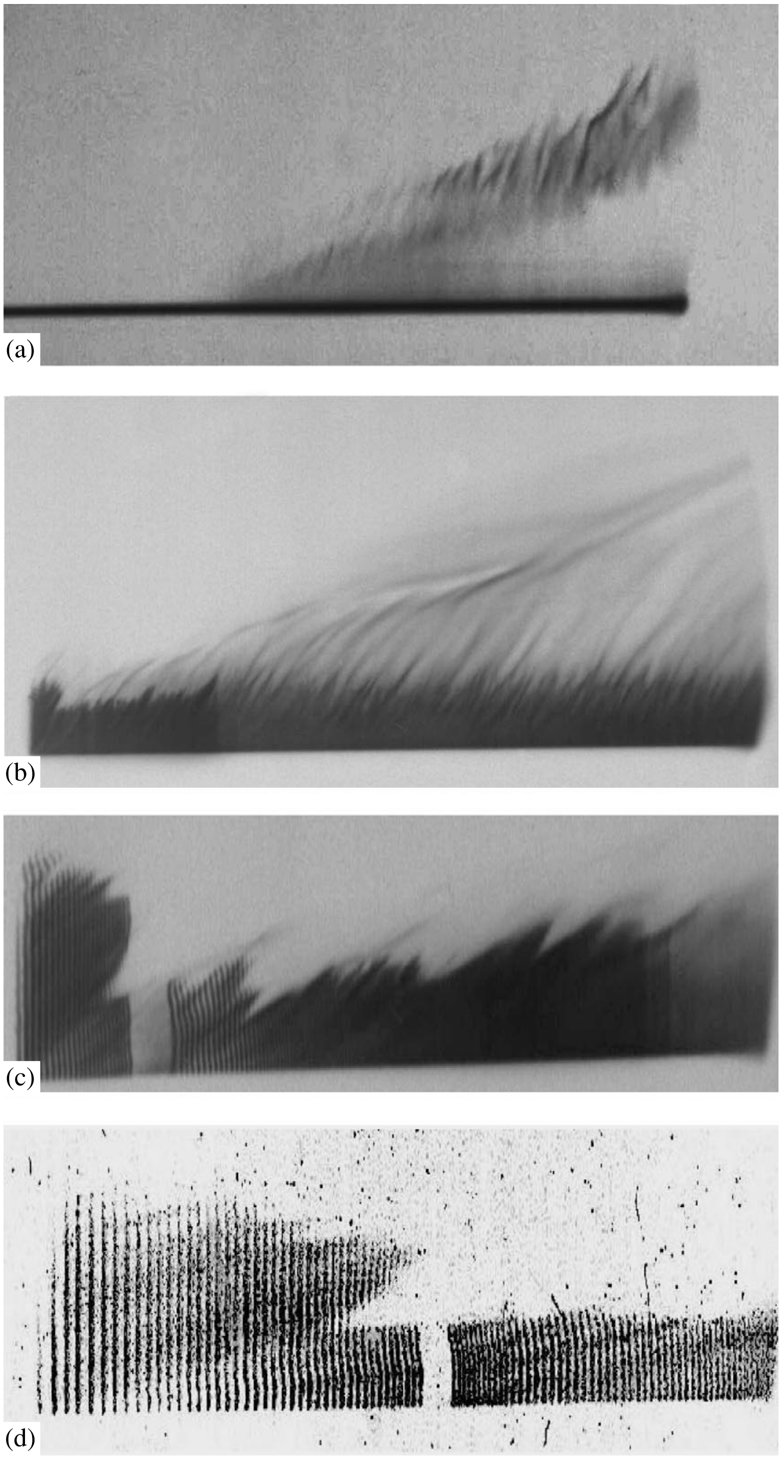

Fig. 5. Streak images of a microwave torch illustrating the torch evolution during a microwave pulse (time and the distance from the nozzle are plotted on the horizontal and vertical axes, respectively): (a) the working gas is N_2 (the full horizontal/vertical size of the image is 3 ms/8 cm) and (b)–(d) the working gas is Ar (the horizontal/vertical size is (b) 3 ms/8 cm, (c) 750 μs/2 cm, (d) 250 μs/2 cm).

of the core glow is accompanied by the generation of a sequence of short high-power (up to 10–20 kW) microwave pulses. Figure 6 shows signals of the torch glow intensity measured with the help of a collimated photomultiplier with different sweep speeds and signals of the microwave radiation power measured by a half-

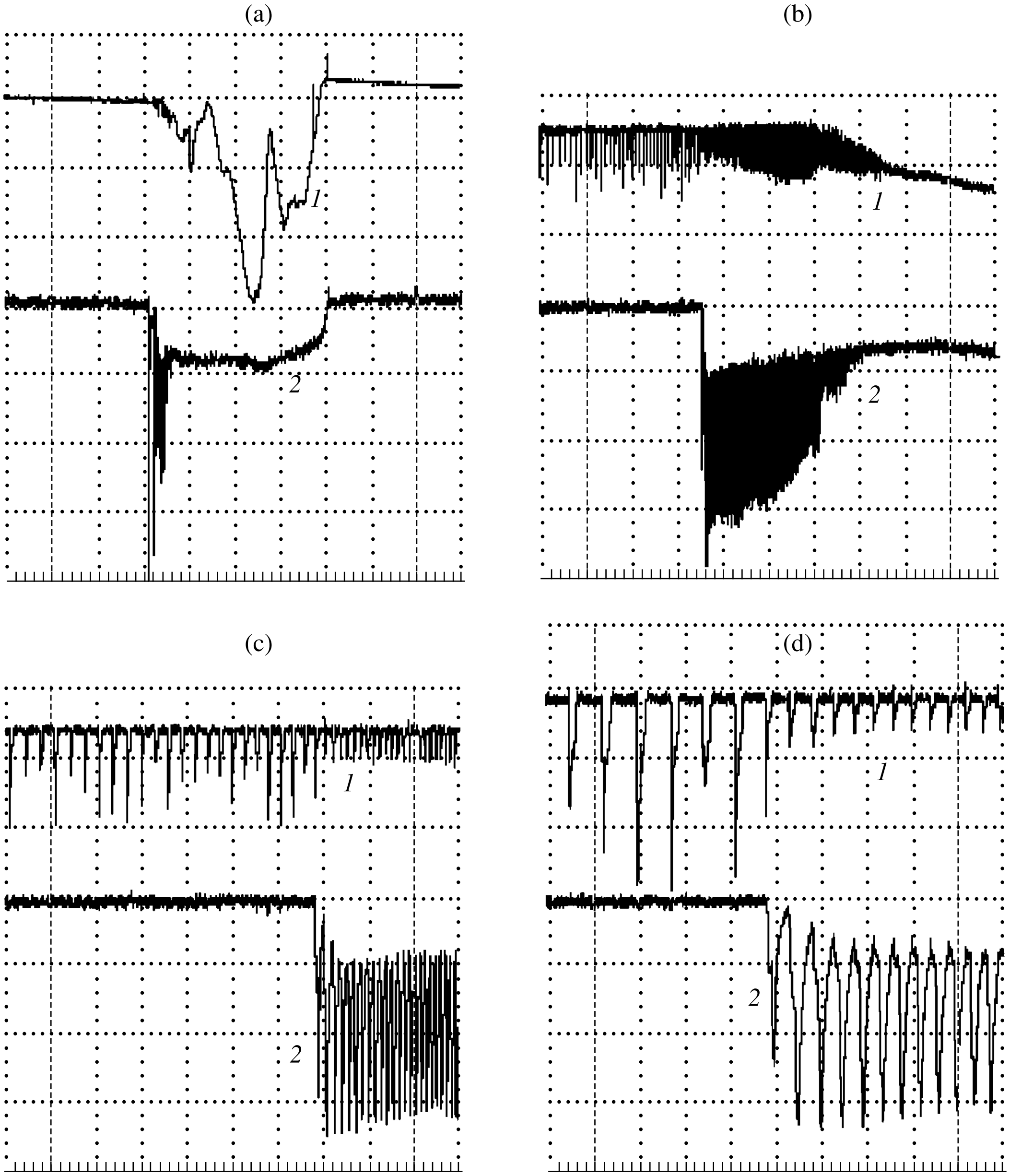

Fig. 6. Typical signals from the (*1*) microwave antenna (the voltage scales are (a) 200, (b)100, (c) 100, and (d) 50 mV/division), and (*2*) photomultiplier (50 mV/division). The time scales are (a) 2500, (b) 100, (c) 25, and (d) 10 μs/division.

wave antenna located near the torch. It follows from these signals that the magnetron initially generates short pulses with a repetition rate of 100–200 kHz. The repetition rate gradually increases over several hundred microseconds, after which the core emerges. Then, the core bursts occur synchronously with the microwave pulses. The pulse repetition rate gradually increases, and the generation goes over to a quasi-continuous mode, which lasts ≈8 ms. The glow intensity in the stage of quasi-continuous generation is several times lower than that in the stage of periodical short-pulse generation. The duration of periodical short-pulse generation, as well as the pulse repetition rate in this stage, depends on the magnetron load. The latter is a complicated nonsteady electrodynamic load that depends on the torch parameters. In the case of a completely matched load (free generation), the quasi-continuous mode is established after generating five to ten microwave pulses (Fig. 6a). In contrast, when the end of the coaxial line is short circuited, the generation is eventually suppressed, not reaching a quasi-continuous stage.

The plasma density in the torch was measured using a cw probing microwave radiation with a frequency of $\omega_d \cong 8.2 \times 10^{11}$ s^{-1} ($\lambda_d \cong 2.3$ mm). In the torch core, where the plasma density was higher, we used submillimeter ($\lambda_d \cong 337\ \mu$m) radiation of an HCN laser.

A schematic of the microwave diagnostics is shown in Fig. 2. Probing radiation generated by a horn antenna was focused by a lens onto the torch axis and was received by another antenna with the help of the second lens having the same caustic surface as the first one. The diameter of the probing beam in the waist (about 1.5 cm long) was no larger than 0.4 cm. Most of the experiments were performed with argon or nitrogen at flow rates of 5–20 l/min. The probing of the torch was performed at different distances z from the nozzle. Figure 7 shows typical signals from the detector measuring the transmitted radiation. One can see that, at distances $0 \le z \le 20$ mm from the nozzle, a significant (up to 80%) attenuation of probing radiation is observed throughout almost the entire pulse. These distances correspond to the axial length of the core. We note that the core diameter is less than the probing-beam diameter, so that only the central part of the probing beam is apparently cut off inside the core, while the peripheral part of the beam undergoes strong refraction. At $20 \le z \le 60$ mm, strong modulation (from 20 to 100%) of the transmitted signal is observed. The modulation frequency is about 1 kHz. At $z > 60$ mm (i.e., near the torch end), the modulation depth decreases, while the transmission coefficient increases. The modulation of the transmitted signal (and, hence, of the plasma density) correlates with the low-frequency modulation of the torch glow, i.e., the generation of secondary glow waves in the torch (see Fig. 5). The generation of bright dense plasma bunches moving in the direction of the gas flow is observed throughout the entire pulse (about 8 ms).

The significant attenuation of the probing microwave beam passed through the torch means that the electron density in the torch is close to or even higher than the critical density n_{ecr} (see [9]); i.e., the following inequality is satisfied:

$$n_e \ge n_{\mathrm{ecr}}, \qquad (1)$$

where

$$n_{\mathrm{ecr}} = m_e(\omega_d^2 + \nu_{em}^2)/4\pi e^2, \qquad (2)$$

and ν_{em} is the frequency of electron collisions with neutrals (atoms and molecules). In an argon plasma at atmospheric pressure, a gas temperature of $T_0 = 300$ K, and an electron temperature of $T_e \cong 1.5$–2.5 eV, the electron–neutral collision frequency is $\nu_{em}^{(0)} \cong (6.8$–$16.1) \times 10^{11}\ \mathrm{s}^{-1}$ (see [9]); i.e., according to [10, 11], we have $\nu_{em}^{(0)} \sim \omega_d$. Taking the gas heating into account obviously leads to the inequality $\nu_{em}^2 \ll \omega_d^2$, which means that the torch plasma can be considered collisionless. In view of this fact, the electron density is

$$n_e \ge n_{\mathrm{ecr}} = m_e\omega_d^2/4\pi e^2 \cong 2.1 \times 10^{14}\ \mathrm{cm}^{-3}. \qquad (3)$$

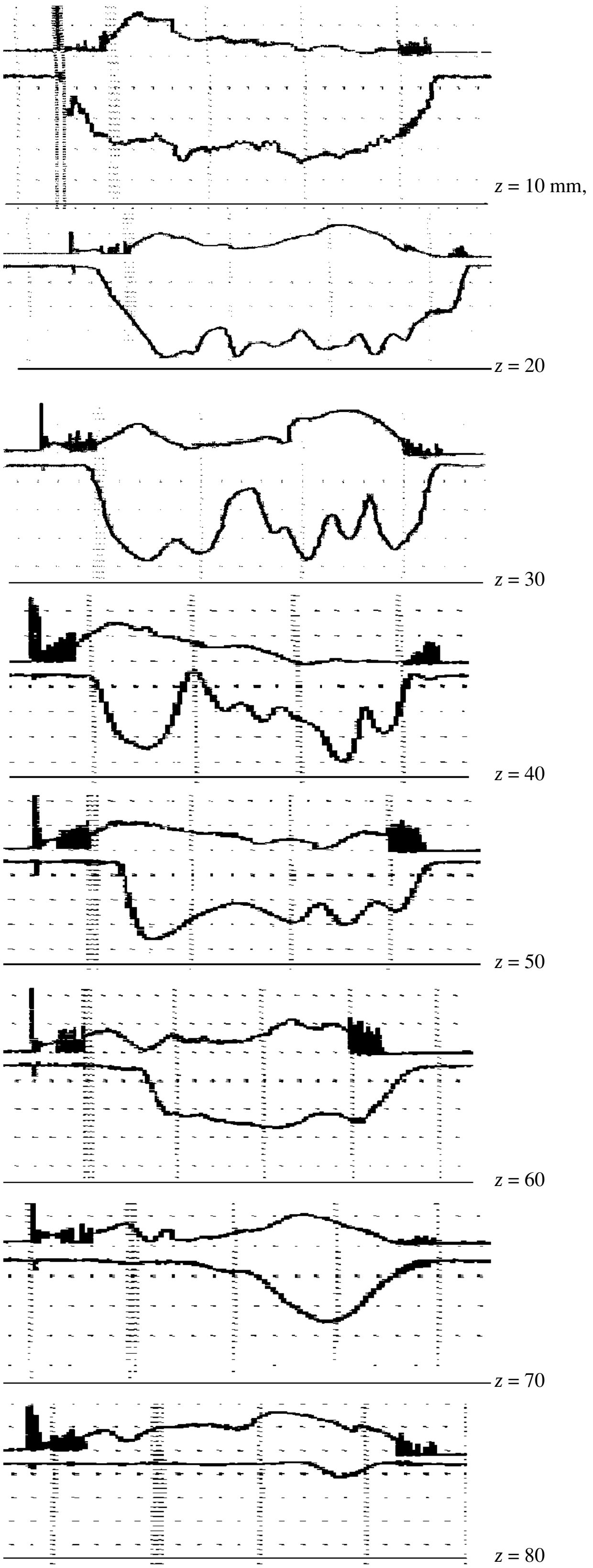

Fig. 7. Typical signals from the detectors of probing microwave radiation ($f \cong 130$ GHz) at different distances from the nozzle: (*1*) scattered and (*2*) transmitted probing radiation. The time scale is 2.5 ms/division.

Figure 2 also shows the arrangement of submillimeter diagnostics. The diameter of the HCN laser beam was lower than 3–4 mm. The critical density for the probing laser radiation was $n_{\mathrm{ecr}} \approx 10^{16}$ cm^{-3}. A significant (up to 60%) attenuation of the laser beam in an argon plasma was observed only near the nozzle. At a distance of 1 cm from the nozzle, the attenuation of submillimeter laser radiation passed through the torch did not exceed 20%, while at $z \geq 2$ cm, the probing radiation was attenuated only slightly.

Thus, the results of microwave and submillimeter probing of the microwave torch allow us to conclude that the torch consists of a core with an electron density on the order of or higher than 10^{16} cm^{-3} and a fluctuating plasma jet with a density of $n_e \cong (1–3) \times 10^{14}$ cm^{-3} downstream from the core.

4. DISCUSSION OF MEASUREMENT RESULTS

The design and the operating regimes of the microwave plasmatron described in this paper determine the specific features of the generated plasma jet (the plasma torch). First of all, this concerns the structure and parameters of the plasma jet that is produced in a coaxial waveguide when the working gas is pumped through the central electrode. The torch observed in these experiments differs from that produced in conventional devices in which the lengths of the outer and inner electrodes are approximately equal to each other [1–4]. Thus, when operating with argon, the torch consists of a bright core adjacent to the nozzle and stretched along the z axis over a distance of 1–1.5 cm and an extended plasma jet (the torch itself). The volume occupied by the plasma jet is much larger than the core volume. In conventional devices (known in the literature as coaxial TIA plasmatrons [1–4]), the torch structure is quite different: downstream from the centimeter-long plasma jet that is adjacent to the nozzle and goes beyond the end of the coaxial line, there is a recombination region in which the plasma density (and, hence, the energy deposition) decreases sharply because of a decrease in the ionization rate. In this case, the torch only partially absorbs the pump wave energy. The unabsorbed microwave power is emitted into space by the torch acting as a rod antenna. Hence, in TIA plasmatrons operating with argon, there is no specific spatial structure observed in a coaxial waveguide with a shortened inner electrode and the torch consists of a core alone. In our device, the microwave power that was not absorbed by the core produces a plasma jet adjacent to the core and propagates along the waveguide as if it were a coaxial line, because the plasma jet plays the role of the central electrode. The presence of a substantially longer (up to 10 cm) torch inside the coaxial line provides indirect evidence that, in this case, the efficiency with which microwave energy is absorbed by the plasma jet (and is eventually spent on gas heating) is higher than in TIA plasmatrons. Measurements of microwave radiation near the end of the coaxial waveguide also testify to the high efficiency of microwave energy absorption in a device with a shortened central electrode. At distances shorter than 0.5–1.0 m, the measured microwave intensity was no higher than 6 μW/m^2.

We suppose that, in our plasmatron, the boundary between the bright core and the bulk of the torch ($z \cong$ 1.0–1.5 cm) lies at the depth to which the surrounding air penetrates into the argon torch. Presumably, it is this region in which argon electronically exited in the core is quenched in reactions with nitrogen and oxygen molecules.

The experimental results show the rather complicated character of the formation and maintenance of a microwave torch in every microwave pulse. The peak radiation power in repetitive discharges is higher than the average power by a factor of κ (the off-duty factor). At an average power of 1 kW, the peak power in the plasmatron under study is about 2 kW. This facilitates gas breakdown near the sharp edge of the nozzle. However, an even more important factor facilitating the breakdown of a gas jet is the scenario by which the electrodynamic system gets into the generation mode. It was found that, in the initial stage of a microwave pulse, the magnetron generates a sequence of high-power ($P_i \cong$ 10–20 kW) spikes. After a relatively short time, the microwave spikes are accompanied by plasma bursts near the central-electrode nozzle. The transition to a pulse-periodic mode and the unusual generation behavior with a relatively low average power ($P \leq$ 1 kW) that is observed in the initial stage is typical of a system consisting of three coupled resonators (the magnetron cavity, the rectangular waveguide, and the coaxial line). This explains why a discharge can be excited in different gases at a pressure close to atmospheric pressure without applying additional initiators.

The sequence of short bursts is accompanied by the generation of an ionization wave that propagates along the z axis, thus forming the bulk of the torch. The first ionization wave in argon is followed by a sequence of waves that leave the nozzle and catch up with the first wave front.

We suppose that the bulk of the plasma jet extending along the z axis is formed by an internal surface wave, as is described in [12]. The surface electromagnetic wave produces a rod plasma electrode, which, in turn, promotes the wave propagation along the coaxial line. These self-consistent ionization and electrodynamic processes underlie the well-known surfatron mechanism for the excitation of microwave discharges [13]. The use of surface waves for the excitation of discharges assumes that the plasma electron density n_e in the torch should exceed the critical electron density n_{ecr} for microwaves propagating along the torch. Measurements of n_e performed with the help of microwave and laser interferometers confirm that this is indeed the case in our plasmatron.

To conclude, we note that steady TIA coaxial torches are described by theory in close detail (see, e.g., [12, 13]), whereas rather complicated pulse-periodic torches excited in coaxial lines require thorough theoretical analysis based on an adequate physical model.

5. CONCLUSIONS

The formation dynamics, spatial structure, and parameters of pulse-periodic microwave discharges initiated inside a coaxial waveguide have been investigated.

The microwave plasmatron under study allows the stable generation of a plasma jet (torch) in molecular and atomic gas flows and gaseous mixtures at gas flow rates of ≤100 l/min, pressures close to atmospheric pressure, and an average microwave power lower than 1 kW without applying additional initiators.

The special design of the outer coaxial electrode makes it possible to carefully examine the torch dynamics and structure.

The torch length is on the order of 10 cm. When working with argon, a specific structure has been observed: the torch itself, which is stretched along the system axis, and a relatively small bright core (with a length less than 1–2 cm) adjacent to the nozzle. The torch volume is two to three orders of magnitude greater than the core volume. The electron density in the core is as high as $\sim 10^{16}$ cm^{-3}), while the electron density in the bulk of the torch is lower than $(2–3) \times 10^{14}$ cm^{-3}.

The formation dynamics of the core and the torch itself have been examined. The occurrence of the core is apparently related to the specific operating regime of the electrodynamic system, which moves to a quasi-continuous microwave generation mode through a sequence of short (≤5 μs) and relatively high-power (up to 10–20 kW) microwave pulses. The bulk of the torch is formed by a sequence of ionization waves that originate at the nozzle due to the excitation and propagation of surface electromagnetic waves.

ACKNOWLEDGMENTS

We thank V.P. Silakov for fruitful discussions and A.A. Letunov and V.P. Logvinenko for their help in carrying out the experiments. This work was supported in part by ISTC (project no. 908) and NWO (Netherlands) (project no. 047.011.000.01).

REFERENCES

1. M. Moisan, J. Margot, Z. Zakrewski, and A. Popov, *High-Density Plasma Sources* (Noyes, New Jersey, 1995).
2. E. Rauchle, J. Phys. IV (France) **8**, Pr7-99 (1998).
3. M. Moisan, G. Sauve, Z. Zakrzewski, and J. Hubert, Plasma Sources Sci. Technol. **3**, 584 (1994).
4. Y. Mitsuda, T. Yoshida, and K. Akashi, Rev. Sci. Instrum. **60**, 249 (1989).
5. S. I. Gritsinin, I. A. Kossyi, N. I. Malykh, *et al.*, in *Proceedings of the 14th International Symposium on Plasma Chemistry, Prague, 1999*, Vol. 2, p. 675.
6. S. I. Gritsinin, I. A. Kossyi, and M. A. Misakyan, in *Proceedings of the 11th European Sectional Conference on Atomic and Molecular Physics of Ionized Gases, Miskolc-Lillafured, 2000*; ECA **24F**, 216 (2000).
7. S. I. Gritsinin, I. A. Kossyi, A. A. Letunov, *et al.*, in *Proceedings of the 15th International Symposium on Plasma Chemistry, Orleans, 2001*, Vol. 4, p. 1479.
8. N. N. Fedorov, *Fundamentals of Electrodynamics* (Vysshaya Shkola, Moscow, 1980).
9. Yu. P. Raizer, *Gas Discharge Physics* (Nauka, Moscow, 1987; Springer-Verlag, Berlin, 1991).
10. M. Hayashi, Preprint No. IPPJ-AM-19 (Nagoya Institute of Technology, Nagoya, 1981).
11. S. K. Srivastava, H. Tanaka, A. Chutjian, and S. W. Trajmar, Phys. Rev. A **23**, 2156 (1981).
12. H. Nowakowska, Z. Zakrzewski, and M. Moisan, J. Phys. D **34**, 1474 (2001).
13. Yu. M. Aliev, I. Ghanashev, H. Schluter, *et al.*, Plasma Sources Sci. Technol. **3**, 216 (1994).

Translated by E.L. Satunina

Plasma Physics Reports, Vol. 30, No. 3, 2004, pp. 263–268. Translated from Fizika Plazmy, Vol. 30, No. 3, 2004, pp. 292–297.
Original Russian Text Copyright © 2004 by Isaev, Chmil', Shustin.

LOW-TEMPERATURE PLASMA

Ion Flows from a Beam–Plasma Discharge

N. V. Isaev, A. I. Chmil', and E. G. Shustin

Institute of Radio Engineering and Electronics (Fryazino Branch), Russian Academy of Sciences,
pl. Vvedenskogo 1, Fryazino, Moscow oblast, 141190 Russia
e-mail: shustin@ms.ire.rssi.ru

Received April 1, 2003

Abstract—The results of measurements of the energy distribution function of ions escaping from a beam–plasma discharge are compared with the data from probe measurements in the discharge region. It is shown that, on the discharge axis, there is a region with a higher degree of ionization, whose position depends on the external parameters, in particular, on the gas pressure. The mean energy of the ions that leave the plasma from the outside of this region is determined by the potential of the plasma column. Inside the region with a higher degree of ionization, there is an additional mechanism for ion acceleration; as a result, the energy of the ions that leave the plasma from this region is higher than the energy of the electrostatically accelerated ions by a factor of 1.5 to 5. The results obtained show promise for creating a plasma-processing reactor with controlled ion parameters for the purposes of treating materials for microelectronics. *© 2004 MAIK “Nauka/Interperiodica”.*

1. INTRODUCTION

In order to optimize the treatment of materials in plasma-processing reactors operating at low gas pressures, it is very important to control the parameters of the ions bombarding the processed material. Thus, in devices for the ion etching of semiconductor materials in an rf discharge plasma, the ion energy distribution function (IEDF) and the angular distribution of the ions bombarding the material's surface critically affect the rate of etching and the degree of its anisotropy [1]. In order for the structure of films deposited on microelectronics materials to be highly uniform, it is very important to control the energy of the bombarding particles. Control over the parameters of the IEDF (e.g., the mean ion energy and the IEDF width) allows one to selectively affect the physical and chemical processes at a material surface; this is especially important for applications associated with the modification of surfaces [2]. Methods for controlling the shape of the IEDF have been mainly studied for plasma-processing reactors based on rf discharges. It has been shown that it can be controlled, e.g., by applying an rf bias voltage directly to the substrate [3] or by using an auxiliary electron source (either an additional discharge [4–6] or a thermal-cathode gun [7]) to inject electrons into the discharge.

It was shown in [8] that a beam–plasma discharge (BPD) in a low-pressure gas can serve as a source of ions with energies of 10 to 100 eV. In essence, a BPD is a microwave discharge induced by the fields generated in a plasma as a result of the development of a beam instability, so that the BPD parameters are close to those of microwave electron-cyclotron-resonance (ECR) discharges. However, in contrast to an ECR discharge, the BPD does not require high magnetic fields and offers the possibility of generating ion flows with more diverse spatial structures.

In this paper, we compare the results of measurements of the IEDF at the discharge periphery with the data from probe diagnostics of a BPD plasma, namely, with the electron density profile $N_e(R, L)$, the electron temperature profile $T_e(R, L)$, and the plasma potential profile $U_p(R, L)$. We will show that the energy of the ions that drift from the discharge region toward the side wall of the chamber can substantially exceed the energy acquired by the ions in the electrostatic field between the discharge plasma column and the chamber wall.

2. EXPERIMENTAL LAYOUT

A schematic of the experimental device is shown in Fig. 1. The plasma is created in a cylindrical vacuum chamber with a diameter of $2R_0 = 0.5$ m and length of 0.5 m. The chamber is filled with argon at a pressure of 0.006–0.2 Pa. The longitudinal magnetic field with an induction of $B_0 = 1$–5 mT in the chamber is produced by Helmholtz coils. An axial electron beam is generated by a Pierce-type diode gun with a planar cathode that is placed in a separate chamber connected to the main chamber by a pressure-drop tube. In the electron gun and in the drift region ahead of the plasma chamber, the beam moves in a longitudinal magnetic field with $H_d = 10$ mT (this value was adjusted experimentally in such a way that the beam current in a high vacuum was maximum). The parameters of an electron beam at the entrance to the plasma chamber are as follows: the energy is $E_b = 2$ keV, the current is $I_b = 150$ mA, and the characteristic diameter is 1–1.5 cm, the duration of the electron-gun supply voltage pulse being $\tau_b = 150$ ms. The electron collector (a graphite

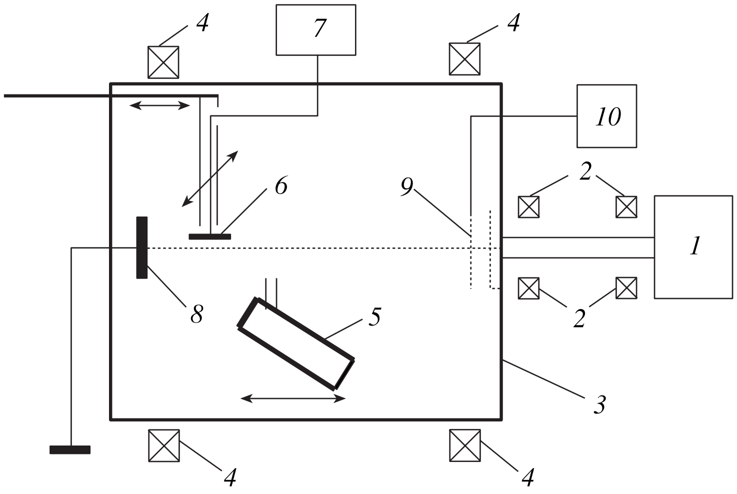

Fig. 1. Experimental layout: (*1*) Pierce gun, (*2*) beam-focusing coils, (*3*) plasma chamber, (*4*) Helmholtz coils, (*5*) ion energy analyzer, (*6*) probe, (*7*) block for recording the probe characteristic, (*8*) collector, (*9*) microwave modulator, and (*10*) microwave oscillator.

disk 10 cm in diameter) is placed at the opposite wall of the plasma chamber and is held at the wall potential.

The plasma diagnostics include a planar Langmuir probe in the form of a 3-mm-diameter tantalum disk, whose plane is oriented parallel to the chamber axis. The probe is mounted on a movable rod in order to provide measurements along the discharge axis and in the radial direction. The shape and orientation of the probe are chosen to minimize the effect of the electron beam on the probe characteristic. The electron temperature $T_e(r, L)$, plasma potential $U_p(r, L)$, and electron plasma density $N_e(r, L)$ are calculated by processing the probe characteristic in a standard way [9], namely, from the slope of the curve $\ln(I_p - I_i) = f(U)$ and from the potential and current of the probe at the inflection point of this curve (here, I_p is the probe current, U is the probe potential, and I_i is the ion current obtained from a linear approximation of the ion part of the probe characteristic). It is well known that, in the presence of an electron beam and oscillations of the plasma potential, the accuracy of determining the plasma parameters from the probe characteristic is rather low; however, it is high enough for our purposes here, because, with the experimentally obtained qualitative dependences, the conclusions drawn in this study are quite justified.

The ion flows are detected by an electrostatic analyzer with a plane deflecting mirror [10]. The analyzer is placed near the side wall of the plasma chamber and can be moved along the chamber axis. The ion collimator is oriented along the normal to the chamber axis. The analyzer is capable of recording energies in the range of 0–100 eV with a sensitivity of ~0.5×10^{-9} A/cm^2 and a resolution of $\Delta W/W_0 = 0.12$. As an analyzing voltage pulse, we use a 50-ms triangular pulse whose peak coincides with the center of the beam current pulse.

The current to the analyzer's collector is equal to

$$I_a = S(\Delta\theta/\Theta_0)J_0\int_0^\infty f_i(W)A(W)dW \tag{1}$$

$$\approx SJ_0 f_i(W)\Delta W\Delta\theta/\Theta_0 = 0.12SWJ_0 f_i(W)\Delta\theta/\Theta_0,$$

where J_0 is the total ion current density in the plane of the input window, S is the area of the receiving window of the analyzer, $f_i(W)$ is the IEDF (according to the measurement results of [8], this function can be assumed to be isotropic), $A(W)$ is the spread function, and $\Delta\theta/\Theta_0$ is the ratio of the solid angle of the input collimator to the total solid angle of the ion flow arriving at the collimator.

Hence, from the experimental data, we obtain

$$f_i(W) = \text{const}\, U(W)/R_l W,$$

where U is the measured voltage and R_l is the load resistance of the analyzer's collector.

The synchronization of the temporal processes is performed with the help of an automatic control system, which is also used to record the time dependences of the current to the analyzer's collector, the probe voltage and current, and other experimental parameters (such as the beam current and voltage, the gas pressure, and the magnetic field in the chamber). The system is based on a Labcard LC-1250 interface and consists of (i) a 12-bit analog-to-digital converter with a 16-channel multiplex and (ii) a digital output channel, which is used to generate the necessary locking signals. The software package developed for the system ensures the synchronous recording of three "fast" temporal processes, the storage of information on the experimental regime, processing of the data from the energy analyzer (the averaging over the given number of data samples,

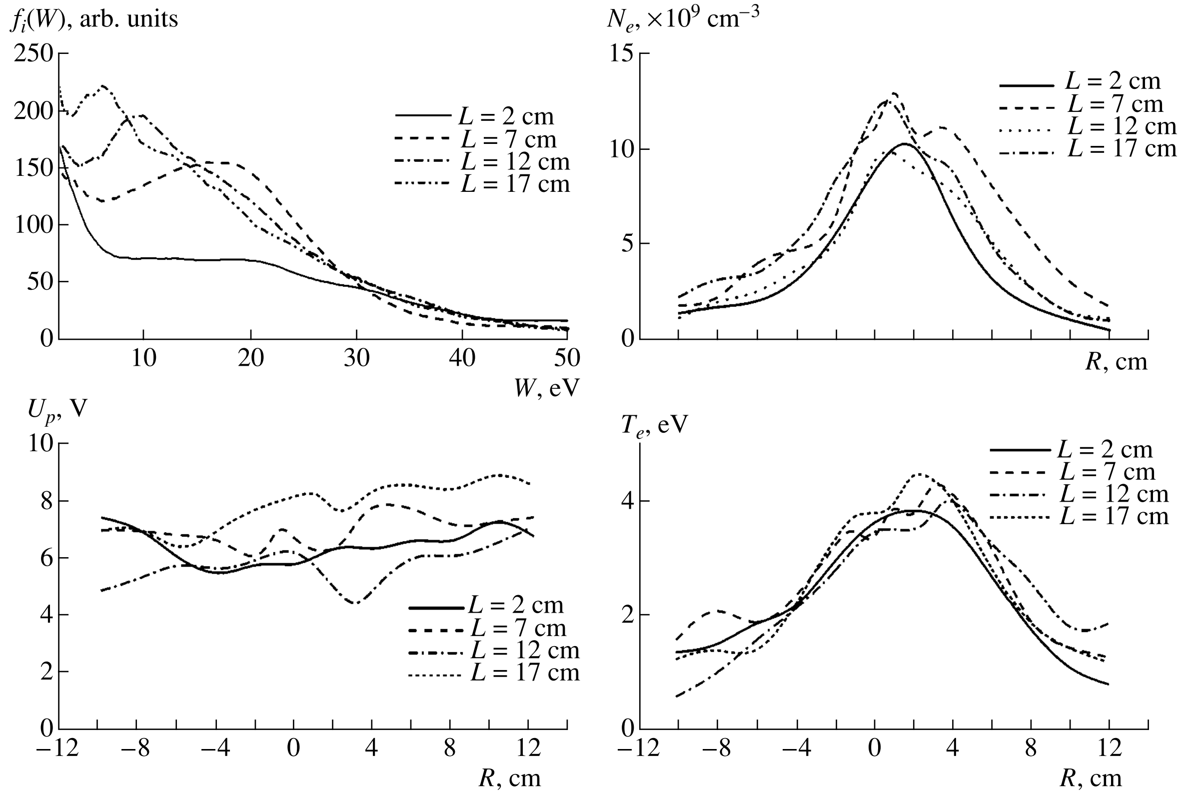

Fig. 2. Energy distribution functions $f_i(W)$ of the ions escaping from the BPD region, measured by the analyzer at different positions L along the discharge axis, and the corresponding radial profiles of the electron density N_e, electron temperature T_e, and plasma potential U_p. The discharge parameters are as follows: the electron beam voltage is 2 kV, the electron beam current is 150 mA, the magnetic field in the chamber is 3.8 mT, and the argon pressure is 0.05 Pa.

the smoothing and filtering of the curve $I(t)$, and the recalculation of this curve into the curve $I(W)$), the recovery of the probe characteristic $I(U)$ from the parametric time evolutions $I(t)$ and $U(t)$, and its processing by the algorithm described above.

In order to investigate the effect of the parameters of high-frequency instability excited in a BPD on the parameters of the ion flow, experiments were carried out with premodulated electron beams. In these experiments, the electron beam velocity was modulated by a capacitive modulator that was installed at the exit from the pressure-drop tube and had the form of a capacitive gap between two planar grids to which a microwave voltage in the 400- to 1200-MHz frequency band was supplied from a master oscillator through a coaxial cable. In order to provide circuit matching, the gap was shunted by a high-frequency resistor with a resistance of 50 Ω, equal to the wave impedance of the cable (at the working frequencies of the master oscillator, the capacitive susceptance of the gap is low compared to the shunt conductance). As a result, the modulating voltage was about 2 V = $10^{-3}U_b$. The spectrum of the generated oscillations was estimated by means of a dipole antenna placed inside the chamber.

3. EXPERIMENTAL RESULTS

Figures 2 and 3 show the IEDF measured by the analyzer at different positions L along the discharge axis. The radial profiles of the electron density $N_e(r, L)$, electron temperature $T_e(r, L)$, and plasma potential $U_p(r, L)$, obtained at the same magnetic field but at different gas pressures are also shown. (A change in the beam current above a certain threshold results in the same qualitative changes of the measured profiles as does the change in the pressure.)

An analysis of the radial profiles of $N_e(r, L)$ and $T_e(r, L)$ shows that, over a certain region along the chamber axis, ionization is more intense than in other discharge regions. In this region, the radial profile N_e is wider (it may even be double humped), the linear plasma density $\int N_e(r) r dr$ is higher, and the radial profile $T_e(r)$ is broader. It was shown in [11, 12] that, at weak magnetic fields, the gas in the BPD is mainly ionized in the region near the maximum of the high-frequency field, which increases along the discharge axis away from the injection plane of the electron beam (below, this region will be referred to as the microwave discharge region). The plasma diffuses from this region both along and across the beam path. The double-humped top of the radial

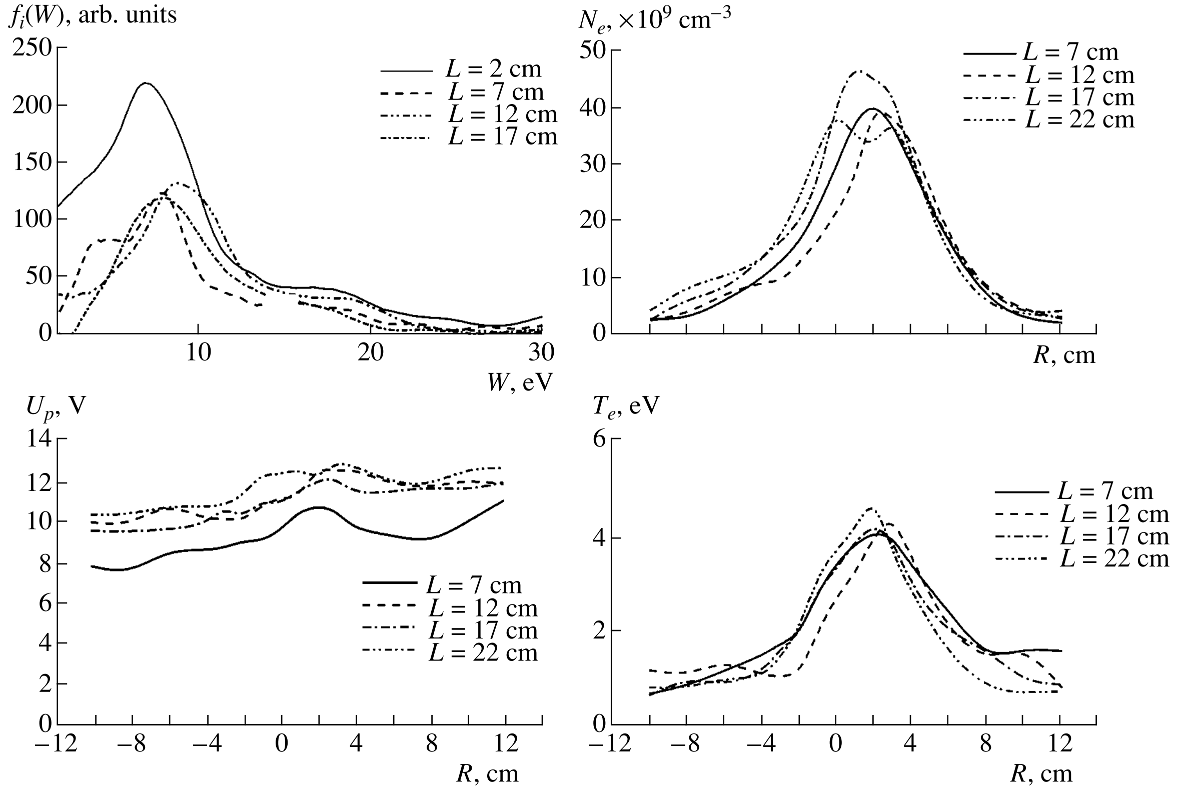

Fig. 3. The same as in Fig. 2, but for an argon pressure of 0.08 Pa.

profile of the electron density is presumably attributable to the ponderomotive force, which pushes the plasma away from the microwave discharge region. At pressures close to the threshold pressure for initiating a BPD, this region is located near the collector. As the pressure increases, this region shifts toward the electron gun.

The plasma potential changes insignificantly along the discharge region: it increases from the collector toward the electron injector, remaining everywhere no higher than 12–13 V. A distinctive feature of the transverse profiles of the plasma potential is that the potential changes abruptly in the central region of the microwave discharge, which indicates the charge separation in this region.

The energy distributions of the ions escaping from the discharge to the side wall of the chamber are markedly different within the microwave discharge region and at the periphery. At the discharge periphery, the IEDF is peaked at an energy approximately equal to eU_p. Consequently, the most probable ion velocity is determined by the acceleration of the ions in the electrostatic field between the plasma column and the chamber wall. The mean energy of the ions that leave the plasma column from the microwave discharge region is considerably higher than the energy corresponding to the plasma potential. This effect is especially pronounced at low gas pressures ($p < 0.5$ mtorr), at which the maximum ion energy is two to five times higher than the energy eU_p. However, at higher pressures, the ion flow is also observed to be “hotter”: the IEDF is enriched with higher energy ions.

Preliminary results from our investigation of the effect of the dynamic premodulation of an electron beam on the IEDF can be summarized as follows. Premodulation of the electron beam at frequencies in the spectral band corresponding to spontaneous emission of the highest spectral density from the plasma either causes high-frequency oscillations to become monochromatic or leads to the suppression of these oscillations. In both cases, the mean energy of the ion flow detected by the analyzer is observed to decrease; as a rule, this is also true for the effective temperature of the flow and for its intensity (see Fig. 4). This allows us to suggest that the mechanism responsible for the above properties of the ion flow is associated with a nonlinear conversion of the waves excited during the development of a BPD. Of course, this suggestion requires a further study.

In experiments with premodulated electron beams, we did not observe any correlation between the changes in the parameters of the ion flow and in the spectral characteristics of the low-frequency oscillations of the plasma density (these characteristics were investigated with the help of a microwave probe in the form of a helix immersed in the plasma [13]). Thus, the sugges-

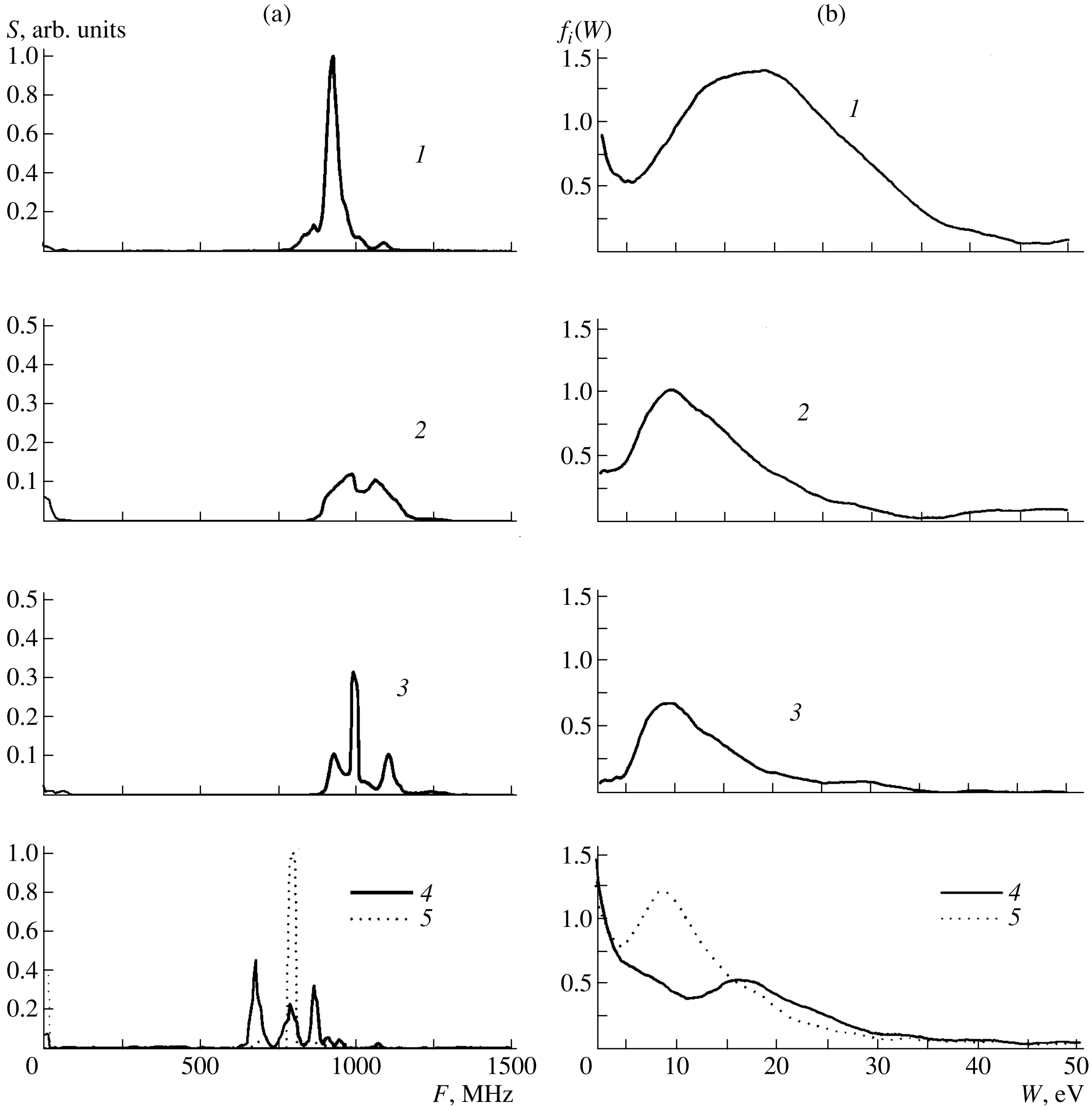

Fig. 4. (a) Emission spectra from a BPD for different electron beam modulation frequencies and (b) the corresponding energy distribution functions of the ions escaping from the discharge region. Curves *1* and *4* are for an unmodulated electron beam, while curves *2*, *3*, and *5* are for an electron beam modulated at frequencies of F_m = 950, 1000, and 800 MHz, respectively. Curves *1–3* refer to the conditions of Fig. 2, and curves *4* and *5* refer to the conditions of Fig. 3.

tion made in [8] that the ions are accelerated at the expense of intense ion oscillations in a BPD was not confirmed by our experiment.

Hence, we have shown that, by changing the external parameters of a beam–plasma discharge in the equipotential interaction chamber and by using electron beams premodulated in velocity, the energy of the ions bombarding the surface of a sample placed near the side wall of the chamber can be varied within a range of 8–50 eV. Note that it is precisely this ion energy range that is characteristic of plasma-processing reactors for surface treatment (such as deposition of thin films and etching) of materials for semiconductor electronics and acoustoelectronics.

ACKNOWLEDGMENTS

We are grateful to A.A. Rukhadze and I.M. Kotelyansky for fruitful discussions of the results obtained.

REFERENCES

1. E. Kawamura, V. Vahedi, M. A. Lieberman, and C. K. Birdsall, Plasma Sources Sci. Technol. **8**, 45 (1999).

2. M. R. Wertheimer, L. Martinu, and M. Moisan, in *Processing of Polymers*, Ed. by R. d'Agustino, F. Fracassi, and P. Favia (Kluwer, Dordrecht, 1997), p. 101.
3. L. Martinu, J. E. Klemberg-Sapieha, O. M. Küttel, *et al.*, J. Vac. Sci. Technol. A **12**, 1360 (1994).
4. N. Sato, H. Kobayashi, T. Tanabe, *et al.*, Jpn. J. Appl. Phys. B **34**, 2158 (1995).
5. R. Miyano, S. Izumi, R. Kitada, *et al.*, Plasma Sources Sci. Technol. **6**, 551 (1997).
6. D. J. Heason and J. W. Bradley, Plasma Sources Sci. Technol. **10**, 627 (2001).
7. N. J. Braithwaite, Plasma Sources Sci. Technol. **6**, 133 (1997).
8. N. V. Isaev, L. Yu. Kochmarev, and E. G. Shustin, Fiz. Plazmy **23**, 966 (1997) [Plasma Phys. Rep. **23**, 891 (1997)].
9. O. V. Kozlov, *Electrical Probe in Plasma* (Atomizdat, Moscow, 1969).
10. I. G. Kozlov, *Modern Problems of Electronic Spectroscopy* (Atomizdat, Moscow, 1978).
11. V. P. Popovich, T. A. Novskova, I. F. Kharchenko, and E. G. Shustin, Izv. Vyssh. Uchebn. Zaved., Radiofiz. **16**, 1109 (1973).
12. E. G. Shustin, Doctoral Dissertation (Institute of Radioengineering and Electronics, USSR Acad. Sci., Moscow, 1986).
13. A. A. Lisitskaya, L. I. Pangonis, A. I. Chmil', and E. G. Shustin, Prib. Tekh. Éksp., No. 2, 101 (2001) [Instrum. Exp. Tech. **44**, 224 (2001)].

Translated by G.V. Shepekina

Plasma Physics Reports, Vol. 30, No. 3, 2004, pp. 269–271. Translated from Fizika Plazmy, Vol. 30, No. 3, 2004, pp. 298–300.
Original Russian Text Copyright © 2004 by Naumov.

BRIEF COMMUNICATIONS

Pulsations of a Bunch of Charged Particles in a Penning Trap

N. D. Naumov
Central Institute of Physics and Technology, Defense Ministry of the Russian Federation,
Sergiev Posad, Moscow oblast, 141300 Russia

Received April 16, 2003

Abstract—A method has been developed for calculating the gas-dynamic parameters of the initial stage of pulsations of a nonuniform bunch of charged particles in a Penning trap. An analysis is made of the arguments given by V.A. Syrovoy in his comments [Plasma Phys. Rep. **29**, 92 (2003)] on the interpretation of the solution in the form of a uniform bunch that was derived earlier by the author. © *2004 MAIK "Nauka/Interperiodica".*

An important approach to the study of the properties of nonlinear systems is the construction of analytic solutions to equations [1]. A particle bunch in a Penning trap is a particular example of an object that is characterized by a spatially bounded distribution of charged particles and whose equation of motion admits a self-consistent solution. An exact solution to the gas-dynamic equations for a uniform spherical bunch in a Penning trap was obtained in my earlier paper [2]. In a recent paper [3], Syrovoy doubted the correctness of the interpretation that was developed in [2] in order to explain the solution. The goal of the present paper is twofold: (i) to show that, under certain conditions, the problem of a self-consistent description of the initial stage of pulsations of a nonuniform bunch of charged particles in a Penning trap reduces to that of solving two ordinary differential equations and (ii) to analyze the arguments given by Syrovoy in his paper [3].

The external field in a Penning trap is a superposition of a uniform magnetic field $\mathbf{B} = B\mathbf{e}_z$ and a nonuniform electric field whose potential in cylindrical coordinates has the form

$$\Phi = A(\rho^2 - 2z^2).$$

This electric field can be produced by a system of three hyperbolically shaped electrodes: two electrodes having hyperbolic surfaces $2z^2 = \rho^2 + 2d^2$, each held at a negative electric potential $-U$, and one electrode having a hyperbolic surface $\rho^2 = 2z^2 + 2d^2$, held at a positive electric potential U, in which case the coefficient in the expression for the electric-field potential is equal to $A = U/2d^2$.

Let us consider whether it is possible to construct a solution in the form of a spherically symmetric bunch that satisfies the equations of motion of a cold gas of charged particles in a Penning trap. We start with the following Lagrange equations for the gas motion, in which the velocity vector components in spherical coordinates are denoted by u_r, u_θ, and u_φ:

$$\frac{\partial u_r}{\partial t} - \frac{1}{r}(u_\theta^2 + u_\varphi^2)] = \frac{e}{m}[E - 2Ar(1 - 3\cos^2\theta)] + 2\Omega u_\varphi \sin\theta,$$

$$\frac{\partial u_\theta}{\partial t} + \frac{1}{r}(u_r u_\theta - u_\varphi^2 \cot\theta) = 2\Omega u_\varphi \cos\theta - 3\frac{e}{m}Ar\sin 2\theta,$$

$$\frac{\partial u_\varphi}{\partial t} + \frac{1}{r}(u_r u_\varphi + u_\theta u_\varphi \cot\theta) = -2\Omega(u_r \sin\theta + u_\theta \cos\theta),$$

where $\Omega = eB/2mc$ and E is the strength of the collective electric field.

It is easy to verify that, for $A = -m\Omega^2/6e$, possible solutions to the last two equations have the form $u_\theta = 0$ and $u_\varphi = -\Omega r \sin\theta$, in which case the first equation can be substantially simplified to become

$$\frac{\partial u_r}{\partial t} = \frac{e}{m}E - \frac{2}{3}\Omega^2 r. \qquad (1)$$

Hence, under the above conditions, an element of the gas rotates with the Larmor frequency and simultaneously oscillates in the radial direction. If the gas elements that are at the same distance from the bunch center have equal initial velocities, then they move in the same manner. Consequently, for spherically symmetric initial conditions, it is sufficient to consider only the pulsations of spherical layers of the gas in a bunch rotating as a single entity. In this case, the Lagrangian variable r is the radius of the layer: it depends on the time t and on the initial layer radius r_0, $r = r(t, r_0)$.

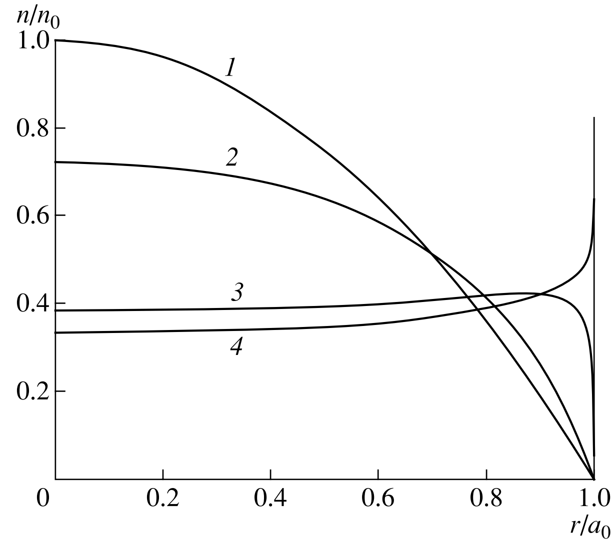

Formation of a peak in the particle density profile.

The condition for the mass of a layer in a moving gas to be conserved has the form $4\pi n(t, r_0)r^2dr = 4\pi n_0 w(r_0) r_0^2 dr_0$. This yields the following expression for the particle density:

$$n(t, r_0) = n_0\frac{r_0^2 w(r_0)}{r^2 R(t, r_0)}, \quad R(t, r_0) = \frac{\partial r(t, r_0)}{\partial r_0}. \qquad (2)$$

Under the condition that the particle layers move radially without overtaking one another, the strength of the collective electric field acting on each gas layer is determined by both its initial radial position r_0 and the prescribed initial particle density in it, $n(r, 0) = n_0 w(r)$:

$$E = 4\pi n_0\frac{e}{r^2}W(r_0), \quad W(r_0) = \int_0^{r_0} w(x)x^2dx.$$

According to Eq. (1), the radial velocity of a layer of a cold gas changes under the action of the external and collective fields (for the sake of brevity, the time derivative will be denoted by the superior dot):

$$\ddot r = \frac{\omega^2}{r^2}W(r_0) - \frac{2}{3}\Omega^2 r, \qquad (3)$$

where $\omega^2 = 4\pi n_0 e^2/m$. The initial conditions for Eq. (3) have the form $r(0, r_0) = r_0$ and $\dot r(0, r_0) = v(r_0)$, where $v(r)$ is the prescribed initial profile of the radial gas velocity.

In order to obtain the equation for the function $R(t, r_0)$, we differentiate Eq. (3) with respect to r_0:

$$\ddot R = \omega^2 w(r_0)\frac{r_0^2}{r^2} - 2\left[\frac{1}{3}\Omega^2 + W(r_0)\frac{\omega^2}{r^3}\right]R. \qquad (4)$$

This equation should be supplemented with the obvious initial conditions $R(0, r_0) = 1$ and $\dot R(0, r_0) = dv(r_0)/dr_0$.

Unfortunately, it is only up to a certain time t_k that the solutions to Eqs. (3) and (4) allow us to follow the change in the gas-dynamic parameters of a nonuniform bunch. The applicability range of the results obtained is restricted to a finite time interval because the basic condition for the particle layers to move without overtaking one another can be violated. The condition for a layer to begin overtaking another layer at the time $t = t_k$ has the form $R(t_k, r_0) = 0$, which indicates that, at this time, the particle density approaches infinity (this effect was called the gradient catastrophe [1, 4]).

The formation of a peak in the radial profile of the plasma density in the bunch is illustrated in the figure, which shows the particle density calculated from formula (2) and Eqs. (3) and (4) at the dimensionless times $\tau = 0.5$ (curve *2*), $\tau = 1$ (curve *3*), and $\tau = 1.12$ (curve *4*). The dimensionless time is defined as $\tau = \Omega t$. Curve *1* in the figure gives the initial particle density profile

$$w(r) = \begin{cases} 1 - (r/a_0)^2, & r \le a_0 \\ 0, & r > a_0, \end{cases}$$

where a_0 is the initial radius of the bunch. The calculations were carried for $v(r) = 0$ and for the condition $\omega^2 = 5\Omega^2$, which, in view of Eq. (3), reflects a balance of forces between the space charge and external field for the surface gas layer.

For a uniform bunch, we have $w(r) = H(1 - r/a_0)$, where $H(x)$ is the Heaviside step function. In this case, Eqs. (3) and (4) take the form

$$\ddot r = \frac{1}{3}\omega^2\frac{r_0^3}{r^2} - \frac{2}{3}\Omega^2 r, \qquad (5)$$

$$\ddot R = \omega^2\frac{r_0^2}{r^2} - \frac{2}{3}\left(\Omega^2 + \omega^2\frac{r_0^3}{r^3}\right)R. \qquad (6)$$

According to Eqs. (5) and (6), the function $f = R - r/r_0$ should satisfy the equation

$$\ddot f + \frac{2}{3}\left(\Omega^2 + \omega^2\frac{r_0^3}{r^3}\right)f = 0. \qquad (7)$$

If the initial velocity is proportional to the distance from the center of symmetry of the bunch, $v(r) = kr$ (where k is a constant), then the initial conditions for this function have the form $f_0 = 0$ and $\dot f_0 = 0$.

Equation (7) can be regarded as the equation of motion of an oscillator with a varying frequency. As is known [5], the dynamical parameters of such an oscillator depend linearly on their initial values. Since, in the case in question, the dynamical parameters are initially equal to zero, the function f will remain zero at any time t: $f \equiv 0$; i.e., we have $\partial r/\partial r_0 \equiv r/r_0$, which yields $r(t, r_0) = r_0 R(t)$.

Hence, the problem of calculating the pulsations of a uniform bunch reduces to that of solving an ordinary differential equation for the function R,

$$3\ddot{R} + 2\Omega^2 R - \frac{\omega^2}{R^2} = 0 \tag{8}$$

with the initial conditions $R_0 = 1$ and $\dot{R}_0 = k$. For the gas-dynamic parameters of a uniform bunch, we obtain

$$\begin{gathered} n = \frac{n_0}{R^3}, \quad u_r = r_0 \dot{R}, \quad u_\theta = 0, \\ u_\varphi = -\Omega r_0 R \sin\theta. \end{gathered} \tag{9}$$

Let us now analyze the arguments given by Syrovoy [3] in his interpretation of the solution derived in my earlier paper [2], in which the problem of pulsations of a uniform bunch of charged particles in a Penning trap was considered by means of the Eulerian approach to describing gas motions. In Cartesian coordinates, the motion of a gas element in a uniform bunch can be described by the following equations (which are written in the notation of [3] for clarity):

$$x = \alpha x_0 + \beta y_0, \quad y = \mu x_0 + \nu y_0, \quad z = \kappa z_0.$$

In order for the spherical surface at which a gas element occurs at the initial time to keep its spherical shape during the gas motion, the five functions $\alpha(t)$, $\beta(t)$, $\mu(t)$, $\nu(t)$, and $\kappa(t)$ should also satisfy the conditions

$$\begin{gathered} \alpha\mu + \beta\nu = 0, \\ \alpha^2 + \beta^2 = \mu^2 + \nu^2 = \frac{1}{\kappa^2}(\alpha\nu - \beta\mu)^2. \end{gathered} \tag{10}$$

Since these functions are uniquely determined by the equations of motion, it seems that three additional conditions (10) are impossible to satisfy. Syrovoy [3] decided that this was a contradiction and concluded that the solution to the gas-dynamic equations that was obtained in [2] can be regarded as true but should be interpreted in a manner different from that given in [2]. Specifically, he proposed to understand the solution as describing oscillations of the density of an electron flow (or, in his terminology, of an "infinite uniform beam"). The solution to the gas-dynamic equation for the distribution of charged particles that corresponds to such a beam was considered by Syrovoy in his earlier paper [6].

However, the solution obtained in [2] does not actually lead to a contradiction. The above five functions are determined by the equations of motion and, according to expressions (9) for the gas-dynamic parameters of a uniform bunch, have the form

$$\alpha = \nu = R\cos\Omega t, \quad \beta = -\mu = R\sin\Omega t, \quad \kappa = R,$$

in which case conditions (10) become identities. Setting $r_0 = a_0$, we see that the function R characterizes the time dependence of the bunch radius: $a(t) = a_0 R(t)$.

Hence, the problems considered in [2] and in [6] are physically different. It can be said that the solution obtained in [2] is a new solution to the gas-dynamic equations for a spatially bounded configuration of a gas of charged particles.

Syrovoy [3] also doubted whether the use of the term "self-similar motion" in [2] is justified. In this connection, it is instructive to recall the definition of this term given in a familiar book by Ya.B. Zel'dovich and Yu.P. Raizer [7]: "… the motion during which the profiles of the gas-dynamic quantities remain similar to themselves and change only at the expense of changes in the scales of the quantities is called self-similar or automodel." In the Eulerian approach, the gas-dynamic parameters of a uniform bunch of charged particle in a Penning trap can be represented as

$$\begin{gathered} n = \frac{n_0}{R^3} H(1-\xi), \quad V_r = \xi \dot{R} H(1-\xi), \\ V_\theta = 0, \quad V_\varphi = -\Omega R \xi \sin\theta H(1-\xi), \end{gathered}$$

where $\xi = r/R$. As is seen, the pulsations of the bunch satisfy Zel'dovich and Raizer's definition of the self-similar motion. In [2], an analogous representation was obtained for the gas-dynamic parameters of a bunch in Cartesian coordinates.

REFERENCES

1. A. A. Samarskii and A. P. Mikhailov, *Principles of Mathematical Modeling: Ideas, Methods, Examples* (Nauka, Moscow, 1997; Taylor & Francis, London, 2002).
2. N. D. Naumov, Fiz. Plazmy **19**, 1406 (1993) [Plasma Phys. Rep. **19**, 738 (1993)].
3. V. A. Syrovoy, Fiz. Plazmy **29**, 101 (2003) [Plasma Phys. Rep. **29**, 92 (2003)].
4. V. P. Bykov, A. V. Gerasimov, and V. O. Turin, Usp. Fiz. Nauk, No. 8, 955 (1995) [Phys. Usp. **38**, 911 (1995)].
5. A. I. Baz', Ya. B. Zel'dovich, and A. M. Perelomov, *Scattering, Reactions, and Decays in Nonrelativistic Quantum Mechanics* (Nauka, Moscow, 1971).
6. V. A. Syrovoy, Radiotekh. Élektron. (Moscow) **29**, 2430 (1984).
7. Ya. B. Zel'dovich and Yu. P. Raizer, *Physics of Shock Waves and High-Temperature Hydrodynamic Phenomena* (Nauka, Moscow, 1963; Academic Press, New York, 1967).

Translated by O.E. Khadin

Plasma Physics Reports, Vol. 30, No. 3, 2004, pp. 272–273. Translated from Fizika Plazmy, Vol. 30, No. 3, 2004, pp. 301–302.
Original Russian Text Copyright © 2004 by Baranov, Muromkin, Shafranov.

In Memory of Aleksandr Ivanovich Karchevskiĭ (April 26, 1931–August 31, 2003)

Aleksandr Ivanovich Karchevskiĭ, a remarkable experimental physicist, professor, and the head of the Laboratory of New Methods of Isotope Separation at the Institute of Molecular Physics of the Russian Research Centre Kurchatov Institute, died tragically on August 31, 2003, in Siberia as the result of an accident during his vacation.

Aleksandr Ivanovich Karchevskiĭ was born April 26, 1931 in the village of Emilovka, Odessa oblast. In 1945, his family moved to Lvov. In 1948, he graduated from school with honors and enrolled at the Physicotechnical Faculty of Moscow State University. In 1951, part of the faculty (including Karchevskiĭ) was attached, by government decree, to the Moscow Institute for Physics and Technology (MIPT; at that time, the Moscow Mechanical Institute). After graduating from MIPT in 1954, he began work at the Atomic Energy Institute, in the Department of Heat Control Apparatus (the future Institute of Molecular Physics) headed by I.K. Kikoin (a colleague of I.V. Kurchatov in the field of nuclear research), where he engaged in studies on solid-state physics. In 1957, Karchevskiĭ joined the investigations on magnetic confinement of high-temperature plasma in a relatively small ZETA-type toroidal device. Later, he carried out a series of experiments on the auxiliary heating of a toroidal plasma by compressing it by an external magnetic field. The results of these experiments were reported at the First IAEA Conference on Controlled Nuclear Fusion (Salzburg, 1961).

At the same time, Karchevskiĭ continued his participation in Kikoin’s seminar on solid-state physics. There, he chose the subject for his candidate’s thesis: measurements of the isotopic shift of the Curie point in passing from uranium hydride to uranium deuteride. He worked on his thesis in the evening hours and on Sundays (at that time, Saturday was not yet a day off), while his daytime hours were occupied by studies on fusion research problems. The difference between the Curie temperatures was determined very precisely: Karchevskiĭ succeeded in measuring the magnetocaloric effect in both compounds. This is still the most reliable method for determining the Curie point in ferromagnetics. In the autumn of 1961, Karchevskiĭ defended this candidate’s thesis on this subject.

Kikoin held the scientific activity of Karchevskiĭ in high esteem. In 1962, he became the youngest division head at the Institute of Molecular Physics and held this position for more than ten years. Under his leadership, a large-scale magnetic mirror device was created. Since 1965, he concentrated mainly on the study of current instability in plasmas. His experiments in this field continued up to the beginning of 1970s. During this period, he performed a comprehensive study of the conditions for the formation of pulsed electron beams in gas discharges. In 1971, Karchevskiĭ defended his doctoral thesis on the problem of “Experimental Investigations of High-Current Toroidal Discharges and Current Instability.”

At the beginning of 1970s, Kikoin invited Karchevskiĭ to investigate the basic subject of the Institute of Molecular Physics: the development of new methods for isotope separation, including plasma methods. Karchevskiĭ accepted his offer and devoted more than thirty years to this subject.

His first success in the field of plasma methods of isotope separation was the observation of isotope enrichment of xenon in two types of discharge: a steadstate RF discharge in a running magnetic field and a pulsed discharge in crossed electric and magnetic fields (pulsed plasma centrifuge).

Although these methods for isotope separation have not found application in the isotope industry because of their high energy expenditure, Karchevskiĭ, being a talented researcher, discovered many new effects related to the diffusion and magnetohydrodynamic processes occurring in gas discharges. Observations of isotope separation effects became a new method of plasma diagnostics.

Simultaneously, Karchevskiĭ carried out experiments on the selective dissociation of uranium hexafluoride under the action of infrared laser radiation. For the rest of his life, he continued experiments on the selective dissociation of various molecules.

Karchevskiĭ devoted the last ten years of his life to experiments on isotopically selective ion-cyclotron resonant (ICR) plasma heating. He considered ICR separation to be the only method (of all the other new ones) that can be implemented in the isotope separation industry in the near future. Despite his ironic treatment of inventors, he himself introduced substantial improvements in this method. It was the problem of creating a pilot device for ICR isotope separation in which Karchevskiĭ was actively engaged before his fatal trip to Siberia.

Karchevskiĭ always aspired to transmit his experience and knowledge to his colleagues. Many candidate's and doctoral theses were prepared under his supervision. For some time, Karchevskiĭ successfully taught at MIPT; he left this work only at the request of Kikoin, who insisted that nothing should distract him from experiments. For several decades, Karchevskiĭ edited the section on plasma physics in the abstract journal *Fizika*.

Karchevskiĭ possessed amazing energy. Many people remember his work as a scientific secretary of the seminar on the problem of controlled nuclear fusion headed by M.A. Leontovich (before Leontovich, this seminar was headed by Kikoin). No one will ever know how many telephone calls were made by Karchevskiĭ to the different regions of the Soviet Union.

Karchevskiĭ spent a great deal of time and energy on the development of international collaboration. His laboratory carried on experiments in cooperation with laboratories of the Research Center at Saclay and the Tokyo Institute of Technology for several years. He had many friends among European and American scientists. By invitation of his American colleagues, he presented a report at the Oak-Ridge National Laboratory on the method of ICR isotope separation.

For his long and productive work, Karchevskiĭ was rewarded diplomas, premiums, and other awards. He was a man of great authority among his colleagues and friends. Everyone admired his love of life. He knew literature, history, and art very well. He never missed any worthwhile event held at the Recreation Center of the Kurchatov Institute. He recorded the performances with a tape recorder and distributed these recordings among his friends and acquaintances. He always came to the aid of the people around him in their hours of need. It turned out, however, that in the last, tragic moments of his life, Karchevskiĭ was alone.

He loved nature and, for many years, spent his vacations floating on a boat down the Bakhta river (a tributary of the Yenisei) together with his friends. This is a difficult and breathtaking route: the riverbed is broken by rapids and gorges. Many times, Karchevskiĭ braved these rapids together with his wife and, once, with his favorite granddaughter, who was only eleven that time. This year, he had to go alone because at the last moment, his partner could not joint him. Karchevskiĭ believed that he was sufficiently prepared for such a trip and did not care to abandon it in changed circumstances. At the end of the second day of his trip, having landed safely on the shore, he, as usual, decided to spend the night in a hunting lodge. He knew well the locations of such lodges along the river. At the entrance to the one he chose, someone had installed a *samostrel*.[1] The wound turned out to be fatal.

The memory of Aleksandr Ivanovich Karchevskiĭ will always remain in the hearts of all those who were lucky enough to know this vigorous, cheerful, and hardworking man.

On behalf of all the friends and colleagues
of A.I. Karchevskiĭ,
V.Yu. Baranov, Yu.A. Muromkin, and V.D. Shafranov

---

[1] A fixed, large-caliber gun aimed at the entrance. Such a gun is used to keep bears from entering a lodge, with a mandatory note posted at the door to warn people. The inquiry has shown that there was no such note. For many years, Karchevskiĭ had spent his vacations on the Bakhta river, but had never encountered a *samostrel* in a hunting lodge before.

Plasma Physics Reports, Vol. 30, No. 3, 2004, pp. 274–275. Translated from Fizika Plazmy, Vol. 30, No. 3, 2004, pp. 303–304.
Original Russian Text Copyright © 2004 by Shafranov.

In Memory of Marshall Nicholas Rosenbluth (February 5, 1927–September 28, 2003)

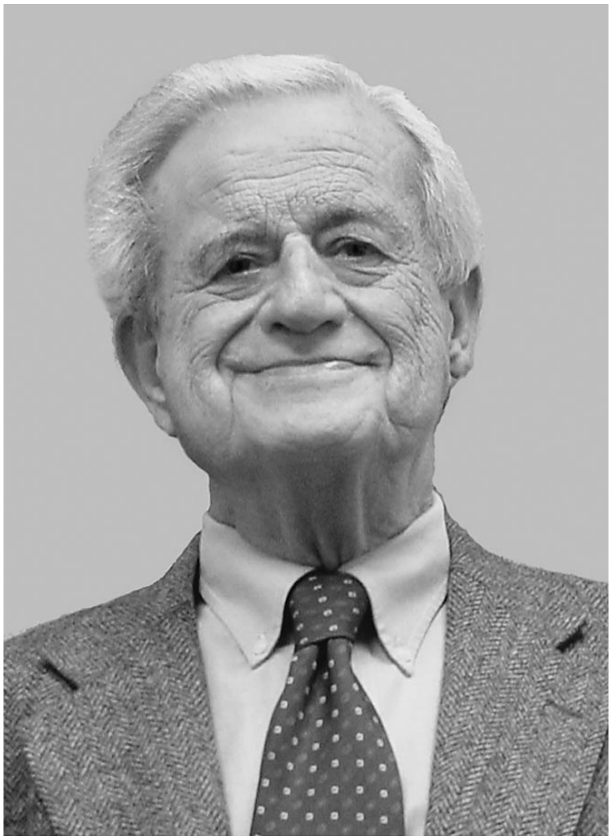

Marshall Nicholas Rosenbluth, an eminent physicist who made an invaluable contribution to the development of high-temperature plasma physics and controlled magnetic fusion research, died on September 28, 2003 in San Diego.

Marshall Rosenbluth was born February 5, 1927 in Albany, N. Y., into a middle-class family. His grandfather had emigrated to America from Odessa at the end of the 19th century. Marshall's father was a friend of New York Governor Franklin Roosevelt, the future president of the United States. There is even a children's photo of Marshall with Eleanor Roosevelt in Rosenbluth's family archive.

Marshall was a very talented student. When he was fifteen years old, he was enrolled at Harvard University. At the age of eighteen, he took an associate bachelor degree and went on to study physics at the University of Chicago. He served for a year as a radio operator on a warship participating in military operations against Japan. After demobilization, he continued studying at the University of Chicago. Among his teachers were those who had recently helped to invent the atomic bomb. Thus, he defended his doctoral thesis before Enrico Fermi and Edward Teller in 1949. In 1950, Teller recruited Dr. Rosenbluth to join the Los Alamos National Laboratory, where he took part in creating the hydrogen bomb. Dr. Rosenbluth also participated in the first tests of the H-bomb. In 1952, the night before the scheduled explosion, he realized that the scientists had made a serious mistake that could have resulted in a dud. The problem was soon fixed with a new explosive core. In 1954, again in the South Pacific, Dr. Rosenbluth was aboard a U.S. Navy destroyer when a hydrogen bomb test turned out to be unexpectedly strong and showered his ship with radioactive fallout. Soon after this sobering test, he reflected on using nuclear fusion for peaceful ends. His first idea was to use a pinch discharge in which deuterium-tritium plasma was to be compressed by a magnetic field. The magnetic flux, detaching along with the plasma from a conductive cylindrical wall, was also to stabilize the plasma column (it turned out, however, that this was insufficient to completely stabilize the plasma).

In 1956, Dr. Rosenbluth joined General Atomics in San Diego, where he began to work on the problem of controlled nuclear fusion. Dr. Rosenbluth became widely known as a theorist after the Third International Conference on Phenomena in Ionized Gases (Venice, 1957), where he presented a report on a stabilized pinch—a subject of controlled fusion research, which was top secret that time. An extended version of this report was presented at the Second International Conference on the Peaceful Uses of Atomic Energy (Geneva, 1958); by that time, all studies on controlled fusion research had already been declassified.

The problem of creating an electrical energy generator based on controlled fusion reactions turned out to be even more complicated than was thought by the most skeptical critics of the idea. Very soon, it became evident that the physics of the magnetic confinement of rarified high-temperature plasma needed to be examined in more detail, which would require many more years of intensive developmental work.

His subsequent theoretical works on the physics of high-temperature plasma brought him to the forefront of plasma physics theory. At the First International Conference on Plasma Physics and Controlled Nuclear Fusion (Salzburg, 1961), Dr. Rosenbluth was given the honor of surveying the theoretical studies presented at this conference (the review of the experimental works was made by Lev Artsimovich).

The later works by Dr. Rosenbluth on the theory of magnetic plasma confinement gained wide recognition. In particular, he investigated the flute plasma instability in open systems (with Conrad Longmire), the suppression of instabilities by an “average magnetic well” in periodic magnetic mirror devices (with Harold Furth), the stabilization of flute perturbations by the finite-Larmor-radius effect (with Nicholas Krall and Norman Rostoker), oscillations of a rotating plasma (with Albert Simon), cone instability (with Richard Post), and the trapped particle-driven instability in open systems (with Herbert Berk *et al.*). As a rule, he concentrated on the instabilities that were most important for the physics of plasma confinement, rather than merely wandering the length and breadth of the boundless field of plasma instabilities. He proposed an original method of integrating along the trajectories of the collisionless kinetic equation. This method, which found broad application in the physics of rarified high-temperature plasmas and is now widely used to analyze plasma instabilities, has been recognized as classical. The Rosenbluth potential technique is widely applied to evaluate the collision integral in the plasma kinetic theory.

In 1960, Dr. Rosenbluth became a professor at the University of California at San Diego. In 1967, he joined the Institute for Advanced Study at Princeton. From 1980 to 1987, he directed the Institute for Fusion Studies at the University of Texas. In 1987, he returned to San Diego, where retired in 1993 as an emeritus professor of physics. He had been the chief US expert on the ITER project since 1992.

The range of Dr. Rosenbluth’s scientific interests was very wide. He made many important discoveries concerning the physics of essentially all types of magnetic confinement systems, such as mirror devices, cusps, bumpy tori, and tokamaks. These discoveries still serve as the classical basis for present-day plasma physicists.

Dr. Rosenbluth had a unique ability to generate new ideas, as well to grasp the ideas of his colleagues and present them in an extremely clear and perfect form. He trained a school of remarkable theorists in plasma physics. Under his leadership as the chief US expert on the ITER project, practical recommendations were elaborated on how to prevent undesirable effects during the operation of a tokamak reactor. For example, the escape of runaway electrons onto a tokamak wall can have disastrous results. Dr. Rosenbluth and his colleagues proposed an elegant mathematical model describing the propagation of a liquid hydrogen jet injected into a hot plasma in order to prevent the runaway effect. The model was also capable of describing the phenomena accompanying this propagation (the instability of jet evaporation, cavitation, decay of the jet into drops, etc.). Recommendations were also given on how to use this method in existing tokamaks and the future ITER reactor.

Marshall Rosenbluth was a very kind and sympathetic man. During his infrequent visits to Russia, he very much took our problems to heart; thus, he was deeply concerned for the fate of Andrei Sakharov. Once, while staying in Moscow, he organized a letter of support to a seriously ill American physicist from his Russian colleagues.

It is difficult to believe that Marshall is no longer with us.

V.D. Shafranov[1]

---

[1] In preparing this obituary, I used the article by William J. Broad *M.N. Rosenbluth, 76, an H-Bomb Developer Who Sought Peaceful Uses for Fusion, is Dead* (The New York Times, September 30, 2003). I am grateful to V.V. Arsenin, A.V. Timofeev, V.P. Pastukhov, and S.V. Putvinskiĭ for their help in preparing the obituary.